UNIVERSITY OF CALIFORNIA

Los Angeles

Characterizing Low-mass Stars and Brown Dwarfs and Upgrading NIRSPEC

A dissertation submitted in partial satisfaction
of the requirements for the degree
Doctor of Philosophy in Astronomy

by

Emily Catherine Martin

2018

ABSTRACT OF THE DISSERTATION

Characterizing Low-mass Stars and Brown Dwarfs
and Upgrading NIRSPEC

by

Emily Catherine Martin
Doctor of Philosophy in Astronomy
University of California, Los Angeles, 2018
Professor Ian S. McLean, Chair

This dissertation combines near-infrared spectroscopic and astrometric analysis of low-mass stars and brown dwarfs with instrumentation work to upgrade the NIRSPEC spectrometer for the Keck II Telescope. The scientific goals of my thesis are to discover and characterize the physical properties of brown dwarfs, the lowest-mass (<0.08 M_{Sun}) products of the star formation process. These relatively cold objects ($T_{\rm eff}$< 2500K, compared to $T_{\rm Sun}$ ∼5800K) emit the bulk of their light in the infrared. Project I of my thesis used near-infrared spectroscopy from NIRSPEC to study the surface gravities of 228 low-mass stars and brown dwarfs in the NIRSPEC Brown Dwarf Spectroscopic Survey (Martin et al., 2017). Project II utilizes imaging data from the Spitzer Space Telescope to study the coldest and lowest-mass brown dwarfs. I measure distances to 22 late-T and Y dwarfs and use those distances to measure absolute physical properties. Project III encompasses my work to upgrade the NIRSPEC instrument and compliments my scientific research interests. My work on the upgrade includes project management, infrared detector characterization and testing, optical design of the new slit-viewing camera, electronics design, and mechanical testing and prototyping (see Martin et al., 2014, 2016).

The dissertation of Emily Catherine Martin is approved.

Michael P. Fitzgerald

J. Davy Kirkpatrick

Edward L. Wright

Edward Donald Young

Ian S. McLean, Committee Chair

University of California, Los Angeles

2018

To my parents, whose love and support for me
extends to the edge of the universe and back.

TABLE OF CONTENTS

LIST OF FIGURES

LIST OF TABLES

ACKNOWLEDGMENTS

As my advisor Ian says, instrumentation is a team effort, and that truth extends to the entirety of my studies. So many people were helpful to me throughout this journey, and this short section only grazes the surface of my gratitude!

First, to my Ph.D. advisors, Ian McLean and Mike Fitzgerald, thank you both for your patience and continued confidence in me. Ian, what an honor it has been to be your last graduate student! I remember how excited I was to start working with the man who literally wrote the book on astronomical instrumentation, and the experience has more than lived up to my expectations. I am so grateful I got to train with you. Thank you for supporting me, encouraging me, and for building and leading a lab where students can thrive and great instruments get built. Mike, thank you for your quiet guidance and belief in me throughout my graduate career. Thanks for giving me the space to make mistakes and learn from them, for giving me the opportunity to help lead a project, and for pushing me when I doubted myself.

To my IR Labmates: I couldn't ask for a better group of people to work with. We've had our ups and downs, but I am so grateful to you all for being patient and flexible about working with students, and letting me get my hands dirty! Ted Aliado, John Canfield, Chris Johnson, Evan Kress, Ken Magnone, Ji Man Sohn, Eric Wang, and Jason Weiss, thank you all for your friendship and your help over the years.

To the folks at IPAC: Davy Kirkpatrick, I am so grateful that I got to work with you! You are an excellent mentor and your support came along at the right time. Thanks for being willing to troubleshoot with me, for your endless patience, and the fun word games and book discussions! Chas Beichman, thank you for all of the opportunities and doors you have opened for me! From laser combs to observing on Keck, I am thankful for your support. Ricky Smart, thanks for sharing your astrometric expertise with me.

To Ned Wright and Ed Young, thank you both for being on my committee and generously

providing your time and expertise.

To my mentors: Smadar Naoz, you are a blessing to the UCLA community. Within a few short years you have already made such a positive impact and there are so many of us who are grateful to you! Thank you for being my mentor and for listening to my rants and raves, my insecurities, and my triumphs with a kind ear. Greg Mace, you are a gem. Thanks for being a voice for inclusion in our community, for mentoring me through my first scientific research project, and for your continued support. You are an excellent role model!

To my fellow UCLA graduate students: our community is one of my favorite things about UCLA and I am grateful to have been part of it! In particular, I would like to thank: Sarah Logsdon, my lab sister and one of my best friends, I could not have survived grad school without you! Thank you for putting up with my 4 am observing silliness (craziness)? and for being my shoulder (and couch) to cry on. Anna Boehle, you were one of my first friends when I got to UCLA and I'm so glad I got to work with you in the lab, too! Thanks for being my knitting buddy and fellow cat lover. Breann Sitarski, I triangle you! I am so thankful for your friendship and for girl talk and having you to look up to as a strong, smart, confident woman in instrumentation. Adam and Marissa Greenberg, thank you for the countless Shabbat dinners and your endless support; your friendship means so much to me. Pauline Arriaga, thank you for saving me multiple times with your LaTeX and python powers! I've enjoyed mentoring you and am so grateful for your friendship and support. Alex Latshaw, thanks for keeping me sane during WIPA meetings and events!

Linda Antinone, you taught me how fun it is to do physics! Thank you for encouraging me to pursue a career in STEM and for giving me one of my first teaching opportunities.

Jennifer Marshall and Darren DePoy, I cannot thank you enough for the incredible opportunities you offered me in the lab. Thank you for your continued support throughout my career and for introducing me to my passion for instrumentation. When I look back now on how little I knew when I worked in your lab, I am so grateful for the way you let me learn things on my own, albeit slowly, and for all of the patience and effort you put in to training an undergraduate!

To my friends who support me and help me to grow: Krista Grimes, Louise Nordlander Svensson, Michael Ip, Amanda Friese, Kotrina Kajokaite, Mary and Conrad Friesen, Sara Lerner, Kevin Weng and Hannah Howard, Rachel and Brett Dahlenburg, Angelisha Lilly, Gary Chen and May Wang, and many more, thank you for the good times and fun adventures!

Lastly and most importantly to my family, my backbone and my cheering section! I am lucky to have a wonderful extended family on both sides. Thanks to my fantastic grandparents Granny and Papaw, and Babu and Bibi, for loving me and supporting me always, even when I move far away! Maggie and Jason, you are the best sister and brother-in-law I could ask for. I love that we continue to have a strong connection despite the distance. Mom and Papa, words cannot express how lucky I am to be your daughter. You are some of the best parents in the universe; I would know, because I've searched it! Thank you for giving me space to grow, encouraging me and Maggie to develop into strong, independent women, and gently showing us how to open our minds. You two are my ultimate role models in how to be compassionate, kind, and impactful citizens of the world. Thanks for teaching me the value of the great outdoors, being a goofball, and taking care of myself. I couldn't have done it without you!

Chapter 2 of this dissertation contains material from Martin et al. (2017), *Surface Gravities for 228 M, L, and T Dwarfs in the NIRSPEC Brown Dwarf Spectroscopic Survey*, 2017, ApJ, 838, 73, doi:10.3847/1538-4357/aa6338, which is reproduced by permission of the Astrophysical Journal. I would like to acknowledge my collaborators on this work: Gregory N. Mace, Ian S. McLean, Sarah E. Logsdon, Emily L. Rice, J. Davy Kirkpatrick, Adam J. Burgasser, Mark R. McGovern, and Lisa Prato.

Chapter 3 of this dissertation contains material from Martin et al., (2018), *Y Dwarf Trigonometric Parallaxes from the Spitzer Space Telescope*, 2018, ApJ submitted, which is reproduced by permission of the Astrophysical Journal. I would like to acknowledge my collaborators on this work: J. Davy Kirkpatrick, Charles A. Beichman, Richard L. Smart, Jacqueline K. Faherty, Christopher R. Gelino, Michael C. Cushing, Adam C. Schneider,

Edward L. Wright, Patrick J. Lowrance, James Ingalls, C. G. Tinney, Ian S. McLean, Sarah E. Logsdon, and Jérémy Lebreton.

Chapter 4 of this dissertation includes work completed in the UCLA IR Lab. I would like to acknowledge my colleagues in the lab: Ted Aliado, George Brims, John Canfield, Chris Johnson, Evan Kress, Ken Magnone, Ji Man Sohn, Eric Wang, and Jason Weiss. I would also like to acknowledge my colleagues from W. M. Keck Observatory who have helped with the NIRSPEC upgrade: Greg Doppmann, Kyle Lanclos, and Marc Kassis.

Chapter 4 of this dissertation also includes material from Martin et al. (2014), *Performance modeling of an upgraded NIRSPEC on Keck*, 2014, Proc. SPIE, 9147, 81, `doi:10.1117/12.2056896`, and Martin et al. (2016), *Optical design of the slit-viewing camera for the NIRSPEC upgrade*, 2016, Proc. SPIE, 9908, 2R, `doi:10.1117/12.2233767`, which are reproduced by permission of the SPIE. I would like to acknowledge my collaborators on those proceedings: Michael P. Fitzgerald, Ian S. McLean, Sean M. Adkins, Ted Aliado, George Brims, Chris Johnson, Ken Magnone, Eric Wang, Jason Weiss, Evan Kress.

Chapter 4 also includes material from Yi et al. (2016), *Demonstration of a Near-IR Line-Referenced Electro-Optical Laser Frequency Comb for Precision Radial Velocity Measurements in Astronomy*, 2016, Nature Communications, 7, 10436, `doi:10.1038/ncomms10436`. I would like to acknowledge my coauthors on this work: X. Yi, K. Vahala, J. Li, S. Diddams, G. Ycas, P. Plavchan, S. Leifer, J. Sandhu, G. Vasisht, P. Chen, P. Gao, J. Gagné, E. Furlan, M. Bottom, M. P. Fitzgerald, G. Doppmann, and C. Beichman.

Chapter 4 also includes material from Suh et al. (2018), *Searching for Exoplanets Using a Microresonator Astrocomb*, submitted. I would like to acknowledge my coauthors on this work: Myoung-Gyun Suh, Xu Yi, Yu-Hung Lai, S. Leifer, Ivan S. Grudinin, G. Vasisht, Michael P. Fitzgerald, Scott B. Papp, Scott A. Diddams, C. Beichman, Kerry Vahala.

The NIRSPEC upgrade work was made possible in part by the National Science Foundation award AST-1532315. I am very grateful to Renate Kupke and John Rayner for their advice and assistance on this project. I would also like to thank Teledyne Imaging Sensors for their gracious support of the UCLA IR Lab throughout the prototyping process.

This dissertation includes data obtained at the W.M. Keck Observatories on Maunakea, Hawaii. I wish to recognize and acknowledge the very significant cultural role and reverence that the summit of Maunakea has always had within the indigenous Hawaiian community. I am most fortunate to have had the opportunity to conduct observations from this mountain. This research also makes use of data products from the *Wide-field Infrared Survey Explorer*, which is a joint project of the University of California, Los Angeles, and the Jet Propulsion Laboratory/ California Institute of Technology, funded by the National Aeronautics and Space Administration. This work is based in part on observations made with the *Spitzer Space Telescope*, which is operated by the Jet Propulsion Laboratory, California Institute of Technology under a contract with NASA.

This research has further benefited from (1) the Brown Dwarf Spectroscopic Survey (BDSS) Archive housed at bdssarchive.org, (2) the M, L, T, and Y dwarf compendium housed at DwarfArchives.org and curated by Chris Gelino, Davy Kirkpatrick, Mike Cushing, David Kinder, and Adam Burgasser, (3) the NASA/ IPAC Infrared Science Archive, which is operated by the Jet Propulsion Laboratory, California Institute of Technology, under contract with the National Aeronautics and Space Administration, (4) the tools developed and operated at CDS, Strasbourg, France (including the SIMBAD database and the Aladin sky atlas), and (5) The European Space Agency (ESA) mission Gaia (`http://www.cosmos.esa.int/gaia`), processed by the Gaia Data Processing and Analysis Consortium (DPAC, `http://www.cosmos.esa.int/web/gaia/dpac/consortium`). Funding for the DPAC has been provided by national institutions, in particular the institutions participating in the Gaia Multilateral Agreement. (6) The Hale Telescope at Palomar Observatory, which is operated by the California Institute of Technology.

VITA

2012 B.S. Physics
B.A. French
Texas A & M University

2014 M.S. Astronomy
University of California, Los Angeles

PUBLICATIONS

E. C. Martin, J. Davy Kirkpatrick, C. A. Beichman, R. L. Smart, J. K. Faherty, C. R. Gelino, M. C. Cushing, A. C. Schneider, E. L. Wright, P. J. Lowrance, J. Ingalls, C. G. Tinney, I. S. McLean, S. E. Logsdon, and J. Lebreton. *Y Dwarf Trigonometric Parallaxes from the Spitzer Space Telescope.* Submitted to ApJ.

S. E. Logsdon, G. N. Mace, I. S. McLean, **E. C. Martin**. *Probing Late-T dwarf J-H Color Outliers for Signs of Age.* Submitted to ApJ.

M. G. Suh, X. Yi, Y. H. Lai, et al., including **E. C. Martin**. *Searching for Exoplanets Using a Microresonator Astrocomb.* Submitted to Nature.

E. C. Martin, G. N. Mace, I. S. McLean, S. E. Logsdon, E. L. Rice, J. Davy Kirkpatrick, A. J. Burgasser, M. R. McGovern, L. Prato. *Surface Gravities for 228 M, L, and T Dwarfs in the NIRSPEC Brown Dwarf Spectroscopic Survey.* 2017. ApJ, 838, 73.

E. C. Martin, M. P. Fitzgerald, I. S. McLean, E. Kress, E. Wang. *Optical Design of the Slit-Viewing Camera for the NIRSPEC Upgrade.* 2016 Proceedings SPIE.

J. Davy Kirkpatrick, K. Kellogg, A. C. Schneider, et al. including **E. C. Martin**. *The AllWISE Motion Survey, Part 2.* 2016. ApJS, 224, 36.

X. Yi, K. Vahala, J. Li, et al., including **E. C. Martin**, *Demonstration of a Near-IR Line-Referenced Electro-Optical Laser Frequency Comb for Precision Radial Velocity Measurements in Astronomy.* 2016, Nature Communications, 7, 10436.

J. L. Marshall, J. P. Rheault, D. L. DePoy, et al., including **E. C. Martin**. *DECal: A Spectrophotometric Calibration System for DECam.* 2016 Proceedings Astronomical Society of the Pacific, The Science of Calibration.

E. C. Martin, M. P. Fitzgerald, I. S. McLean, S. M. Adkins, T. Aliado, G. Brims, C. Johnson, K. Magnone, E. Wang, J. Weiss. *Performance Modeling of an Upgraded NIRSPEC on Keck.* 2014 Proceedings SPIE.

J. L. Marshall, D. L. DePoy, T. Prochaska, et al., including **E. C. Martin**. *VIRUS Instrument Collimator Assembly.* 2014 Proceedings SPIE.

E. C. Martin, G. N. Mace, I. S. McLean, S. E. Logsdon, E. L. Rice. *Preliminary Analysis of M and L Dwarf Surface Gravities in the NIRSPEC Brown Dwarf Spectroscopic Survey.* 2014 Cool Stars 18 Proceedings.

E. C. Martin, D. L. DePoy, J. L. Marshall. *Optical Design of a Red Sensitive Spectrograph.* 2012 Proceedings SPIE.

CHAPTER 1

Introduction

We, this people, on a small and lonely planet

Traveling through casual space

Past aloof stars, across the way of indifferent suns

To a destination where all signs tell us

It is possible and imperative that we learn

A brave and startling truth

Maya Angelou

Since the discovery of the first brown dwarfs and extrasolar planets in 1995 (Nakajima et al., 1995; Rebolo et al., 1995; Mayor & Queloz, 1995), we have made significant progress in our understanding of the formation and evolution of substellar gaseous objects. However, many fundamental questions remain regarding star formation at the lowest masses and our understanding of atmospheric physics of Jupiter-mass objects. Is there a low-mass cutoff to star formation? How efficient is star formation at the lowest-mass end? Who are our nearest neighbors and what does our Solar Neighborhood look like? Attempts to answer these questions and others drives my own interest in the fields of low-mass stars, brown dwarfs, and giant planets. Advancing our understanding of the universe requires a combination of new observations, theoretical models, and instrumentation. Each of these techniques feeds back into the others, improving our understanding and driving the development of new technologies and computing techniques. My goal over the past six years has been to develop a program of observational astronomy and instrumentation to contribute to the study of brown dwarfs. My work uses the NIRSPEC instrument, a medium- and high-resolution infrared spectrometer on the Keck II telescope on MaunaKea, Hawaii to obtain near infrared spectra

of low-mass stars and brown dwarfs. At the same time, I am the Instrument Scientist for the NIRSPEC upgrade, which aims to improve NIRSPEC and enable observers to obtain higher quality data, more efficiently. My dissertation is divided into three parts, consisting of two closely related observational projects and an instrumentation component, which I outline below.

For Project I (Chapter 2) of my dissertation, I use near-infrared spectroscopy from NIRSPEC to study the surface gravities of 228 low-mass stars and brown dwarfs in the NIRSPEC Brown Dwarf Spectroscopic Survey (BDSS). I measure neutral potassium (K I) and iron hydride (FeH) absorption in the brown dwarf spectra as indicators of surface gravity and proxies for object age. This allows us to disentangle the effects of mass, radius, age, and temperature in the spectra of these objects. Detailed studies of the atmospheres of isolated brown dwarfs are useful for comparisons to model atmospheres used to explain the properties of gas giant exoplanets, which are typically much harder to study when not resolved from their parent star. Our results will provide additional constraints for theorists as they adjust their atmospheric and evolutionary models. This project resulted in a first-author publication in the Astrophysical Journal, Martin et al. (2017). Additionally, we are publishing all of our spectra on the bdssarchive.org website, which is freely available to everyone in the brown dwarf community. My work contributes 131 new spectra to the pre-existing archive of 97 brown dwarf spectra in the BDSS.

Project II (Chapter 3) utilizes imaging data from the Spitzer Space Telescope to study the coldest and lowest-mass brown dwarfs in our Solar Neighborhood. As part of my work as an IPAC Visiting Graduate Fellow in 2016, I measured precise locations over baselines of many years to determine distances to 22 of the coldest objects in our Spitzer Parallax Program. Precise distance measurements are essential to better understand other physical properties of brown dwarfs, such as their absolute magnitudes and radii. Furthermore, having a volume-limited survey of the coldest brown dwarfs in the Solar Neighborhood allows us to better constrain star formation at the lowest masses. We will be able to set limits on the low-mass cutoff of star formation and better understand the star-formation efficiencies at the lowest-mass end. This project presents the most precise parallaxes for the largest sample of

Y dwarfs, to-date, as well as the discovery of six new T dwarfs and one new Y dwarf. Project II is submitted and will be published in the Astrophysical Journal this Spring/Summer. My work is also aiding in the completion of the entire Spitzer Parallax Program, which will measure distances to over 300 of the coldest brown dwarfs out to 20pc from the Sun.

Project III (Chapter 4) encompasses my work in the infrared laboratory to upgrade NIRSPEC. The NIRSPEC infrared spectrometer has been a workhorse instrument at the W. M. Keck Observatory (WMKO) since it was delivered in 1999 by my advisor, Professor Ian McLean. Since that time, however, advancements in infrared technology have improved detector and data acquisition systems significantly. WMKO approved a UCLA proposal to upgrade NIRSPEC's detector and electronics, the slit-viewing camera, and the motion control system. Funding was provided by an NSF MRI grant under the leadership of my co-advisor, Professor Mike Fitzgerald. I have been a member of the NIRSPEC upgrade team since joining the UCLA IR lab in 2012. As the instrument scientist for the upgrade, my roles include optical design and characterization, electronics design and testing, characterizing the new infrared detectors for both the spectrometer and slit-viewing camera, and much more. In Fall 2018, we will install the upgrade on the Keck II Telescope on the summit of MaunaKea in Hawaii. The NIRSPEC upgrade is being highly anticipated throughout the astronomical community. Astronomers studying everything from our own solar system out to the farthest galaxies will use NIRSPEC to make fainter and more precise observations. The new electronics, optics, and detectors will allow NIRSPEC to continue operations for decades to come.

1.1 Brown Dwarfs

Brown dwarfs occupy the lowest-mass end of the star formation process. Having masses lower than $\lesssim 75\ M_{\rm Jup}$, they are unable to generate stable fusion of hydrogen into helium in their cores and thus do not produce a stable energy source. Instead of maintaining a stable temperature and size over their lifetimes, brown dwarfs contract and cool as they age. Brown dwarfs are classified by spectral types M, L, T, and Y, with M dwarfs being the hottest and

Y dwarfs being the coldest brown dwarfs. There is overlap between the stellar and brown dwarf spectral types in the M's and L's. The lowest-mass stars appear as L dwarfs after they have cooled onto the main sequence. T and Y dwarfs are entirely made up of brown dwarfs and planetary mass objects that are free-floating in the field.

Because they are so cold, brown dwarf atmospheres are complicated by many different atomic and molecular absorbers. Extensive work has been done to model the atmospheres of brown dwarfs and giant exoplanets but we are still unable to produce physical models that match all of our observations, making this a field of active research. My first observational program made use of the NIRSPEC Brown Dwarf Spectroscopic Survey to measure and characterize the surface gravities of over 200 M, L, and T dwarfs.

1.1.1 NIRSPEC Brown Dwarf Spectroscopic Survey

The NIRSPEC Brown Dwarf Spectroscopic Survey (BDSS), a survey of a large sample of brown dwarfs and low-mass stars, was one of the key science drivers for the NIRSPEC spectrometer. The low temperatures ($T_{\rm eff} \lesssim$ 2500 K) of brown dwarfs make them excellent targets for near-infrared studies. The primary goal of the BDSS as outlined in McLean et al. (2003) is to gather a large suite of near-infrared spectra of low-mass stars and brown dwarfs in order to examine their spectral properties and make comparisons to evolutionary and atmospheric models.

Over the past 20 years, the BDSS team has gathered a large spectroscopic database of brown dwarfs and low-mass stars (see Chapter 2, Appendix A). McLean et al. (2001) presented preliminary results from the BDSS. This inaugural work was followed by five BDSS papers, which are briefly summarized below to give context to Chapter 2.

McLean et al. (2003) (also called Paper I of the BDSS) presented the first set of medium resolution (R $\sim$ 2000) near-infrared spectra in *Y, J, H*, and *K* bands for dwarfs of types M6-T8. Flux calibrated spectra were provided for 25 objects, covering most spectral types between M6-T8. Spectral indices based on H_2O, CH_4, CO, and FeH absorption were calculated and compared, and equivalent widths of Al I, Ca I, and K I were also computed. This

paper presented the first large and consistent sample of medium resolution near infrared spectra of brown dwarfs and low mass stars, permitting a deeper spectral analysis than had previously ever been done for such a large sample.

McGovern et al. (2004) presented the first comprehensive infrared observations to reveal and quantify gravity-sensitive spectral signatures in young low-mass stars and brown dwarfs. The infrared and optical spectra of late-type giant stars and old field dwarfs were compared with the spectra of several young brown dwarfs to establish gravity-sensitive features, such as the neutral potassium lines in the J-band, as well as TiO, VO, and FeH absorption systems. The paper also reported on the use of these spectral features to test the membership of potential very low mass brown dwarfs in young clusters. McGovern et al. (2004) therefore forms the basis of the current more extensive study of gravity features presented in Chapter 2.

The first high resolution data set was presented in McLean et al. (2007), also called Paper II of the BDSS. This paper included J-band spectra at R $\sim$ 20,000 for 16 M, L, and T dwarfs. Weak FeH and H_2O features were identified via comparisons to line lists and opacity plots, and the effects of rotation and surface gravity on J-band spectra of brown dwarfs and low mass stars were analyzed.

In Rice et al. (2010), high resolution spectra of late-type M dwarfs were compared to updated PHOENIX model atmospheres (Hauschildt et al., 1997). Physical properties such as effective temperature, surface gravity, projected rotational velocity, and radial velocity were inferred for 21 young and field-age brown dwarfs and low-mass stars.

Prato et al. (2015) described a study to monitor 25 field brown dwarf systems in the BDSS for radial velocity variations in the search for faint companions. No radial velocity variability was found at the level of $\sim$ 2 km/s. Even with a null detection, the 1 σ upper limit for very low mass binary frequency is 18%.

1.1.2 Parallaxes of brown dwarfs

Distances are crucial for determining absolute physical properties of objects, such as their absolute magnitudes. Trigonometric parallaxes are one of the most basic methods for determining distances to objects in space, and provide the base for the cosmic distance ladder. Though based on fairly simple methodology, in practice, precision astrometry is complicated by instrumental systematics, such as optical distortion and detector non-uniformities. Large, all-sky surveys like the Gaia mission are revolutionizing the field by providing well-calibrated, extremely precise parallaxes and proper motions for over 1 billion sources. However, the Gaia mission utilizes a broadband optical G filter, which is not optimized for extremely red objects, like the coldest brown dwarfs. Furthermore, ground-based astrometric programs for low-mass stars and brown dwarfs tend to work in near-infrared bands, where L and early T dwarfs are brightest and the sky background is not too high.

For the coldest brown dwarfs, the late-T and Y dwarfs, the majority of their light is emitted in the mid-infrared, 3–5 μm regime, which is much more difficult to observe from the ground and/or requires the use of the largest telescopes, which are over-subscribed. However, the coldest brown dwarfs are the most crucial to locate because their number densities can put the best constraints on star formation at the lowest-mass end. Chapter 3 presents the results of a project using the *Spitzer Space Telescope* to measure trigonometric parallaxes for 22 late-T and Y dwarfs. The project also includes the discovery of 3 new T dwarfs and one new Y dwarf, which we characterized using the NIRSPEC instrument. These late-T and Y dwarfs are so faint that NIRSPEC on Keck is one of the few instruments capable of obtaining medium-resolution spectra from the ground.

1.2 NIRSPEC Upgrade

NIRSPEC on Keck is one of the most-used ground-based instruments for taking infrared spectra of brown dwarfs. I have observed with NIRSPEC over 15 nights and it has contributed to both of my first-author publications. Upgrading the NIRSPEC instrument aligns

with my science and instrumentation goals because it will enable me to take better quality spectra of even fainter objects and it has given me the opportunity to develop as an instrumentalist. As a member of the upgrade team, I have had the opportunity to work on many different projects related to the upgrade. I have honed my skills in optical design, vacuum-cryogenic testing, infrared detector handling, mechanical prototyping, and project management, among others. I have gained insight into the workings of a facility instrument, which has improved my understanding of how best to use the instrument and how to calibrate it. Similarly, my experience using the instrument enlightens my work in the lab. I am able to translate engineering requirements into scientific outcomes and vice-versa. Instrumentation has a symbiotic relationship between engineering and science that fulfills my passion for discovery and understanding the universe as well as my desire to create useful tools for the community. The training I have received in the UCLA IR Lab is a unique experience that I hope to carry forward in my academic career as I continue to build new instruments.

CHAPTER 2

Surface gravities for 228 M, L, and T dwarfs in the NIRSPEC Brown Dwarf Spectroscopic Survey

2.1 Introduction

Brown dwarfs are the lowest-mass products of star formation, with masses so low that they will never achieve stable hydrogen fusion in their cores (Kumar, 1962, 1963; Hayashi & Nakano, 1963). Substellar objects are classified by their spectral morphology as types M, L, T, and Y, a sequence which represents both a decrease in effective temperature and changes in chemical abundances. Since their discovery 20 years ago (Nakajima et al., 1995; Rebolo et al., 1995), most brown dwarfs have been found through infrared large area surveys such as the Two Micron All Sky Survey (2MASS; Skrutskie et al. 2006), the Sloan Digital Sky Survey (SDSS; York et al. 2000), the United Kingdom Infrared Deep Sky Survey (UKIDSS; Lawrence et al. 2007), and the Wide-field Infrared Survey Explorer (WISE; Wright et al. 2010), among others. See, for example, Kirkpatrick et al. (1991); Kirkpatrick et al. (1999); Hawley et al. (2002); Burgasser et al. (2006); Chiu et al. (2006); Burningham et al. (2010); Cushing et al. (2011) for details on brown dwarf discoveries made by the various surveys.

Extensive follow-up using both optical and infrared imaging and spectroscopy has enabled astronomers to begin characterizing the physical properties of brown dwarfs, primarily through comparisons to atmospheric and evolutionary models, like those of Burrows et al. (2001), Saumon & Marley (2008), Allard et al. (2012), and Baraffe et al. (2015). It is possible to constrain the effective temperatures, surface gravities, and metallicities of brown dwarfs within the limits of current models, e.g. Cushing et al. (2008); Rice et al. (2010). As the number of confirmed brown dwarfs has increased, the properties typical of field brown

dwarfs have been constrained, outliers have been recognized, and methods of identifying extremely young or old objects have emerged (see Kirkpatrick et al. 2010; Allers & Liu 2013 and references therein).

2.1.1 Surface Gravity as an Age Indicator

Unlike stars, brown dwarfs contract and cool as they age, producing a degeneracy between the mass, age, and temperature such that temperature alone cannot reveal the mass or age of a given brown dwarf. For example, an L dwarf could be a young, planetary-mass brown dwarf, a moderately aged high-mass brown dwarf, or an old low-mass star. Brown dwarfs contract considerably in their first $\sim$ 300 Myr and significantly increase their surface gravity ($g = GM/R^2$) from log $g \sim 3.5$ to log $g \sim 5$ in units of cm s^{-2} (Burrows et al., 2001). Obtaining a surface gravity estimate is an important step towards disentangling the mass and age of a brown dwarf.

Surface gravity affects several features in the optical and near infrared (NIR) spectra of brown dwarfs. Photospheric pressure, which is proportional to surface gravity assuming hydrostatic equilibrium, broadens atomic features and influences the chemical pathways of both atomic and molecular species (Lodders, 1999). Neutral alkali lines such as K I and Na I are weaker in low-gravity objects compared to higher gravity objects at similar spectral types because lower photospheric pressure decreases the column densities of the absorbing species above the photosphere, causing the absorption features to appear weaker in low gravity dwarfs. FeH absorption also appears weaker in lower gravity objects, while VO shows stronger absorption at lower gravity, as noted by McGovern et al. (2004) and Allers & Liu (2013). Additionally, the overall shape of the H-band spectral energy distribution is much "peakier" at lower gravities (Lucas et al., 2001; Allers et al., 2007; Looper et al., 2008; Rice et al., 2011), likely due to lower H_2 collision induced absorption (CIA), which is a result of the lower photospheric pressure at lower gravities (Kirkpatrick et al., 2006; Saumon & Marley, 2008).

Kirkpatrick (2005) proposed a scheme in which a gravity classification (i.e. α, β, γ, δ) is

appended to the spectral type of a brown dwarf as a means of distinguishing between field, intermediate, low, and very-low gravity objects with similar temperatures. For each spectral type, the gravity sequence acts as a proxy for an age sequence, and low-gravity objects of a particular spectral type are younger than their field counterparts at the same spectral type. Cruz et al. (2009) explored this gravity classification scheme using red-optical spectroscopy of 23 L dwarfs, primarily distinguishing the young objects from field-age objects by the weakness of their alkali lines, though also using the FeH, CrH, TiO and VO absorption bands as diagnostics.

Allers & Liu (2013), hereafter A13, were the first to present a systematic technique using NIR spectroscopy to determine surface gravities of low-mass stars and brown dwarfs. A13 defines spectral indices and pseudo-equivalent widths (EWs) of various gravity-sensitive features in lower resolution NIR spectra to classify the spectra into three groups: low (VL-G), intermediate (INT-G), and high (FLD-G) gravity objects, roughly corresponding to young ($\lesssim$ 30 Myr), intermediate ($\sim$30–200 Myr), and field age ($\gtrsim$ 200 Myr) objects. Because brown dwarfs are significantly brighter in the NIR than the optical, a NIR gravity classification scheme is applicable to more targets. A13 determined gravity classifications for 73 low-mass stars and brown dwarfs showing signs of youth. Gagné et al. (2015c) applied the method prescribed in A13 to 182 objects of spectral types M4–L7 in the search for low-mass members of young moving groups.

In this paper we follow up on prior NIR spectroscopy by our group and use a modified A13 method to determine surface gravities for 228 M, L, and T dwarfs. Twenty of these targets overlap with the A13 sample, and 5 objects overlap with the Gagné et al. (2015c) sample. Many previously unpublished NIR spectra from the NIRSPEC Brown Dwarf Spectroscopic Survey (BDSS) are reported and analyzed.

2.1.2 The NIRSPEC Brown Dwarf Spectroscopic Survey

In 1999, the Near-Infrared Spectrometer (NIRSPEC; McLean et al. 1998) was commissioned for the W.M. Keck II 10-m telescope on Mauna Kea in Hawaii. NIRSPEC was built at the

University of California, Los Angeles (UCLA), and designed for both medium (R=$\lambda/\Delta\lambda \sim$ 2000) and high (R$\sim$20,000) resolution spectroscopy in the 1–5 μm regime. The BDSS was one of the key science drivers for NIRSPEC. The primary goal of the BDSS as outlined in McLean et al. (2003) is to gather a large suite of NIR spectra of low-mass stars and brown dwarfs in order to examine their spectral properties and make comparisons to evolutionary and atmospheric models. The low temperatures (T $\lesssim$ 2500 K) of brown dwarfs make them excellent targets for NIR studies. Over the past 15 years, the BDSS team has gathered a large spectroscopic database of brown dwarfs and low-mass stars (see §2, Appendix), much of which is presented in McLean et al. (2001, 2003); McGovern et al. (2004); McLean et al. (2007); Rice et al. (2010); Prato et al. (2015).

McGovern et al. (2004) presented the first comprehensive infrared observations to reveal gravity-sensitive spectral signatures in young low-mass stars and brown dwarfs. The infrared and optical spectra of late-type giant stars and old field dwarfs were compared with the spectra of several young brown dwarfs to identify gravity-sensitive features, such as the K I lines in the J-band, as well as TiO, VO, and FeH absorption systems. The paper also reported on the use of these spectral features to test the membership of potential very low mass brown dwarfs in young clusters. McGovern et al. (2004) therefore forms the basis of the surface gravity analysis presented in this paper.

In this paper, we measure equivalent widths of K I lines in the J-band and FeH absorption at 1.2 μm for all targets in the BDSS, and use the A13 method to determine surface gravities for all objects for which the method is viable (spectral types M5– L7). We expand upon previous surface gravity studies by calibrating the surface gravity classifications against objects of known ages from the literature, and discuss the extension of the gravity classifications beyond type L7. In Section 2, we discuss our observations and data reduction methods. Section 3 describes our method of determining surface gravity, and Section 4 discusses general trends, interesting objects revealed by our analysis, and the ability of the gravity indices to distinguish the ages of objects. Section 5 summarizes our results.

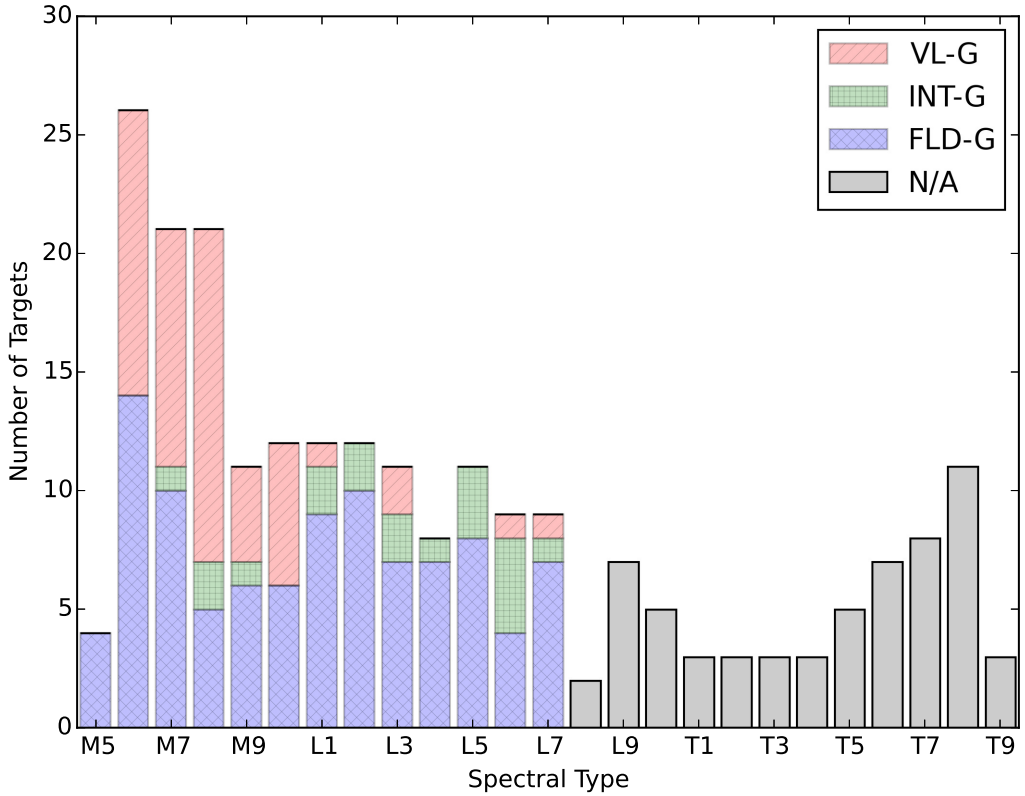

Figure 2.1: Number of targets versus spectral type for all 228 objects in the BDSS. Shading represents gravity classifications, as defined by A13 and as determined in this paper. Red shading represents targets with a gravity classification of VL-G. These objects are likely very young. Green shaded regions denote targets with INT-G classification, indicating youth (∼30–200 Myr). Blue targets have FLD-G gravity classifications, and are generally older than ∼200 Myr. Objects cooler than type L7 cannot be gravity typed by A13's methods and are shown in grey.

2.2 Sample

We present medium-resolution J-band spectra of 85 M dwarfs, 92 L dwarfs, and 51 T dwarfs, obtained as part of the BDSS. Ninety-seven spectra were published previously in McLean et al. (2003), Burgasser et al. (2003b), McGovern et al. (2004), Rice et al. (2010), Kirkpatrick et al. (2010), Luhman (2012), Thompson et al. (2013), Mace et al. (2013a), Mace et al. (2013b) and Kirkpatrick et al. (2014), and the remaining 131 are presented here for the first time. By design, our sample spans a large range of spectral types, ages, and distances. In addition to known standards and field objects, we have observed peculiar objects such

as $J - K_s$ color outliers and known young and old objects. Sixty-four of our targets have age estimates based on their likely associations with clusters or moving groups, such as the Pleiades, Upper Scorpius, and Taurus regions, or from spectral analysis of stellar companions. However, the majority of the sample comprises field brown dwarfs and low-mass stars selected from the 2MASS and WISE surveys. As illustrated in Figure 2.1, our largest population of objects is late-type M dwarfs.

2.2.1 Observations

Targets were observed using the strategy described in McLean et al. (2003) for the NIRSPEC instrument on the Keck II telescope in the non-echelle (medium-resolution) mode. For this mode, the slit used is typically 0.38″ wide (two pixels), though for several fainter T dwarfs and for observing conditions with sub-optimal seeing, the 0.57″ slit was used. For most observations, 300 s exposures were taken in nod pairs of 20″ separation along the 42″ slit. These nods were generally done in ABBA format for a total observing time of 20 minutes per target. Fainter objects were observed for longer, as needed. An A0V star at a similar airmass to each target was used for telluric corrections. If there were no nearby A0V stars, calibrators as early as B9 or as late as A3 were used instead. In the N3 filter (∼1.15–1.35 μm), the A0V stars typically only contain the Paβ absorption line at 1.282 μm which we interpolate over in the reduction process. In addition to telluric calibrators, flat field and dark frames were taken, as well as spectra of Ne and Ar lamps for wavelength calibration. Observation information for all targets in our sample is listed in Table 2.1, as well as spectral types taken from the literature.

2.2.2 Data Reduction

All spectroscopic reductions were made using the REDSPEC package[1], software produced at UCLA by S. Kim, L. Prato, and I. McLean specifically for the reduction of NIRSPEC data as described in McLean et al. (2003). The REDSPEC code first corrects for spatial

and spectral distortion on the array using Ne and Ar lamp lines with wavelengths taken from the National Institute of Standards and Technology (NIST)[2] (Kramida et al., 2015). Nod pairs of the target and calibrator are then background subtracted and divided by a flat field. Known bad pixels are removed as well. Spectra are obtained by summing over a range of ∼10 pixels (depending on seeing) and then dividing by the A0V calibrator spectrum to remove telluric features. Each pair of spectra was normalized and combined with other pairs (when available) to achieve a higher signal-to-noise ratio (SNR). This sample contains targets with SNR ∼10–200, though the majority of the spectra have SNR of at least 20. Finally, heliocentric velocity corrections were applied to the normalized spectra. We also performed a quality check on all data to ensure that wavelength dispersion solutions differed by less than $\sim 10^{-5}$ Å/pixel. Plots and data files for all of our reduced spectra are available publicly through the BDSS archive[3] or by request.

2.3 Surface Gravity: Methods and Results

Below we describe our method for calculating the EWs and spectral indices used to determine the surface gravities of our objects. We then present surface gravity estimates for all M6–L7 objects in the BDSS, as well as EW and spectral index values for all BDSS objects.

2.3.1 Equivalent Widths

We compute pseudo-EWs for the four neutral potassium lines in the J-band following the method described in A13. For accurate comparison, we use the same line and pseudo-continuum windows as defined in A13 (see Figure 2.2). The light grey shaded regions indicate the line windows used, while the dark grey shows the continuum windows. The K I doublet at 1.1692 μm and 1.1778 μm share the continuum windows on either side of the doublet,

[1]http://www2.keck.hawaii.edu/inst/nirspec/redspec.html

[2]http://physics.nist.gov/asd

[3]http://bdssarchive.org

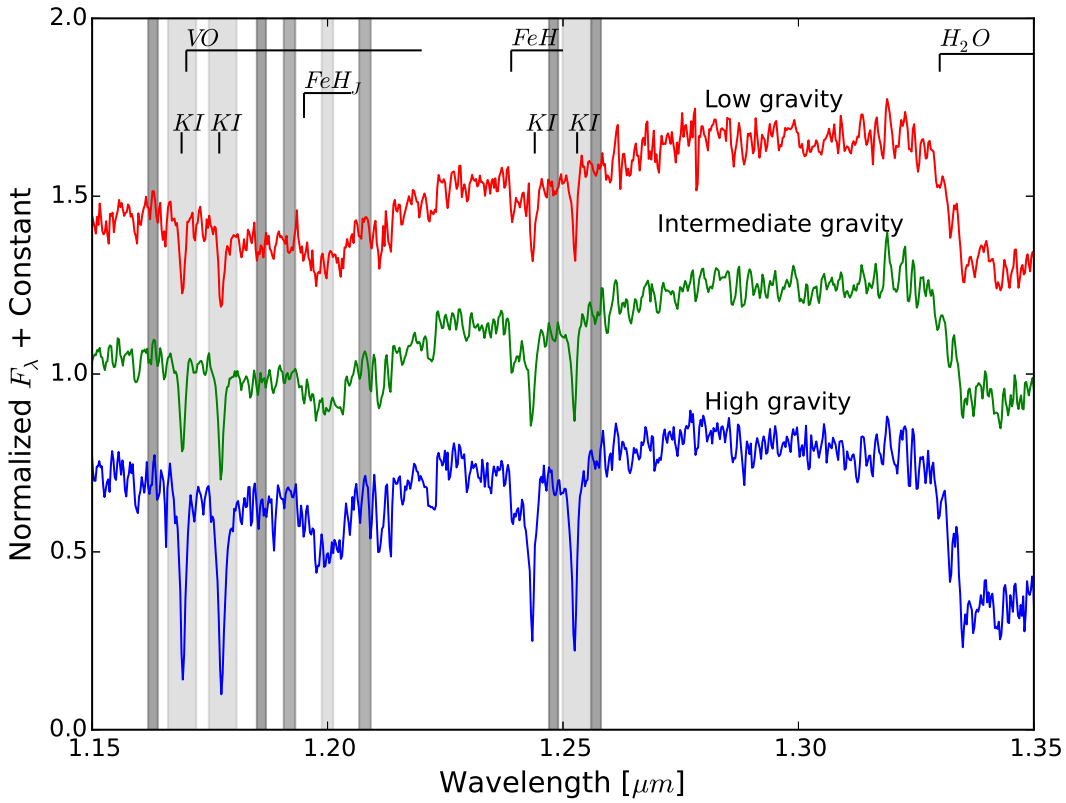

Figure 2.2: Three example J-band spectra of spectral type L3 objects from the BDSS. Each spectrum represents a different gravity type: low gravity (2MASS 2208+2921), intermediate gravity (2MASS 1726+1538), and high gravity (2MASS 1300+1912). Major absorption features in the J-band are also labeled. Light grey shaded regions denote the locations used to calculate K I EWs and the FeH_J index. Dark grey regions denote locations of the pseudo-continua used in our calculations. The K I line at 1.2437 μm is marked, but not shaded. This line was not used to determine gravity types because of contamination from FeH absorption at $\sim$1.24 μm.

and the 1.2437 μm and 1.2529 μm lines share the continua surrounding the 1.2529 μm line. A13 chooses to exclude the 1.2437 μm line from their final analysis because of the FeH contamination on the blue side of the line. For completeness, we compute and report EWs for this line. Indeed, we find that the 1.2437 μm line exhibits more scatter and weaker correlation with surface gravity at this resolving power, and thus we also exclude it from our analysis.

Following a similar method to A13, we estimate a continuum value using a linear regression fit to the flux in the continuum windows. The EW calculations are performed using a Monte Carlo technique of 1000 iterations to estimate our uncertainties. Unlike A13, we do not use the rms scatter about the continuum fit to estimate the flux uncertainty. Instead, for each iteration of the Monte Carlo calculation, we modulate the flux in each pixel by adding a noise factor calculated by multiplying a random number drawn from a Gaussian centered at 0 with a sigma of 1, multiplied by the estimated noise determined by the SNR of that pixel. The equivalent width for each flux modulation is recorded, and we then compute the median and standard deviation of the EWs as the best estimate and 1σ uncertainties. This is a similar method to the one described in Aller et al. (2016), who found that the method in A13 tended to underestimate flux errors in modest SNR spectra (SNR $\lesssim$ 200).

We tested this technique using a range of number of iterations in our Monte Carlo calculations. We found that $\gtrsim$ 500 iterations were required to achieve stable results and that there is no significant difference between 10^3 and 10^6 iterations. In the interest of computational time, we opted for 10^3 iterations.

Table 2.2 lists our values for EW and uncertainties for the four K I lines in the J-band for all objects in the BDSS. The first K I doublet at 1.17 μm disappears from the J-band spectra of dwarfs of spectral types $\sim$T5 and later. The K I doublet at 1.25 μm persists through $\sim$T7 (see spectral plots in Appendix). For this reason, objects later than T5 will have no K I EW measurements at 1.17 μm and objects later than T7 will have no K I EW measurements at 1.25 μm.

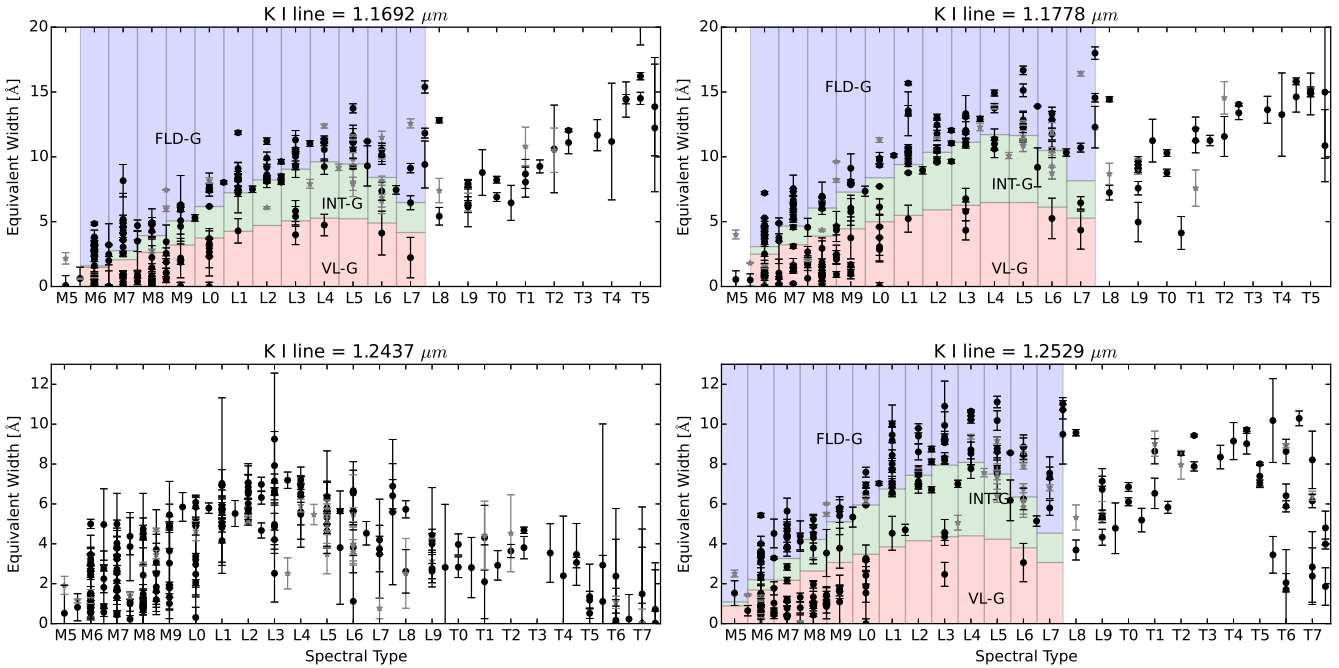

Figure 2.3: K I pseudo equivalent width vs spectral type for all M, L, and T dwarfs in the BDSS for which EWs can be measured. Field dwarfs are shown in black and binaries and subdwarfs are shown as grey stars. Uncertainties are calculated using a Monte Carlo technique with 1000 iterations of modulating the flux by the SNR and re-calculating the EW. The K I lines at 1.1692 μm and 1.1778 μm disappear from T dwarf spectra later than ∼T5 and the K I lines at 1.2437 μm and 1.2529 μm are not found in T dwarfs later than spectral type ∼T7. Shaded regions denote differing gravity types as defined by A13. Objects lying within the salmon shaded regions receive a score of "2" (indicating low gravity), objects in the green shaded regions receive a score of "1" (intermediate gravity), and objects within the blue shaded regions receive a score of "0" ("field" or high gravity). These scores are used along with the FeH_J score to compute a median gravity type. VL-G and INT-G designations are not distinguishable for M5 dwarfs for the K I lines at 1.1692 and 1.1778 μm, and gravity types are not designated for dwarfs of spectral type L8 and later. FeH contamination of the 1.2437 μm line results in larger measurement uncertainties as well as a less-distinguishable low-gravity sequence. For this reason, A13 did not determine cutoff values for gravity types for this line.

In Figure 2.3, we show results for the four K I EWs versus spectral type for all M, L, and T dwarfs in the sample. Spectral types are taken from the literature (see Table 2.1) and are measured in the NIR, if available. Shaded regions in Figure 3 show the boundaries proposed by A13 to designate low, intermediate, and high surface gravity objects, for objects of spectral type M6–L7.

It should be noted that for some objects with apparently very low K I absorption, the calculated EW can be less than zero. Visual inspection of these spectra shows that they do have very small or nonexistent K I lines. In these cases, we have plotted these targets with EW values of zero, but the values listed in Table 2.2 are as measured. We believe this effect is because the EW calculation windows were chosen for objects with much deeper absorption lines. Objects with very weak K I lines and a slightly higher continuum within the line-calculating region than the continuum region can thus have a negative EW. The negative EW does not affect the gravity classification of VL-G for these objects, so we chose to stay consistent with the A13 line and continuum boundaries when computing EWs.

2.3.2 FeH$_J$ Index

In addition to the K I equivalent width measurements, we studied the FeH$_J$ index from A13. This index measures the 1.2 μm FeH absorption feature for medium-resolution (R$\sim$750–2000) data for objects of spectral type M6-L6. Figure 2.2 shows the window used for computing the index in light grey, and the windows used for estimating the continuum in dark grey. FeH absorption is found in late-type M dwarfs, most L dwarfs, and seen weakly in some T dwarfs. FeH absorption depth is known to correlate with surface gravity (McGovern et al., 2004). Objects near the L/T transition do not show signs of FeH because the atmospheric conditions (i.e. cooler temperatures) have caused this molecule to precipitate (see, e.g. Marley & Robinson 2014). Spectral types later than $\sim$ T1 show a slight re-emergence of the molecule (Burgasser et al., 2002), perhaps due to cloud-clearing, allowing flux to emerge from deeper layers within the brown dwarf, where some FeH remains in gaseous form (see also Tremblin et al. 2016 for an alternate interpretation).

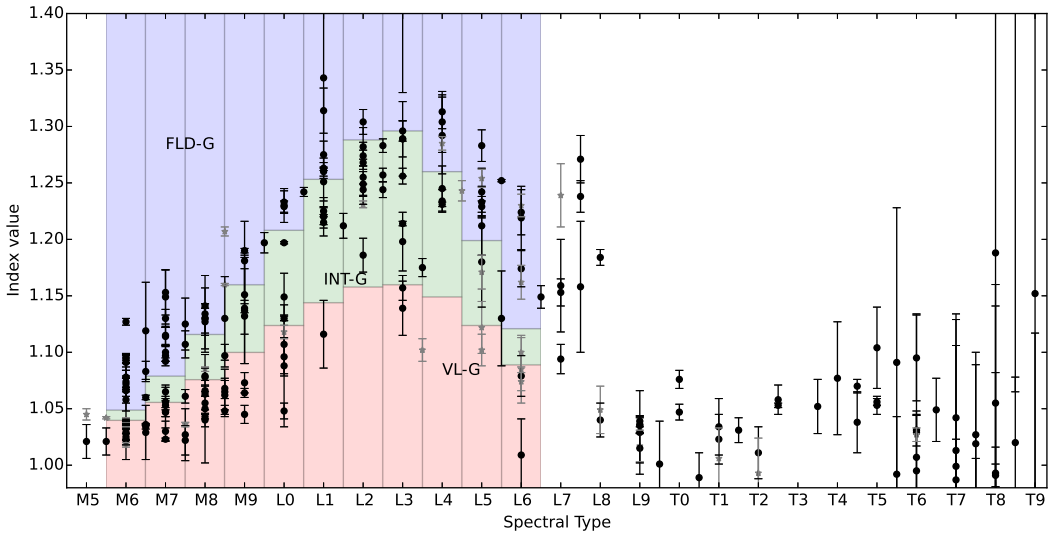

Figure 2.4: FeH$_J$ index vs spectral type for all M, L , and T dwarfs in the BDSS. Normal dwarfs are shown in black and binaries and subdwarfs are shown as grey stars. Shading is the same as in Figure 2.3. This index measures the FeH absorption feature at 1.2 μm using the continuum and absorption bands shown in Figure 2.2. FeH is found in late-type M dwarfs and most L dwarfs. Spectral types later than $\sim$ L8 have atmospheres cool enough to condense this molecule. Index values of $\sim$1.0 indicate the absorption feature is nearly absent in the spectra of L/T transition objects. This index re-emerges slightly in the mid-type T dwarfs.

We present our FeH$_J$ index values for all objects in the BDSS in Figure 2.4. An index value of $\sim$1 is expected for the L/T transition dwarfs, indicating little to no absorption present in this spectral region. FeH$_J$ values for all BDSS targets are listed in Table 2.2.

2.3.3 Gravity Scores

A13 determined gravity score cutoff values for each K I EW for spectral types M5–L7 and for the FeH$_J$ index for spectral types M6–L6 using a sample of known young and field objects. They assigned final gravity types using a median value of scores from multiple spectral indices across the 0.9 – 2.5 μm range, at both low and moderate resolutions. A13 gravity types for moderate resolution spectra are calculated from four scores determined by the following indices: VO (z-band), H-band continuum, FeH (either z or J band), and the mean score of the Na I and K I EWs. As described above, we used similar methods and cutoff ranges to calculate our spectral indices and EWs. However, because we only had J-band spectra for

most of our targets, we determined a gravity type using only the J-band medium-resolution indices from A13.

Gravity scores were computed for the K I EWs at 1.1692 μm, 1.1778 μm, and 1.2529 μm as well as for the FeH_J index. To determine gravity scores for our sample, we compared our computed EW and FeH_J values to the cutoffs tabulated in A13. If the index value was higher than the INT-G cutoff, it received a score of "0", indicating field gravity. If the index value was between the INT-G and VL-G cutoffs, it received a score of "1" and if the index value was smaller than the VL-G cutoff it received a value of "2", indicating low surface gravity. Similar to Aller et al. (2016), we opted not to use the "?" value, defined in A13, if the object receives a score that hints at intermediate gravity but has 1σ uncertainties that overlap with field gravity values. These objects received a score of "1". We computed the median score from these four indices to determine the final gravity designation for each target. Following the method from A13, median scores less than or equal to 0.5 are classified as "FLD-G", scores between 0.5 and 1.5 are classified as "INT-G", and scores greater than or equal to 1.5 receive "VL-G" classification. Table 2.2 lists gravity scores and the resultant gravity classification for objects of spectral type M5-L7. When available, the gravity score given by A13 is also listed.

Using multiple indices to characterize the surface gravity allows some objects to be seen as having borderline gravity classifications between VL-G and INT-G or INT-G and FLD-G. The combination of multiple indices is more robust against any particular index skewing the classification. Errors in an index might come from measurement errors or from physical effects causing the absorption in one index to be abnormal compared to the other indices calculated for a particular target. Sixty-two objects out of the 159 for which A13 gravity types were computed had more than one type of score. However, only 7 targets received individual index scores spanning all three gravity types, and three of these objects are binaries or subdwarfs (see § 2.3.5).

2.3.4 Radial Velocity

One consideration we made in our calculations was the effect of radial velocity (RV) on the EW measurements and therefore on the gravity estimations. One resolution element in the medium-resolution mode of NIRSPEC is equivalent to 150 km s^{-1}. Though rarely occurring, high RV targets could have their spectra shifted by a large enough amount that the calculation of a gravity estimate would be significantly altered. In order to understand the effect of RV on our EW and spectral index values, we examined 21 objects in our sample with known RVs from the literature, with RV magnitudes ranging from $\sim$5 km s^{-1} to 195 km s^{-1}. First, we shifted their spectra to account for the known RV offset. Then, we recalculated their K I EWs and FeH$_J$ indices and gravity types, and compared these values to our original calculations. Only two of our targets, the known L subdwarfs 2MASS 0532+8246, SDSS 1256-0224 had RVs in excess of 100 km s^{-1}(Burgasser et al. 2003b, 2009, respectively). The other 19 targets had RVs $\lesssim$ 30 km s^{-1}.

None of our RV-shifted targets had differing gravity types from our original calculations. K I EW and FeH$_J$ index values differed by less than $\sim$5 % for all of the targets. Few dwarfs have measured RVs in excess of 200 km s^{-1} as the majority belong to the disk population and have similar space motions to the Sun. Because non-echelle NIRSPEC spectra can only resolve radial velocities greater than 150 km s^{-1} without cross-correlating to known RV targets, we estimate that this has a minimal impact on our measured gravity types.

We performed additional analysis to test the effect of RV on the EW measurements by performing a Monte Carlo simulation of 1000 iterations on high SNR spectra of both field age and young targets, each time drawing a random RV from a normal distribution with σ_{RV} of 100 km s^{-1} and re-calculating the EW. The resulting median and standard deviation of the distribution were entirely consistent with our original measurements. We therefore conclude that the RV of the target does not influence these calculations.

2.3.5 Excluded Objects

We present J-band spectra and measure equivalent widths and FeH absorption for all BDSS targets, where relevant. However, two sub-populations of our sample were removed from the surface gravity analysis: known binaries and subdwarfs, whose spectral features are known to vary from the general field population for reasons other than their surface gravity.

2.3.5.1 Binaries

LP 213-67 (M8+L0; Close et al. 2003), 2MASS 0850+1057 (L6+L7; Reid et al. 2001; Burgasser et al. 2011a), SDSS 0805+4812 (L4+T5; Burgasser 2007; Burgasser et al. 2016a), 2MASS 2140+1625 (M8.5+L2; Close et al. 2003), 2MASS 2152+0937 (L6+L6; Reid et al. 2006), 2MASS 1315-2649 (L3.5+T7; Burgasser et al. 2011b) are known spectral binaries in our sample. We caution against inferring a gravity type or age estimate for these objects, as their combined spectra could have an effect on the gravity-sensitive indices. For example, 2MASS 1315-2649 (L3.5+T7), which Burgasser et al. (2011b) finds to be at least 1 Gyr old given its kinematics, has an INT-G gravity type, which would imply an age of $\lesssim$ 100 Myr. It is possible that this discrepancy in age estimate is caused by binarity.

2.3.5.2 Subdwarfs

Four targets in our sample are known subdwarfs, LHS 1135 (d/sd M5; Kirkpatrick et al. 2010), WISE 0435+2115 (sd L0; Kirkpatrick et al. 2014), SDSS 1256-0224 (sd L3.5; Burgasser et al. 2009), and 2MASS 0532+8246 (sd L7; Burgasser 2007). These objects tend to have large space motions, are typically found to be part of the Galactic halo population, and generally have sub-solar metallicity, although they exhibit stronger hydride features than similarly classified dwarfs. Because of their low metal content, we chose to exclude these objects from our analysis and do not determine gravity types for the subdwarfs in our sample. It should be noted that subdwarfs can exhibit small K I EWs due to their lower metal content. These smaller EWs can be misleading as it is thought that these objects are quite old, and should not exhibit signs of low gravity. For example, the red K I doublet in

the J band of SDSS 1256-0224 is weak enough to infer low gravity, though the strength of its FeH_J index implies high gravity and as a subdwarf it is likely older than $\sim$ 5 Gyr.

2.4 Discussion

2.4.1 Comparison to Allers & Liu (2013)

In Figure 2.5, we plot our K I EW values (left) and FeH_J index values (right) versus those of A13, for the overlapping targets in our samples. We find that although the two data sets use different instruments with different resolving powers, our results are consistent within the uncertainties. The 1.1778 μm EW values appear to be slightly higher on average in A13 than in our own analysis, but our values are consistent within 2σ. The 1.2529 μm line appears to have the opposite result, with our values being slightly higher than those presented in A13. The major outlier is G196-3B, which has a lower SNR spectrum in A13, as indicated by its larger error bar. A13's value is less than 2σ away from our result.

We find that the modified technique using only J-band indices with NIRSPEC R $\sim$ 2000 spectra produces consistent results to the gravity classifications determined using spectral indices across the *z, J, H,* and K bands. Of the 20 matching targets between the two samples, all targets except one receive the same designation as found by A13, allowing for overlap in the borderline designations. For example, A13 finds that PC0025+0447 has intermediate gravity, while we classify it as borderline VL-G/INT-G. The exception is GL 417 BC (L4.5+L6) which we exclude because of its binary nature. When compared to the index value cutoffs for an L5 dwarf, we designate this object as FLD-G, as does A13.

2.4.2 Overall Trends

Before discussing overall trends in our sample, we must clarify that all spectral types for our objects were compiled from the references listed in Table 2.1. Some objects were classified in the red-optical, while others were classified in the NIR, and objects can have a spectral type uncertainty as large as $\pm$2 spectral types.

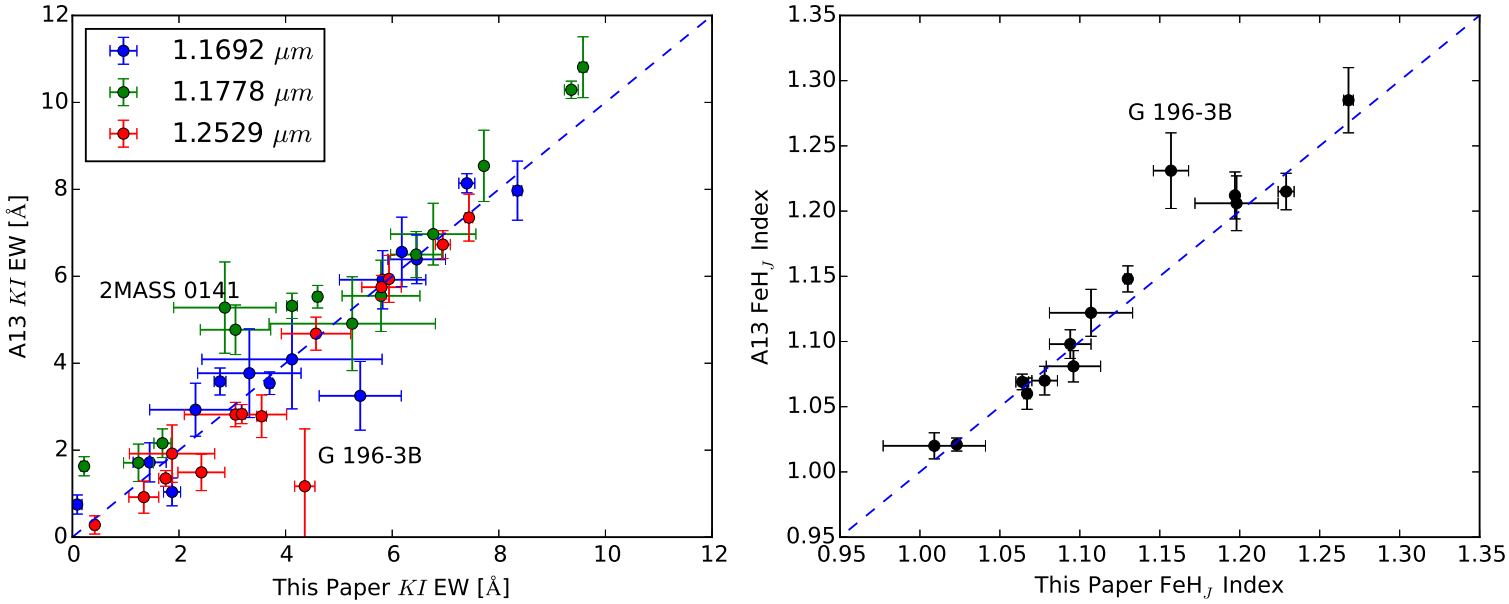

Figure 2.5: Left: comparison of K I EW values between A13 and this paper. Colors indicate the particular line at which the EWs were calculated. The one-to-one line is shown to aid comparison. Right: comparison of FeH$_J$ index values from A13 and this paper. Despite differing instruments and resolving powers, our values are consistent within the uncertainties.

Such discrepancies have been well documented in the literature and several methods have been presented in various papers for determining spectral types. For this reason, we can expect that the uncertainty in spectral type will cause larger uncertainty in the the overall trends.

As noted in Burgasser et al. (2002) and McLean et al. (2003), potassium equivalent widths in the J-band tend to rise with increasing spectral type from M5 to ∼L5 and at ∼L5–L7 the EWs drop, rising again with increasing spectral type around L8. We see this same trend in the full sample (Figure 2.3), though it shows a large amount of scatter. Objects lying below the trend exhibited by the field dwarfs are primarily those exhibiting signs of youth (VL-G and INT-G). However, some objects show signs of low gravity in one absorption feature, while exhibiting field-like features elsewhere in their spectrum. For this reason, gravity types should be based on multiple gravity-sensitive indices, as A13 also cautions.

The behavior of the FeH_J index follows a similar trend to the K I EWs (Figure 2.4), although the FeH_J index peaks at ∼L3, drops out almost entirely near the L/T transition, and then re-emerges at much lower levels of absorption in the mid-T spectral types, before again dropping out almost entirely in the late T's. This trend is similar to results seen by Burgasser et al. (2003) for the FeH feature at 0.9896 μm. They note a weakening in FeH band strength in late-type L dwarfs followed by a slight strengthening, near spectral type ∼T5.5, before disappearing again. Burgasser et al. (2003) proposes that the re-emergence of this feature in the T dwarfs is an indication of cloud clearing. Holes in the cloud deck or a complete lack of clouds in the upper atmosphere allow the observer to detect light from deeper within the atmosphere of the brown dwarf, where the temperatures are warm enough to sustain the presence of the FeH molecule. This interpretation has recently been challenged by Tremblin et al. (2016), who find that the FeH reversal can be reproduced by thermochemical instability effects, rather than cloud opacity changes. Regardless of the interpretation, we verify the trend in the re-emergence of FeH absorption.

The A13 gravity classifications do not extend to spectral types cooler than L7. We are unable to extend these classifications to later spectral types, even with our larger sample. Establishing a low gravity sequence requires a large enough sample of field dwarfs to deter-

mine the field sequence. Additionally, a large sample of known young objects are required to determine the location of the low gravity objects. Currently there are very few known young late-type L or early T dwarfs, none of which are in our sample. Searches for very low mass objects in nearby young moving groups could yield a larger sample to carry out such a study, but this is not possible with the sample presented here.

Some of the VL-G and INT-G objects in our sample are known "red" L dwarfs because their $J-K_s$ colors are significantly redder than the $J-K_s$ colors of typical field dwarfs. Red $J-K_s$ color can be an indication of youth, though the term "red" should be reserved for those L dwarfs with red $J-K_s$ color that do not otherwise show signs of youth (see Kirkpatrick et al. 2010 for further discussion of the red and blue L dwarfs). Likewise, L dwarfs with significantly bluer $J-K_s$ colors compared to typical field dwarfs are called "blue", though this nomenclature should also be reserved for those L dwarfs with significantly bluer colors that do not exhibit signs of very low metallicity. In general, we find that the "red" and "blue" L dwarfs do not show consistent signs of low or high gravity, respectively.

2.4.3 Comparison of Objects of Known Age

To understand the age limits represented by the gravity classifications, we compare objects with known or predicted ages in the literature, determined by independent methods, such as kinematics or companionship to a well characterized star. Table 2.3 lists age estimates and gravity types for 64 objects in the BDSS with previously determined ages. All BDSS targets that are candidate or suspected members of nearby young associations are included. Likelihood of membership (where available in the literature) is noted as well. Also included are several targets with age estimates from their more massive companions. Figure 2.6 shows the three adopted gravity-sensitive K I EWs and the FeH_J index versus spectral type for objects with known ages for dwarfs of spectral type M5.5-L0. Binaries from Table 2.3 are not shown, nor is the only single object of spectral type later than L0 in our sample of known-age objects, 2MASS 2244+2043 (L6, VL-G, AB Dor). Red symbols represent objects of ages < 30 Myr, green symbols denote objects between $\sim$30 and 100 Myr, and blue symbols

represent objects >100 Myr. Varying shapes are used to distinguish between the different young associations (see figure legend for more details).

As seen in Figure 2.6 and Table 2.3, members of various associations tend to have the gravity type corresponding to the estimated age of the association. A few targets have previously been found to be interlopers, so we exclude these from our analysis. Additionally, several objects with known ages are also tight binaries with potentially contaminated spectra (see § 2.3.5.1). Binaries of known ages are listed in Table 2.3, but are excluded from Figure 2.6 and any additional age calibration analysis (§ 2.4.5). Below we discuss each of the associations in order of estimated age.

All six of the ρ Ophiuchi candidates (<1 Myr, Greene & Meyer 1995), all thirteen Taurus ($\sim$ 1.5 Myr, Briceño et al. 2002) candidates, and 2MASS 2234+4041 (1 Myr; Companion to LkHα 233; Allers et al. 2009), have VL-G classifications, as expected. For targets with σ Orionis (3 Myr, Brown et al. 1994) designations, all but one of the six targets is classified as VL-G. Only S Ori 47 is classified as INT-G (not shown in Figure 2.6 or Table 2.3). Unlike the other σ Orionis candidates, this target's J-band spectrum shows very clear K I absorption features, more akin to a field dwarf, as noted in McGovern et al. (2004). McGovern et al. (2004) conclude that this object is likely a several Gyr old object located $\sim$120 pc away, with a mass near the hydrogen burning limit, and is not associated with the σ Orionis cluster. Our analysis of S Ori 47 suggests that S Ori 47 is likely much younger than 1 Gyr, but certainly older than $\sim$30 Myr and very unlikely to be associated with σ Orionis. Based on the age vs. EW values in Section 2.4.5, we estimate that S Ori 47 has an age closer to $\sim$150 Myr, and is likely an intermediate aged field dwarf. For this reason, we have excluded S Ori 47 from the age-calibrated sample in § 2.4.5.

Both TW Hya ($\sim$10 Myr, Bell et al. 2016) targets have VL-G classifications. Of the fifteen objects with Upper Scorpius (11 $\pm$ 2 Myr, Pecaut et al. 2012) designations in our sample, all but three have VL-G classifications.

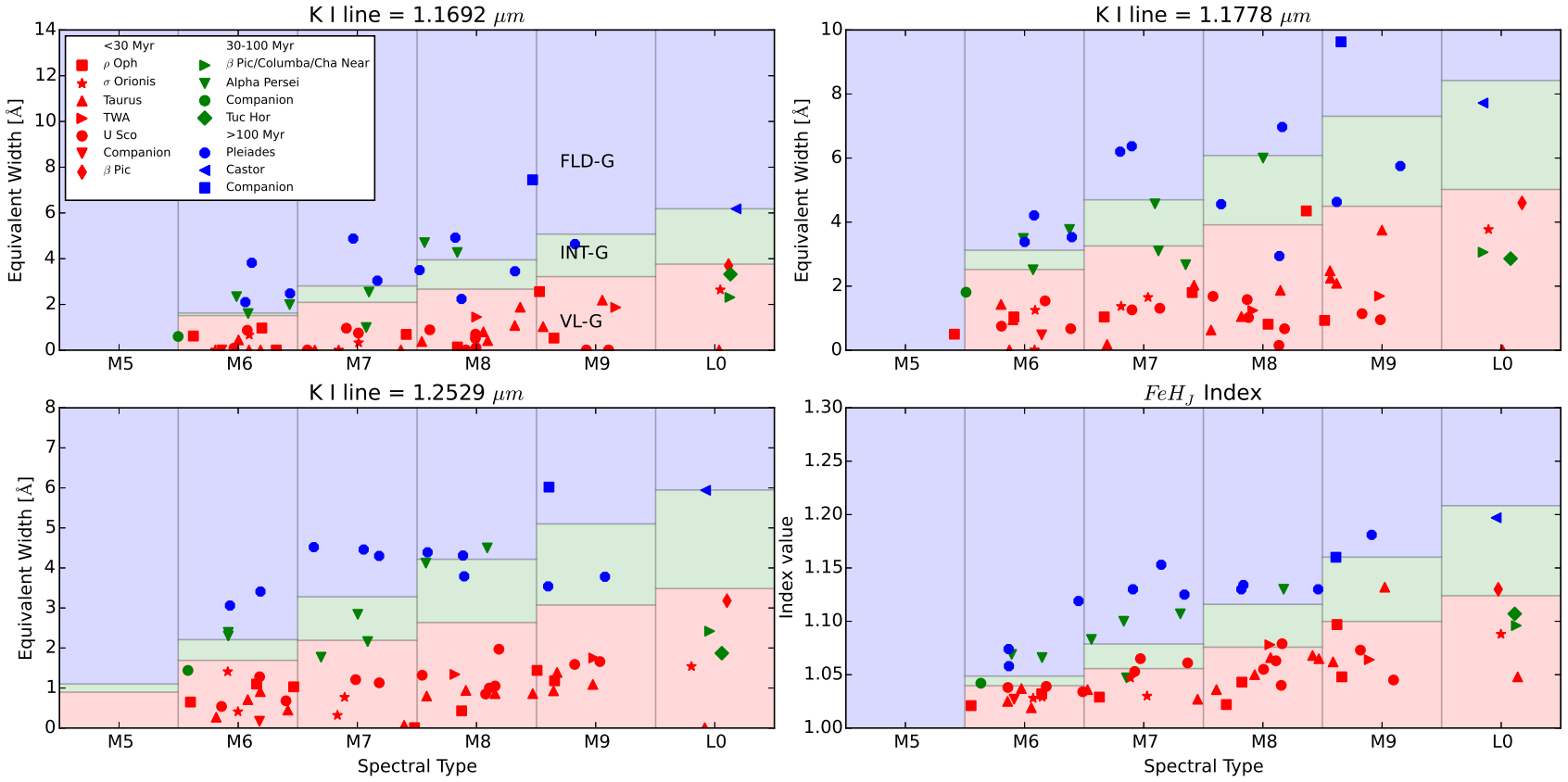

Figure 2.6: EW vs SpT and FeH_J vs SpT for dwarfs of spectral type M5.5-L0 with known ages. Different shaped symbols represent the methods used to estimate ages, i.e. group membership or an age estimate from a more massive stellar companion. For references, see Table 2.3. Symbols are colored by their known ages as follows: Red symbols have ages < 30 Myr, green symbols are $\sim 30 - 100$ Myr, and blue symbols are >100 Myr. Binaries from Table 2.3 are not shown, nor is the only single object of spectral type later than L0 in our sample, 2MASS 2244+2043 (L6, VL-G, AB Dor). Spectral types have been distributed randomly in each spectral type bin for ease of viewing.

U Sco 121, 85, and 132 each have FLD-G designations, and they are all previously suspected non-members (Muzerolle et al., 2003). Our analysis supports this conclusion. These three objects are not shown in Figure 2.6 or Table 2.3 and are excluded from the age-calibrated sample in § 2.4.5. The β Pic (21–26 Myr; Bell et al. 2016) target, 2MASS 0443+0002, is classified as VL-G.

2MASS 0141-4633 in Tucana Horlogium (45 ±4 Myr, Bell et al. 2016) is classified as VL-G. 2MASS 0608-2753 also receives a VL-G classification. Based on results from Gagné et al. (2014) and Faherty et al. (2016), we list this target as a candidate member of three groups: Cha-Near (∼10 Myr, Zuckerman & Song 2004), β Pic, and Columba (42^{+6}_{-4} Myr, Bell et al. 2016).

Of the Alpha Persei (80–100 Myr, Stauffer et al. 1999) members, one is classified VL-G, one is INT-G, and the other five are FLD-G. AP 270, which receives a VL-G classification, is less likely to be a member of Alpha Persei and could potentially be a young interloper. Gl 577 BC (70 Myr; companion) is classified as FLD-G.

The majority of the Pleiades (∼125 Myr) targets receive FLD-G classifications. Two Pleiades members (Roque 7 and Roque 4) are classified as INT-G, and Teide 1 is a borderline VL-G/INT-G object, but all three of these targets have much lower SNR spectra (SNR ∼10) and thus have much more uncertain gravity types. Simon et al. (2006) used a comparison to the Pleiades to date Gl 569 BC at ∼100 Myr. Gl 569 BC receives a FLD-G classification using our method, similar to the Pleiades objects studied here.

Surprisingly, the AB Doradus (149^{+51}_{-19} Myr, Bell et al. 2016) candidate 2MASS 2244+2043 is classified as VL-G in our analysis. Several other studies of the members of AB Doradus have determined a variety of gravity classifications for different members. A13 and Faherty et al. (2016) also present AB Doradus members with VL-G signatures, as well as members with INT-G and FLD-G classifications. Aller et al. (2016) presents new AB Doradus members with INT-G classifications.

LP 944-20 has been identified as a member of the Castor moving group (400 ±40 Myr, Zuckerman et al. 2013), though the existence of the group is disputed and age estimates vary

broadly for proposed members. (See e.g., Monnier et al. 2012 and Mamajek et al. 2013). However, LP 944-20 also has a Li measurement in Reiners & Basri (2009), suggesting an age < 500 Myr and implying that this target is younger than the typical "old" field dwarf. This target receives a FLD-G designation.

The object in our sample with the oldest measured age is Gl 417BC, which Allers et al. (2010) estimate to be 750^{+140}_{-120}, based on gyrochronology. Kirkpatrick et al. (2001) estimates an age of 80–300 Myr based on various dating methods for Gl 417A. This target is also a FLD-G object.

Our analysis suggests that the VL-G classification is only sensitive to ages as old as ∼20–30 Myr, as originally proposed in A13. The INT-G designation appears to probe only the ∼30–100 Myr range, while the FLD-G designation probes $\gtrsim$100 Myr, not $\gtrsim$200 Myr as suggested by A13. However we see that, similar to the results seen in Faherty et al. (2016), there is a spread in gravity classifications even amongst targets belonging to the same association although they are assumed to be coeval. In Section 2.4.5 we further examine the age ranges probed by each gravity designation as a function of spectral type and K I line.

2.4.4 Potentially Young Objects

Here we highlight targets with VL-G and INT-G designations that are not previously discussed in A13, and are not known members of nearby young associations or young clusters. For each of the targets, we calculate the BANYAN II v1.4 likelihood of membership in various nearby young moving groups, as well as likelihood of being a young (<1 Gyr) or old (> 1 Gyr) field object (Gagné et al., 2014; Malo et al., 2013). The BANYAN II tool utilizes the 3D space motions and positions of many nearby young moving groups to determine via bayesian statistics the likelihood of a target being a member of a nearby young association. Not all associations are accounted for, so a BANYAN II "young field" object could be a member of a young association not included in BANYAN II, or it could indeed be a young field dwarf, that is, a field dwarf exhibiting signs of youth. BANYAN II requires at least target coordinates and proper motion to estimate membership probability, but we input dis-

tance and radial velocity information for the BANYAN II online tool when available from the literature. We used the priors developed by and outlined in Gagné et al. (2014) and did not use the uniform priors option.

2MASS 1459+0004 is an M6 dwarf with a VL-G designation. Kirkpatrick et al. (2010) present the discovery of this object as well as a proper motion of μ_α= 308 ± 248 mas yr^{-1}and μ_δ= -342 ± 275 mas yr^{-1}. BANYAN II results for this target suggest $\lesssim$ 1 % likelihood of this object belonging to Argus or AB Dor, a 13.9 % probability of being a young field object, and 85.85 % likelihood of being an old field object, based solely on the target's coordinates and proper motion. If we assume the target is $<$ 1 Gyr old, it then receives a 98.2 % probability of being a young field object.

2MASS 1331+3407 in an L1pec object with an INT-G classification noted as being particularly red by Kirkpatrick et al. (2010). Gagné et al. (2014) found that this object has no likelihood of belonging to a nearby young moving group, so this is most likely an intermediate-aged field dwarf. Having particularly red spectroscopic or photometric features can be an indication of youth, though Kirkpatrick et al. (2010) emphasizes that the term "red" should be reserved for objects with significantly red $J - K_s$ colors or spectra that do not show signs of youth.

2MASS 0543+6422 is an L2 dwarf with an INT-G classification. Gagné et al. (2015c) also gave this object an INT-G classification based on an IRTF SpeX spectrum and do not find any probability of this object belonging to currently known young moving groups.

2MASS 1841+3117 is an L4pec dwarf with an INT-G designation. The optical spectrum for this object in Kirkpatrick et al. (2000) is noticeably blue, which can imply higher gravity, however the K I lines in the J band exhibit signs of lower gravity. It is possible that the peculiar nature of its spectrum is implying that a physical mechanism other than low-gravity could be the cause of the smaller K I EWs, or that its blueness could be caused by some reason other than high surface gravity. BANYAN II results using coordinates, proper motion, and parallax for this object (Faherty et al., 2009) suggest a 54 % probability that this object is a young field object.

2MASS 1553+2109 is an L5.5 dwarf with an INT-G classification. This object is known to have red NIR colors and strong Li absorption (Kirkpatrick et al., 1999), a further indication that it is a young field dwarf. Based on the BANYAN II results using the kinematics from Schmidt et al. (2010), this object has 30.5 % likelihood of being a young field dwarf, and a 69.5 % likelihood of being an old field dwarf.

2MASS 0740+2009 is an INT-G classified L6 dwarf, previously found to have unusually red $J - K_s$ colors (Thompson et al., 2013). Its red colors could be attributed to lower surface gravity, in this case, and is likely younger than $\sim$ 100 Myr. Using the kinematics and distance from Faherty et al. (2009) and the the BANYAN II predictions, we find only a 2.4 % likelihood that this object belongs to the young field population and a 97.6 % likelihood of being an old field dwarf.

2MASS 2151+3402 is an L7pec dwarf with a VL-G classification. However, (Kirkpatrick et al., 2010) find that it has slightly blue NIR colors. This particular object has a low SNR spectrum and it is likely that the noise contaminated the estimation of the K I EWs. We smoothed the spectrum using a Gaussian 1D Kernel with a width of 3 pixels and re-calculated the K I EWs using the methods described above. After smoothing, the gravity scores this object receives are "1", "1", and "0". Additionally, if FeH_J were defined for L7 dwarfs, this would likely receive a FLD-G designation for that index, making it more likely a FLD-G object overall. Schneider et al. (2014) publish a measurement of the $\mathrm{H}_2(K)$ index for this object, which they measure to be larger than the median $\mathrm{H}_2(K)$ value for L7 dwarfs. The $\mathrm{H}_2(K)$ index (Canty et al., 2013) is an index designed to measure the slope of the K-band continuum, which is known to be "peakier" in low-gravity objects. A high $\mathrm{H}_2(K)$ for this object is further indication that this is likely to be a field-gravity object. However, BANYAN II predictions based on the proper motion from Kirkpatrick et al. (2010) and the sky coordinates suggest a slight ($< 1\%$) probability that this object could be a member of β Pic or Columba, a $\sim$1–2 % probability of belonging to Argus or AB Dor, and a 34.4 % likelihood of being a young field object.

2.4.5 Determining Ages

To further investigate the ability of the gravity indices to determine ages, we study the dependence of object age, taken from the literature, with K I EW for the lines at 1.1692 μm, 1.1778 μm, and 1.2529 μm binned by spectral type (Figure 2.7). There are a total of 73 objects used in this analysis, which are not known to be binaries and are assumed to be reliable age calibrators. Of these, 51 objects are BDSS targets, 15 objects come from A13, and 7 objects overlap both the BDSS and A13 samples. An additional 24 BDSS targets without known associations to young moving groups that received FLD-G designations in all four indices are also plotted, with age estimates of 5±4 Gyr. Each panel plots age vs. K I EW for a bin of three spectral types, because of the need to remove the previously shown trend of EW with spectral type. In general, spectral types are only known to ± 1 type, so this coarser grouping of spectral types is analogous to the inherent spread in spectral features seen by objects of the same given spectral type. There is a clear linear trend between the K I EWs and log(Age) as displayed in Figure 2.7. Thus, for each graph we perform a weighted orthogonal distance regression to determine a best fit function of the form in Equation 2.1 using the *scipy.odr* package [1] in python.

$$Age = A \times 10^{B \times EW} \tag{2.1}$$

Parameters and 3σ uncertainties for the best fit lines for each spectral type bin from M6 to L0 and each K I line are listed in Table 2.4. For ages in units of Myr and EWs measured in Å, the coefficient A is in units of Myr and B is $Å^{-1}$.

Figure 2.7 shows only three of the spectral type bins. The figures for spectral types M7 ± 1 and M9 ± 1 show similar trends and are not shown, however the best fit parameters for these spectral type bins are listed in Table 2.4.

[1] https://docs.scipy.org/doc/scipy/reference/odr.html

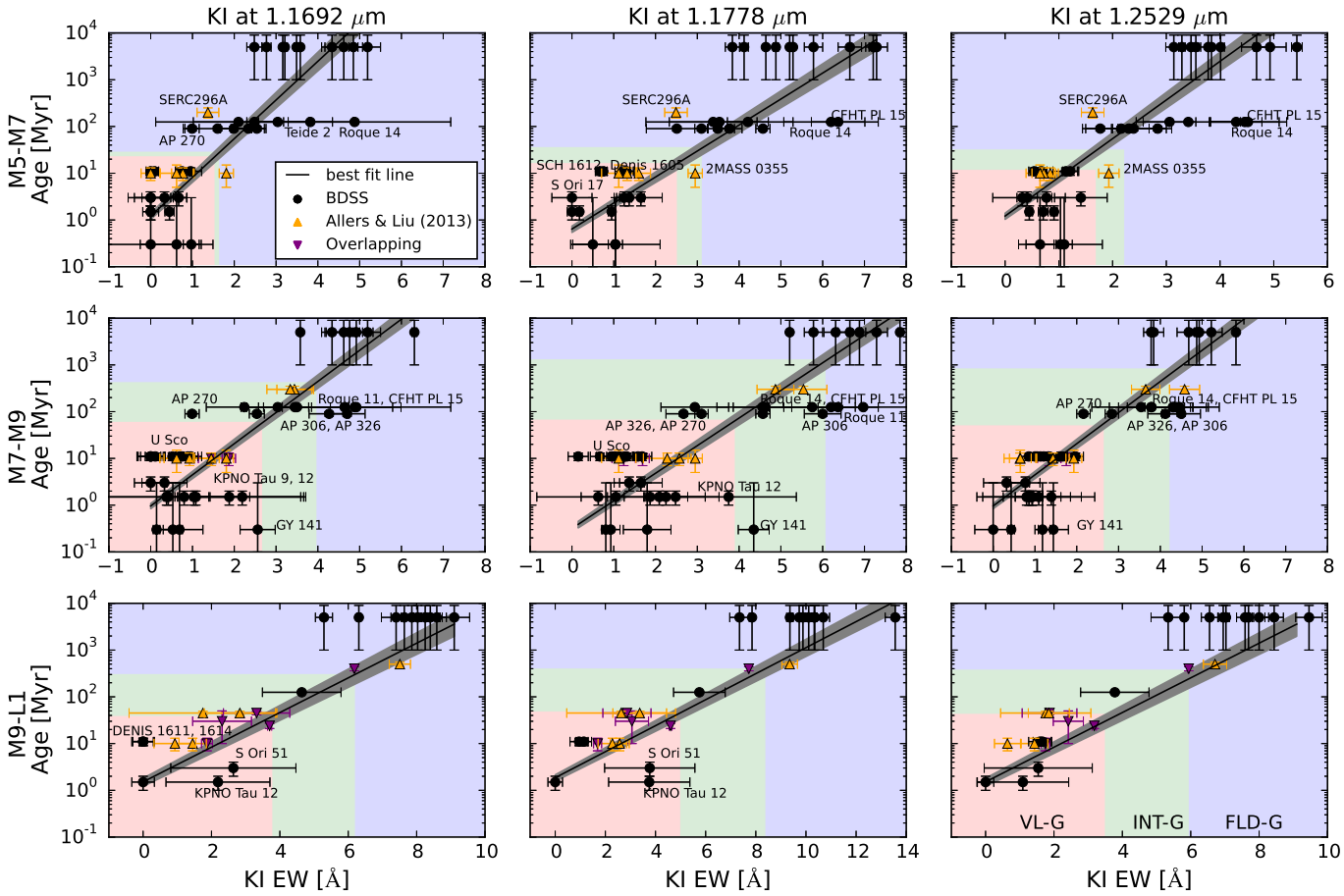

Figure 2.7: Age vs K I EW at 1.1692 μm, 1.1778 μm, and 1.2529 μm, binned by spectral type. Blue, green, and red shaded regions are the same as Figure 2.3. BDSS objects with known ages are shown in black circles, alongside a field sample selected from targets with "FLD-G" designations and given ages of 5 $\pm$ 4 Gyr to bound the upper limit of age as a function of EW. To increase our sample size we include objects from A13 with moderate resolution data and known ages (yellow upward-facing triangles). Objects with overlapping data between the A13 sample and our sample are marked by purple downward-facing triangles. Significant outliers are denoted in each panel as well. The black line represents the best-fit line as determined by a weighted orthogonal distance regression using the *scipy.odr* package in python. The grey shaded region represents the 1σ uncertainties in both slope and intercept.

We were unable to achieve satisfactory fits to the function of log(Age) vs. FeH_J index, likely because the range of values for the FeH_J index is much smaller. Additionally, we were unable to extend the age vs. EW relationship beyond ∼L0 because of the lack of later-type, age-calibrated objects in our sample.

The red, green, and blue shaded regions in Figure 2.7 are taken from the A13 boundaries for VL-G, INT-G, and FLD-G for the average spectral type at each wavelength. These aid in demonstrating the large and varying age ranges probed by each of the gravity types. From this figure, one can see that the large inherent spread in EW value makes it difficult to draw firm conclusions about the age of an object solely based on the measurement of its K I EWs. Coeval objects of similar spectral types can have widely varying EWs, as mentioned previously in regards to the AB Doradus moving group.

Although it is tempting to assign ages to each of the targets based on the relationships shown in Figure 2.7 and Table 2.4, we discourage against this because of the inability to significantly determine an age by combining the age estimates from each of the K I EWs. Instead, we have determined broad age limits for each of the gravity classifications at each spectral type and for each K I line. These are provided in Table 2.5 and shown in Figure 2.8. We determine the age at which each of the gravity classifications intersects the best-fit lines from Figure 2.7 for each spectral type bin and each K I line. The lower age limits are set by ρ Oph at 0.3 Myr and the upper age limits are set by age estimates of the field population at ∼10 Gyr. The results in Table 2.5 and Figure 2.8 show how large of a spread in age estimates there can be for objects of similar spectral types with varying gravity types. For example, an M8 target with an INT-G classification would be estimated to have an age ranging from 50 Myr – 1.21 Gyr depending on the K I line used. An M9 INT-G target on the other hand, has age estimates ranging from 17 – 290 Myr. Additionally, the bounds of the intermediate age range for a single K I index across all 5 spectral types show large variation. The most extreme example of the range in age estimates for a single K I line is seen for the upper age limit probed by INT-G for the K I line at 1.1778 μm, which ranges from 35 Myr to 1.21 Gyr depending on spectral type. We find that assigning a specific age range to the A13 gravity classifications is beyond the scope of this paper.

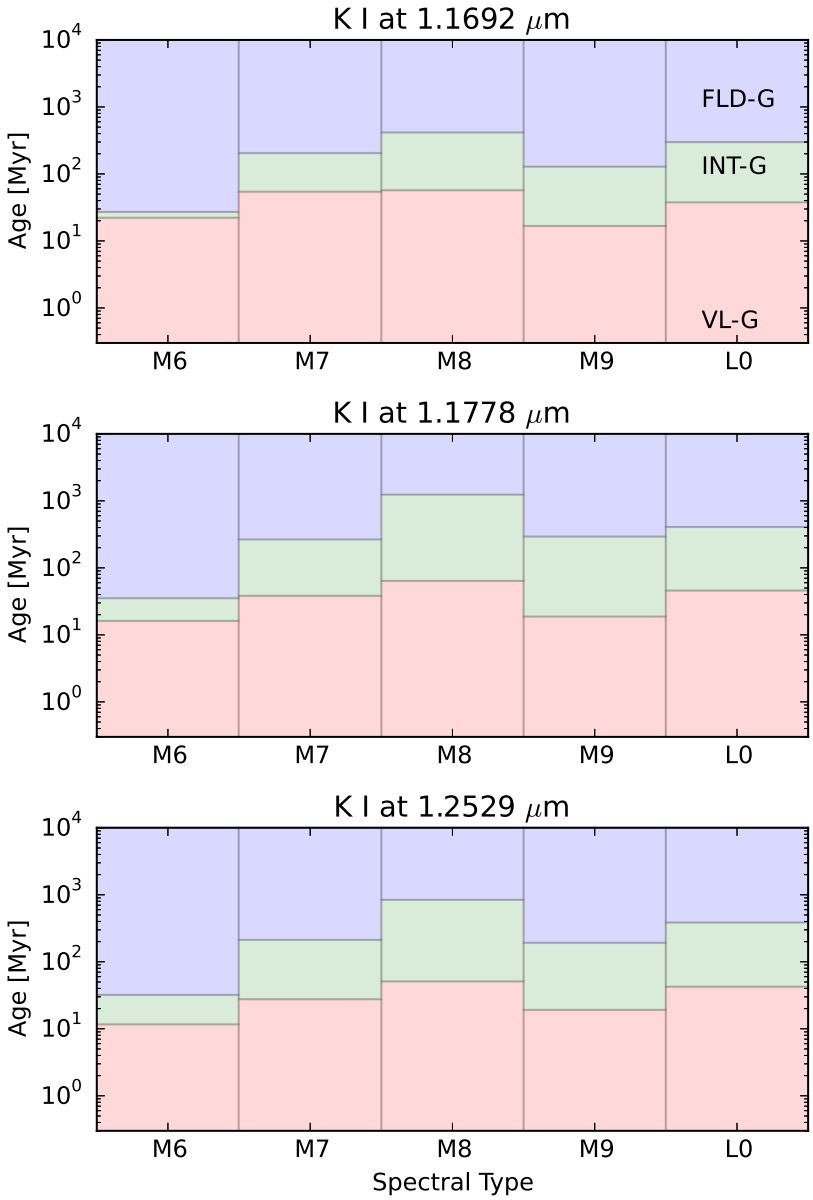

Figure 2.8: Age vs. Spectral Type for each gravity index in A13. Ages were estimated by applying the best fit parameters for each spectral type bin and K I line in Table 2.4 to the A13 EW boundaries between each gravity classification. Red shaded regions represent VL-G classifications, green shading denotes INT-G classification, and blue shading represents FLD-G ages.

Uncertainty in age determination and gravity classification was also discussed in Aller et al. (2016). The authors of that paper determined uncertainties on the gravity types using a Monte Carlo approach in order to distinguish borderline objects that might otherwise be classified as FLD-G objects, but show hints of youth. The broad range of ages associated with each gravity classification indicates the importance of further age analysis using other techniques. For example, kinematic information, potential young moving group membership, or stellar/sub-stellar benchmark companions could further distinguish the age of a particular object. Low-mass stars and brown dwarfs exhibiting signs of low gravity merit follow-up observations to confirm or refute their potential youth status.

2.4.6 The Future for Surface Gravity Analysis

With the aforementioned limitations of gravity classification as a method for establishing the age of a young brown dwarf, we can make significant advances in this field in several ways. First, a larger sample of young L and T dwarfs of known ages is needed to extend the A13 classifications to later spectral types. In this paper, we do not have a large enough sample of young objects with spectral types later than $\sim$ L6 in order to expand these classifications into the L/T transition. The unshaded regions of Figures 2.3 and 2.4 display the regime in which significant progress can be made in furthering our understanding of gravity and age at varying masses and temperatures for these substellar objects.

Several recent works have highlighted discoveries in this area. Examples include the new bonafide T5.5 member of AB Doradus (Gagné et al., 2015a), the young L7 TW Hya interloper presented in Gagné et al. (2016), the two new candidate L7 members of TW Hya presented in Kellogg et al. (2016) and Schneider et al. (2016), and the 10 candidate YMG members of spectral type L7-T4.5 found with Pan-STARRS and WISE in Best et al. (2015). Additionally, discoveries of jovian exoplanets around young stars present a method for studying objects that appear very similar to young field L and T dwarfs. Some examples of these exciting discoveries include 51 Eri b (Macintosh et al., 2015) and GU Psc b (Naud et al., 2014). Progress in extending the sample of known-age late-M and early-L dwarfs

will also further our understanding of observational signatures of brown dwarf evolution. To this end, Burgasser et al. (2016b) presented the first planetary-mass member of 32 Ori (L1). Kinematic information of M and L dwarfs with Gaia (Gaia Collaboration et al., 2016b,a) will confirm or refute the membership of young moving group candidates and allow for discoveries of new members.

Second, high-resolution spectroscopy obtained with the next generation of 30-m class telescopes in conjunction with improved atmospheric models will allow us to better correlate surface gravity with age in these young brown dwarfs. The current atmospheric models have incomplete line lists and do not accurately represent the observed behavior of the K I lines. The diversity of spectral features present in low-mass stars and brown dwarfs likely stems from physical properties and atmospheric conditions that we cannot probe at these moderate resolving powers or using these particular diagnostics. If atmospheric models continue to improve in tandem with observational capabilities, it may be possible to better isolate the effect that surface gravity has on brown dwarf spectral features.

2.5 Summary

We presented 228 *J*-band spectra of M, L, and T dwarfs in the BDSS, the largest set of publicly available NIR spectra at R $\sim$ 2000. Using the same J-band gravity sensitive indices as Allers & Liu (2013), we calculated K I equivalent widths and FeH absorption to determine gravity classifications for objects of spectral type M6–L7. Our technique is verified with 20 overlapping targets from A13, for which we derive similar gravity classifications despite using fewer spectral indicators. A subset of 73 objects with known (or suspected) ages from the literature (after excluding binaries from the full sample of known-age objects) define the trend of K I EW with age. By assigning ages to the boundaries of each gravity designation for spectral types M6–L0, we find that the age ranges probed by each of the K I lines vary widely. With a larger sample of age-calibrated M, L, and T dwarfs it will be possible to estimate ages for the entire sample with much greater certainty. This level of precision will likely require high signal-to-noise, high-resolution spectra of benchmark systems and detailed

model comparison. Until then, the gravity designations from A13 remain a useful tool for dividing the low-mass products of star formation by relative age.

2.6 Acknowledgements

The authors wish to recognize and acknowledge the very significant cultural role and reverence that the summit of Mauna Kea has always had within the indigenous Hawaiian community. We are most fortunate to have the opportunity to conduct observations from this mountain. This research has benefitted from the M, L, T, and Y dwarf compendium housed at DwarfArchives.org. This research has made use of the SIMBAD database, operated at CDS, Strasbourg, France. We thank the anonymous referee for their insightful comments, which improved the paper.

Table 2.1. Observations and Designations

Designation	Disc. Ref	Short Name	SpT	SpT Ref	UT Date of Observation	A0V Calibrator	Slit Width [arcsec]	Exp. Time [s]
2MASS J06195260-2903592	29	2MASS 0619-2903	M5	1	11/21/2004	HD 41473	0.38	1200
2MASS J00433134+2054316	68	LHS 1135	d/sdM5	54	12/4/2003	HD 7215	0.38	600
GJ 577 BC	64	Gl 577 BC	M5.5+M5.5	88	3/24/2003	HD 132072	0.38	600
2MASS J16262152-2426009	40	ρ Oph GY 5	M5.5	81	5/14/2003	HD 151736	0.38	600
WDS J04325+1732Ba	27	GG Tau Ba	M6	103	11/7/2004	HD 28354	0.38	1200
2MASS J14594626+0004427	54	2MASS 1459+0004	M6	54	7/19/2005	HD 123233	0.38	1200
2MASS J22344161+4041387	29	2MASS 2234+4041AB	M6+M6	2	12/4/2003	BD +39 4890	0.38	600
2MASS J16051403-2406524	78	DENIS-P 1605-2406	M6	78	5/2/2004	HD 147384	0.38	1200
2MASS J04262939+2624137	11	KPNO Tau 3	M6	11	11/7/2004	24 Tau	0.38	600
2MASS J04312405+1800215	10	MHO Tau 4	M6	11	12/4/2003	HD 27761	0.38	600
2MASS J16262780-2426418	102	ρ Oph GY 37	M6	104	5/12/2003	HD 151736	0.38	1200
2MASS J05375745-0238444	8	SOri 12	M6	8	12/4/2003	HD 37887	0.38	1200
2MASS J05390449-0238353	8	SOri 17	M6	8	2/9/2004	HD 294285 (A1V)	0.38	1200
2MASS J16014955-2351082	3	USco CTIO 66AB	M6+M6	3	5/12/2003	HD 151736	0.38	600
2MASS J02535980+3206373	29	2MASS 0253+3206	M6	1	12/4/2003	BD+3i 500 (A3)	0.38	600
2MASS J08402975+1824091	42	2MASS 0840+1824	M6	48	12/4/2003	HD 89239	0.38	480
2MASS J10494146+2538535	36	2MASS 1049+2538	M6	36	12/4/2003	HD 89239	0.38	600
2MASS J03230483+4816111	97	AP 310	M6	97	7/20/2003	HD 22401	0.38	1200
Cl* Melotte 20 AP 316	97	AP 316	M6	97	11/22/2004	HD 20842	0.38	1200
2MASS J14121215-0035165	68	GJ 3828B	M6	45	4/30/2004	HD123233	0.38	1200
2MASS J03473900+2436226	108	Roque 16	M6	108	11/22/2004	24 Tau	0.38	1200
2MASS J03520670+2416008	73	Teide 2	M6	73	12/4/2003	HD 23512	0.38	1200
2MASS J15514732-2623477	3	USco CTIO 121	M6	3	7/19/2003	HD 141442	0.38	1200
UScoCTIO 85	3	UScoCTIO 85	M6	3	3/25/2003	HD 142703	0.38	1200

Table 2.1 (cont'd)

Designation	Disc. Ref	Short Name	SpT	SpT Ref	UT Date of Observation	A0V Calibrator	Slit Width [arcsec]	Exp. Time [s]
2MASS J10562886+0700527	107	Wolf 359	M6	47	12/6/2000	HD 93346	0.38	120
2MASS J04321606+1812464	10	MHO Tau 5	M6.5	10	2/8/2003	HD 25175	0.38	480
2MASS J16262226-2424070	89	ρ Oph GY 11	M6.5	104	7/22/2004	HD 151736	0.38	1800
2MASS J16121185-2047267	94	SCH 1612-2047	M6.5	94	4/7/2009	HD 144925	0.38	1200
2MASS J03180906+4925189	97	AP 301	M6.5	97	7/20/2003	HD 22401	0.38	1200
2MASS J07401922-1724449	82	Gl 283B	M6.5	48	12/31/2001	HD 61486	0.38	400
2MASS J03454126+2354099	95	PPL 1	M6.5	72	12/29/2001	HD 34317	0.38	600
2MASS J04351455-1414468	29	2MASS 0435-1414	M7	1	12/4/2003	HD 31743	0.38	600
2MASS J03204346+5059396	83	AP 270	M7	6	12/4/2003	HD 20842	0.38	2400
2MASS J05382088-0246132	8	SOri 31	M7	5	2/9/2004	HD 294285 (A1V)	0.38	1200
2MASS J05373648-0241567	8	SOri 40	M7	8	12/4/2003	HD 37887	0.38	1200
2MASS J16020429-2050425	3	USco CTIO 100	M7	3	5/13/2003	HD 151736	0.38	600
2MASS J15591135-2338002	3	USco CTIO 128	M7	3	3/25/2003	HD 142703	0.38	1200
2MASS J03354735+4917430	97	AP 325	M7	97	12/4/2003	HD 20842	0.38	1800
2MASSI J0952219-192431	36	2MASS 0952-1924	M7	36	12/4/2003	HD 90606	0.38	600
2MASS J03551257+2317378	9	CFHT PL 15	M7	96	2/8/2003	HD 25175	0.38	1200
2MASS J11571691+2755489	47	CTI 115638.4+28	M7	47	4/30/2004	HD105388	0.38	1200
2MASS J11061897+0428327	68	LHS 2351	M7	54	12/14/2000	HD 75159	0.38	600
2MASS J03464298+2424506	108	Roque 14	M7	108	12/4/2003	HD 7215	0.38	600
2MASS J15593777-2254136	3	USco CTIO 132	M7	3	5/14/2003	HD 151736	0.38	400
2MASS J16553529-0823401	101	VB 8	M7	44	6/10/2001	HD 152515 (A2V)	0.38	600
2MASS J18355309-3217129	54	2MASS 1835-3217	M7p	54	7/19/2005	HD 168086	0.38	1200
2MASS J04361038+2259560	77	CFHT-BD-Tau 2	M7.5	11	12/23/2002	HD 40686	0.38	600
2MASS J16261882-2426105	28	ISO-Oph 23	M7.5	104	5/2/2004	HD 147384	0.38	1800

Table 2.1 (cont'd)

Designation	Disc. Ref	Short Name	SpT	SpT Ref	UT Date of Observation	A0V Calibrator	Slit Width [arcsec]	Exp. Time [s]
2MASS J15594366-2014396	3	USco CTIO 130	M7.5	3	4/30/2004	HD 147013	0.38	1200
Cl* Melotte 20 AP 326	97	AP 326	M7.5	97	11/6/2004	HD 23860	0.38	2400
2MASS J03455065+2409037	108	Roque 13	M7.5	108	11/21/2004	24 Tau	0.38	1200
WDS J04325+1732Bb	27	GG Tau Bb	M7.5	103	11/7/2004	HD 28354	0.38	1200
2MASS J12073346-3932539	35	2MASS 1207-3932	M8	53	12/30/2001	HD 112832 (A3V)	0.38	1200
2MASS J04363893+2258119	77	CFHT-BD-Tau 3	M8	11	11/21/2004	HD 105388	0.38	1200
2MASS J16191646-2347235	78	DENIS 1619-2347	M8	78	7/18/2005	HD 151736	0.38	1200
2MASS J16192988-2440469	78	DENIS 1619-2440	M8	78	7/22/2004	HD 151736	0.38	1200
2MASS J04305718+2556394	11	KPNO Tau 7	M8	11	11/21/2004	HD 28354	0.38	600
2MASS J16262189-2444397	40	ρ Oph GY 3	M8	105	5/2/2004	HD 147384	0.38	1200
2MASS J16224385-1951057	94	SCH 1622-1951	M8	94	4/7/2009	HD 144254	0.38	600
2MASS J16235155-2317270	94	SCH 1623-2317	M8	94	4/7/2009	HD 144925	0.38	600
2MASS J03471792+2422317	84	Teide 1	M8	72	11/7/2004	24 Tau	0.38	1200
2MASS J10471265+4026437	69	LP 213-67	M8+L0	26	12/4/2003	HD 98152	0.38	480
2MASS J03194133+5030451	97	AP 306	M8	97	2/8/2003	HD 21038	0.38	1200
2MASSI J2349489+122438	69	LP 523-55	M8	36	11/6/2004	HD 222749	0.38	600
2MASS J03471208+2428320	108	Roque 11	M8	33	11/22/2004	25 Tau	0.38	1200
2MASS J19165762+0509021	100	VB 10	M8	44	6/10/2001	HD 180759	0.38	600
2MASS J04151471+2800096	11	KPNO Tau 1	M8.5	11	11/22/2004	HD 28354	0.38	1200
2MASS J04300724+2608207	11	KPNO Tau 6	M8.5	11	11/7/2004	HD 28354	0.38	1200
2MASS J04355143+2249119	11	KPNO Tau 9	M8.5	11	12/4/2003	HD 27761	0.38	1200
2MASS J16265128-2432419	89	ρ Oph GY 141	M8.5	66	5/13/2003	HD 151736	0.38	960
2MASS J16273863-2438391	40	ρ Oph GY 310	M8.5	104	4/30/2004	HD 147013	0.38	960
2MASS J03434028+2430113	9	Roque 7	M8.5	76	11/21/2004	24 Tau	0.38	1200

Table 2.1 (cont'd)

Designation	Disc. Ref	Short Name	SpT	SpT Ref	UT Date of Observation	A0V Calibrator	Slit Width [arcsec]	Exp. Time [s]
2MASS J21402931+1625183	36	2MASS 2140+1625	M8.5+L2	26	11/8/2009	HD 210501	0.38	600
BD+16 2708B	75	Gl 569 BC	M8.5+M9	59	4/23/2002	HD131714 (A3V)	0.38	480
2MASS J11395113-3159214	35	2MASS 1139-3159	M9	87	12/30/2001	HD 102412 (A2V)	0.38	1200
2MASS J16110360-2426429	78	DENIS 1611-2426	M9	78	5/2/2004	HD 147384	0.38	1200
2MASS J16145258-2017133	78	DENIS 1614-2017	M9	78	7/18/2005	HD 151736	0.38	1200
2MASS J04190126+2802487	67	KPNO Tau 12	M9	67	11/7/2004	HD 28354	0.38	1200
2MASS J03435353+2431115	108	Roque 4	M9	108	12/24/2002	HD 23489 (A2V)	0.38	1200
2MASS J01400263+2701505	36	2MASS 0140+2701	M9	80	11/8/2009	HD 7215	0.38	600
2MASS J12391934+2029519	49	2MASS 1239+2029	M9	49	12/24/2002	HD 109055	0.38	600
2MASS J22085600-1227448	54	2MASS 2208-1227	M9	54	7/18/2005	HD 213030	0.38	1200
2MASS J08533619-0329321	68	LHS 2065	M9	47	4/22/2002	CCDM J08581+0132AB (A2V)	0.38	480
2MASS J22373255+3922398	51	G 216-7B	M9.5	51	12/24/2002	BD+394890	0.38	600
2MASS J01415823-4633574	52	2MASS 0141-4633	L0	52	11/6/2004	HD 8977	0.38	1200
2MASSI J0443376+000205	43	2MASS 0443+0002	L0	1	11/21/2004	24 Tau	0.38	1200
2MASS J06085283-2753583	29	2MASS 0608-2753	L0	1	12/4/2003	HD 31743	0.38	600
2MASS J04272799+2612052	11	KPNO Tau 4	L0	23	12/24/2002	HD 23489 (A2V)	0.38	1200
2MASS J00274197+0503417	91	PC 0025+0447	L0	1	12/24/2002	BD+0345	0.38	1200
UGCS J053903.20-023019.9	110	SOri 51	L0	23	12/24/2002	HD 40686	0.38	1200
2MASS J17312974+2721233	87	2MASS 1731+2721	L0	87	4/14/2014	HD 165029	0.38	1200
2MASS J21073169-0307337	29	2MASS 2107-0307	L0	29	11/7/2004	HD202990	0.38	1200
2MASS J10221489+4114266	106	HD 89744B	L0	106	3/6/2001	HD 90470 (A2V)	0.38	1200
2MASS J03393521-3525440	68	LP 944-20	L0	1	12/4/2003	HD 23536	0.38	600
WISEA J043535.82+211508.9	56	WISE 0435+2115	sdL0	56	12/14/2013	HD 35036	0.38	2400
2MASS J14413716-0945590	74	DENIS 1441-0945	L0.5	53	3/24/2003	HD 132072	0.38	1200

Table 2.1 (cont'd)

Designation	Disc. Ref	Short Name	SpT	SpT Ref	UT Date of Observation	A0V Calibrator	Slit Width [arcsec]	Exp. Time [s]
2MASS J04062677-3812102	54	2MASS 0406-3812	L1	54	11/12/2014	HD 30397	0.38	2400
2MASS J00332386-1521309	38	2MASS 0033-1521	L1	1	11/7/2004	HD 218639	0.38	1200
2MASS J02081833+2542533	50	2MASS 0208+2542	L1	50	12/5/2000	BD +18 337A	0.38	1200
2MASS J03454316+2540233	57	2MASS 0345+2540	L1	54	12/4/2000	NSV 1280	0.38	2400
2MASS J10352455+2507450	50	2MASS 1035+2507	L1	50	12/31/2001	HD 98154 (A3V)	0.38	1200
2MASS J14532582+1420410	54	2MASS 1453+1420	L1	54	7/19/2005	HD 123233	0.38	1200
2MASS J21304464-0845205	53	2MASS 2130-0845	L1	54	6/11/2001	HD 205147 (A2)	0.38	1200
2MASS J02355993-2331205	37	GJ 1048B	L1	37	12/31/2001	HR 8569 (A2V)	0.38	1200
2MASS J13313310+3407583	54	2MASS 1331+3407	L1p	54	6/9/2011	10 Boo	0.38	1800
2MASS J14403186-1303263	54	2MASS 1440-1303	L1p	54	6/9/2011	HD 132072	0.38	1200
2MASS J17561080+2815238	54	2MASS 1756+2815	L1p	54	9/3/2012	HD 165029	0.38	1800
2MASS J05381462-0240154	109	SOri 47	L1.5	79	3/24/2003	HD 63741	0.38	3600
WISEA J054318.95+642250.2	56	WISE 0543+6422	L2	56	12/14/2013	HD 33654	0.38	1440
2MASS J00154476+3516026	50	2MASS 0015+3516	L2	50	12/5/2000	BD +18 122A	0.38	1200
2MASS J00311925-3840356	55	2MASS 0031-3840	L2	55	12/2/2014	HD 224622	0.38	1200
2MASS J08472872-1532372	29	2MASS 0847-1532	L2	29	12/4/2003	HD 74284	0.38	600
2MASS J20575409-0252302	29	2MASS 2057-0252	L2	1	10/6/2009	HD 203769	0.38	1800
2MASS J13054019-2541059	90	Kelu-1	L2+L3.5	98	4/29/1999	HR 5146 (A1V)	0.38	1200
WISEA J065958.55+171710.9	56	WISE 0659+1717	L2	56	11/20/2013	HD 39953	0.38	960
WISEA J235459.79185222.4	56	WISE 2354-1852	L2	56	12/14/2013	HD 219833	0.38	1800
2MASS J14313097+1436539	92	2MASS 1431+1436	L2p	92	6/9/2011	HD 131951	0.38	2400
2MASS J16202614-0416315	106	Gl 618.1B	L2.5	106	5/12/2003	SAO 160448	0.38	2400
2MASS J21041491-1037369	29	2MASS 2104-1037	L2.5	53	8/9/2011	HD 202990	0.38	1800
WISEA J060742.13+455037.0	56	WISE 0607+4550	L2.5	56	12/14/2013	HD 45105	0.38	1800

Table 2.1 (cont'd)

Designation	Disc. Ref	Short Name	SpT	SpT Ref	UT Date of Observation	A0V Calibrator	Slit Width [arcsec]	Exp. Time [s]
2MASS J22081363+2921215	50	2MASS 2208+2921	L3	30	12/31/2001	HR 8569 (A2V)	0.38	1200
2MASS J10042066+5022596	85	G 196-3B	L3	30	3/6/2001	HD 83869 (A1V)	0.38	1200
2MASS J17260007+1538190	50	2MASS 1726+1538	L3	30	9/1/2002	HD 160765 (A1V)	0.38	1200
2MASS J11463449+2230527	49	2MASS 1146+2230	L3	49	11/21/2004	HD 105388	0.38	1200
2MASS J13004255+1912354	36	2MASS 1300+1912	L3	20	4/7/2009	HD 116960	0.38	600
2MASS J15065441+1321060	36	2MASS 1506+1321	L3	54	4/26/2000	ups Ser (A3V)	0.38	1200
2MASS J14243909+0917104	7	GD 165B	L3	58	6/3/1999	HD 135775 (A2)	0.38	600
WISEA J053257.29+041842.5	56	WISE 0532+0418	L3	56	11/20/2013	HD 39953	0.38	720
2MASS J13023811+5650212	54	2MASS 1302+5650	L3p	54	4/9/2012	81 UMa	0.38	2400
2MASS J22244381-0158521	50	2MASS 2224-0158	L3.5	58	10/7/2011	HD 210501	0.38	2400
2MASS J12563716-0224522	93	SDSS 1256-0224	sdL3.5	21	4/7/2009	q Vir	0.38	1800
2MASS J00361617+1821104	86	2MASS 0036+1821	L4	58	7/28/2000	HD 216716	0.38	1200
2MASS J11550087+2307058	49	2MASS 1155+2307	L4	49	11/22/2004	HD 105389	0.38	1200
2MASS J21580457-1550098	53	2MASS 2158-1550	L4	54	10/9/2001	HD 211278	0.38	1200
2MASS J09211410-2104446	87	SIPS 0921-2104	L4	20	4/7/2009	HD 82724	0.38	600
2MASS J18410861+3117279	50	2MASS 1841+3117	L4p	50	10/10/2001	BD +27 3016A	0.38	1200
WISEA J071552.38114532.9	56	WISE 0715-1145	L4p	56	11/20/2013	HD 43607	0.38	960
2MASS J08053189+4812330	43	SDSS 0805+4812	L4+T5.5	58	4/7/2009	HD 71906	0.38	1200
2MASS J11122567+3548131	50	Gl 417 BC	L4.5+L6	1	12/29/2001	HD 96951 (A1V)	0.38	1200
2MASS J08350622+1953050	25	2MASS 0835+1953	L5	54	11/11/2014	HD 74721	0.38	1800
2MASS J17430860+8526594	65	G 259-20 B	L5	65	6/8/2012	HD 172864 (A2)	0.57	1920
2MASS J14460061+0024519	34	SDSS 1446+0024	L5	58	7/19/2005	HD 123233	0.38	1200
2MASS J17210390+3344160	29	2MASS 1721+3344	L5p	20	6/9/2011	HD 165029	0.38	1800
2MASS J18212815+1414010	54	2MASS 1821+1414	L5p	54	7/18/2005	HD 165029	0.38	1200

Table 2.1 (cont'd)

Designation	Disc. Ref	Short Name	SpT	SpT Ref	UT Date of Observation	A0V Calibrator	Slit Width [arcsec]	Exp. Time [s]
2MASS J23512200+3010540	54	2MASS 2351+3010	L5p	54	10/7/2011	HD 210501	0.38	1200
2MASS J00043484-4044058	39	GJ 1001 B	L5+L5	58	11/6/2004	HD 2339	0.38	1200
2MASS J17281150+3948593	50	2MASS 1728+3948	L5+L6.5	50	4/27/2000	HR 6814 (A3V)	0.38	2400
2MASS J02052940-1159296	32	DENIS 0205-1159	L5+L8	58	8/20/1999	rho Cet	0.38	1200
2MASS J13153094-2649513	41	2MASS 1315-2649	L5+T7	53	3/24/2003	HD 132072	0.38	1200
2MASS J15532142+2109071	49	2MASS 1553+2109	L5.5	49	7/19/2005	HD 123233	0.38	1200
2MASS J15074769-1627386	86	2MASS 1507-1627	L5.5	58	6/3/1999	HR 6061	0.38	600
2MASS J22443167+2043433	31	2MASS 2244+2043	L6	1	10/10/2001	HD 210501	0.38	1200
2MASS J07400712+2009216	58	2MASS 0740+2009	L6	25	12/2/2014	HD 58296	0.38	2400
2MASS J10101480-0406499	29	2MASS 1010-0406	L6	29	3/30/2015	HD 79752	0.38	1200
2MASS J21522609+0937575	87	2MASS 2152+0937	L6+L6	87	11/7/2004	HD 210501	0.38	1200
2MASS J12281523-1547342	32	DENIS 1228-1547	L6+L6	58	6/3/1999	HR 4911	0.38	600
2MASS J08503593+1057156	49	2MASS 0850+1057	L6+L7	49	12/6/2000	HD 48481	0.38	2400
2MASS J22521073-1730134	46	2MASS 2252-1730	L6+T2	46	11/7/2004	HD218639	0.38	1200
2MASS J04234858-0414035	34	SDSS 0423-0414	L6+T2	19	12/31/2001	HD 34317	0.38	1200
2MASS J03001631+2130205	54	2MASS 0300+2130	L6p	54	10/8/2011	HD 232258	0.38	3000
2MASS J11181292-0856106	54	2MASS 1118-0856	L6p	54	4/14/2014	HD 93346	0.38	2400
2MASS J21481633+4003594	54	2MASS 2148+4003	L6.5p	54	8/9/2011	HD 209932	0.38	1200
2MASS J01033203+1935361	50	2MASS 0103+1935	L7	54	12/4/2000	HD 16694 (B9)	0.38	2400
2MASS J15261405+2043414	50	2MASS 1526+2043	L7	50	6/4/2005	26 Ser	0.38	1200
2MASS J21513979+3402444	54	2MASS 2151+3402	L7p	54	10/7/2011	HD 210501	0.38	2400
2MASS J05325346+8246465	17	2MASS 0532+8246	sdL7	22	12/24/2002	HD 34360	0.38	600
2MASS J09310955+0327331	58	SDSS 0931+0327	L7.5	58	4/7/2009	HD 79108	0.38	1800
2MASS J11211858+4332464	25	SDSS 1121+4332	L7.5	25	4/12/2014	HD 109615	0.38	2400

Table 2.1 (cont'd)

Designation	Disc. Ref	Short Name	SpT	SpT Ref	UT Date of Observation	A0V Calibrator	Slit Width [arcsec]	Exp. Time [s]
2MASS J00150206+2959323	54	2MASS 0015+2959	L7.5p	54	10/8/2011	HD 9711	0.38	2400
2MASS J16322911+1904407	49	2MASS 1632+1904	L8	54	8/31/2002	SAO 102579 (B9.5V)	0.38	1200
2MASS J13314894-0116500	43	SDSS 1331-0116	L8	58	4/7/2009	HD 116960	0.38	1800
2MASS J09121469+1459396	106	Gl 337CD	L8+T0	19	12/29/2001	HD 80613 (A1V)	0.38	1200
DENIS-P J025503.3-470049	74	2MASS 0255-4700	L9	19	12/3/2014	HD 28812	0.38	1200
2MASS J03105986+1648155	50	2MASS 0310+1648	L9+L9	19	10/9/2001	34 Ari	0.38	1200
2MASS J14053729+8350248	24	2MASS 1405+8350	L9	24	6/8/2012	HD 172864 (A2)	0.57	960
WISEA J082640.45164031.8	56	WISE 0826-1640	L9	56	12/14/2013	HD 72282	0.38	2400
WISE J020625.27+264023.6	55	WISE 0206+2640	L9p	55	12/2/2014	HD 19600	0.38	2400
2MASS J16471580+5632057	55	WISE 1647+5632	L9p	55	4/12/2014	HD 143187	0.38	900
2MASS J03284265+2302051	50	2MASS 0328+2302	L9.5	58	12/29/2001	HD 23409 (A2V)	0.38	1200
2MASS J12074717+0244249	43	2MASS 1207+0244	T0	19	12/14/2013	HD 111744	0.38	1800
2MASS J15203974+3546210	25	SDSS 1520+3546	T0	25	4/7/2009	26 Ser	0.38	1800
2MASS J15164306+3053443	25	SDSS 1516+3053	T0.5	25	6/20/2014	26 Ser	0.38	1800
2MASS J01514155+1244300	34	SDSS 0151+1244	T1	19	10/9/2001	34 Ari	0.38	1200
SDSS J083717.21-000018.0	60	SDSS 0837-0000	T1	19	12/5/2000	69 Leo	0.38	2400
2MASS J10210969-0304197	60	SDSS 1021-0304	T1+T5	19	6/11/2001	HD 90212	0.38	2000
2MASS J09090085+6525275	25	SDSS 0909+6525	T1.5	25	4/7/2009	39 UMa	0.38	1800
2MASS J12545393-0122474	60	SDSS 1254-0122	T2	19	3/7/2001	k Vir (A3V)	0.38	1200
2MASS J12095613-1004008	14	2MASS 1209-1004	T2+T7.5	19	4/9/2012	Q Vir	0.38	2400
2MASS J11061197+2754225	63	2MASS 1106+2754	T2.5	63	4/7/2009	HD 105388	0.38	600
2MASS J01365662+0933473	4	SIMP 0136+0933	T2.5	4	11/8/2009	BD +18 337A	0.38	1800
2MASS J17503293+1759042	34	SDSS 1750+1759	T3.5	19	10/9/2001	HD 165029	0.38	1200
2MASS J22541892+3123498	15	2MASS 2254+3123	T4	19	7/25/2000	HD 216716	0.38	1200

Table 2.1 (cont'd)

Designation	Disc. Ref	Short Name	SpT	SpT Ref	UT Date of Observation	A0V Calibrator	Slit Width [arcsec]	Exp. Time [s]
2MASS J05591914-1404488	14	2MASS 0559-1404	T4.5	19	12/4/2000	NSV 1280	0.38	1200
2MASS J09261537+5847212	34	SDSS 0926+5847	T4.5	19	12/23/2002	HD 77692 (A2V)	0.38	1200
2MASS J07554795+2212169	15	2MASS 0755+2212	T5	15	3/30/2015	HD 71906	0.38	600
2MASS J15031961+2525196	16	2MASS 1503+2525	T5	19	4/9/2012	HD 140775	0.38	1200
WISE J133750.46+263648.6	70	WISE 1337+2636	T5	70	6/8/2012	HD 122945	0.57	1440
2MASS J23565477-1553111	15	2MASS 2356-1553	T5.5	19	8/19/1999	SAO 191988	0.38	1200
WISE J195436.15+691541.3	70	WISE 1954+6915	T5.5	70	6/9/2012	HD 172728	0.57	1440
2MASS J16241436+0029158	111	SDSS 1624+0029	T6	19	6/2/1999	HR 6255 (A2Vs)	0.38	1200
WISE J003830.54+840517.7	70	WISE 0038+8405	T6	70	8/9/2011	HD 33541	0.76	3600
WISE J184041.77+293229.2	70	WISE 1840+2932	T6	70	9/3/2012	HD 165029	0.38	1800
WISE J223720.39+722833.8	70	WISE 2237+7225	T6	70	9/8/2011	HD 207636	0.38	1200
2MASS J09373487+2931409	15	2MASS 0937+2931	T6p	19	3/7/2001	AG +27 1006	0.38	1200
2MASS J12255432-2739466	12	2MASS 1225-2739	T6+T8	19	4/7/2009	HD 119752	0.38	1800
WISE J125015.56+262846.9	70	WISE 1250+2628	T6.5	70	6/8/2012	HD 122945	0.57	1440
2MASS J07271824+1710012	15	2MASS 0727+1710	T7	19	12/29/2001	HD 74721	0.38	1200
WISE J113949.24-332425.1	99	WISE 1139-3324	T7	99	2/21/2013	HD 101169	0.57	2400
WISE J175929.37+544204.7	70	WISE 1759+5442	T7	70	6/8/2012	HD 172728	0.57	1440
WISE J233543.79+422255.2	70	WISE 2335+4222	T7	70	9/5/2011	HD 222749	0.76	1800
2MASS J15530228+1532369	15	2MASS 1553+1532	T7+T7	19	6/11/2001	HD 147005	0.38	2400
2MASS J14571496-2121477	13	Gl 570 D	T7.5	19	3/6/2001	HD 133569	0.38	1000
WISE J042417.94+072744.1	70	WISE 0424+0727	T7.5	70	9/24/2012	HD 31411	0.57	2400
WISE J214706.78-102924.0	70	WISE 2147-1029	T7.5	70	6/9/2012	HD 203769	0.57	1440
2MASS J04151954-0935066	15	2MASS 0415-0935	T8	19	12/6/2000	HD 48481	0.38	2400
WISE J031624.35+430709.1	70	WISE 0316+4307	T8	70	9/5/2011	HD 21038	0.76	6000

Table 2.1 (cont'd)

Designation	Disc. Ref	Short Name	SpT	SpT Ref	UT Date of Observation	A0V Calibrator	Slit Width [arcsec]	Exp. Time [s]
WISE J043052.92+463331.6	70	WISE 0430+4633	T8	70	9/24/2012	HD 31069	0.57	2400
WISE J105047.9+505606.2	70	WISE 1050+5056	T8	70	6/9/2012	HD 99966	0.57	1800
WISE J144806.48-253420.3	99	WISE 1448-2534	T8	99	2/21/2013	HD 129544	0.57	2400
WISE J173623.03+605920.2	70	WISE 1736+6059	T8	70	9/3/2012	HD 172728	0.38	1800
WISE J181329.40+283533.3	70	WISE 1813+2835	T8	70	6/8/2012	HD 165029	0.57	1800
WISE J195500.42-254013.9	70	WISE 1955-2540	T8	70	6/9/2012	HD 190285	0.57	1440
WISE J200520.38+542433.9	71	WISE 2005+5424	sdT8	71	6/8/2012	HD 199217/HD 205314	0.57	6600
WISE J051208.66-300404.4	70	WISE 0512-3004	T8.5	70	9/25/2012	HD 36965	0.57	2400
WISE J054047.00+483232.4	70	WISE 0540+4832	T8.5	70	9/25/2012	HD 45105	0.57	2400
WISE J000517.48+373720.5	70	WISE 0005+3737	T9	70	10/7/2011	HD 9711	0.38	2400
WISE J003829.05+275852.1	70	WISE 0038+2758	T9	70	9/8/2011	HD 7215	0.38	4800
WISE J033515.01+431045.1	70	WISE 0335+4310	T9	70	9/25/2012	HD 21038	0.57	2400

Note. — 1. Allers & Liu 2013, 2. Allers et al. 2009, 3. Ardila et al. 2000, 4. Artigau et al. 2006, 5. Barrado y Navascués et al. 2003, 6. Basri & Martín 1999, 7. Becklin & Zuckerman 1988, 8. Béjar et al. 1999, 9. Bouvier et al. 1998, 10. Briceño et al. 1998, 11. Briceño et al. 2002, 12. Burgasser et al. 1999, 13. Burgasser et al. 2000b, 14. Burgasser et al. 2000a, 15. Burgasser et al. 2002, 16. Burgasser et al. 2003a, 17. Burgasser et al. 2003b, 18. Burgasser 2004, 19. Burgasser et al. 2006, 20. Burgasser 2008, 21. Burgasser et al. 2009, 22. Burgasser et al. 2007, 23. Canty et al. 2013, 24. Castro et al. 2013, 25. Chiu et al. 2006, 26. Close et al. 2003, 27. Cohen & Kuhi 1979, 28. Comeron et al. 1993, 29. Cruz et al. 2003, 30. Cruz et al. 2009, 31. Dahn et al. 2002, 32. Delfosse et al. 1997, 33. Festin 1998, 34. Geballe et al. 2002, 35. Gizis 2002, 36. Gizis et al. 2000, 37. Gizis et al. 2001, 38. Gizis et al. 2003, 39. EROS Collaboration et al. 1999, 40. Greene & Young 1992, 41. Hall 2002, 42. Haro & Chavira 1966, 43. Hawley et al. 2002, 44. Henry & Kirkpatrick 1990, 45. Jenkins et al. 2009, 46. Kendall et al. 2004, 47. Kirkpatrick et al. 1991, 48. Kirkpatrick 1992, 49. Kirkpatrick et al. 1999, 50. Kirkpatrick et al. 2000, 51. Kirkpatrick et al. 2001, 52. Kirkpatrick et al. 2006, 53. Kirkpatrick et al. 2008, 54. Kirkpatrick et al. 2010, 55. Kirkpatrick et al. 2011, 56. Kirkpatrick et al. 2014, 57. Kirkpatrick et al. 1997, 58. Knapp et al. 2004, 59. Konopacky et al. 2010, 60. Leggett et al. 2000, 61. Lépine et al. 2002, 62. Lépine et al. 2003, 63. Looper et al. 2007, 64. Lowrance et al. 2005, 65. Luhman 2012, 66. Luhman et al. 1997, 67. Luhman et al. 2003, 68. Luyten 1979a, 69. Luyten 1979b, 70. Mace et al. 2013, 71. Mace et al. 2013, 72. Martin et al. 1996, 73. Martín et al. 1998, 74. Martín et al. 1999, 75. Martín et al. 2000b, 76. Martín et al. 2000a, 77. Martín et al. 2001, 78. Martín et al. 2004, 79. McGovern et al. 2004, 80. McLean et al. 2007, 81. Natta et al. 2002, 82. Probst 1983, 83. Prosser 1994, 84. Rebolo et al. 1995, 85. Rebolo et al. 1998, 86. Reid et al. 2000, 87. Reid et al. 2008, 88. Rice et al. 2010, 89. Rieke & Rieke 1990, 90. Ruiz et al. 1997, 91. Schneider et al. 1991, 92. Sheppard & Cushing 2009, 93. Sivarani et al. 2009, 94. Slesnick et al. 2006, 95. Stauffer et al. 1989, 96. Stauffer et al. 1998, 97. Stauffer et al. 1999, 98. Stumpf et al. 2008, 99. Thompson et al. 2013, 100. van Biesbroeck 1944, 101. van Biesbroeck 1961, 102. Vrba et al. 1975, 103. White et al. 1999, 104. Wilking et al. 1999, 105. Wilking et al. 2005, 106. Wilson et al. 2001, 107. Wolf 1919, 108. Zapatero Osorio et al. 1997, 109. Zapatero Osorio et al. 1999, 110. Zapatero Osorio et al. 2000, 111. Strauss et al. 1999

Table 2.2. Equivalent Widths and Spectral Index values for the BDSS J band spectra

Name	SpT	K I EW (Å) 1.1692μm	K I EW (Å) 1.1778μm	K I EW (Å) 1.2437μm	K I EW (Å) 1.2529μm	FeH_J 1.20μm	Gravity Scores K1 K2 K4 FeH	Gravity Type
2MASS 0619-2903	M5	0.1±0.64	0.52±0.58	0.41±1.24	1.51±0.57	1.021±0.014	n n 0. n	N/A
LHS 1135	d/sdM5	2.15±0.37	4.0±0.3	1.91±0.4	2.51±0.16	1.045±0.004	N/A	N/A
Gl 577 BC	M5.5	0.6±0.04	1.81±0.04	1.15±0.1	1.44±0.05	1.042±0.001	n n 0. n	N/A
Rho Oph GY 5	M5.5	0.55±0.82	0.5±0.46	0.81±0.61	0.65±0.24	1.021±0.01	n n 2. n	N/A
2MASS 1459+0004	M6	0.79±0.76	1.49±0.7	1.53±1.47	1.57±0.68	1.021±0.018	2. 2. 2. 2.	VL-G
2MASS 2234+4041	M6	-0.02±0.64	0.53±0.51	0.97±0.83	0.15±0.3	1.026±0.011	2. 2. 2. 2.	VL-G
DENIS-P 1605-2406	M6	0.1±0.1	0.74±0.09	0.8±0.2	0.53±0.09	1.039±0.002	2. 2. 2. 2.	VL-G
KPNO Tau 3	M6	-0.71±0.17	-0.81±0.1	1.19±0.19	0.7±0.09	1.025±0.002	2. 2. 2. 2.	VL-G
MHO Tau4	M6	0.45±0.1	0.96±0.08	1.0±0.12	0.91±0.06	1.037±0.002	2. 2. 2. 2.	VL-G
Rho Oph GY 37	M6	0.96±0.16	1.04±0.14	0.58±0.31	1.1±0.14	1.032±0.003	2. 2. 2. 2.	VL-G
SOri 12	M6	0.67±0.2	1.23±0.18	0.74±0.41	0.42±0.18	1.027±0.005	2. 2. 2. 2.	VL-G
SOri 17	M6	-0.94±0.52	-0.04±0.49	0.77±1.05	1.39±0.46	1.029±0.011	2. 2. 2. 2.	VL-G
USco CTIO 66	M6	0.87±0.19	1.54±0.18	1.38±0.37	1.29±0.17	1.039±0.004	2. 2. 2. 2.	VL-G
2MASS 0253+3206	M6	2.77±0.12	4.12±0.1	2.39±0.19	3.56±0.09	1.067±0.002	0. 0. 0. 0.	FLD-G
2MASS 0840+1824	M6	3.49±0.06	5.29±0.03	3.47±0.04	4.01±0.02	1.095±0.001	0. 0. 0. 0.	FLD-G
2MASS 1049+2538	M6	2.48±0.21	3.83±0.18	3.06±0.34	3.15±0.15	1.072±0.005	0. 0. 0. 0.	FLD-G
AP 310	M6	2.32±0.4	3.52±0.37	0.5±0.84	2.38±0.39	1.066±0.01	0. 0. 0. 0.	FLD-G
AP 316	M6	1.53±0.86	2.54±0.79	2.58±1.81	2.29±0.81	1.07±0.02	1. 1. 0. 0.	FLD-G
GJ 3828 B	M6	4.86±0.1	7.22±0.09	5.02±0.21	5.43±0.1	1.126±0.003	0. 0. 0. 0.	FLD-G
Roque 16	M6	2.13±1.1	3.48±0.99	1.48±2.16	3.42±0.93	1.056±0.024	0. 0. 0. 0.	FLD-G
Teide 2	M6	3.83±0.5	4.19±0.49	2.46±1.02	3.05±0.48	1.073±0.013	0. 0. 0. 0.	FLD-G
USco CTIO 85	M6	2.99±0.16	4.14±0.14	2.65±0.3	3.45±0.14	1.095±0.003	0. 0. 0. 0.	FLD-G
USco CTIO 121	M6	3.48±0.32	4.76±0.29	3.26±0.59	3.65±0.28	1.09±0.007	0. 0. 0. 0.	FLD-G
Wolf 359	M6	3.16±0.03	4.64±0.03	2.93±0.05	3.46±0.02	1.078±0.001	0. 0. 0. 0.	FLD-G
MHO Tau 5	M6.5	-2.16±0.06	0.18±0.05	0.87±0.12	0.45±0.05	1.036±0.001	2. 2. 2. 2.	VL-G
Rho Oph GY 11	M6.5	-0.72±0.74	1.01±0.71	1.67±1.51	1.08±0.68	1.027±0.017	2. 2. 2. 2.	VL-G
SCH 1612-2047	M6.5	-0.06±0.12	0.68±0.1	0.58±0.21	0.68±0.1	1.034±0.002	2. 2. 2. 2.	VL-G
AP 301	M6.5	1.97±0.32	3.79±0.29	2.24±0.68	1.76±0.32	1.083±0.008	0. 0. 1. 0.	FLD-G
Gl 283 B	M6.5	3.21±0.07	4.88±0.06	2.78±0.14	3.29±0.06	1.06±0.002	0. 0. 0. 0.	FLD-G
PPL 1	M6.5	2.61±2.03	3.57±1.61	5.1±1.75	4.54±0.7	1.119±0.035	0. 0. 0. 0.	FLD-G
2MASS 0435-1414	M7	0.09±0.06	0.22±0.05	0.47±0.1	0.42±0.04	1.023±0.001	2. 2. 2. 2.	VL-G
AP 270	M7	0.99±0.18	3.11±0.17	1.66±0.34	2.15±0.16	1.047±0.004	2. 2. 2. 2.	VL-G
SOri 31	M7	-0.0±0.36	1.37±0.34	0.49±0.7	0.76±0.34	1.03±0.008	2. 2. 2. 2.	VL-G
SOri 40	M7	0.35±0.51	1.62±0.47	1.82±1.08	0.33±0.52	1.048±0.012	2. 2. 2. 2.	VL-G
USco CTIO 100	M7	0.75±0.16	1.32±0.16	1.3±0.33	1.21±0.14	1.053±0.004	2. 2. 2. 2.	VL-G

Table 2.2 (cont'd)

Name	SpT	K I EW (Å) 1.1692μm	K I EW (Å) 1.1778μm	K I EW (Å) 1.2437μm	K I EW (Å) 1.2529μm	FeH$_J$ 1.20μm	Gravity Scores K1 K2 K4 FeH	Gravity Type
USco CTIO 128	M7	0.97±0.25	1.26±0.21	2.1±0.5	1.13±0.23	1.065±0.006	2. 2. 2. 1.	VL-G
AP 325	M7	2.54±0.17	4.56±0.17	2.55±0.36	2.85±0.16	1.1±0.004	1. 1. 1. 0.	INT-G
LHS 2351	M7	4.31±0.26	5.77±0.20	3.76±0.52	3.83±0.23	1.11±0.008	0. 0. 0. 0.	FLD-G
2MASS 0952-1924	M7	3.58±0.02	5.21±0.03	3.4±0.04	3.78±0.02	1.092±0.001	0. 0. 0. 0.	FLD-G
CFHT 15	M7	3.06±0.67	6.36±0.59	3.18±1.36	4.45±0.59	1.155±0.016	0. 0. 0. 0.	FLD-G
CTI 115638.4+28	M7	5.19±0.31	7.27±0.27	4.06±0.58	4.69±0.26	1.116±0.007	0. 0. 0. 0.	FLD-G
Roque 14	M7	5.02±1.93	6.18±0.95	3.77±1.17	4.28±0.44	1.131±0.006	0. 0. 0. 0.	FLD-G
USco CTIO 132	M7	8.07±1.42	7.6±1.04	5.06±1.4	5.63±0.62	1.149±0.021	0. 0. 0. 0.	FLD-G
VB 8	M7	4.63±0.44	6.64±0.27	3.82±0.5	4.93±0.26	1.096±0.008	0. 0. 0. 0.	FLD-G
2MASS 1835-3217	M7p	4.01±0.71	5.45±0.6	2.76±1.37	3.89±0.63	1.056±0.016	0. 0. 0. 1.	FLD-G
CFHT BD Tau 2	M7.5	0.65±2.62	0.55±1.23	1.02±0.52	0.8±0.25	1.029±0.02	2. 2. 2. 2.	VL-G
ISO-Oph 23	M7.5	0.63±0.35	1.83±0.34	0.2±0.77	-0.22±0.37	1.023±0.008	2. 2. 2. 2.	VL-G
USco CTIO 130	M7.5	0.87±0.24	1.68±0.22	1.11±0.42	1.32±0.2	1.061±0.005	2. 2. 2. 1.	VL-G
AP 326	M7.5	4.7±0.38	2.69±0.39	4.42±0.83	4.12±0.38	1.106±0.01	0. 2. 0. 0.	FLD-G
Roque 13	M7.5	3.56±0.72	4.55±0.69	3.79±1.58	4.38±0.69	1.124±0.019	0. 1. 0. 0.	FLD-G
GG Tau Bb	M7.5dbl	-0.33±0.08	2.03±0.07	1.53±0.16	-0.04±0.08	1.038±0.002	2. 2. 2. 2.	VL-G
2MASS 1207-3932	M8	1.45±0.29	1.22±0.27	1.11±0.59	1.32±0.27	1.077±0.007	2. 2. 2. 1.	VL-G
CFHT BD Tau 3	M8	0.8±0.17	1.06±0.16	1.26±0.38	0.95±0.17	1.065±0.004	2. 2. 2. 2.	VL-G
DENIS 1619-2347	M8	-0.41±0.22	0.67±0.2	0.86±0.42	1.96±0.19	1.055±0.005	2. 2. 2. 2.	VL-G
DENIS 1619-2440	M8	0.12±0.23	0.17±0.22	1.45±0.44	0.84±0.21	1.04±0.005	2. 2. 2. 2.	VL-G
KPNO Tau 7	M8	0.31±2.93	1.94±1.44	0.91±2.97	0.94±1.22	1.051±0.041	2. 2. 2. 2.	VL-G
Rho Oph GY 3	M8	0.13±0.07	0.81±0.07	1.11±0.16	0.43±0.07	1.043±0.002	2. 2. 2. 2.	VL-G
SCH 1622-1951	M8	0.69±0.11	1.56±0.09	1.03±0.23	1.0±0.1	1.063±0.002	2. 2. 2. 2.	VL-G
SCH 1623-2317	M8	0.52±0.08	1.02±0.05	0.64±0.09	1.05±0.04	1.079±0.003	2. 2. 2. 1.	VL-G
Teide 1	M8	2.27±0.8	2.94±0.71	4.8±1.58	3.86±0.76	1.132±0.021	2. 2. 1. 0.	VL-G
AP 306	M8	4.29±0.46	5.98±0.4	0.9±0.94	4.49±0.41	1.132±0.01	0. 1. 0. 0.	FLD-G
LP 523-55	M8	4.81±0.56	6.3±0.28	4.61±0.68	5.22±0.25	1.127±0.01	0. 0. 0. 0.	FLD-G
Roque 11	M8	4.9±1.08	7.01±1.04	2.66±2.34	4.25±1.04	1.133±0.029	0. 0. 0. 0.	FLD-G
VB 10	M8	4.93±0.08	6.87±0.06	4.34±0.13	4.88±0.05	1.141±0.002	0. 0. 0. 0.	FLD-G
LP 213-67	M8dbl	2.73±0.15	4.34±0.08	2.97±0.1	3.25±0.05	1.085±0.002	N/A	N/A
KPNO Tau 1	M8.5	1.07±0.68	2.43±0.59	2.51±1.31	0.91±0.66	1.064±0.016	2. 2. 2. 2.	VL-G
KPNO Tau 6	M8.5	1.02±0.32	2.11±0.29	1.86±0.59	0.86±0.29	1.068±0.007	2. 2. 2. 2.	VL-G
KPNO Tau 9	M8.5	1.85±0.42	2.26±0.42	1.58±0.93	1.36±0.41	1.062±0.01	2. 2. 2. 2.	VL-G
Rho Oph GY 141	M8.5	2.55±0.38	4.4±0.34	3.75±0.73	1.45±0.32	1.097±0.008	2. 1. 2. 1.	VL-G
Rho Oph GY 310	M8.5	0.53±0.15	0.94±0.14	1.16±0.32	1.17±0.15	1.047±0.003	2. 2. 2. 2.	VL-G

Table 2.2 (cont'd)

Name	SpT	K I EW (Å) 1.1692μm	K I EW (Å) 1.1778μm	K I EW (Å) 1.2437μm	K I EW (Å) 1.2529μm	FeH$_J$ 1.20μm	Gravity Scores K1 K2 K4 FeH	Gravity Type
Roque 7	M8.5	3.4±1.12	4.59±1.06	3.08±2.5	3.58±1.09	1.131±0.029	1. 1. 1. 0.	INT-G
Gl 569 BC	M8.5dbl	7.45±0.04	9.63±0.03	4.71±0.08	6.02±0.03	1.16±0.001	0. 0. 0. 0.	FLD-G
2MASS 1139-3159	M9	1.86±0.14	1.68±0.14	1.8±0.28	1.74±0.13	1.064±0.003	2. 2. 2. 2.	VL-G
DENIS 1611-2426	M9	-0.16±0.32	0.95±0.31	1.02±0.68	1.54±0.31	1.073±0.008	2. 2. 2. 2.	VL-G
DENIS 1614-2017	M9	-0.34±0.26	1.12±0.27	1.34±0.56	1.67±0.24	1.045±0.006	2. 2. 2. 2.	VL-G
KPNO Tau 12	M9	2.23±1.37	3.73±1.16	2.36±2.66	0.99±1.24	1.132±0.032	2. 2. 2. 1.	VL-G
Roque 4	M9	4.6±0.91	5.7±0.81	3.06±1.96	3.86±0.91	1.177±0.025	1. 1. 1. 0.	INT-G
2MASS 0140+2701	M9	5.95±0.17	8.1±0.13	4.83±0.24	5.76±0.11	1.139±0.003	0. 0. 0. 1.	FLD-G
2MASS 1239+2029	M9	6.09±2.76	9.02±1.21	5.37±1.51	5.7±0.5	1.134±0.04	0. 0. 0. 1.	FLD-G
2MASS 2208-1227	M9	5.08±1.01	6.04±0.89	3.77±1.96	5.38±0.89	1.151±0.028	0. 1. 0. 1.	FLD-G
LHS 2065	M9	6.31±0.05	7.85±0.04	4.93±0.1	5.81±0.05	1.19±0.001	0. 0. 0. 0.	FLD-G
2MASS 2140+1625	M9dbl	6.0±0.19	8.19±0.12	3.45±0.21	5.47±0.09	1.207±0.003	N/A	N/A
G 216-7B	M9.5	5.31±0.21	7.39±0.34	5.86±0.65	5.28±0.48	1.198±0.007	0. 0. 0. 0.	FLD-G
2MASS 0141-4633	L0	3.29±0.78	2.89±0.65	3.25±1.52	1.83±0.72	1.105±0.017	2. 2. 2. 2.	VL-G
2MASS 0443+0002	L0	3.7±0.06	4.6±0.05	2.06±0.13	3.18±0.05	1.13±0.001	2. 2. 2. 2.	VL-G
2MASS 0608-2753	L0	2.23±0.67	3.1±0.5	2.44±0.92	2.44±0.36	1.095±0.012	2. 2. 2. 2.	VL-G
KPNO Tau 4	L0	-1.97±0.24	-0.1±0.2	0.3±0.43	-1.15±0.21	1.048±0.005	2. 2. 2. 2.	VL-G
PC0025+0447	L0	2.94±0.62	6.05±0.54	3.35±1.35	3.29±0.61	1.149±0.016	2. 1. 2. 1.	VL-G
SOri 51	L0	2.44±1.58	3.84±1.36	2.77±2.89	1.47±1.41	1.089±0.039	2. 2. 2. 2.	VL-G
2MASS 1731+2721	L0	7.41±0.14	9.35±0.12	6.07±0.28	6.96±0.13	1.229±0.004	0. 0. 0. 0.	FLD-G
2MASS 2107-0307	L0	7.67±0.26	9.73±0.23	5.86±0.51	7.59±0.23	1.234±0.007	0. 0. 0. 0.	FLD-G
HD 89744 B	L0	7.8±0.73	9.89±0.35	4.88±0.41	6.56±0.21	1.23±0.011	0. 0. 0. 0.	FLD-G
LP 944-20	L0	6.18±0.02	7.72±0.02	5.07±0.03	5.94±0.02	1.197±0.001	0. 1. 0. 1.	FLD-G
WISE 0435+2115	sdL0	8.17±0.25	11.3±0.22	4.64±0.53	6.19±0.23	1.119±0.006	N/A	N/A
DENIS 1441-0945	L0.5	8.03±0.11	10.11±0.09	5.81±0.22	7.03±0.1	1.242±0.003	0. 0. 0. 0.	FLD-G
2MASS 0406-3812	L1	4.31±0.79	5.28±0.76	4.72±1.74	4.61±0.8	1.116±0.021	1. 2. 1. 2.	VL-G
2MASS 0033-1521	L1	8.24±0.36	10.34±0.3	5.12±0.74	6.86±0.3	1.22±0.01	0. 0. 0. 1.	FLD-G
2MASS 0208+2542	L1	8.23±0.11	10.33±0.1	5.73±0.22	7.69±0.1	1.261±0.003	0. 0. 0. 0.	FLD-G
2MASS 0345+2540	L1	7.37±0.07	8.77±0.06	5.59±0.14	7.07±0.07	1.225±0.002	0. 1. 0. 1.	FLD-G
2MASS 1035+2507	L1	8.2±0.39	9.93±0.36	4.16±0.87	6.99±0.37	1.25±0.012	0. 0. 0. 1.	FLD-G
2MASS 1453+1420	L1	9.08±0.38	13.54±0.34	5.92±0.87	9.43±0.33	1.315±0.013	0. 0. 0. 0.	FLD-G
2MASS 2130-0845	L1	8.6±0.26	10.69±0.23	5.75±0.57	8.45±0.24	1.262±0.007	0. 0. 0. 0.	FLD-G
GJ 1048 B	L1	8.38±0.27	10.36±0.23	7.01±0.57	8.01±0.23	1.274±0.008	0. 0. 0. 0.	FLD-G
2MASS 1331+3407	L1p	7.17±0.21	9.46±0.18	5.74±0.4	6.58±0.18	1.221±0.006	1. 0. 1. 1.	INT-G
2MASS 1440-1303	L1p	7.72±1.65	13.49±1.37	6.63±3.54	9.23±1.52	1.345±0.051	0. 0. 0. 0.	FLD-G

Table 2.2 (cont'd)

Name	SpT	K I EW (Å) 1.1692μm	K I EW (Å) 1.1778μm	K I EW (Å) 1.2437μm	K I EW (Å) 1.2529μm	FeH_J 1.20μm	Gravity Scores K1 K2 K4 FeH	Gravity Type
2MASS 1756+2815	L1p	11.86±0.13	15.67±0.11	4.97±0.32	10.01±0.12	1.215±0.004	0. 0. 0. 1.	FLD-G
SOri 47	L1.5	7.51±0.25	8.97±0.25	5.54±0.55	4.7±0.25	1.212±0.008	0. 1. 1. 1.	INT-G
WISE 0543+6422	L2	8.25±0.1	9.74±0.11	6.04±0.23	6.89±0.11	1.245±0.004	0. 1. 1. 1.	INT-G
2MASS 0015+3516	L2	8.28±0.21	10.52±0.11	5.14±0.17	6.94±0.06	1.249±0.007	0. 0. 1. 1.	FLD-G
2MASS 0031-3840	L2	11.21±0.2	13.04±0.19	6.81±0.5	9.78±0.22	1.303±0.007	0. 0. 0. 0.	FLD-G
2MASS 0847-1532	L2	8.65±0.56	10.59±0.26	6.62±0.38	7.74±0.13	1.274±0.008	0. 0. 0. 1.	FLD-G
2MASS 2057-0252	L2	8.36±0.07	9.58±0.05	5.69±0.14	7.44±0.06	1.268±0.002	0. 1. 0. 1.	FLD-G
Kelu 1	L2	6.08±0.08	11.46±0.06	5.23±0.15	7.74±0.06	1.231±0.002	1. 0. 0. 1.	FLD-G
WISE 0659+1717	L2	9.13±0.53	11.75±0.45	6.64±1.13	7.17±0.49	1.255±0.016	0. 0. 1. 1.	FLD-G
WISE 2354-1852	L2	8.13±0.44	10.49±0.39	6.56±0.91	8.59±0.37	1.282±0.013	1. 0. 0. 1.	FLD-G
2MASS 1431+1436	L2p	9.88±0.34	12.45±0.3	7.04±0.77	9.42±0.32	1.185±0.01	0. 0. 0. 1.	FLD-G
Gl 618.1 B	L2.5	8.04±0.14	9.65±0.12	4.67±0.31	6.72±0.13	1.244±0.004	1. 1. 1. 1.	INT-G
2MASS 2104-1037	L2.5	8.5±0.12	12.04±0.1	6.32±0.25	8.11±0.11	1.283±0.004	0. 0. 0. 1.	FLD-G
WISE 0607+4550	L2.5	9.61±0.14	11.05±0.13	7.01±0.3	8.74±0.13	1.258±0.004	0. 0. 0. 1.	FLD-G
2MASS 2208+2921	L3	3.96±0.51	4.33±0.46	2.53±1.07	2.47±0.44	1.141±0.013	2. 2. 2. 2.	VL-G
G 196-3B	L3	5.41±0.38	5.79±0.36	4.21±0.36	4.35±0.15	1.157±0.005	1. 2. 2. 2.	VL-G
2MASS 1726+1538	L3	5.83±0.51	6.82±0.45	5.14±1.04	4.55±0.48	1.199±0.014	1. 1. 1. 1.	INT-G
2MASS 1146+2230	L3	9.23±0.16	10.87±0.15	6.51±0.37	8.2±0.16	1.296±0.005	0. 1. 0. 0.	FLD-G
2MASS 1300+1912	L3	10.33±0.1	13.07±0.08	6.66±0.15	9.07±0.07	1.214±0.002	0. 0. 0. 1.	FLD-G
2MASS 1506+1321	L3	10.55±0.14	11.85±0.1	7.16±0.31	9.36±0.13	1.257±0.005	0. 0. 0. 1.	FLD-G
GD 165 B	L3	9.33±0.3	11.14±0.27	4.81±0.59	8.3±0.26	1.289±0.012	0. 0. 0. 1.	FLD-G
WISE 0532+0418	L3	10.05±1.26	13.37±1.13	9.22±2.83	10.92±1.19	1.404±0.044	0. 0. 0. 0.	FLD-G
2MASS 1302+5650	L3p	11.3±0.58	12.05±0.53	7.89±1.35	9.95±0.59	1.288±0.021	0. 0. 0. 1.	FLD-G
2MASS 2224-0158	L3.5	11.03±0.16	12.93±0.15	7.19±0.34	7.01±0.16	1.175±0.005	0. 0. 1. 1.	FLD-G
SDSS 1256-0224	sdL3.5	7.9±0.36	12.28±0.28	2.52±0.7	5.08±0.35	1.102±0.009	N/A	N/A
2MASS 0036+1821	L4	11.1±0.2	13.78±0.29	6.51±0.37	10.24±0.16	1.313±0.009	0. 0. 0. 0.	FLD-G
2MASS 1155+2307	L4	4.76±0.6	10.6±0.48	6.28±1.2	8.51±0.48	1.304±0.017	2. 1. 0. 0.	FLD-G
2MASS 2158-1550	L4	10.58±0.69	11.39±0.6	5.7±1.6	8.67±0.63	1.289±0.021	0. 1. 0. 0.	FLD-G
SIPS 0921-2104	L4	11.13±0.04	13.8±0.04	7.2±0.14	10.65±0.06	1.231±0.001	0. 0. 0. 1.	FLD-G
2MASS 1841+3117	L4p	9.26±0.46	10.99±0.4	5.44±1.05	7.75±0.43	1.244±0.013	1. 1. 1. 1.	INT-G
WISE 0715-1145	L4p	11.36±0.18	14.91±0.15	6.9±0.4	10.47±0.17	1.234±0.006	0. 0. 0. 1.	FLD-G
GJ 1001 B	L4.5	11.5±0.16	12.62±0.14	5.73±0.35	9.18±0.14	1.254±0.005	0. 0. 0. 1.	FLD-G
SDSS 0805+4812	L4.5dbl	12.37±0.11	13.85±0.1	5.93±0.25	9.38±0.1	1.285±0.004	N/A	N/A
2MASS 0835+1953	L5	11.14±0.29	12.25±0.24	6.44±0.67	8.61±0.26	1.234±0.009	0. 0. 0. 0.	FLD-G
G 259-20 B	L5	13.71±0.26	16.66±0.23	4.64±0.7	11.09±0.26	1.284±0.009	0. 0. 0. 0.	FLD-G

Table 2.2 (cont'd)

Name	SpT	K I EW (Å) 1.1692μm	K I EW (Å) 1.1778μm	K I EW (Å) 1.2437μm	K I EW (Å) 1.2529μm	FeH$_J$ 1.20μm	Gravity Scores K1 K2 K4 FeH	Gravity Type
Gl 417 B	L5	9.19±0.18	10.11±0.16	5.45±0.4	7.58±0.17	1.243±0.005	1. 1. 0. 0.	FLD-G
SDSS 1446+0024	L5	10.51±0.48	12.83±0.47	5.06±1.26	8.76±0.51	1.212±0.016	0. 0. 0. 0.	FLD-G
2MASS 1721+3344	L5p	11.6±0.41	15.12±0.36	5.77±1.03	10.2±0.42	1.241±0.014	0. 0. 0. 0.	FLD-G
2MASS 1821+1414	L5p	9.22±0.11	11.25±0.1	5.32±0.27	7.79±0.11	1.229±0.003	1. 1. 0. 0.	FLD-G
2MASS 2351+3010	L5p	11.19±0.89	12.35±0.78	6.42±2.18	7.53±0.92	1.18±0.026	0. 0. 0. 1.	FLD-G
2MASS 1553+2109	L5.5	9.24±1.09	9.24±0.96	3.72±2.61	6.01±0.99	1.127±0.031	1. 1. 1. 1.	INT-G
DENIS 0205-1159	L5.5	8.03±0.82	10.91±0.36	3.51±0.85	6.41±0.29	1.122±0.017	1. 1. 1. 2.	INT-G
2MASS 1507-1627	L5.5	11.2±0.02	13.9±0.03	5.64±0.09	8.56±0.04	1.252±0.001	0. 0. 0. 0.	FLD-G
2MASS 1315-2649	L5.5dbl	7.89±0.39	10.86±0.33	4.97±0.86	7.61±0.36	1.171±0.011	N/A	N/A
2MASS 2244+2043	L6	4.2±1.02	5.24±0.91	1.22±2.04	3.03±0.91	1.008±0.023	2. 2. 2. 2.	VL-G
2MASS 0740+2009	L6	7.34±0.56	10.55±0.49	3.9±1.29	6.19±0.52	1.079±0.014	1. 0. 1. 2.	INT-G
2MASS 1010-0406	L6	10.11±0.38	11.74±0.35	5.63±0.86	8.45±0.36	1.174±0.011	0. 0. 0. 0.	FLD-G
DENIS 1228-1547	L6	10.18±0.26	11.92±0.17	5.47±0.27	7.9±0.13	1.229±0.006	0. 0. 0. 0.	FLD-G
2MASS 0850+1057	L6dbl	6.61±0.36	8.78±0.31	3.96±0.76	5.87±0.34	1.1±0.009	N/A .	N/A
2MASS 2152+0937	L6dbl	6.82±0.88	9.33±0.76	5.31±1.86	6.16±0.79	1.083±0.023	N/A	N/A
2MASS 0300+2130	L6p	10.11±0.57	12.88±0.51	6.65±1.29	8.85±0.53	1.219±0.017	0. 0. 0. 0.	FLD-G
2MASS 1118-0856	L6p	10.56±0.41	13.35±0.38	6.68±0.94	8.86±0.42	1.223±0.014	0. 0. 0. 0.	FLD-G
2MASS 2148+4003	L6.5p	7.44±0.2	10.34±0.16	4.55±0.45	5.13±0.2	1.15±0.005	1. 1. 1. 0.	INT-G
2MASS 0103+1935	L7	6.46±0.35	6.42±0.33	3.49±0.75	5.82±0.3	1.093±0.009	1. 1. 0. n	INT-G
2MASS 1526+2043	L7	9.14±0.25	10.71±0.23	4.18±0.58	7.56±0.25	1.153±0.007	0. 0. 0. n	FLD-G
2MASS 1728+3948	L7dbl	9.85±0.33	11.56±0.3	4.6±0.73	7.34±0.31	1.101±0.01	0. 0. 0. n	FLD-G
2MASS 2151+3402	L7p	2.3±1.04	4.33±1.0	3.68±2.19	7.31±0.96	1.163±0.029	2. 2. 0. n	VL-G
2MASS 0532+8246	sdL7	12.59±0.29	16.4±0.14	0.8±0.42	6.81±0.13	1.238±0.018	N/A	N/A
2MASS 2252-1730	L7.5	11.5±0.32	13.06±0.3	3.89±0.8	8.57±0.34	1.161±0.01	0. 0. 0. n	FLD-G
SDSS 0931+0327	L7.5	11.87±0.27	14.58±0.24	6.42±0.64	11.02±0.27	1.238±0.009	0. 0. 0. n	FLD-G
SDSS 1121+4332	L7.5	15.39±0.35	17.96±0.35	6.91±0.99	10.71±0.41	1.271±0.013	0. 0. 0. n	FLD-G
2MASS 0015+2959	L7.5p	9.35±1.27	12.35±1.13	5.76±2.9	9.48±1.24	1.155±0.042	0. 0. 0. n	FLD-G
2MASS 1632+1904	L8	5.44±0.44	7.23±0.4	2.57±1.06	3.69±0.46	1.04±0.011	N/A	N/A
SDSS 1331-0116	L8	12.82±0.15	14.44±0.14	5.74±0.38	9.57±0.14	1.184±0.005	N/A	N/A
2MASS 0255-4700	L9	6.44±0.12	8.95±0.13	2.62±0.32	5.38±0.14	1.039±0.003	N/A	N/A
2MASS 0310+1648	L9	6.58±0.43	9.22±0.41	3.11±1.06	5.62±0.46	1.016±0.011	N/A	N/A
2MASS 1405+8350	L9	7.86±0.22	9.72±0.22	4.14±0.51	7.1±0.22	1.036±0.006	N/A	N/A
WISE 0826-1640	L9	7.95±0.25	9.35±0.22	4.01±0.55	5.27±0.23	1.035±0.006	N/A	N/A
WISE 0206+2640	L9p	6.29±0.37	7.57±0.34	2.77±0.86	4.33±0.36	1.015±0.009	N/A	N/A
WISE 1647+5632	L9p	6.11±1.15	5.12±1.14	4.28±2.35	6.62±1.01	1.028±0.027	N/A	N/A

Table 2.2 (cont'd)

Name	SpT	K I EW (Å) 1.1692μm	K I EW (Å) 1.1778μm	K I EW (Å) 1.2437μm	K I EW (Å) 1.2529μm	FeH$_J$ 1.20μm	Gravity Scores K1 K2 K4 FeH	Gravity Type
2MASS 0328+2302	L9.5	8.79±1.14	11.18±1.08	2.81±2.85	4.75±1.1	1.003±0.028	N/A	N/A
2MASS 1207+0244	T0	6.9±0.22	8.78±0.2	2.82±0.55	6.1±0.2	1.076±0.006	N/A	N/A
Gl 337 C	T0	7.4±0.61	8.71±0.57	2.53±1.6	5.33±0.67	1.049±0.016	N/A	N/A
SDSS 0423-0414	T0	8.14±0.23	10.4±0.21	3.59±0.59	6.83±0.24	1.073±0.006	N/A	N/A
SDSS 1520+3546	T0	8.25±0.18	10.29±0.19	3.97±0.48	6.84±0.2	1.047±0.005	N/A	N/A
SDSS 1516+3053	T0.5	6.47±0.61	4.17±0.62	2.71±1.39	5.21±0.56	0.987±0.015	N/A	N/A
SDSS 0151+1244	T1	8.72±0.78	11.34±0.7	2.11±1.85	6.54±0.74	1.033±0.02	N/A	N/A
SDSS 0837-0000	T1	8.08±0.69	12.22±0.61	4.28±1.56	8.58±0.61	1.023±0.017	N/A	N/A
SDSS 0909+6525	T1.5	9.26±0.27	11.26±0.25	2.89±0.7	5.86±0.29	1.031±0.007	N/A	N/A
SDSS 1254-0122	T2	10.42±1.58	11.67±0.69	3.65±0.28	8.54±0.1	1.012±0.017	N/A	N/A
2MASS 1106+2754	T2.5	11.08±0.41	13.42±0.28	3.82±0.49	7.89±0.21	1.059±0.008	N/A	N/A
SIMP 0136+0933	T2.5	12.04±0.05	14.06±0.05	4.69±0.15	9.42±0.06	1.054±0.002	N/A	N/A
2MASS 1209-1004	T3	10.52±0.56	14.6±0.54	4.55±1.52	8.0±0.64	0.991±0.017	N/A	N/A
SDSS 1021-0304	T3	10.76±0.61	7.58±0.61	4.46±1.39	9.02±0.57	1.006±0.015	N/A	N/A
SDSS 1750+1759	T3.5	11.7±0.53	13.57±0.5	3.48±1.35	8.34±0.53	1.051±0.015	N/A	N/A
2MASS 2254+3123	T4	11.34±1.45	13.15±1.23	2.25±2.58	9.03±0.85	1.077±0.028	N/A	N/A
2MASS 0559-1404	T4.5	14.46±0.11	15.8±0.09	3.05±0.22	9.71±0.08	1.07±0.003	N/A	N/A
SDSS 0926+5847	T4.5	14.47±0.44	14.64±0.47	3.52±1.33	9.01±0.49	1.037±0.014	N/A	N/A
2MASS 0755+2212	T5	16.23±0.07	15.04±0.05	0.52±0.22	8.01±0.06	1.056±0.001	N/A	N/A
2MASS 1503+2525	T5	14.5±0.11	14.99±0.11	1.21±0.35	7.04±0.13	1.054±0.004	N/A	N/A
WISE 1337+2636	T5	20.42±0.4	14.81±0.45	1.27±1.37	7.34±0.51	1.104±0.015	N/A	N/A
2MASS 2356-1553	T5.5	N/A	N/A	2.76±5.53	10.16±1.71	1.094±0.052	N/A	N/A
WISE 1954+6915	T5.5	N/A	N/A	1.14±1.71	3.5±0.77	0.991±0.02	N/A	N/A
2MASS 1225-2739	T6	N/A	N/A	1.07±0.27	8.93±0.11	1.027±0.002	N/A	N/A
SDSS 1624+0029	T6	N/A	N/A	-2.2±0.68	5.89±0.26	1.03±0.005	N/A	N/A
WISE 0038+8405	T6	N/A	N/A	0.23±1.31	6.44±0.49	1.096±0.013	N/A	N/A
WISE 1840+2932	T6	N/A	N/A	-2.36±4.3	1.51±1.68	1.029±0.039	N/A	N/A
WISE 2237+7225	T6	N/A	N/A	2.44±1.49	8.64±0.52	1.009±0.014	N/A	N/A
2MASS 0937+2931	T6p	N/A	N/A	-0.9±1.03	2.05±0.4	0.994±0.021	N/A	N/A
WISE 1250+2628	T6.5	N/A	N/A	0.21±0.95	10.26±0.34	1.049±0.009	N/A	N/A
2MASS 0727+1710	T7	N/A	N/A	-0.97±0.88	6.14±0.3	1.001±0.007	N/A	N/A
2MASS 1553+1532	T7	N/A	N/A	0.0±0.57	6.41±0.22	0.949±0.005	N/A	N/A
WISE 1139-3324	T7	N/A	N/A	-1.03±3.49	2.65±1.41	0.988±0.038	N/A	N/A
WISE 1759+5442	T7	N/A	N/A	-0.86±2.83	2.43±1.13	1.041±0.028	N/A	N/A
WISE 2335+4222	T7	N/A	N/A	2.4±2.49	8.08±0.9	1.07±0.025	N/A	N/A

Table 2.2 (cont'd)

Name	SpT	K I EW (Å) $1.1692\mu m$	K I EW (Å) $1.1778\mu m$	K I EW (Å) $1.2437\mu m$	K I EW (Å) $1.2529\mu m$	FeH_J $1.20\mu m$	Gravity Scores K1 K2 K4 FeH	Gravity Type
Gl 570 D	T7.5	N/A	N/A	N/A	N/A	1.019±0.019	N/A	N/A
WISE 0424+0727	T7.5	N/A	N/A	N/A	N/A	1.028±0.02	N/A	N/A
WISE 2147-1029	T7.5	N/A	N/A	N/A	N/A	0.946±0.016	N/A	N/A
2MASS 0415-0935	T8	N/A	N/A	N/A	N/A	0.99±0.002	N/A	N/A
WISE 0316+4307	T8	N/A	N/A	N/A	N/A	1.17±0.059	N/A	N/A
WISE 0430+4633	T8	N/A	N/A	N/A	N/A	0.821±0.013	N/A	N/A
WISE 1050+5056	T8	N/A	N/A	N/A	N/A	0.859±0.016	N/A	N/A
WISE 1448-2534	T8	N/A	N/A	N/A	N/A	0.98±0.034	N/A	N/A
WISE 1736+6059	T8	N/A	N/A	N/A	N/A	1.051±0.022	N/A	N/A
WISE 1813+2835	T8	N/A	N/A	N/A	N/A	0.971±0.01	N/A	N/A
WISE 1955-2540	T8	N/A	N/A	N/A	N/A	0.966±0.023	N/A	N/A
WISE 2005+5424	sdT8	N/A	N/A	N/A	N/A	0.893±0.011	N/A	N/A
WISE 0512-3004	T8.5	N/A	N/A	N/A	N/A	0.118±0.05	N/A	N/A
WISE 0540+4832	T8.5	N/A	N/A	N/A	N/A	1.021±0.012	N/A	N/A
WISE 0005+3737	T9	N/A	N/A	N/A	N/A	0.896±0.035	N/A	N/A
WISE 0038+2758	T9	N/A	N/A	N/A	N/A	1.149±0.025	N/A	N/A
WISE 0335+4310	T9	N/A	N/A	N/A	N/A	0.664±0.02	N/A	N/A

Table 2.3. BDSS Objects With Known Ages

Designation	Short Name	Right Ascension	Declination	SpT	Age [Myr]	Gravity Type	Notes	% Membership	Membership Ref.
2MASS J22443167+2043433	2MASS 2244+2043	22 44 31.674	+20 43 43.30	L6	149^{+51}_{-19}	VL-G	AB Dor	99.6	7
2MASS J03230483+4816111	AP 310	03 23 04.83	+48 16 11.2	M6	90 ± 10	FLD-G	Alpha Persei	100	25
Cl* Melotte 20 AP 316	AP 316	03 27 01.3	+49 14 40	M6	90 ± 10	FLD-G	Alpha Persei	100	25
2MASS J03180906+4925189	AP 301	03 18 09.06	+49 25 19.0	M6.5	90 ± 10	FLD-G	Alpha Persei	100	25
2MASS J03204346+5059396	AP 270	03 20 43.47	+50 59 39.6	M7	90 ± 10	VL-G	Alpha Persei	54	12
2MASS J03354735+4917430	AP 325	03 35 47.36	+49 17 43.1	M7	90 ± 10	INT-G	Alpha Persei	62	12
Cl* Melotte 20 AP 326	AP 326	03 38 55.2	+48 57 31	M7.5	90 ± 10	FLD-G	Alpha Persei	100	25
2MASS J03194133+5030451	AP 306	03 19 41.334	+50 30 45.15	M8	90 ± 10	FLD-G	Alpha Persei	100	25
2MASSI J0443376+000205	2MASS 0443+0002	04 43 37.610	+00 02 05.18	L0	24 ± 3	VL-G	Beta Pic	99.8	7
-	-	-	-	-	<500	-	Lithium	-	34
2MASS J03393521-3525440	LP 944-20	03 39 35.220	-35 25 44.09	L0	400±40	FLD-G	Castor	99.7	7,24
-	-	-	-	-	<500	-	Lithium	-	34
2MASS J06085283-2753583	2MASS 0608-2753	06 08 52.836	-27 53 58.35	L0	30 ± 20	VL-G	β Pic/Columba/ Cha-Near	Ambiguous	7, 35
GJ 577 BC	Gl 577 BC	15 05 50.07	+64 02 49.0	M5.5+M5.5	70^{+30}_{-40}	N/A	Companion	-	13
2MASS J22344161+4041387	2MASS 2234+4041	22 34 41.62	+40 41 38.8	M6	$1^{+1}_{-.5}$	VL-G	Companion	-	1
-	-	-	-	-	-	-	LkHα 233	-	1
BD+16 2708B	Gl 569 BC	14 54 29.36	+16 06 08.9	M8.5+M9	112.5±12.5	FLD-G	Companion	-	30
2MASS J11122567+3548131	Gl 417 BC	11 12 25.674	+35 48 13.17	L4.5+L6	750^{+140}_{-120}	FLD-G	Gyrochronology	-	31
-	-	-	-	-	80-300	-	Companion	-	32
2MASS J03473900+2436226	Roque 16	03 47 39.01	+24 36 22.7	M6	125±8	FLD-G	Pleiades	100	27
2MASS J03520670+2416008	Teide 2	03 52 06.71	+24 16 00.9	M6	125±8	FLD-G	Pleiades	68	11
2MASS J03454126+2354099	PPL 1	03 45 41.265	+23 54 09.95	M6.5	125±8	FLD-G	Pleiades	69	11
2MASS J03551257+2317378	CFHT PL 15	03 55 12.571	+23 17 37.82	M7	125±8	FLD-G	Pleiades	100	3

Table 2.3 (cont'd)

Designation	Short Name	Right Ascension	Declination	SpT	Age [Myr]	Gravity Type	Notes	% Membership	Membership Ref.
2MASS J03464298+2424506	Roque 14	03 46 42.99	+24 24 50.6	M7	125±8	FLD-G	Pleiades	100	26
2MASS J03455065+2409037	Roque 13	03 45 50.65	+24 09 03.8	M7.5	125±8	FLD-G	Pleiades	65	11
2MASS J03471208+2428320	Roque 11	03 47 12.08	+24 28 32.0	M8	125±8	FLD-G	Pleiades	100	26
2MASS J03471792+2422317	Teide 1	03 47 17.925	+24 22 31.71	M8	125±8	VL-G	Pleiades	68	11
2MASS J03434028+2430113	Roque 7	03 43 40.289	+24 30 11.40	M8.5	125±8	INT-G	Pleiades	100	3
2MASS J03435353+2431115	Roque 4	03 43 53.53	+24 31 11.5	M9	125±8	INT-G	Pleiades	100	27
2MASS J16262152-2426009	Rho Oph GY 5	16 26 21.528	-24 26 00.96	M5.5	$0.3^{+2.7}_{-.2}$	N/A	Rho Oph	100	8
2MASS J16262780-2426418	Rho Oph GY 37	16 26 27.810	-24 26 41.82	M6	$0.3^{+2.7}_{-.2}$	VL-G	Rho Oph	100	8
2MASS J16262226-2424070	Rho Oph GY 11	16 26 22.269	-24 24 07.06	M6.5	$0.3^{+2.7}_{-.2}$	VL-G	Rho Oph	100	8
2MASS J16261882-2426105	ISO-Oph 23	16 26 18.821	-24 26 10.52	M7.5	$0.3^{+2.7}_{-.2}$	VL-G	Rho Oph	100	8
2MASS J16262189-2444397	Rho Oph GY 3	16 26 21.899	-24 44 39.76	M8	$0.3^{+2.7}_{-.2}$	VL-G	Rho Oph	100	8
2MASS J16265128-2432419	Rho Oph GY 141	16 26 51.284	-24 32 41.99	M8.5	$0.3^{+2.7}_{-.2}$	VL-G	Rho Oph	100	8
2MASS J16273863-2438391	Rho Oph GY 310	16 27 38.631	-24 38 39.19	M8.5	$0.3^{+2.7}_{-.2}$	VL-G	Rho Oph	100	22
2MASS J05375745-0238444	S Ori 12	05 37 57.457	-02 38 44.44	M6	3±1	VL-G	Sigma Orionis	75	2
2MASS J05390449-0238353	S Ori 17	05 39 04.491	-02 38 35.37	M6	3±1	VL-G	Sigma Orionis	75	2
2MASS J05382088-0246132	S Ori 31	05 38 20.882	-02 46 13.27	M7	3±1	VL-G	Sigma Orionis	75	2
2MASS J05373648-0241567	S Ori 40	05 37 36.485	-02 41 56.73	M7	3±1	VL-G	Sigma Orionis	75	2
UGCS J053903.20-023019.9	S Ori 51	05 39 03.21	-02 30 19.9	L0	3±1	VL-G	Sigma Orionis	75	2
2MASS J12073346-3932539	2MASS 1207-3932	12 07 33.467	-39 32 54.00	M8	10±3	VL-G	TWA	100	18
2MASS J11395113-3159214	2MASS 1139-3159	11 39 51.140	-31 59 21.50	M9	10±3	VL-G	TWA	100	18
WDS J04325+1732Ba	GG Tau Ba	04 32 30.25	+17 31 30.9	M6	1.5±.5	VL-G	Taurus	100	28
2MASS J04262939+2624137	KPNO Tau 3	04 26 29.392	+26 24 13.79	M6	1.5±.5	VL-G	Taurus	100	16
2MASS J04312405+1800215	MHO Tau 4	04 31 24.057	+18 00 21.53	M6	1.5±.5	VL-G	Taurus	100	5
2MASS J04321606+1812464	MHO Tau 5	04 32 16.067	+18 12 46.45	M6.5	1.5±.5	VL-G	Taurus	100	5
2MASS J04361038+2259560	CFHT BD Tau 2	04 36 10.387	+22 59 56.03	M7.5	1.5±.5	VL-G	Taurus	100	19
WDS J04325+1732Bb	GG Tau Bb	04 32 30.31	+17 31 29.9	M7.5	1.5±.5	VL-G	Taurus	100	28
2MASS J04363893+2258119	CFHT BD Tau 3	04 36 38.938	+22 58 11.90	M8	1.5±.5	VL-G	Taurus	100	19
2MASS J04305718+2556394	KPNO Tau 7	04 30 57.187	+25 56 39.48	M8	1.5±.5	VL-G	Taurus	100	4
2MASS J04151471+2800096	KPNO Tau 1	04 15 14.714	+28 00 09.61	M8.5	1.5±.5	VL-G	Taurus	100	4

Table 2.3 (cont'd)

Designation	Short Name	Right Ascension	Declination	SpT	Age [Myr]	Gravity Type	Notes	% Membership	Membership Ref.
2MASS J04300724+2608207	KPNO Tau 6	04 30 07.244	+26 08 20.79	M8.5	1.5±.5	VL-G	Taurus	100	4
2MASS J04355143+2249119	KPNO Tau 9	04 35 51.432	+22 49 11.95	M8.5	1.5±.5	VL-G	Taurus	100	4
2MASS J04190126+2802487	KPNO Tau 12	04 19 01.270	+28 02 48.70	M9	1.5±.5	VL-G	Taurus	100	15
2MASS J04272799+2612052	KPNO Tau 4	04 27 27.997	+26 12 05.27	L0	1.5±.5	VL-G	Taurus	100	16
2MASS J01415823-4633574	2MASS 0141-4633	01 41 58.233	-46 33 57.43	L0	45±4	VL-G	Tucana Horlogium	99.5	33
2MASS J16051403-2406524	DENIS 1605-2406	16 05 14.033	-24 06 52.48	M6	11±2	VL-G	U Sco	100	20
2MASS J16014955-2351082	U Sco CTIO 66AB	16 01 49.557	-23 51 08.20	M6+M6	11±2	VL-G	U Sco	100	10
2MASS J16121185-2047267	SCH 1612-2047	16 12 11.860	-20 47 26.72	M6.5	11±2	VL-G	U Sco	100	14
2MASS J16020429-2050425	U Sco CTIO 100	16 02 04.296	-20 50 42.57	M7	11±2	VL-G	U Sco	100	14
2MASS J15591135-2338002	U Sco CTIO 128	15 59 11.359	-23 38 00.24	M7	11±2	VL-G	U Sco	100	14
2MASS J15594366-2014396	U Sco CTIO 130	15 59 43.665	-20 14 39.61	M7.5	11±2	VL-G	U Sco	100	14
2MASS J16191646-2347235	DENIS 1619-2347	16 19 16.463	-23 47 23.54	M8	11±2	VL-G	U Sco	100	14
2MASS J16192988-2440469	DENIS 1619-2440	16 19 29.882	-24 40 46.97	M8	11±2	VL-G	U Sco	100	14
2MASS J16224385-1951057	SCH 1622-1951	16 22 43.854	-19 51 05.77	M8	11±2	VL-G	U Sco	100	14
2MASS J16235155-2317270	SCH 1623-2317	16 23 51.560	-23 17 27.03	M8	11±2	VL-G	U Sco	100	14
2MASS J16110360-2426429	DENIS 1611-2426	16 11 03.609	-24 26 42.94	M9	11±2	VL-G	U Sco	100	14
2MASS J16145258-2017133	DENIS 1614-2017	16 14 52.588	-20 17 13.32	M9	11±2	VL-G	U Sco	100	14

Note. — Membership References: 1.Allers et al. 2009, 2. Béjar et al. 2011, 3. Bouvier et al. 1998, 4. Briceño et al. 2002, 5. Briceño et al. 1998, 6. Cruz et al. 2009, 7. Gagné et al. 2014, 8. Geers et al. 2011, 9. Kirkpatrick et al. 2010, 10. Kraus et al. 2005, 11. Lodieu et al. 2012a, 12. Lodieu et al. 2012b, 13. Lowrance et al. 2005, 14. Luhman & Mamajek 2012, 15. Luhman et al. 2003, 16. Luhman et al. 2006, 17. Luhman et al. 2008, 18. Mamajek 2005, 19. Martín et al. 2001, 20. Martín et al. 2004, 21. Muzerolle et al. 2003, 22. Mužić et al. 2012, 23. Pavlenko et al. 2006, 24. Ribas 2003, 25. Stauffer et al. 1999, 26. Stauffer et al. 2007, 27. Zapatero Osorio et al. 1997, 28. Cohen & Kuhi 1979, 29. Wilson et al. 2001, 30. Simon et al. 2006, 31. Allers et al. 2010, 32. Kirkpatrick et al. 2001, 33. Gagné et al. 2015b, 34. Reiners & Basri 2009, 35. Faherty et al. 2016

Table 2.4. Best Fit Parameters for Age vs. K I Equivalent Width

SpT	A [Myr]	$3\sigma_A$	B [$\mathring{A}^{-1}$]	$3\sigma_B$
		K I at 1.1692 μm		
M6±1	1.21397	0.18509	0.82751	0.03330
M7±1	1.11259	0.13018	0.80449	0.02633
M8±1	0.96102	0.12268	0.66583	0.02163
M9±1	0.49177	0.08032	0.47582	0.01421
L0±1	1.51591	0.29961	0.37076	0.01813
		K I at 1.1778 μm		
M6±1	0.64072	0.09984	0.55605	0.02238
M7±1	0.49738	0.06485	0.58026	0.01879
M8±1	0.31632	0.04927	0.59087	0.01819
M9±1	0.23653	0.04466	0.42362	0.01261
L0±1	1.85884	0.29051	0.27824	0.01156
		K I at 1.2529 μm		
M6±1	0.43282	0.07065	0.84337	0.03082
M7±1	0.46584	0.06145	0.80843	0.02697
M8±1	0.46064	0.06628	0.77101	0.02500
M9±1	0.59026	0.07495	0.49215	0.01194
L0±1	1.86551	0.29311	0.38854	0.01493

Note. — The parameters in this table may be applied to determine an age estimate using the following equation: $\text{Age[Myr]} = A \times 10^{B \times EW[\mathring{A}]}$

Table 2.5. Age Ranges For A13 Gravity Classifications for K I EWs

	Age Ranges [Myr]								
SpT	K I at 1.1692 μm			K I at 1.1778 μm			K I at 1.2529 μm		
	VL-G	INT-G	FLD-G	VL-G	INT-G	FLD-G	VL-G	INT-G	FLD-G
M6	0.3–22	22–27	27–10 Gyr	0.3–16	16–35	35–10 Gyr	0.3–12	12–32	32–10 Gyr
M7	0.3–55	55–205	205–10 Gyr	0.3–39	39–262	262–10 Gyr	0.3–27	27–208	208–10 Gyr
M8	0.3–57	57–413	413–10 Gyr	0.3–64	64–1.21 Gyr	1.21 Gyr–10 Gyr	0.3–50	50–817	817–10 Gyr
M9	0.3–17	17–128	128–10 Gyr	0.3–19	19–290	290–10 Gyr	0.3–19	19–190	190–10 Gyr
L0	0.3–38	38–296	296–10 Gyr	0.3–46	46–403	403–10 Gyr	0.3–42	42–378	378–10 Gyr

2.7 Chapter 2 Appendix

Here we present all J-band spectra for the BDSS, ordered by spectral type and then surface gravity (if applicable) in Figures 2.9, 2.10, 2.11, 2.12, and 2.13. Many of these spectra were previously published in McLean et al. (2003), McGovern et al. (2004), Kirkpatrick et al. (2010), Mace et al. (2013), but the majority are published here for the first time. All spectra will be available for download on bdssarchive.org. In addition to the K I, FeH, VO, and H_2O absorption features noted in Figure 2.2, some spectra have the Al doublet at 1.32 μm, the Paβ emission line at 1.28 μm, and some show significant reddening. The A13 indices were shown to be robust against reddening, so this should not affect our results.

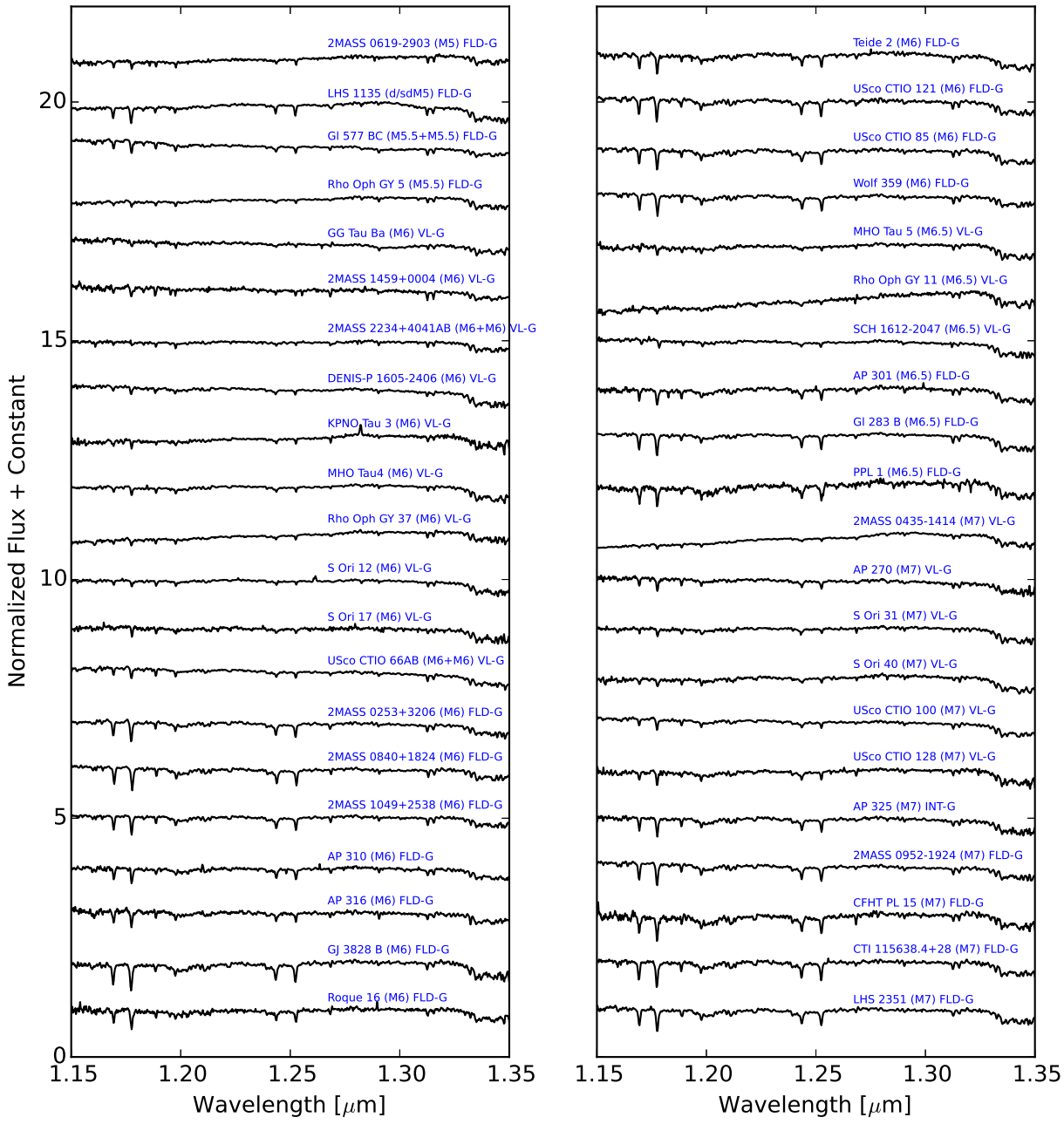

Figure 2.9: M5–M7 dwarfs, ordered by spectral type and then surface gravity type (if applicable)

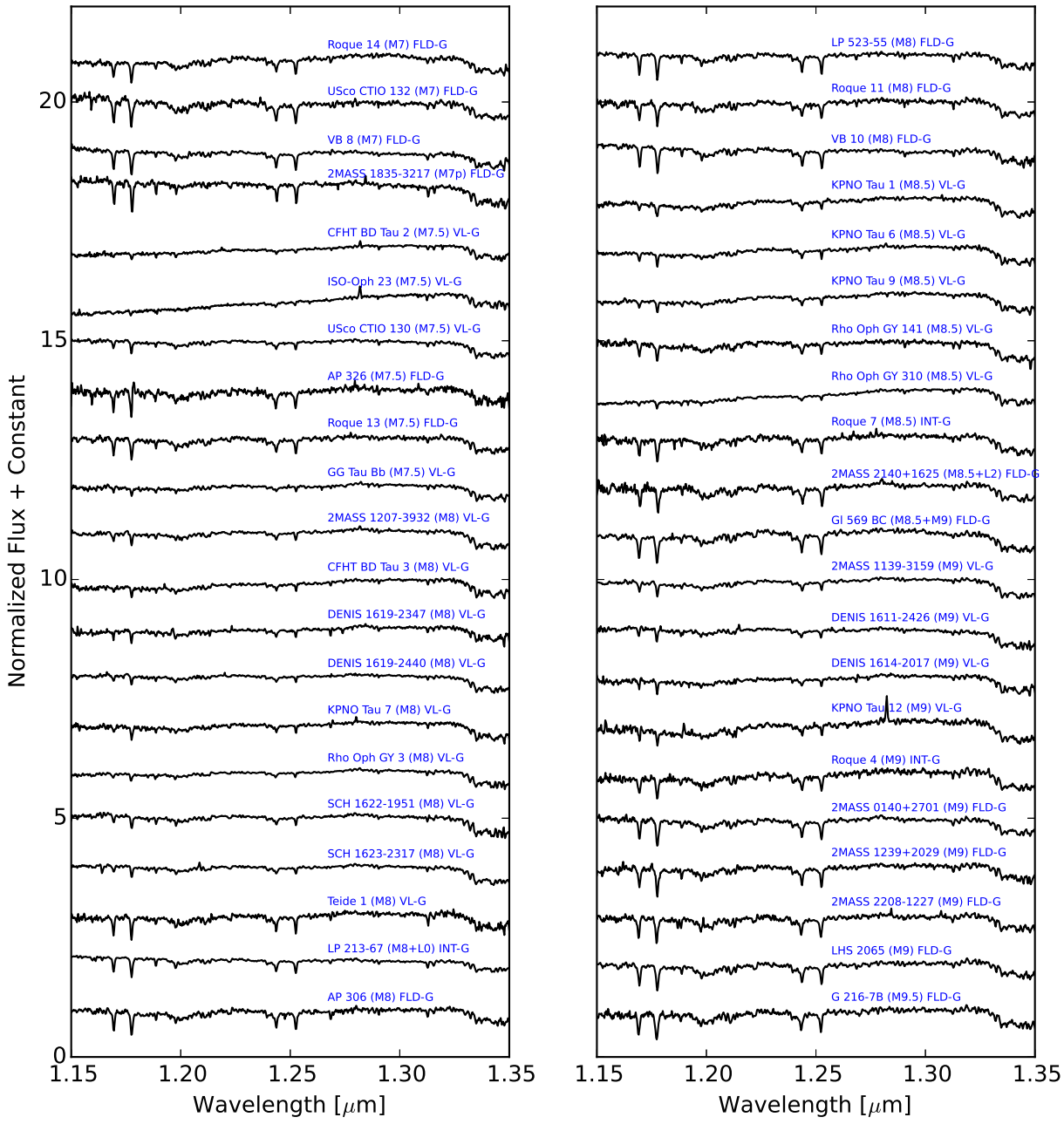

Figure 2.10: M7–M9.5 dwarfs, ordered by spectral type and then surface gravity type (if applicable)

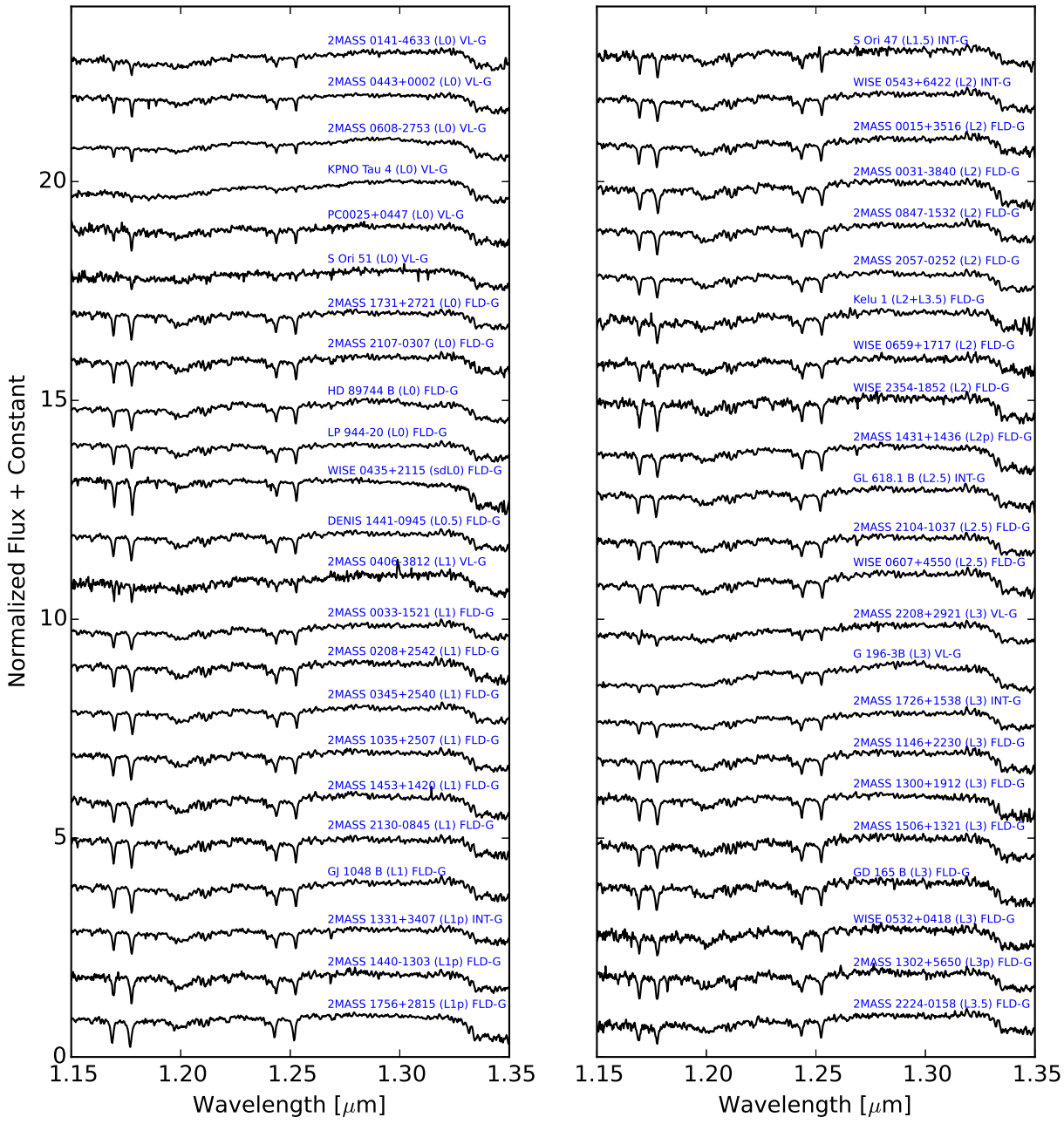

Figure 2.11: L0–L3.5 dwarfs, ordered by spectral type and then surface gravity type (if applicable)

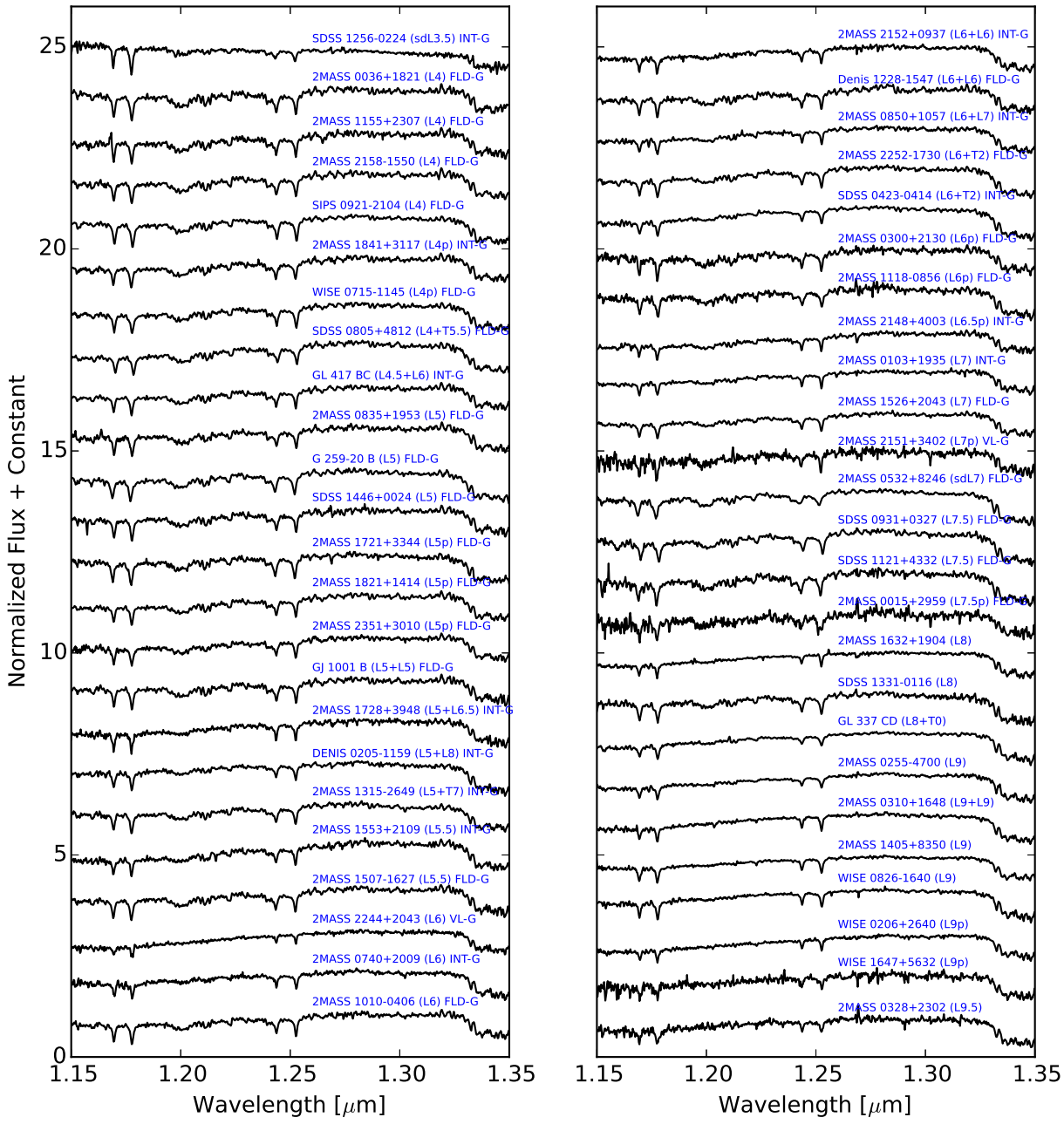

Figure 2.12: L3.5–L9.5 dwarfs, ordered by spectral type and then surface gravity type (if applicable)

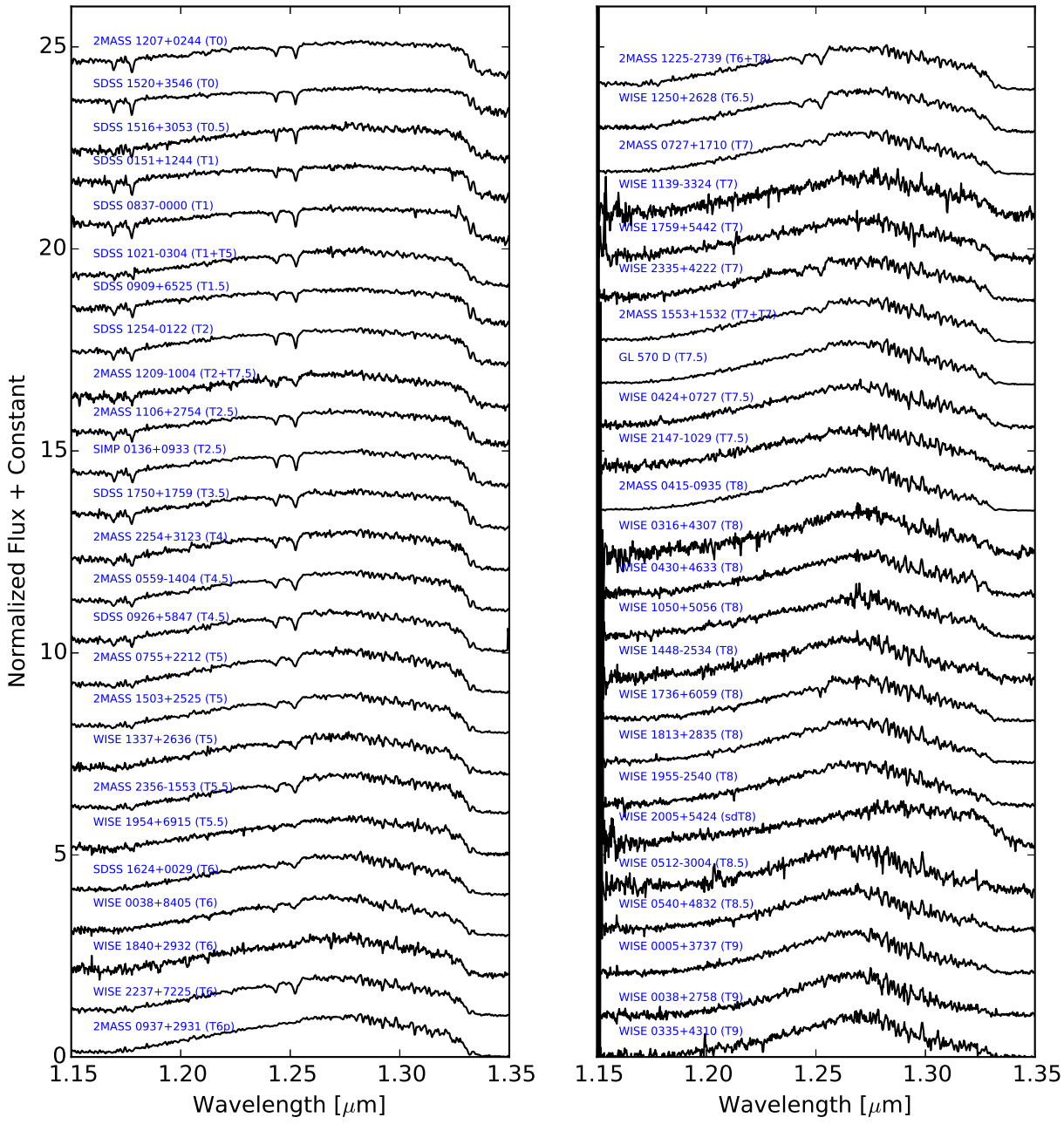

Figure 2.13: T0–T9 dwarfs, ordered by spectral type and then surface gravity type (if applicable)

CHAPTER 3

Y dwarf Trigonometric Parallaxes from the *Spitzer Space Telescope*

3.1 Introduction

Y dwarfs (Cushing et al., 2011; Kirkpatrick et al., 2012) have effective temperatures ($T_{\rm eff}$) $\lesssim$ 500 K, are extremely faint, and emit the majority of their light in the mid-infrared. The all-sky, space-based *Wide-field Infrared Survey Explorer* mission (*WISE*; Wright et al. 2010) has specifically designed $W1$ and $W2$ filter bandpasses such that the $W1$ filter covers the strong, fundamental CH_4 bandhead at 3.3 μm, a known absorber in the atmospheres of cold brown dwarfs, and the $W2$ filter centers on the peak of emission expected at 4.5 μm. Thus cold brown dwarfs have very red $W1 - W2$ colors and can be easily identified.

The first Y dwarfs were confirmed using a combination of ground-based and space-based spectroscopy. With typical J- and H- band magnitudes $\gtrsim$ 19, these observations are at the limit of the capabilities of the largest ground-based telescopes, and supplemental *Hubble Space Telescope (HST)* observations are often required. However, the faintest Y dwarf candidates, with near-infrared magnitudes $\gtrsim$ 23, are difficult even for *HST*, and will require *James Webb Space Telescope (JWST)* observations to fully characterize their atmospheres. Observations of the brightest Y dwarfs revealed nearly equal flux, sharp emission peaks (in units of f_λ) in the shorter wavelength near-infrared Y, J, and H bands, and relatively shallower, broader K-band fluxes (Cushing et al., 2011; Leggett et al., 2016). CH_4 and H_2O are the major absorbers in the atmospheres of Y dwarfs, carving out large swaths of their spectra in the near- and mid-infrared. Initial atmospheric models (Burrows et al., 2003) suggested that NH_3 would also be present in the atmospheres of Y dwarfs. Observers have yet to find direct

spectroscopic evidence of this molecule in the near-infrared (Leggett et al., 2013; Schneider et al., 2015); however, Line et al. (2015) and Line et al. (2017) find unambiguous detections of NH_3 in cold brown dwarf spectra using advanced atmospheric retrieval techniques. Such difficulties in directly observing NH_3 absorption features suggests that non-equilibrium chemistry likely plays an important role in mixing the atmosphere faster than it can achieve chemical equilibrium (Morley et al., 2014).

For such cold substellar objects to exist at the current age of the universe, they must inherently have lower masses on average than the M, L, and T dwarf field populations. Based on predictions from evolutionary models (e.g. Burrows et al. 2001; Saumon & Marley 2008), Y dwarfs occupy the mass range of $\sim 1-30\ M_{\rm Jup}$. Y dwarfs represent the very bottom of the stellar/sub-stellar main sequence, as well as the lowest-mass end of the field-mass function, and are thus crucial targets for follow-up to better understand star formation at the lowest masses.

Y dwarfs share similar temperatures, masses, and chemical compositions with gas-giant exoplanets, making them useful testbeds for atmospheric physics of the coldest objects. Atmospheric observations of exoplanets are difficult because of the extreme contrast needed to differentiate the light of the planet from its host star. Single, free-floating brown dwarfs in the field do not suffer from being outshone by a brighter, more massive companion, and thus make excellent laboratories for studying the atmospheres of planetary-mass objects at temperatures ranging from $\sim$ 200–500 K (Beichman et al., 2014; Faherty et al., 2016; Skemer et al., 2016).

Additionally, because Y dwarfs are so small and faint, most of the known Y dwarfs are located within the nearest $\lesssim$ 15 pc to the Sun. Y dwarfs that are farther than $\sim$ 20 pc are too faint to be observable with *WISE*. The farthest known Y dwarf, WD 0806-661B, at $\sim$ 19 pc, was found as a companion to a white dwarf (Luhman et al., 2011), through a common-proper-motion search of the nearest stellar systems. Recent studies (e.g., Smart et al. 2010, Winters et al. 2017) have focused on completing the census of low-mass stars in the solar neighborhood. Kirkpatrick et al. (2012) presented a preliminary volume-limited survey of the coldest ($T_{\rm eff} \lesssim 1000$ K) substellar objects within the nearest 8 pc, but was

only able to place lower limits on the number density of the coldest and lowest-mass brown dwarfs below 600 K. Precise distances of a larger sample of ultracool brown dwarfs will allow us to better characterize the solar neighborhood down to the lowest masses.

Our current understanding of the star formation process lacks empirical data to place bounds on the lowest mass capable of forming from the collapse and turbulent fragmentation of a massive molecular cloud, if such a bound even exists. The so-called minimum Jeans mass has been examined from a theoretical perspective by several groups (see, e.g. Low & Lynden-Bell 1976; Bate 2005; Padoan et al. 2007 and references therein) and shown to vary from $\sim 3\ M_{\rm Jup}$ to $\sim 10\ M_{\rm Jup}$. Burgasser (2004) used simulations of varying birthrates and mass functions along with evolutionary models from Burrows et al. (1997) and Baraffe et al. (2003) to show the estimated luminosity functions and temperature distributions that could be produced. The local number density of Y dwarfs is shown to be the most critical constraint in determining the minimum Jeans mass. Furthermore, the relatively small number of low-mass brown dwarfs that are companions to nearby stars can be used to infer that gravitational instability is not likely to produce objects below $\sim 15\ M_{\rm Jup}$ (Zuckerman & Song, 2009).

Recent studies have presented trigonometric parallaxes and proper motions for small samples of nearby brown dwarfs. Several of these objects were discovered to be within 3 pc (WISE 10495319AB, WISE 0855−0714 Luhman 2013; Luhman 2014) and have dramatically altered our understanding of the solar neighborhood since these systems were found to be the 3rd and 4th closest systems to the Sun. Previous studies of the parallaxes of late-T and Y dwarfs include Dupuy & Kraus (2013) and Leggett et al. (2017), who use data from the *Spitzer Space Telescope* to measure astrometric fits. Beichman et al. (2014) uses a combination of *Spitzer* and ground-based astrometry, and Smart et al. (2017) and Tinney et al. (2014) both utilize ground-based near-infrared observations to measure parallaxes. Luhman & Esplin (2016) published initial parallaxes for three Y dwarfs presented in this paper, using a subset of the data from the *Spitzer* programs reported here. We provide updated parallaxes for these objects using a longer time baseline.

Our *Spitzer* parallax program (PI: Kirkpatrick) aims to measure distances to all of the nearby late-T and Y dwarfs within 20 pc that are not being covered by ground-based as-

trometric monitoring. We are astrometrically monitoring 143 objects with *Spitzer*/IRAC channel 2 imaging through 2018 (Cycle 13). In this paper, we present *Spitzer* photometry for 27 objects, including preliminary parallaxes for 19 Y dwarfs and 3 late-T dwarfs in our *Spitzer* parallax program. The *Spitzer* observations cover baselines of $\sim$ 2–7 years.

We also present spectroscopic confirmation and spectrophotometric distance estimates for several AllWISE late-T and Y dwarf candidates with *Keck*/NIRSPEC J band observations. The AllWISE processing of the $WISE$ database combined all of the photometry from the original $WISE$ mission and selected high-proper motion candidates (see Kirkpatrick et al. 2014 for the initial results from the AllWISE motion survey). The new brown dwarfs presented in this paper were found in the AllWISE processing but were only recently followed-up spectroscopically to confirm their substellar nature.

In §2 we present our sample of targets and candidate selection methods. Section 3 describes our ground-based photometric and spectroscopic follow-up. Our *Spitzer* photometric and astrometric data acquisition and reduction methods are explained in §4, and astrometric analysis is detailed in §5. We present our results in §6, followed by a discussion in §7. We summarize our findings in §8.

Table 3.1. Coordinates, Spectral Types, and Photometry of Target Objects

WISEA Designation (1)	Infrared Sp. Type (2)	Ref (3)	J_{MKO} (mag) (4)	H_{MKO} (mag) (5)	Ref (6)	$W1$ (mag) (7)	$W2$ (mag) (8)	[3.6] (mag) (9)	[4.5] (mag) (10)
J014656.66+423409.9AB	T9+Y0	2	19.40±0.25[b]	18.71±0.24[a]	2	>19.137	15.083±0.065	17.360±0.089	15.069±0.022
J033605.04−014351.0	Y0[b]	1	>21.1	>20.2	1	18.449±0.470	14.557±0.057	17.199±0.076	14.629±0.019
J035000.31−565830.5	Y1	2	22.178±0.073	22.263±0.135	5	>18.699	14.745±0.044	17.832±0.131	14.712±0.019
J035934.07−540154.8	Y0	2	21.566±0.046	22.028±0.112	5	>19.031	15.384±0.054	17.565±0.108	15.357±0.023
J041022.75+150247.9	Y0	3	19.325±0.024	19.897±0.038	5	>18.170	14.113±0.047	16.578±0.047	14.149±0.018
J053516.87−750024.6	≥Y1:	2	22.132±0.071	23.34±0.34	5,8	17.940±0.143	14.904±0.047	17.648±0.112	15.116±0.022
J055047.86−195051.4	T6.5	1	17.925±0.021	—	1	18.727±0.437	15.594±0.095	16.536±0.039	15.303±0.021
J061557.21+152626.1	T8.5	1	18.945±0.052	—	1	>18.454	15.324±0.117	17.189±0.057	15.199±0.019
J064223.48+042343.1	T8	1	17.677±0.012	—	1	>18.583	15.418±0.110	16.654±0.039	15.177±0.019
J064723.24−623235.4	Y1	4	22.854±0.066	23.306±0.166	5	>19.539	15.224±0.051	17.825±0.128	15.151±0.021
J071322.55−291752.0	Y0	2	19.98±0.05	20.19±0.08	9	>18.776	14.462±0.052	16.646±0.052	14.208±0.018
J073444.03−715743.8	Y0	2	20.354±0.029	21.069±0.071	5	18.749±0.281	15.189±0.050	17.605±0.100	15.271±0.022
J082507.37+280548.2	Y0.5	5	22.401±0.050	22.965±0.139	5	>18.444	14.578±0.060	17.424±0.097	14.642±0.019
J105130.02−213859.9	T8.5	1	18.939±0.099	19.190±0.391	10	17.301±0.141	14.596±0.056	16.467±0.042	14.640±0.019
J105553.62−165216.5	T9.5	1	20.703±0.212	>20.1	1	>18.103	15.067±0.078	17.352±0.085	15.011±0.021
J120604.25+840110.5	Y0	5	20.472±0.030	21.061±0.062	5	>18.734	15.058±0.054	17.258±0.088	15.320±0.022
J122036.38+540717.3	T9.5	1	20.452±0.100	—	1	19.227±0.517	15.757±0.091	17.896±0.101	15.694±0.022
J131833.96−175826.3	T8	1	18.433±0.187[c]	17.714±0.232[b]	10	17.513±0.160	14.666±0.058	16.789±0.056	14.712±0.019
J140518.32+553421.3	Y0 pec?	3	21.061±0.035	21.501±0.073	5	18.765±0.396	14.097±0.037	16.850±0.059	14.069±0.017
J154151.65−225024.9[c]	Y1	5	21.631±0.064	22.085±0.170	5	16.736±0.165	14.246±0.063	16.512±0.046	14.227±0.018
J163940.84−684739.4	Y0 pec	6	20.626±0.023	20.746±0.029	5	17.266±0.187	13.544±0.059	16.293±0.029	13.679±0.016
J173835.52+273258.8	Y0	3	19.546±0.023	20.246±0.031	5	17.710±0.157	14.497±0.043	16.973±0.064	14.475±0.018
J182831.08+265037.6	≥Y2	3	23.48±0.23	22.85±0.24	2,8	>18.248	14.353±0.045	16.907±0.018	14.321±0.018

Table 3.1 (cont'd)

WISEA Designation (1)	Infrared Sp. Type (2)	Ref (3)	$J_{\rm MKO}$ (mag) (4)	$H_{\rm MKO}$ (mag) (5)	Ref (6)	$W1$ (mag) (7)	$W2$ (mag) (8)	[3.6] (mag) (9)	[4.5] (mag) (10)
J205628.88+145953.6	Y0	3	19.129±0.022	19.643±0.026	5	16.480±0.075	13.839±0.037	16.068±0.032	13.905±0.017
J220304.18+461923.4	T8	1	18.573±0.017	—	1	>18.919	14.967±0.069	16.351±0.021	14.643±0.016
J220905.75+271143.6	Y0:	7	22.859±0.128	22.389±0.152	5	>18.831	14.770±0.055	17.733±0.121	14.735±0.019
J222055.34−362817.5	Y0	2	20.447±0.025	20.858±0.035	5	>18.772	14.714±0.056	17.180±0.072	14.742±0.020

[a]Photometry is on the 2MASS system, not MKO. These values are not used elsewhere in this paper because we think they are faulty.

[b]See Section 3.3.3 for discussion on the spectral type of this object.

[c]Photometry is on the 2MASS system, not MKO.

[d]This object does not appear in the AllWISE Source Catalog, so *WISE* data are drawn from the *WISE* All-Sky Source Catalog instead. See Kirkpatrick et al. (2012) for discussion regarding the possible erroneous $W1$ measurement for this object.

Note. — References to spectral types and JH photometry: (1) This paper, (2) Kirkpatrick et al. 2012, (3) Cushing et al. 2011, (4) Kirkpatrick et al. 2014, (5) Schneider et al. 2015, (6) Tinney et al. 2012, (7) Cushing et al. 2014, (8) Leggett et al. 2013, (9) Leggett et al. 2015, (10) Mace et al. 2013.

3.2 Sample

Objects in this paper were selected from two separate lists. The first was a list of nineteen previously published Y dwarfs (Cushing et al. 2011, Kirkpatrick et al. 2012, Tinney et al. 2012, Kirkpatrick et al. 2014, Schneider et al. 2015) that includes one object, WISE J033605.04−014351.0 (hereafter WISE 0336−0143)[1], published earlier as a late-T dwarf (Mace et al. 2013) but now identified here as an early Y (See § 3.3.3). The second was a list of eight objects selected from either the *WISE* All-Sky Source Catalog or the AllWISE Source Catalog as having colors and magnitudes suggesting a late spectral type ($\geq$ T6). Specifically, these eight objects – all classified as late-T dwarfs and listed in Table 3.1 – were selected as (1) having $W1 - W2 > 2.7$ mag and $W2 - W3 < 3.5$ mag, (2) detected with S/N>3 in $W2$, and (3) not flagged as a known artifact in $W2$. These eight late-T dwarfs were also followed up with both *Spitzer*/IRAC channel 1 (3.6 μm band; hereafter, [3.6]) and channel 2 (4.5 μm band; hereafter, [4.5]) and ground-based near-infrared imaging. If the resulting *Spitzer* [3.6]−[4.5] color and $J-$W2 or $H-$W2 color further verified the late type, the object was scheduled for Keck/NIRSPEC spectroscopic follow-up. See Figures 1, 7, 8, and 11 of Kirkpatrick et al. (2011) for color trends as a function of spectral type for T and Y dwarfs.

In this paper, we present *Spitzer*/IRAC [3.6] and [4.5] photometry for all 27 objects. Five of these targets were color-selected too late to have sufficient astrometric monitoring, however we were able to confirm their late-T dwarf nature. We present updated (18) and new (4) parallaxes for the remaining 22 late-T and Y dwarfs.

Table 3.2. NIRSPEC Observations

Short Name	SpT	UT Date of Observation	Integration Time [s]	A0V Calibrator	Seeing Conditions
WISE0336−0143	Y0[a]	2016 Feb 10	2400	HD 27700	clear
WISE0550−1950	T6.5	2016 Feb 10	3000	HD 44704	clear
WISE0615+1526	T8.5	2016 Feb 01	1200	HD 43583	clear
—	—	2016 Feb 11	3000	HD 43583	clear
WISE0642+0423	T8	2016 Feb 01	4200	HD 43583	clear
WISE1051−2138	T8.5	2016 Feb 11	4200	HD 95642	clear
WISE1055−1652	T9.5:	2016 Feb 01	6600	HD 98884	clear
—	—	2016 Feb 10	3600	HD 92079	clear
WISE1220+5407	T9.5	2016 Feb 01	1800	81 UMa	variable seeing
—	—	2016 Feb 11	3600	HD 99966	clear
WISE1318−1758	T8	2016 Feb 11	2400	HD 112304	windy
WISE2203+4619	T8	2014 Oct 06	4800	HD 219238	clear

[a]See Section 3.3.3 for discussion on the spectral type of this object.

3.3 Photometric and Spectroscopic Follow-up

3.3.1 Ground-based photometry with Palomar/WIRC

Near-infrared images of WISE 0336−0143, WISE 0550−1950, WISE 0615+1526, WISE 0642+0423, WISE 1055−1652, WISE 1220+5407, and WISE 2203+4619 were obtained using the Wide-Field Infrared Camera (WIRC; Wilson et al. 2003) on the 200 inch Hale Telescope at Palomar Observatory on 4 Jan 2012 (WISE 0336−0143, WISE 1055−1652), 7 Mar 2014 (WISE 2203+4619) and 26 Feb 2016 (WISE 0550−1950, WISE 0615+1526, WISE 0642+0423, WISE 1220+5407). WIRC has a pixel scale of $0\farcs2487$/pixel providing a total field of view of $8\farcm7$. For each object, fifteen 2-minute images were obtained in the J filter (30 minutes total exposure time). The sky was clear during the observations on all nights.

Images obtained in 2012 and 2014 were reduced using a suite of IRAF scripts and FORTRAN programs provided by T. Jarrett. These scripts first linearize and dark subtract the images. From the list of input images, a sky frame and flat field image are created and subtracted from and divided into (respectively) each input image. At this stage, WIRC images still contain a significant bias that is not removed by the flat field. Comparison of Two Micron All Sky Survey (2MASS; Skrutskie et al. 2006) and WIRC photometric differences

[1]Source designations are abbreviated as WISE hhmm±ddmm. Full designations are given in Table 3.1.

across the array shows that this flux bias has a level of ≈10% and the pattern is roughly the same for all filters. Using these 2MASS-WIRC differences for many fields, we can create a flux bias correction image that can be applied to each of the "reduced" images.

In April 2014, the primary science-grade detector experienced a catastrophic failure and was replaced with a lower quality engineering-grade detector (there are more cosmetic defects, for example). The previous reduction scripts were fine-tuned for the original detector and produced sub-optimal results with the new chip. A WIRC reduction package written in IDL by J. Surace was used for the 2016 data as it was able to better handle the non-uniformity in one of the quadrants. In addition to the quadrant cleaning, the Surace package differed from the Jarrett package in that the reduced data from the former did not exhibit, and thus did not require, a flux bias correction. The other data reduction steps were essentially the same. The processed frames were mosaicked together using a median and had their astrometry and photometry calibrated using 2MASS stars in the field.

Table 3.1 lists the photometry, using Vega system magnitudes. Additional photometry for the remaining targets in this sample was taken from the literature. The majority of the near-infrared photometry listed in Table 3.1 is on the MKO system, though some of the Y dwarfs have synthetic photometry measured with *HST* and corrected to match MKO filter profiles (see Schneider et al. 2015 for further details). We caution the reader that the photometric filter system can significantly change the near-infrared photometry of Y dwarfs.

3.3.2 Ground-based Spectroscopy with Keck/NIRSPEC

Using the NIRSPEC instrument at the W.M. Keck Observatory (McLean et al., 1998), we made J-band spectroscopic observations of 4 targets from the original *Spitzer* Parallax Program with unknown or uncertain spectral types: WISE0336−0143, WISE1051−2138, WISE1055−1652, and WISE 1318−1758. We observed an additional five targets that were likely to be late-type T or Y dwarfs based on their $W1 - W2$ colors from the AllWISE processing (Kirkpatrick et al., 2014). Spectral types and observation information for these targets are listed in Table 3.2.

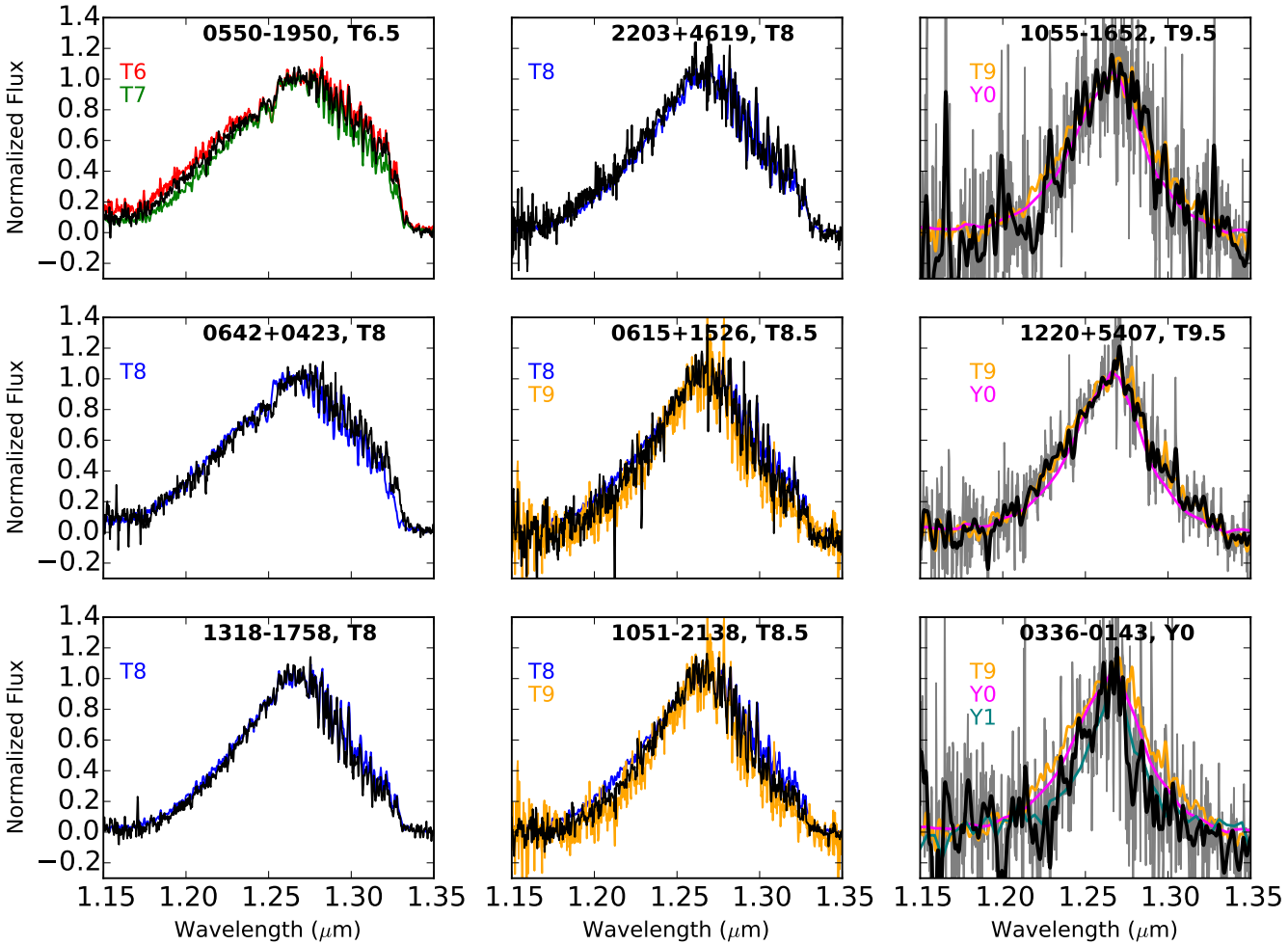

Figure 3.1: NIRSPEC J-band spectra compared to spectral standards. The target spectrum is shown in black and the spectral standards are shown in color, and labeled in each subplot. Spectra for the spectral standards are NIRSPEC observations from McLean et al. (2003), Kirkpatrick et al. (2012), and Mace et al. (2013). The three latest-type objects have low SNR so their observed spectra are plotted in gray, and the binned spectra (R ∼500, smoothed with a gaussian kernel) are overplotted in black.

All targets were observed using AB nod pairs along the 0.″57 (3-pixel) slit, producing a spectral resolution of $R = \lambda/\Delta\lambda \sim 1500$ per resolution element.

Spectroscopic reductions were made using a modified version of the REDSPEC package[2], following a similar procedure to Mace et al. (2013). Frames were spatially and spectrally rectified to remove the instrumental distortion on the image plane of the detector. Frames were then background-subtracted and divided by a flat-field. Spectra from each nod pair were extracted by summing over 9–11 pixels before combining the nods. The extracted spectrum was then divided by an A0V calibrator spectrum to remove telluric features and lastly, corrected for barycentric velocity. Observations made of the same target on separate nights were combined into a single spectrum after being reduced separately.

3.3.3 New late-T and Y dwarfs and updated spectral types

Here we present new and updated spectral types for 9 objects in our sample that we observed with NIRSPEC. J band spectra for these objects and the spectral standards used to classify them are shown in Figure 3.1.

WISE 0336−0143 was originally classified as T8: by Mace et al. (2013). In 2016, we sought to re-observe WISE 0336−0143 for two reasons. First, the spectrum published in Mace et al. (2013) had a low signal-to-noise (SNR) and we wished to obtain a higher SNR spectrum. Second, we hypothesized based on its [3.6]−[4.5] color of 2.57 mag that WISE 0336−0143 should be much colder than a T8 to explain its extreme redness. Typical [3.6]−[4.5] colors for T8 objects are $\sim$ 1.5–2 mag (see Figure 7 in Mace et al. 2013; WISE 0336−0143 is the obvious T8 outlier in that plot.) In Figure 3.2, we plot the normalized NIRSPEC spectra of the 2011 and 2016 observations. The 2016 observations match much better to a Y dwarf (see also Figure 3.1), so we will henceforth classify this object as a Y0:. We have only been able to obtain limits on the near-infrared photometry for this object. With $J > 21$, WISE 0336−0143 will require additional observations with an 8- or 10-m class ground-based telescope, or observations with *HST* or JWST to further characterize its

[2]Available at `http://www2.keck.hawaii.edu/inst/nirspec/redspec.html`

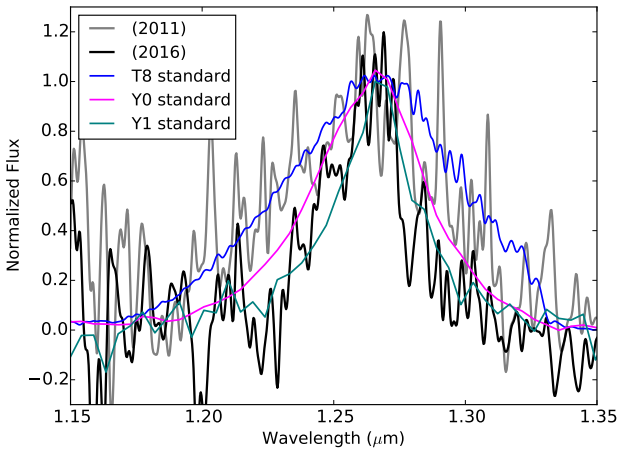

Figure 3.2: Comparison of the (smoothed) NIRSPEC spectra of WISE 0336−0143 as observed in 2011 by Mace et al. (2013) (grey) and as observed in 2016 (this paper, black). The T8 (blue), Y0 (magenta), and Y1 (teal) spectral standards are over-plotted for comparison.

spectrum.

WISE 0550−1950, *WISE 0615+1526*, *WISE 0642+0423*, *WISE 1220+5407*, and *WISE 2203+4619* are new T dwarfs found using the AllWISE color cuts discussed in § 3.2. We find spectral types of T6.5, T8.5, T8, T9.5, and T8, respectively, based on comparison of their J-band spectra to spectral standards.

WISE 1051−2138 was given a spectral type of T9: in Mace et al. (2013). Our re-observed spectrum, shown in Figure 3.1, indicates that this object should be classified as T8.5.

WISE 1055−1652 was placed on our parallax program without having an observed spectrum to confirm its substellar nature. We present the discovery of this new T9.5: dwarf.

WISE 1318−1758 was classified as a T9: in Mace et al. (2013) based on a noisy Palomar/TripleSpec spectrum and we re-classify it here as a T8. As shown in Figure 3.1, the T8 spectral standard is a very good match for WISE 1318−1758.

3.4 *Spitzer* Astrometric Follow-Up

3.4.1 Observations

Spitzer IRAC [4.5] images have a field of view of 5.′2 on a side, over 256x256 pixels, producing a pixel scale of 1.″2 pix^{-1}. The full-width at half-maximum for a centered point response function (PRF) is 1.″8, for the warm mission. The raw images have a maximum optical distortion of 1.6 pixels, on the edge of the array. During *Spitzer* cryogenic operations, [3.6] was more sensitive than [4.5]. After cryogen depletion, however, the deep image noise[3] was found to be 12% worse in [3.6] and 10% better in [4.5], making the channels more comparable in sensitivity for average field stars ([3.6]−[4.5] $\sim$ 0 mag) during warm operations (Carey et al. 2010). The behavior of latent images from bright objects was also found to change during warm operations; whereas latents in [4.5] decay rapidly – typically within ten minutes – [3.6] latents decay on timescales of hours. Moreover, the [4.5] intrapixel sensitivity variation (also known as the pixel phase effect) is about half that of [3.6]. Given these points, the fact that the PRF is better sampled in [4.5] than in [3.6], and the fact that our cold brown dwarfs are also much brighter in [4.5] than in [3.6] (1.0 $<$ [3.6]−[4.5] $<$ 3.0 mag; Figure 11 of Kirkpatrick et al. 2011), we chose to do our imaging in [4.5]. All [4.5] *Spitzer*/IRAC observations of the targets, the MJD range of usable data for each source, and the number of epochs available in each program, are given in Table 3.3.

We have utilized data from 6 *Spitzer* programs (Table 3.3) in our analysis. Of these, program 90007 was specifically designed for parallax and proper motion measurements and used a total integration time of 270s per epoch so that all targets would have SNR>100 in [4.5]. To smear out the effects of intrapixel sensitivity variation, which can bias the astrometry in a frame, we chose a 9-point random dither pattern with 30s exposures per dither. Dither sizes vary for this setup, but are on the order of $\sim$ 5–30 ″.[4] To keep the number

[3]See "Warm IRAC Characteristics" at `http://irsa.ipac.caltech.edu/data/SPITZER/docs/irac/` for a summary of each of the effects discussed here.

[4]For more information on dithers, see `https://irsa.ipac.caltech.edu/data/SPITZER/docs/irac/calibrationfiles/dither/`

of common reference stars between individual exposures high, we chose a dither pattern of medium scale. Timing constraints were imposed so that there was one sample within a few days of maximum parallax factor with (usually) evenly spaced samples throughout the rest of the target's visibility period.

We also used [4.5] data taken as part of earlier programs 551, 70062, and 80109 as well the later program 11059 (PI: Kirkpatrick) to increase the time baseline to help disentangle proper motion from parallax. Program 11059 used the same observing setup as program 90007, described above. All the other programs from which we utilized data (except 551; PI: Mainzer) used a frame time of 30s and a 5-point cycling dither pattern with medium scale, and observations were obtained in both [3.6] and [4.5]. In anticipation of parallax program 90007, we used the same [4.5] setup to re-observe our most promising targets during programs 70062 and 80109 after the original [3.6]+[4.5] Astronomical Observation Request (AOR) was completed.

Program 551, which targeted only WISE1828+2650, used a frame time of 100s and a 36-point Reuleaux with medium dither in [3.6] and a frame time of 12s and a 12-point Reuleaux pattern of medium dither in [4.5]. Program 10135 (PI: Pinfield), which targeted only WISE2203+4619, used a frame time of 30s and a 16-point spiral dither pattern of medium step in both channels; in this case, two exposures were taken at each dithered position.

Table 3.3. *Spitzer* Observations

Short Name (1)	*Spitzer* Program # (# of [4.5] Epochs) (2)	MJD Range of Observations (3)	AORs for Photometry (4)
WISE0146+4234	70062(1), 80109(2), 90007(12)	55656.0 - 56768.1	41808128
WISE0336−0143	70062(1), 80109(1), 90007(12)	55663.2 - 56777.7	41462784
WISE0350−5658	70062(2), 80109(2), 90007(10)	55457.1 - 56925.1	40834560
WISE0359−5401	70062(2), 80109(2), 90007(12)	55457.2 - 57035.8	40819712
WISE0410+1502	70062(2), 80109(2), 90007(12)	55490.0 - 56792.5	40828160
WISE0535−7500	70062(2), 80109(1), 90007(10)	55486.2 - 56875.6	41033472
WISE0550−1950	11059(1)	57175.2	52669696
WISE0615+1526	11059(1)	57175.1	52669952
WISE0642+0423	11059(1)	57175.1	52670208
WISE0647−6232	70062(2), 80109(1), 90007(10)	55458.4 - 56887.1	40829696
WISE0713−2917	80109(1), 90007(12)	55928.8 - 56856.5	44568064
WISE0734−7157	70062(1), 80109(1), 90007(10)	55670.6 - 56790.7	41754880
WISE0825+2805	80109(2), 90007(12)	55933.9 - 56849.0	44221184
WISE1051−2138	70062(1), 90007(11)	55633.6 - 56903.4	41464320
WISE1055−1652	80109(1), 90007(9)	56124.9 - 56900.5	44549632
WISE1206+8401	70062(2), 80109(1), 90007(12)	55539.7 - 57049.1	40823808

Table 3.3 (cont'd)

Short Name (1)	*Spitzer* Program # (# of [4.5] Epochs) (2)	MJD Range of Observations (3)	AORs for Photometry (4)
WISE1220+5407	11059(1)	57063.2	52671232
WISE1318−1758	70062(1), 80109(2), 90007(12)	55663.5 - 56925.0	40824832
WISE1405+5534	70062(1), 80109(2), 90007(10)	55583.1 - 56902.1	40836864
WISE1541−2250	70062(1), 80109(2), 90007(12)	55664.9 - 56812.0	41788672
WISE1639−6847	90007(12), 11059(1)	56431.7 - 57175.3	52672000[a]
WISE1738+2732	70062(2), 80109(2), 90007(12)	55457.5 - 56864.6	40828416
WISE1828+2650	551(1), 70062(1), 80109(2), 90007(12)	55387.3 - 56878.5	39526656, 39526912[b]
WISE2056+1459	70062(2), 80109(2), 90007(12)	55540.0 - 57049.0	40836608
WISE2203+4619	10135(1)	56922.9	50033152
WISE2209+2711	70062(2), 80109(1), 90007(12)	55561.9 - 56925.3	40821248
WISE2220−3628	80109(2), 90007(12)	55949.1 - 56902.9	44552448

[a]This high motion object was blended with a background star during our original observation in program 80109. We reacquired this observation during program 11059 to make up for the loss of a [4.5] astrometric epoch and the loss of our sole [3.6] photometric data point.

[b]The [3.6] and [4.5] observations of this object in program 551 were broken into separate AORs but were observed concurrently.

3.4.2 Astrometric and Photometric Data Reductions

We used the *Spitzer* Heritage Archive[5] to download all of the basic calibrated data (BCD) at [4.5] for the programs listed in Table 3.3. Data were reduced using the Mosaicker and Point Source Extractor (MOPEX[6]) with customized scripts. These scripts use the individually dithered BCD files to create a coadded image at each epoch (i.e., for each AOR) and to detect and characterize sources on the resulting coadd.

The data and scripts have been modified in two ways to utilize new knowledge gained during the *Spitzer* warm mission. First, the headers of the BCD files available at the *Spitzer* Heritage Archive have been updated to include a new *Spitzer*-produced fifth-order distortion correction for the IRAC camera, which is an improvement over the third-order correction included previously (Lowrance et al. 2014). Second, the PRF employed by the code is one created specifically for use on *Spitzer* warm data[7], sampled onto a 5×5 grid to account for small changes in shape across the array. The MOPEX code performs a simultaneous chi-squared minimization[8] using fits of the PRF to the stack of individual frames to measure the photometry and position of the source in that AOR. It should be noted that the random dithers will help to zero out the astrometric bias caused by the intrapixel distortion in each individual frame (Ingalls et al. 2012), so this effect did not have to be specifically addressed in our reduction methodology.

Our [3.6] observations were run identically to the [4.5] data discussed above. We divided the resulting PRF-fit fluxes by the appropriate [3.6] and [4.5] correction factors (1.021 and 1.012, respectively) indicated in Table C.1 of the IRAC Instrument Handbook[9] and converted these fluxes to magnitudes using the [3.6] and [4.5] zero points of 280.9±4.1 Jy and 179.7±2.6

[5]Available at `http://irsa.ipac.caltech.edu/`

[6]Available at `http://irsa.ipac.caltech.edu/data/SPITZER/docs/dataanalysistools/tools/mopex/`

[7]For more information on the PRF maps, see `http://irsa.ipac.caltech.edu/data/SPITZER/docs/irac/calibrationfiles/psfprf/`

[8]For more information, see `http://irsa.ipac.caltech.edu/data/SPITZER/docs/dataanalysistools/tools/mopex/mopexusersguide/88/#_Toc320000081`

[9]Available at `http://irsa.ipac.caltech.edu/data/SPITZER/docs/irac/iracinstrumenthandbook/`

Jy, respectively, as given in Table 4.1 of the same document. The final [3.6] and [4.5] photometry is listed in columns 9–10 of Table 3.1.

Prior studies have shown that the amplitude of [3.6] and/or [4.5] variability in T0–T8 dwarfs can can reach the 10% level, with some objects varying more in one band than the other (Metchev et al. 2015). This amplitude increases at later spectral types. In fact, one Y dwarf, WISE 1405+5534, has already been observed to vary at levels as high as 3.5% in [3.6] and [4.5] based on a limited data set (Cushing et al. 2016). Another Y dwarf observed for variability, WISE 1738+2732, showed peak-to-peak variability of $\sim$ 3 %, at [4.5] with potentially up to 30% variability in the near-infrared (Leggett et al., 2016). Therefore, our tabulated values list photometry only for the one AOR having concurrent [3.6] and [4.5] observations so that the resulting [3.6]$-$[4.5] value represents a physical snapshot of the color at a specific time rather than a possibly non-physical color created from disparate epochs of [3.6] and [4.5] observations. The AORs from which the [3.6] and [4.5] photometry is measured are listed in column 4 of Table 3.3.

The centroid locations determined by the MOPEX routine on each of the epochal coadds (average positions across multiple dithers) were then used as the fundamental source of our astrometric measurements. Our resulting inputs to our astrometric fitting routine at each epoch were the source location, time of observation of the middle frame, and geometric cooordinates of *Spitzer* during the observations.

3.5 Astrometric Analysis

3.5.1 Coordinate Re-Registration

Prior to fitting our astrometric solutions for each target, we re-registered the coordinates of our targets in each epoch onto a single reference frame. We chose to align our coordinates to those provided by the Gaia Mission in Data Release 1 (DR1; Gaia Collaboration et al. 2016b,a). These positions are the best that are currently available across the whole sky. 2MASS positions, which provide the basis for the WCS coordinates given by

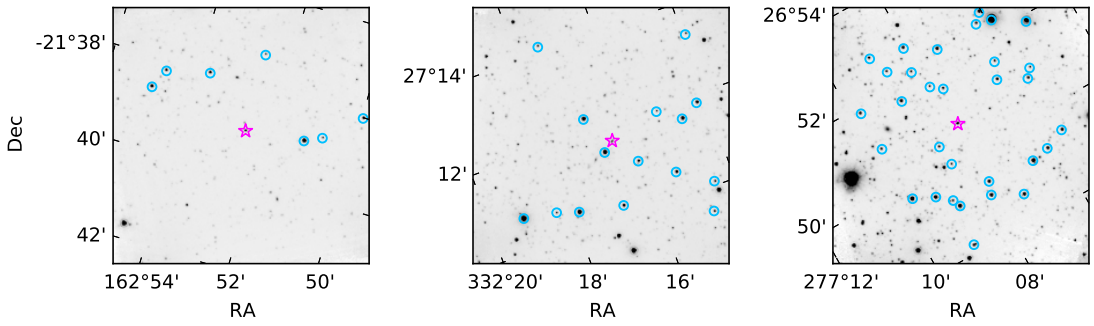

Figure 3.3: Supermosaic frames of WISE 1051−2138, WISE 2209+2711, and WISE 1828+2650, from left to right. Reference stars in each of the fields are circled in blue. Targets are marked by a magenta star. These frames show examples of different target fields, ranging from few reference stars to many.

MOPEX/APEX, have positional uncertainties on the order of $\sim$ 70 mas (McCallon et al., 2007), while Gaia DR1 positions for the brightest, unsaturated reference stars have positional uncertainties on the order of $\lesssim$ 1 mas.

We selected reference background sources for the re-registration process by requiring that the sources be detected in all epochal co-adds, have SNR>100, and have positional uncertainties within 2σ of the median positional uncertainty of the field. Requiring a detection in every co-added frame cut sources on the extreme edge of the field, while the positional uncertainty cut removed any sources with any significant proper motion. We then evaluated each reference target by-eye to discard any non point-like sources. We obtained Gaia coordinates for each reference star, where available, and excluded any with exceptionally high uncertainties ($\gtrsim$ 1 mas) in the Gaia DR1, as well as reference sources that were lacking Gaia coordinates. The resulting set of reference stars varied from 7 to 96, depending on the stellar density in the field. Thumbnail images of three example fields with the target and reference sources highlighted can be found in Figure 3.3, showcasing fields with low, moderate, and high numbers of reference stars.

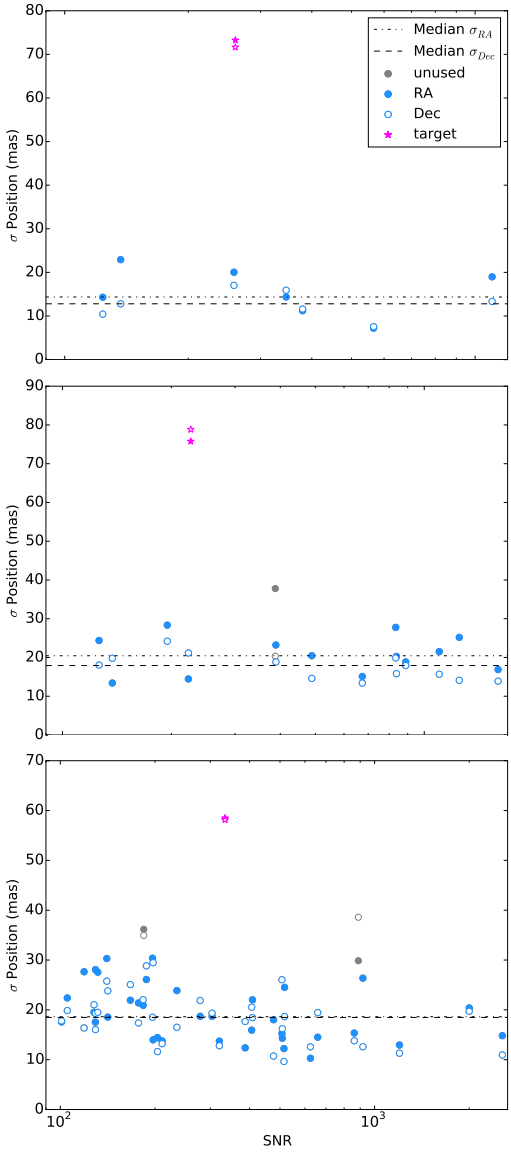

Figure 3.4: Positional uncertainties vs. SNR for stars in the fields of WISE 1051−2138, WISE 2209+2711, and WISE 1828+2650, from left to right. Reference star $\sigma_{\rm RA}$ are in red and $\sigma_{\rm Dec}$ are in blue. Uncertainties were calculated by taking the standard deviation of the centroid location across all epochs, post re-registration. Positional uncertainty drops with increasing SNR, until reaching a systematic floor. We measure the median positional uncertainty for reference stars with SNR > 100 after performing a 1σ clipping to remove outliers. The median value (horizontal lines) is used as the target positional uncertainty, in lieu of the MOPEX-given $\sigma_{\rm RA}$ and $\sigma_{\rm Dec}$ (stars), which significantly overestimates the positional uncertainties.

3.5.2 Positional Uncertainties

We found that the positional uncertainties output by the MOPEX/APEX centroid extractions were overestimated by a factor of $\gtrsim 2$ compared to the uncertainties on background stars with similar SNR. Instead of using these inflated uncertainties, we determined empirical positional uncertainties for each target by comparison to the positional uncertainties of the presumably non-moving field reference stars. For each field, we re-registered the locations of all stars in the field using the correction determined by the reference field stars as detailed above. We then calculated the positional uncertainty of every source in both RA and Dec as the standard deviation of the centroid location across all epochs, post-re-registration. As expected, positional uncertainty drops with increasing SNR until it reaches a systematic floor of ∼15–40 mas, depending on the field. Figure 3.4 shows three examples of positional uncertainty vs. source SNR, given a low, medium, or high number of reference stars. Our target SNRs are typically high enough that their positional uncertainties can be determined from the asymptotic portion of the graph. We measure the median positional uncertainty above a cutoff SNR > 100 after performing a 2σ clipping to remove significant outliers. These outliers could be non-point-like sources, e.g. galaxies, or they could have significant proper motion. The median value rounded to the nearest 5 mas is then the positional uncertainty that we use in each epoch to determine the astrometric fits for each of our targets, with a floor of 15 mas. Positional uncertainties for each target are listed in column 10 of Table 3.4.

After determining our target uncertainties, the selected reference stars that likewise met the sigma clipping requirement were then used to perform a final re-registration. We performed a least-squares affine transformation to adjust each frame onto the Gaia reference frame. To do this, we projected both the Gaia and MOPEX coordinates onto a tangent plane (ξ, η) and then solved for the best-fit generalized 6-term solution, allowing for offsets, rotation, and scaling between the two planes.

3.5.3 Astrometric Solutions

After re-registering each source onto a common reference frame, we then solved simultaneously for 5 parameters: trigonometric parallax π, proper motion in both RA and dec (μ_α, μ_δ), and initial position (α_0, δ_0) at a fiducial time of T_0=2014.0, which falls roughly in the middle of our time baseline for each object. We used the standard astrometric equations (Smart & Green, 1977; Green, 1985), inputing epochal coordinates, time of observation, and rectangular observatory coordinates obtained from the image headers. We then used Pythons' Scipy least squares minimization module[10] to solve for the best fit. Our best-fit astrometric solutions are listed in Table 3.4 and plotted in Figures 3.5 – 3.26. We show both the overall astrometric fit, as well as the parallactic ellipse, after removing the best-fit proper motion component. The best-fit model shown makes use of the *Spitzer* ephemerides from JPL's Horizons[11] to calculate the heliocentric rectangular coordinates of *Spitzer* over a longer time baseline and with higher cadence than our observations. These measurements are for relative parallaxes, not absolute. We estimate that the correction for the systematic offset of the average parallax of the background stars is $\sim$ 1 mas, well within the random errors of our solutions.

One caveat for the targets at high declination ($|\delta| \gtrsim 70°$) is that an unidentifiable problem in the MOPEX mosaicking code leads to much more uncertain astrometry. This is reflected in the larger uncertainties we adopt for their epochal positions and the generally larger reduced chi-squared (χ^2_ν) values we measure. This issue will be further discussed in our forthcoming paper presenting parallaxes for all of the T6 and later brown dwarfs in our parallax program (Kirkpatrick et al., in prep).

[10]https://docs.scipy.org/doc/scipy-0.19.0/reference/generated/scipy.optimize.leastsq.html

[11]https://ssd.jpl.nasa.gov/?horizons

Table 3.4. Best-fit Astrometric Solutions

Object Name (1)	$\alpha_{0,2014}$ (Deg, J2000) (2)	$\delta_{0,2014}$ (Deg, J2000) (3)	σ_{α_0} (mas) (4)	σ_{δ_0} (mas) (5)	μ_α (mas/yr) (6)	μ_δ (mas/yr) (7)	$\pi_{\rm trig}$ (mas, relative) (8)	Distance (pc) (9)	$\sigma_{\rm pos}$ (mas) (10)	$n_{\rm epochs}$ (11)	$n_{\rm ref}$ (12)	χ^2 / dof = χ^2_ν (13)
WISE 0146+4234	26.735579	42.569408	8.69	6.24	−450.67 ± 6.29	−27.90±6.34	45.575 ± 5.74	$21.94^{+3.16}_{-2.45}$	20	15	18	34.0/25 = 1.36
WISE 0336−0143	54.020862	−1.732170	6.65	6.48	−247.35 ± 6.05	−1213.46±6.03	100.90 ± 5.86	$9.91^{+0.61}_{-0.54}$	20	14	13	29.44/23 = 1.28
WISE 0350−5658	57.500996	−56.975638	17.80	9.66	−206.94 ± 6.52	−577.67±6.68	168.84 ± 8.53	$5.92^{+0.32}_{-0.28}$	30	14	8	23.69/23 = 1.03
WISE 0359−5401	59.891827	−54.032517	11.96	6.90	−152.70 ± 4.83	−783.66±4.93	75.36 ± 6.62	$13.27^{+1.28}_{-1.07}$	25	16	8	31.32/27 = 1.16
WISE 0410+1502	62.595853	15.044417	5.00	4.71	959.86 ± 3.57	−2218.64±3.46	153.42 ± 4.05	$6.52^{+0.18}_{-0.17}$	15	16	12	31.32/27 = 1.16
WISE 0535−7500	83.819477	−75.006740	39.31	10.08	−113.23 ± 7.71	23.72±7.52	79.51 ± 8.79	$12.58^{+1.56}_{-1.25}$	30	12	28	32.3/19 = 1.70
WISE 0647−6232	101.846784	−62.542832	14.92	6.74	1.015 ± 5.08	390.97±4.61	83.73 ± 5.68	$11.94^{+0.87}_{-0.76}$	20	13	21	24.43/21 = 1.16
WISE 0713−2917	108.344414	−29.298188	5.51	4.72	341.10 ± 6.57	−411.13±6.00	100.73 ± 4.74	$9.93^{+0.49}_{-0.45}$	15	13	68	9.87/21 = 0.47
WISE 0734−7157	113.681539	−71.962325	32.07	9.94	−566.22 ± 8.85	−77.54±8.82	67.63 ± 8.68	$14.79^{+2.18}_{-1.68}$	30	12	26	21.59/19 = 1.14
WISE 0825+2805	126.280554	28.096545	5.40	4.72	−64.35 ± 5.56	−234.73±5.36	139.02 ± 4.33	$7.19^{+0.23}_{-0.22}$	15	14	13	24.25/23 = 1.05
WISE 1051−2138	162.875233	−21.650040	6.74	6.28	145.57 ± 6.84	−160.68±6.60	49.27 ± 6.47	$20.3^{+3.1}_{-2.4}$	20	12	7	17.79/19 = 0.94
WISE 1055−1652	163.972546	−16.870930	6.98	6.48	−1001.7 ± 9.2	432.16±9.17	71.21 ± 6.82	$14.04^{+1.5}_{-1.2}$	20	10	12	22.8/15 = 1.52
WISE 1206+8401	181.512553	84.019282	93.16	9.09	−557.69 ± 6.54	−241.31±6.51	85.12 ± 9.27	$11.75^{+1.44}_{-1.15}$	30	14	7	19.46/14 = 1.39
WISE 1318−1758	199.641070	−17.974002	7.37	6.97	−514.59 ± 7.20	3.70±6.86	48.06 ± 7.33	$20.81^{+3.74}_{-2.75}$	25	15	7	30.79/15 = 1.23
WISE 1405+5534	211.322480	55.572793	14.60	8.54	−2336.04± 6.91	238.02±7.40	144.35 ± 8.60	$6.93\ ^{+0.44}_{-0.39}$	25	13	7	32.84/21 = 1.56
WISE 1541−2250	235.464061	−22.840554	5.03	4.51	−895.05 ± 4.68	−94.73±4.66	167.05 ± 4.19	$5.99\ ^{+0.154}_{-0.147}$	15	15	26	24.38/25 = 0.98
WISE 1639−6847	249.921736	−68.797280	22.37	7.68	579.09 ± 12.52	−3104.54±12.25	228.05 ± 8.93	$4.39^{+0.18}_{-0.17}$	25	12	96	23.94/19 = 1.26
WISE 1738+2732	264.648443	27.549315	5.32	4.59	343.27 ± 3.45	−340.63±3.35	136.26 ± 4.27	$7.34^{+0.24}_{-0.22}$	15	16	13	28.95/27 = 1.07
WISE 1828+2650	277.130717	26.844012	5.04	4.58	1020.99 ± 3.20	175.55±3.09	100.21 ± 4.23	$9.98^{+0.44}_{-0.40}$	15	16	31	30.58/27 = 1.13
WISE 2056+1459	314.121287	14.998666	4.54	4.39	822.99 ± 3.37	535.72±3.36	138.32 ± 3.86	$7.23^{+0.21}_{-0.20}$	15	16	38	18.19/27 = 0.67
WISE 2209+2711	332.275281	27.194171	6.58	5.95	1199.55± 4.94	−1359.00±4.76	154.41 ± 5.67	$6.48^{+0.25}_{-0.23}$	20	15	15	23.41/25 = 0.94
WISE 2220−3628	335.230875	−36.471639	7.61	6.00	292.91 ± 7.43	−61.46±7.04	84.10 ± 5.90	$11.89^{+0.90}_{-0.78}$	20	14	13	22.71/23 = 0.99

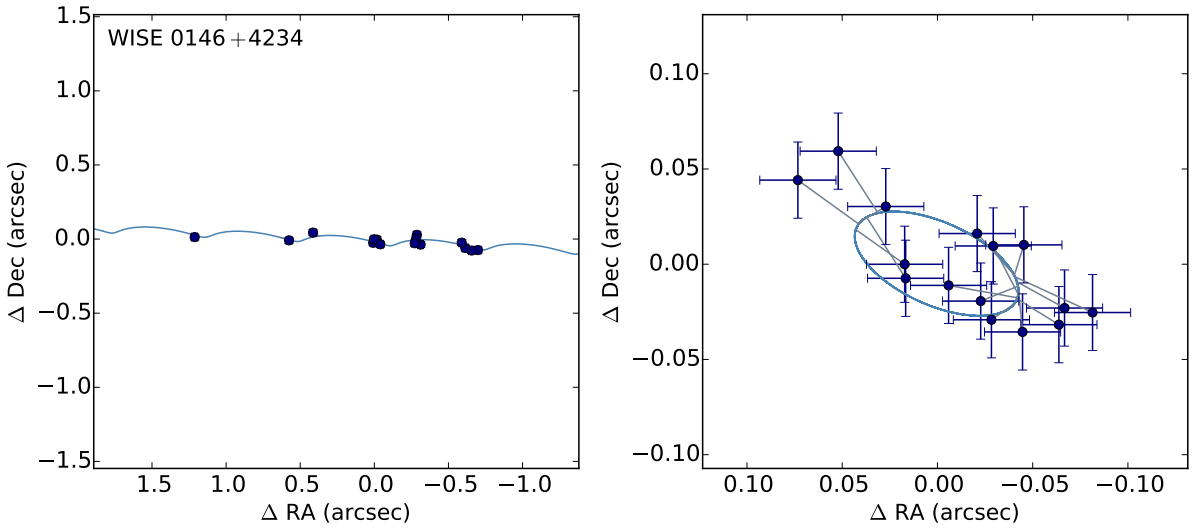

Figure 3.5: Astrometric fit for WISE 0146+4234. We maintained a square scaling for the Δ Declination and Δ RA. Our observations are plotted in navy and the best-fit astrometric model is plotted in light blue. The left plots include proper motion and parallax and the right plots have proper-motion removed. Note the differing scales between the left and right plots. WISE 0146+4234 is an un-resolved binary, which produces systematic offsets of our astrometry and causes the parallactic ellipse to appear smaller than it is.

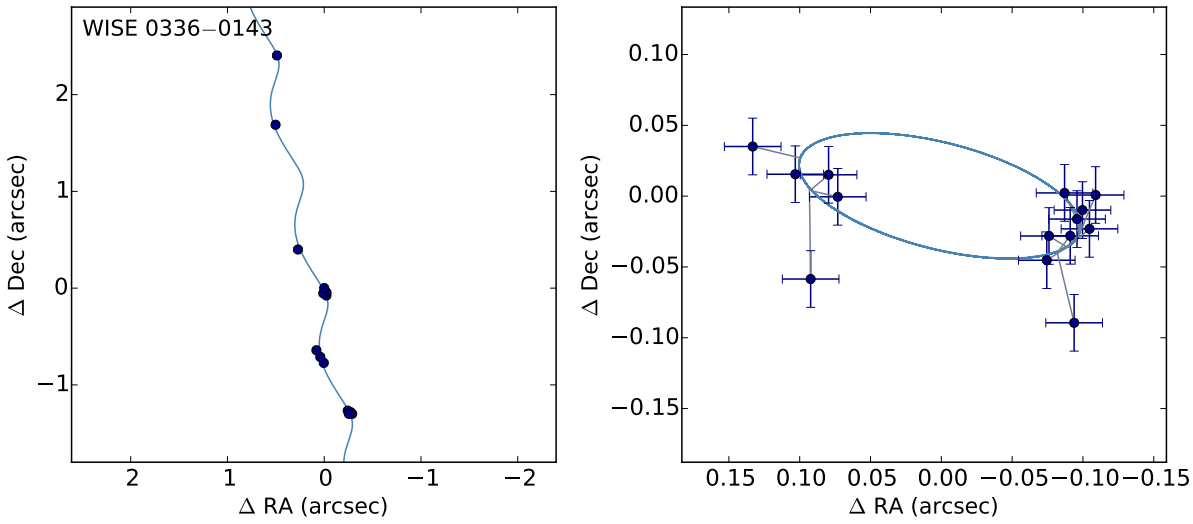

Figure 3.6: Astrometric fit for WISE 0336−0143. See Figure 3.5 for more details.

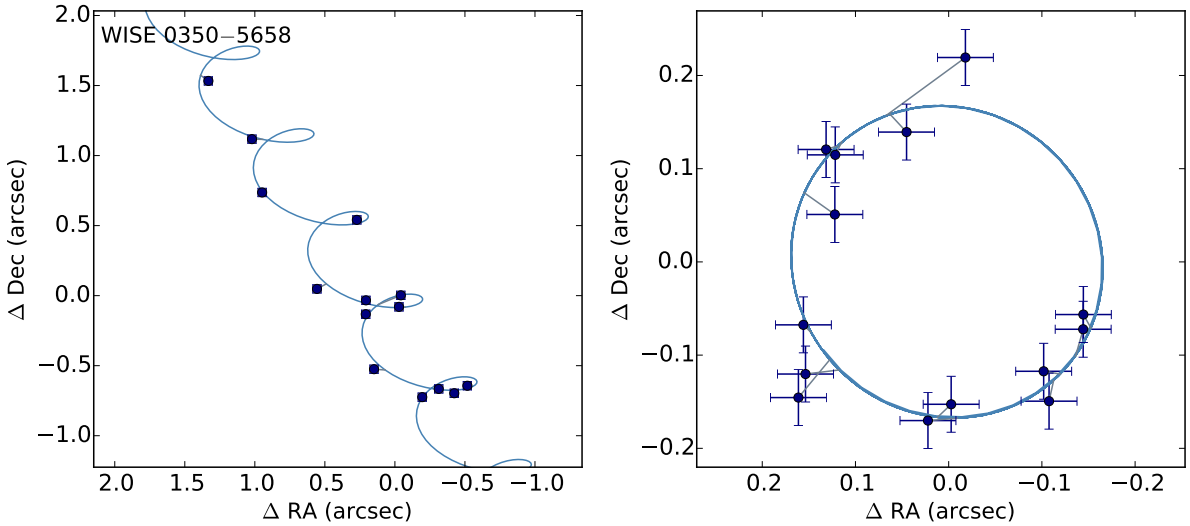

Figure 3.7: Astrometric fit for WISE 0350−5658. See Figure 3.5 for more details.

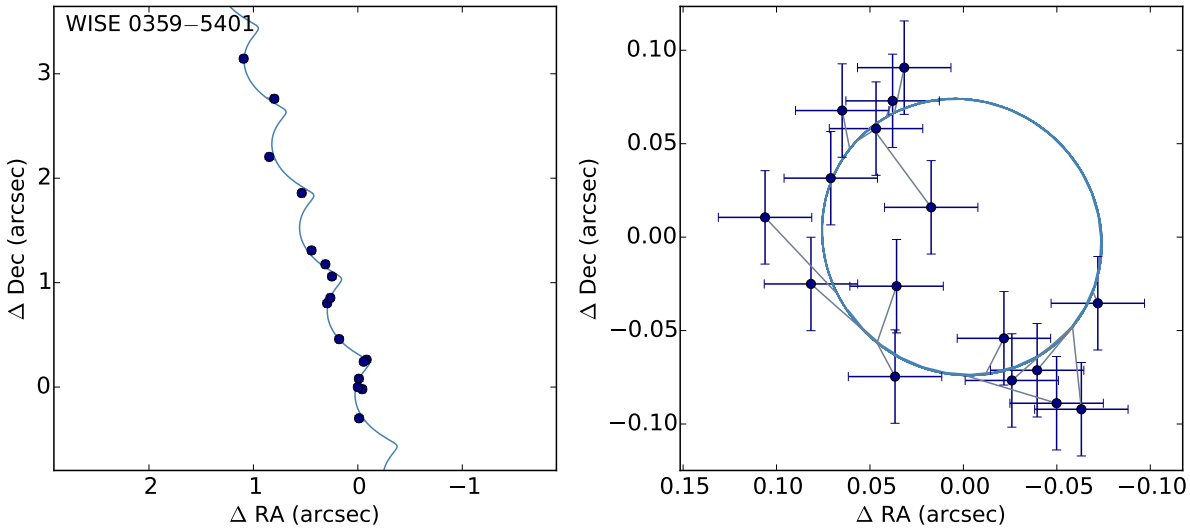

Figure 3.8: Astrometric fit for WISE 0359−5401. See Figure 3.5 for more details.

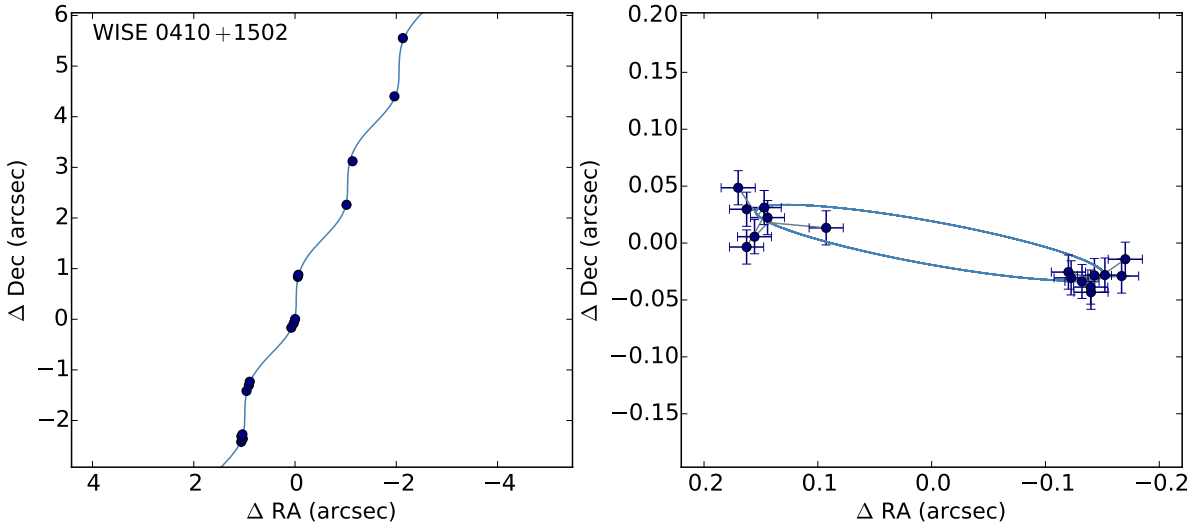

Figure 3.9: Astrometric fit for WISE 0410+1502. See Figure 3.5 for more details.

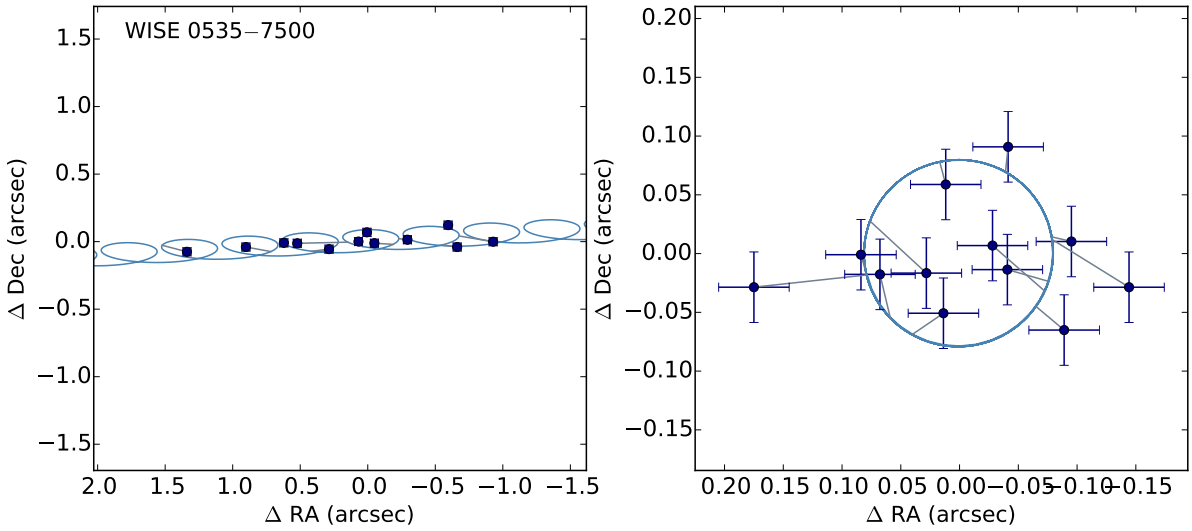

Figure 3.10: Astrometric fit for WISE 0535−7500. See Figure 3.5 for more details.

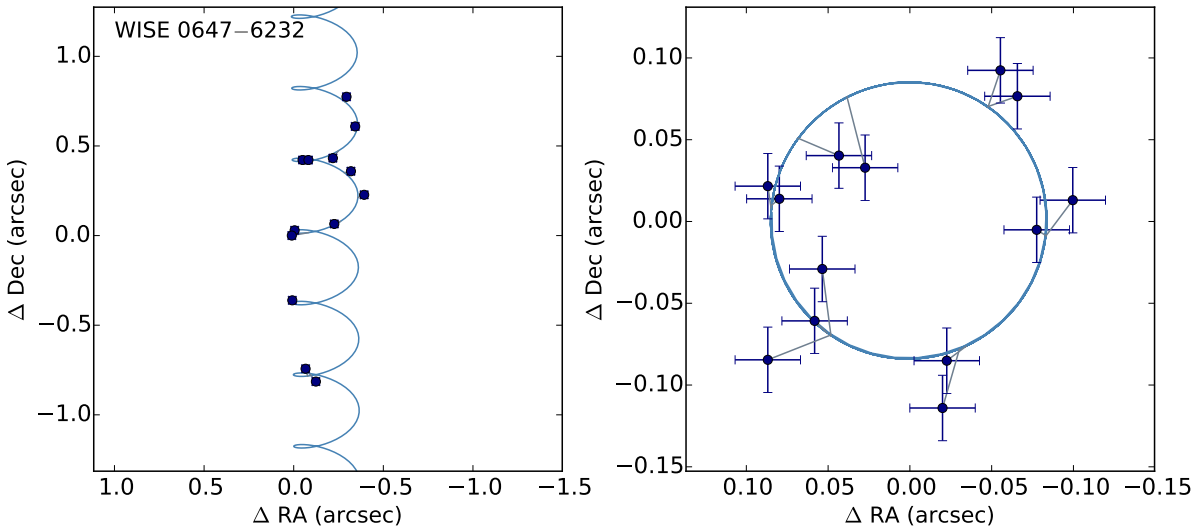

Figure 3.11: Astrometric fit for WISE 0647−6232. See Figure 3.5 for more details.

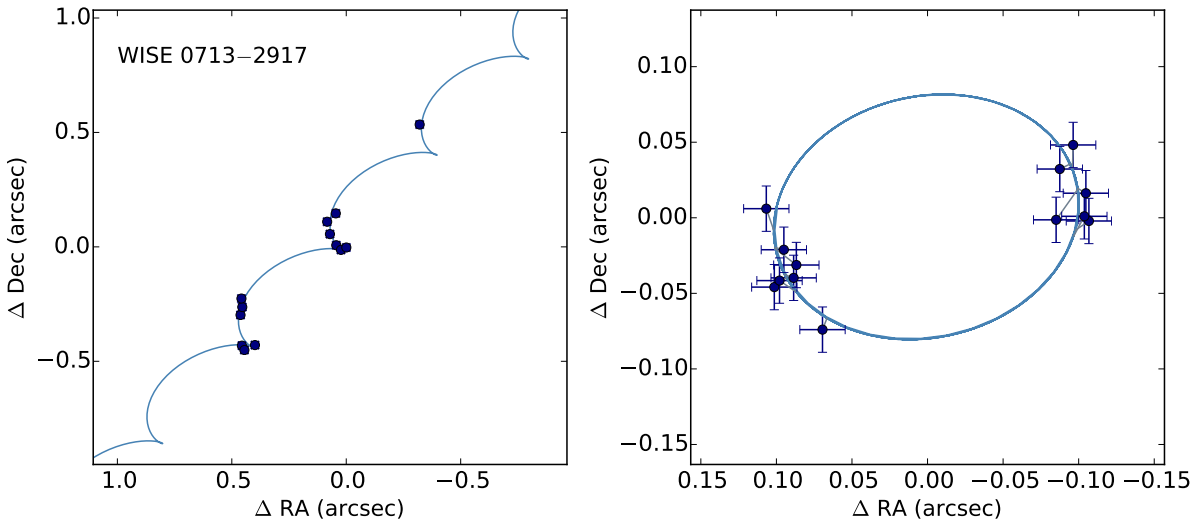

Figure 3.12: Astrometric fit for WISE 0713−2917. See Figure 3.5 for more details.

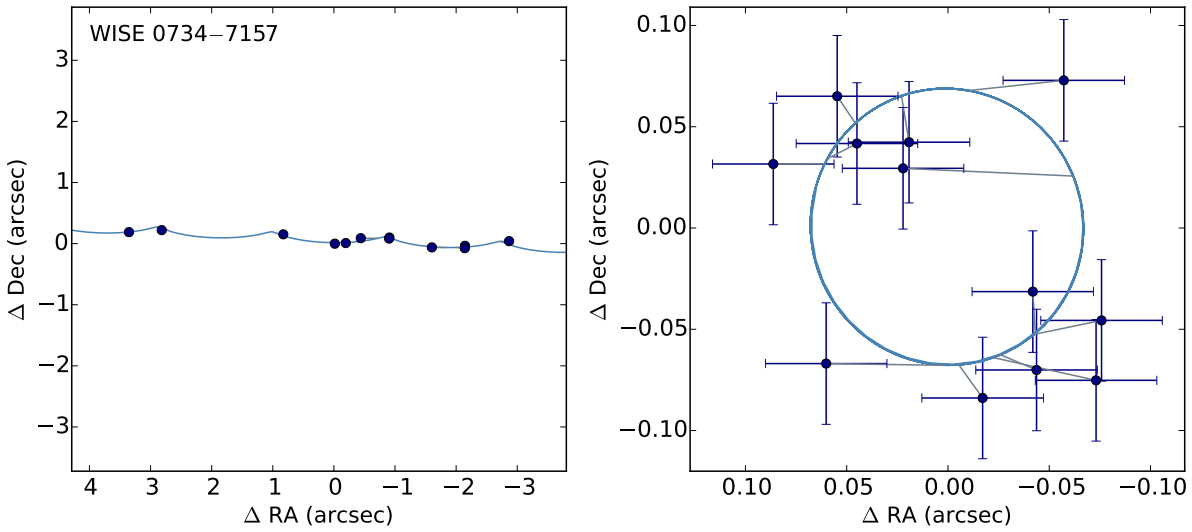

Figure 3.13: Astrometric fit for WISE 0734−7157. See Figure 3.5 for more details.

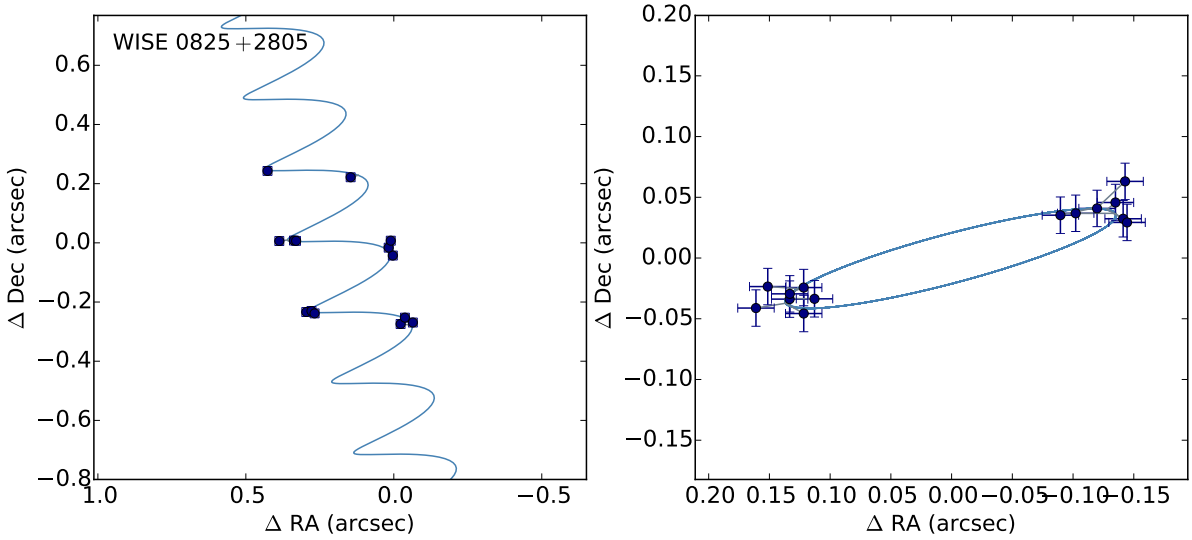

Figure 3.14: Astrometric fit for WISE 0825+2805. See Figure 3.5 for more details.

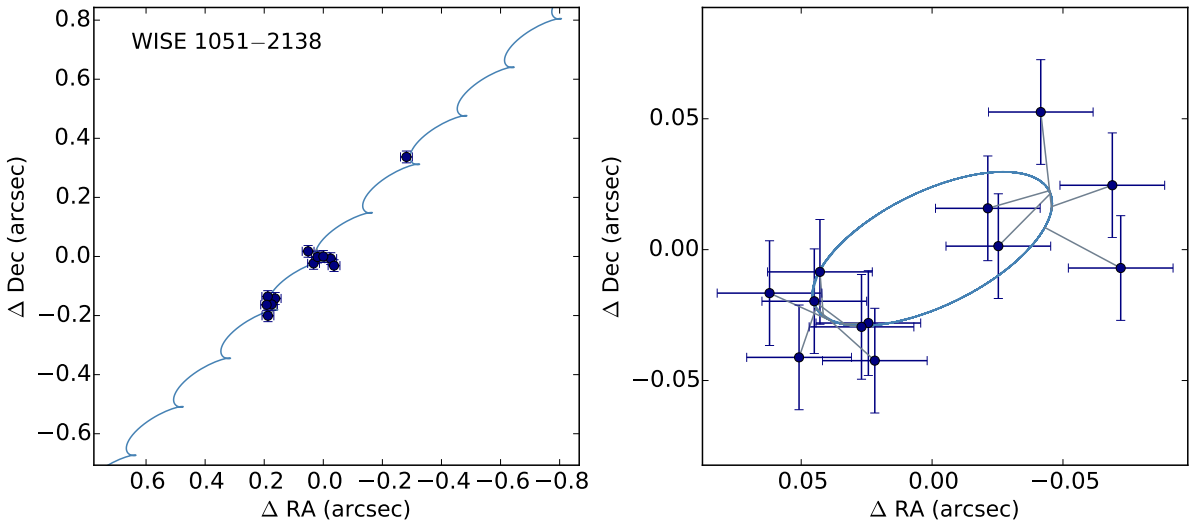

Figure 3.15: Astrometric fit for WISE 1051−2138. See Figure 3.5 for more details.

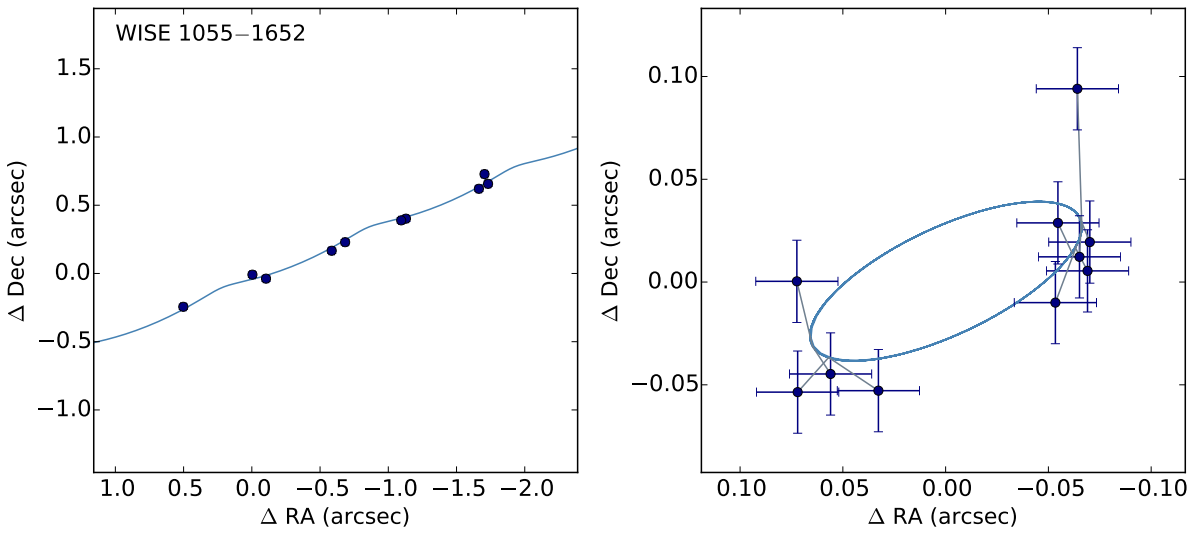

Figure 3.16: Astrometric fit for WISE 1055−1652. See Figure 3.5 for more details.

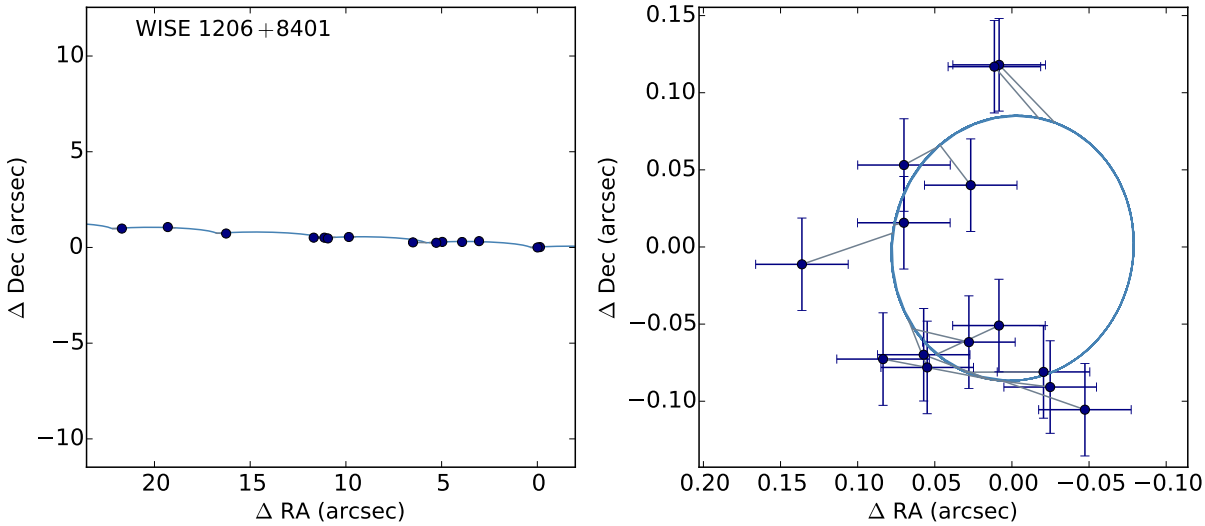

Figure 3.17: Astrometric fit for WISE 1206+8401. See Figure 3.5 for more details.

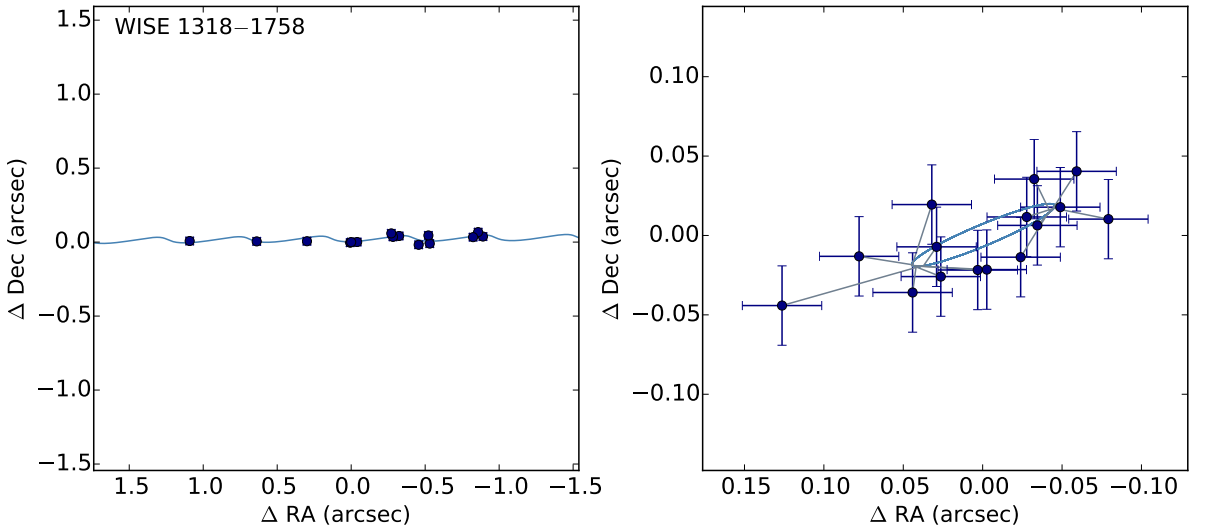

Figure 3.18: Astrometric fit for WISE 1318−1758. See Figure 3.5 for more details.

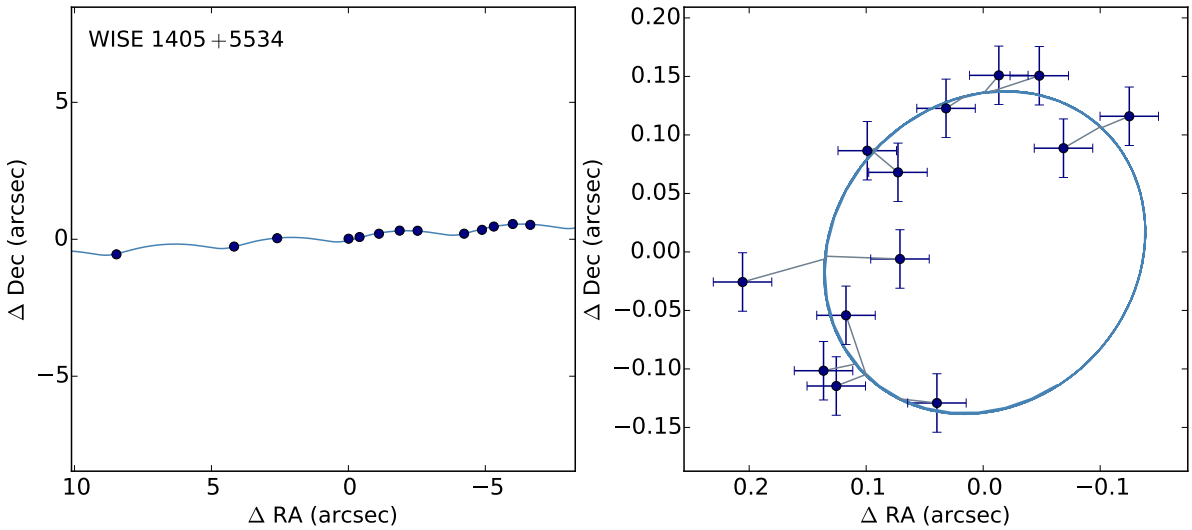

Figure 3.19: Astrometric fit for WISE 1405+5534. See Figure 3.5 for more details.

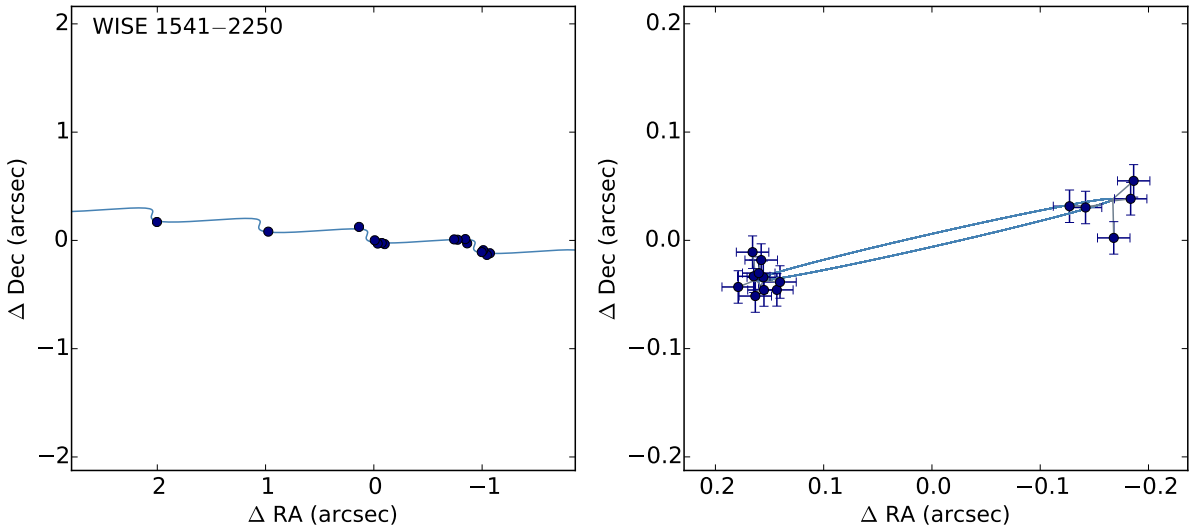

Figure 3.20: Astrometric fit for WISE 1541−2250. See Figure 3.5 for more details.

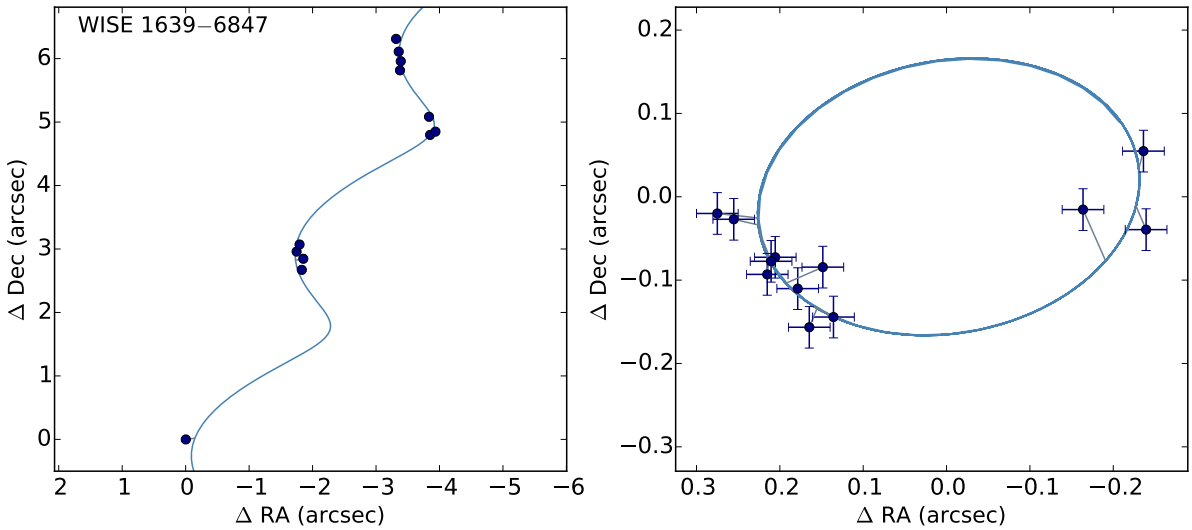

Figure 3.21: Astrometric fit for WISE 1639−6847. See Figure 3.5 for more details.

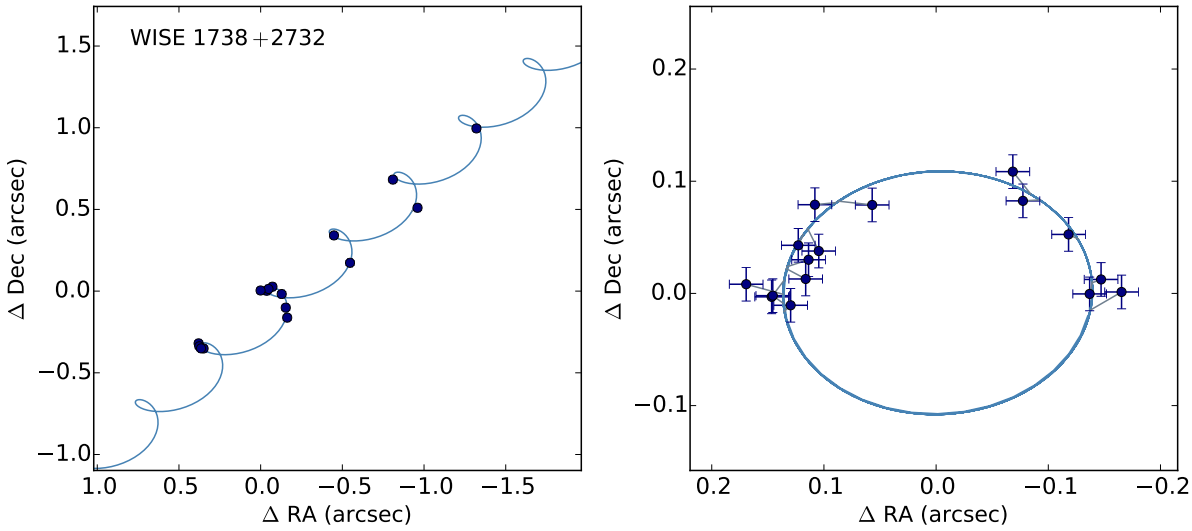

Figure 3.22: Astrometric fit for WISE 1738+2732. See Figure 3.5 for more details.

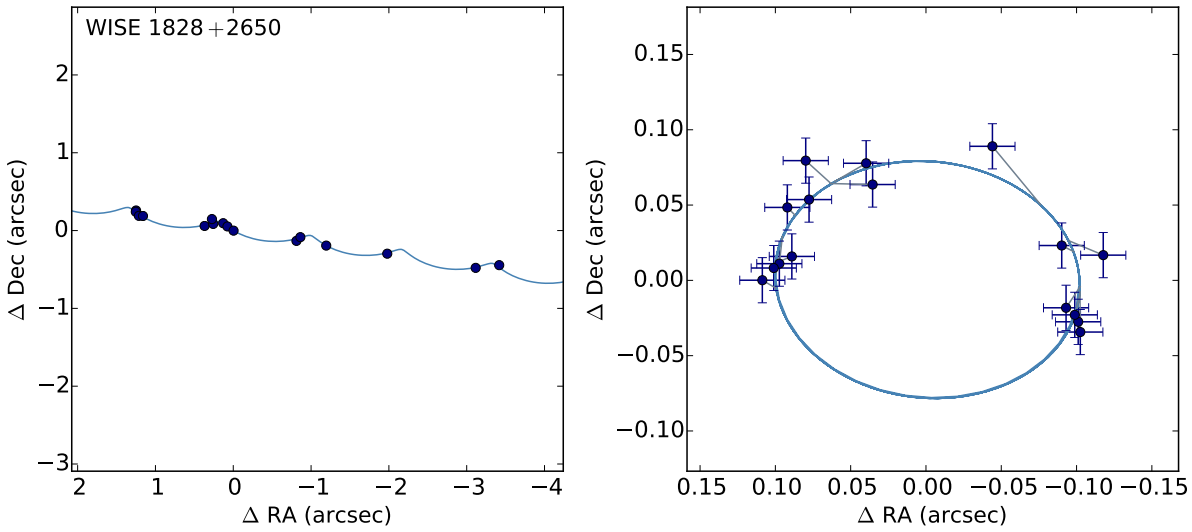

Figure 3.23: Astrometric fit for WISE 1828+2650. See Figure 3.5 for more details.

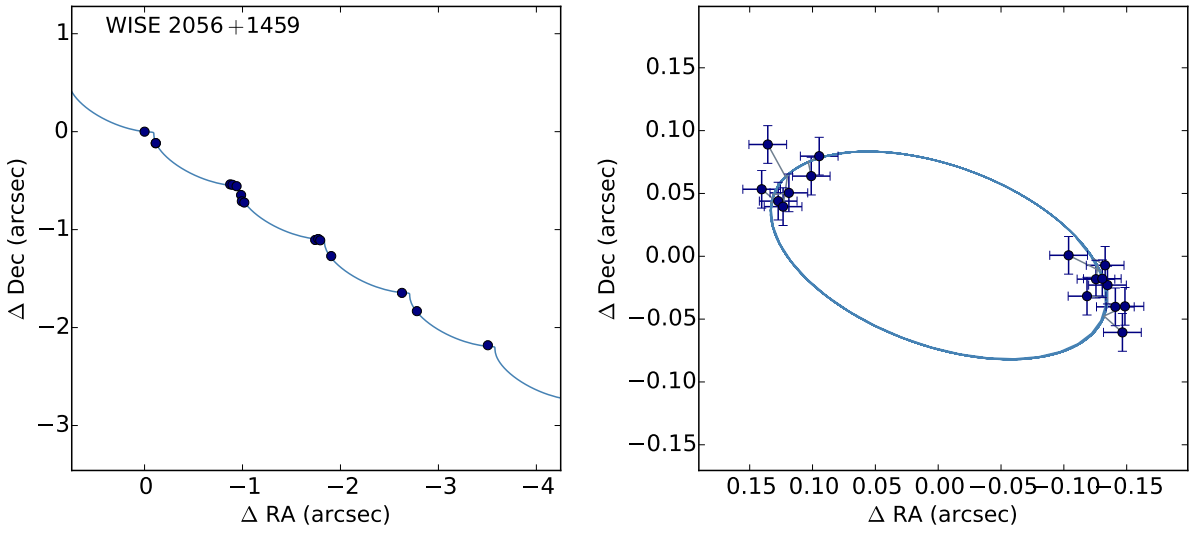

Figure 3.24: Astrometric fit for WISE 2056+1459. See Figure 3.5 for more details.

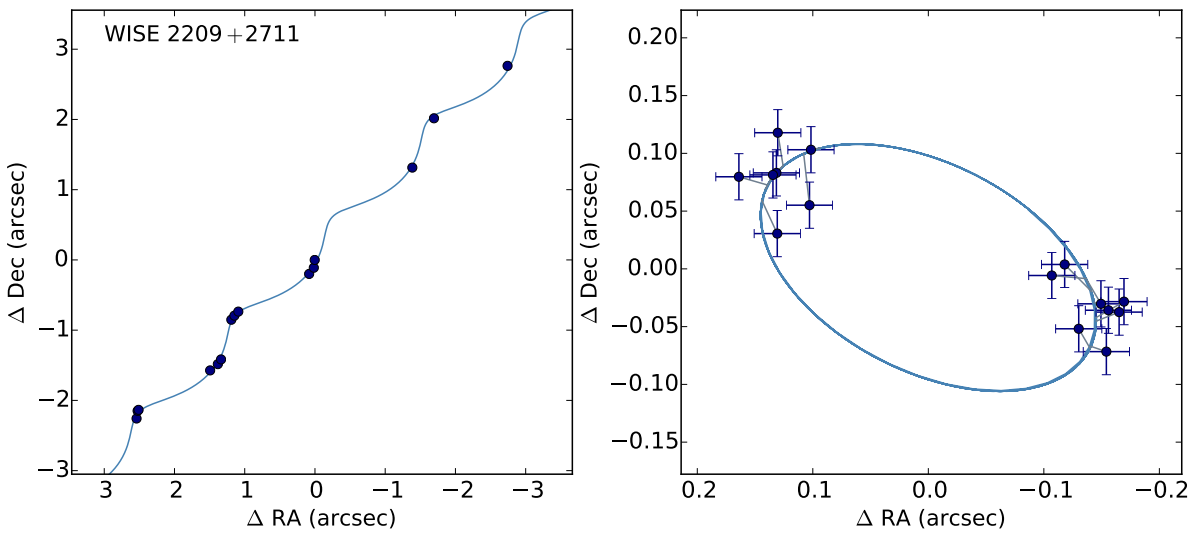

Figure 3.25: Astrometric fit for WISE 2209+2711. See Figure 3.5 for more details.

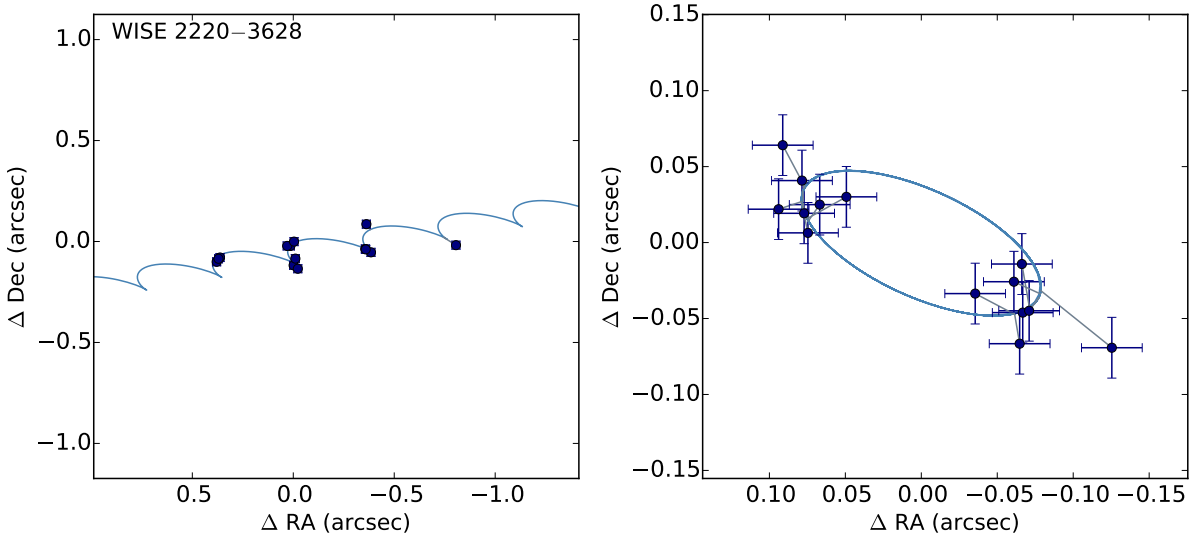

Figure 3.26: Astrometric fit for WISE 2220−3628. See Figure 3.5 for more details.

3.6 Results

3.6.1 Spectrophotometric and Photometric Distances for New Discoveries

In § 3.6.4 we determine photometric distance relationships based on linear fits to M_J vs. $J-W2$ and M_H vs. $H-W2$. These fits are valid for objects with $J-W2$ colors ranging from 2–9 and $H-W2$ from 3–9. Below, we use this photometric distance relationship to estimate distances to the new $\geq$ T8 objects presented here. For objects $<$ T8, we use the spectrophotometric distance relations from Filippazzo et al. (2015).

WISE 0550−1950: We do not have an adequate baseline to measure the parallax of this new T6.5 dwarf, but using the spectrophotometric distance estimates from Filippazzo et al. (2015), we estimate a distance of 32.9 pc to this object.

WISE 0615+1526: We estimate a photometric distance of 22.3 pc for this object.

WISE 0642+0423: We estimate its photometric distance to be 29.6 pc.

WISE 1220+5407 Our photometric distance estimate puts it at 22.5 pc.

WISE 2203+4619 is estimated to be 18.9 pc away, based on our photometric distance relationships in § 3.6.4.

3.6.2 Comparison to Literature

In Table 3.5 and Figure 3.27 we compare our results to previously published astrometric fits all of our targets with previous parallax measurements. We find that our results are mostly consistent with previously published values in the literature, with a few notable exceptions. For WISE 2220−3628, our results are consistent with Tinney et al. (2014), but significantly discrepant from Beichman et al. (2014). Upon further review of the Beichman et al. (2014) dataset, we noticed that their measurements only cover one side of the parallactic ellipse, leaving the other side unconstrained and biasing the measurement. This is likely the cause of their discrepant fit.

We also measure significant offsets in parallax values from Dupuy & Kraus (2013). We

find systematically larger parallax values (closer distances) than they do for 5 out of the 6 targets we have in common. Each object has at least one other measurement in the literature and we find that we are consistently in agreement with the other reference. Tinney et al. (2014) and Smart et al. (2017) also note systematic offsets between their parallax measurements and those of Dupuy & Kraus (2013), concluding that these are likely due to the smaller number of measurements and thus a degeneracy between the parallax and proper motion parameters. For the extreme case of 1541−2250 (not plotted in comparison figures), we note, as did Beichman et al. (2014) and Tinney et al. (2014) that this object has several epochs skewed by a blend with a background star that throw off the fit in the [3.6] data, which explains the > 3-σ difference between the Dupuy & Kraus (2013) results and others in the literature.

We explored several hypotheses to explain the discrepancies between the Dupuy & Kraus (2013) measurements and those presented here. Similar to our parallax measurements, Dupuy & Kraus (2013) uses the IRAC instrument on *Spitzer* to measure the positions of each target. However, they observed in [3.6], whereas the measurements presented here were made using [4.5] data.

Our first hypothesis is that the use of [3.6] data causes a chromatic distortion on the image plane that is different for the target than the background stars, and which would cause a systematic offset in the positions of the targets in the Dupuy & Kraus (2013) dataset. The IRAC instrument design utilizes beam splitters in each of its two fields of view to refract shorter wavelength light ([3.6] and [4.5]) to separate focal planes from the longer wavelength light (ch3 and ch4). Both [3.6] and [4.5] have similar background characteristics during the warm mission (Carey et al. 2010). The brown dwarf targets are significantly fainter in [3.6] compared to [4.5], requiring longer integration times (thus providing more background stars in each field). Late-T and Y dwarfs exhibit extreme methane absorption near the methane fundamental bandhead at 3.3 μm, which produces a dramatic upward slope in the spectral energy distribution within the [3.6] bandpass. Thus the targets have significantly redder effective central wavelengths compared to the relatively flat spectral energy distributions of the background stars. This reddening effect in [3.6] would lead to

a slightly different average angle of refraction, compared to the background stars' average angles of refraction. The target spectral energy distributions in the [4.5] bandpass peak much closer to the center of the bandpass and should not have significantly different effective wavelengths from the background stars, so they should be immune to this effect. We thus expect that this effect would be evident by comparing the offset parallax measurement to the [3.6]–[4.5] color (Figure 3.29). We see a slight correlation between [3.6]−[4.5] color and parallax offset, but there is not enough data to draw a firm conclusion.

Our second hypothesis is that there is a fundamental difference between our fitting analysis and that of Dupuy & Kraus (2013). In Section 2.4 of Dupuy & Liu (2012), they describe their methodology for determining astrometric fits: "We fitted three parameters to the combined (α, δ) data: proper motion in right ascension (μ_α), proper motion in declination (μ_δ), and parallax (π). This is notably different from one standard approach taken in the literature of fitting two separate values of the parallax in α and δ (...) MPFIT minimized the residuals in (α, δ) after subtracting the relative parallax and proper motion offsets (three parameters) and the mean (α, δ) position (effectively removing 2 additional degrees of freedom)."

We interpret this to meant that the subtraction of the average (α, δ) position requires the parallax solution to fit through one point located at the center of the parallactic ellipse. The effect would be averaged out over long time baselines, but we believe this method to be ineffectual for limited epochs. The sense of the bias that we see is in the expected direction; that is, their ellipse fits are artificially smaller because of their choice of data analysis method.

Table 3.5. Comparison to Published Parallaxes and Proper Motions

Object (1)	Measurement (2)	This paper (3)	Smart et al. (2017) (4)	Beichman et al. (2014) (5)	Tinney et al. (2014) (6)	Dupuy & Kraus (2013) (7)	Leggett et al. (2017)[a] (8)
	$\pi_{\rm trig}$ (mas)	45.6±5.7	···	94±14	···	···	54±5
WISE 0146+4234	μ_α (mas/yr)	−450.67±6.3	···	−441±13	···	···	−455±4
	μ_δ (mas/yr)	−27.9±6.3	···	−26±16	···	···	−24±4
	$\pi_{\rm trig}$ (mas)	168.8±8.5	···	···	···	···	184±10
WISE 0350−5658	μ_α (mas/yr)	−206.9±6.5	···	···	···	···	−206±7
	μ_δ (mas/yr)	−577.7±6.7	···	···	···	···	−578±8
	$\pi_{\rm trig}$ (mas)	75.4±6.62	···	···	63.2±6.0	···	···
WISE 0359−5401	μ_α (mas/yr)	−152.7±4.8	···	···	−176.0±10.8	···	···
	μ_δ (mas/yr)	−783.7±4.9	···	···	−744.5±11.9	···	···
	$\pi_{\rm trig}$ (mas)	153.4±4.0	144.3±9.9	160±9	···	132±15	···
WISE 0410+1502	μ_α (mas/yr)	959.9±3.6	956.8±5.6	966±13	···	958±37	···
	μ_δ (mas/yr)	−2218.6±3.5	−2221.2±5.5	−2218±13	···	−2229±29	···
	$\pi_{\rm trig}$ (mas)	79.5±8.8	···	···	74±14	···	70±5
WISE 0535−7500	μ_α (mas/yr)	−113.2±7.7	···	···	−113.4±15.4	···	−127±4
	μ_δ (mas/yr)	23.7±7.5	···	···	36.2±8.8	···	13±4
	$\pi_{\rm trig}$ (mas)	83.7±5.7	···	···	93±13	···	···
WISE 0647−6232	μ_α (mas/yr)	1.0±5.1	···	···	0.6±16.1	···	···
	μ_δ (mas/yr)	391.0±4.6	···	···	368.0±18.0	···	···
	$\pi_{\rm trig}$ (mas)	100.7±4.7	···	106±13	08.7±4.0	···	···
WISE 0713−2917	μ_α (mas/yr)	341.1±6.6	···	388±20	350.1±4.8	···	···
	μ_δ (mas/yr)	−411.1±6.0	···	−419±22	−411.4±5.6	···	···
	$\pi_{\rm trig}$ (mas)	67.6±8.7	···	···	73.7±6.6	···	···
WISE 0734−7157	μ_α (mas/yr)	−566.2±8.8	···	···	−565.8±7.7	···	···
	μ_δ (mas/yr)	−77.5±8.8	···	···	−81.5±8.0	···	···

Table 3.5 (cont'd)

Object (1)	Measurement (2)	This paper (3)	Smart et al. (2017) (4)	Beichman et al. (2014) (5)	Tinney et al. (2014) (6)	Dupuy & Kraus (2013) (7)	Leggett et al. (2017)[a] (8)
	$\pi_{\rm trig}$ (mas)	139.0±4.3	···	···	···	···	158±7
WISE 0825+2805	μ_α (mas/yr)	−64.4±5.6	···	···	···	···	−66±8
	μ_δ (mas/yr)	−234.7±5.4	···	···	···	···	−247±10
	$\pi_{\rm trig}$ (mas)	85.1±9.3	···	···	···	···	85±7
WISE 1206+8401	μ_α (mas/yr)	−557.7±6.5	···	···	···	···	−585±4
	μ_δ (mas/yr)	−241.3±6.5	···	···	···	···	−253±5
	$\pi_{\rm trig}$ (mas)	144.3±8.6	···	···	···	129±19	155±6
WISE 1405+5534	μ_α (mas/yr)	−2336.0±6.9	···	···	···	−2263±47	−2334±5
	μ_δ (mas/yr)	238.0±7.40	···	···	···	288±41	232±5
	$\pi_{\rm trig}$ (mas)	167.1±4.2	···	176±9	175.1±4.4	74±31	···
WISE 1541−2250	μ_α (mas/yr)	−895.0±4.7	···	−857±12	−894.7±4.2	−870±130	···
	μ_δ (mas/yr)	−94.7±4.7	···	−87±13	−87.7±4.7	−13±58	···
	$\pi_{\rm trig}$ (mas)	228.1±8.9	···	···	202.3±3.1	···	···
WISE 1639−6847	μ_α (mas/yr)	579.1±12.5	···	···	586.0±5.5	···	···
	μ_δ (mas/yr)	−3104.5±12.2	···	···	−3101.1±3.6	···	···
	$\pi_{\rm trig}$ (mas)	136.3±4.3	128.5±6.3	128±10	···	102±18	···
WISE 1738+2732	μ_α (mas/yr)	343.3±3.5	345.0±5.7	317±9	···	292±63	···
	μ_δ (mas/yr)	−340.6±3.4	−340.1±5.1	−321±11	···	−396±22	···
	$\pi_{\rm trig}$ (mas)	100.2±4.2	···	106±7	···	70±14	···
WISE 1828+2650	μ_α (mas/yr)	1021.0±3.2	···	1024±7	···	1020±15	···
	μ_δ (mas/yr)	175.6±3.1	···	···	···	173±16	···
	$\pi_{\rm trig}$ (mas)	138.3±3.9	148.9±8.2	140±9	···	144±23	···
WISE 2056+1459	μ_α (mas/yr)	823.0±3.3	826.4±5.5	812±9	···	761±46	···
	μ_δ (mas/yr)	535.7±3.4	530.7±8.5	34±8	···	500±21	···

Table 3.5 (cont'd)

Object (1)	Measurement (2)	This paper (3)	Smart et al. (2017) (4)	Beichman et al. (2014) (5)	Tinney et al. (2014) (6)	Dupuy & Kraus (2013) (7)	Leggett et al. (2017)[a] (8)
WISE 2209+2711	$\pi_{\rm trig}$ (mas)	154.4±5.7	···	147±11	···	···	···
	μ_α (mas/yr)	1199.6±4.9	···	c1217±13	···	···	···
	μ_δ (mas/yr)	−1359.0±4.8	···	−1372±15	···	···	···
WISE 2220−3628	$\pi_{\rm trig}$ (mas)	84.1±5.9	···	136±17	87.2±3.7	···	···
	μ_α (mas/yr)	292.9±7.4	···	283±13	282.7±5.0	···	···
	μ_δ (mas/yr)	−61.5±7.0	···	−97±17	−94.0±3.0	···	···

[a]The data presented in Leggett et al. (2017) include astrometric data first published in Luhman & Esplin (2016).

To test this, we performed a reduction of the same [3.6] data used in their paper but employing our methodology described above. In this case, we used the [3.6] PRF appropriate for Warm *Spitzer* data. The resulting astrometric fits are compared to our [4.5] parallax measurements in Figure 3.30. In Figure 3.30, the original measurements from Dupuy & Kraus (2013) are shown in yellow, and the re-calculation using our fitting analysis and the Dupuy & Kraus (2013) data are in blue. In most cases, our calculations measure parallax solutions that are closer to those measured with our [4.5] data, though consistent with the original Dupuy & Kraus (2013) values within the uncertainties.

Our third hypothesis to explain the discrepant measurements is that the shorter time baseline of the Dupuy & Kraus (2013) dataset made it difficult to disentangle the effects of proper motion when calculating the parallax. We explored this effect by reducing later epochs of [3.6] data, available on the *Spitzer* archive. The addition of 9–10 epochs for each target cannot fully account for the earlier difference seen between the [3.6] and [4.5] parallax measurements. These differences are plotted in Figure 3.30 in red. All targets except for 0410+1502 show an improved comparison, though the systematic offset remains.

We believe that some combination of the three effects contributed to the systematically offset parallaxes published in Dupuy & Kraus (2013). After re-reducing the Dupuy & Kraus (2013) data and adding additional epochs, we were unable to fully account for the discrepancy, but the offset as a function of color also appears to only have a slight trend.

3.6.3 Comparison to Leggett et al. 2017

Leggett et al. (2017) and Luhman & Esplin (2016) presented new astrometric measurements from the *Spitzer* [4.5] data in our parallax program. We note a $\sim$ 1- to 2-σ offset that is largely systematic between their measurements and our own. They find larger parallaxes than we do, by $\sim$ 10–20 mas for four out of six objects. It is unclear what is causing the difference between our parallax measurements.

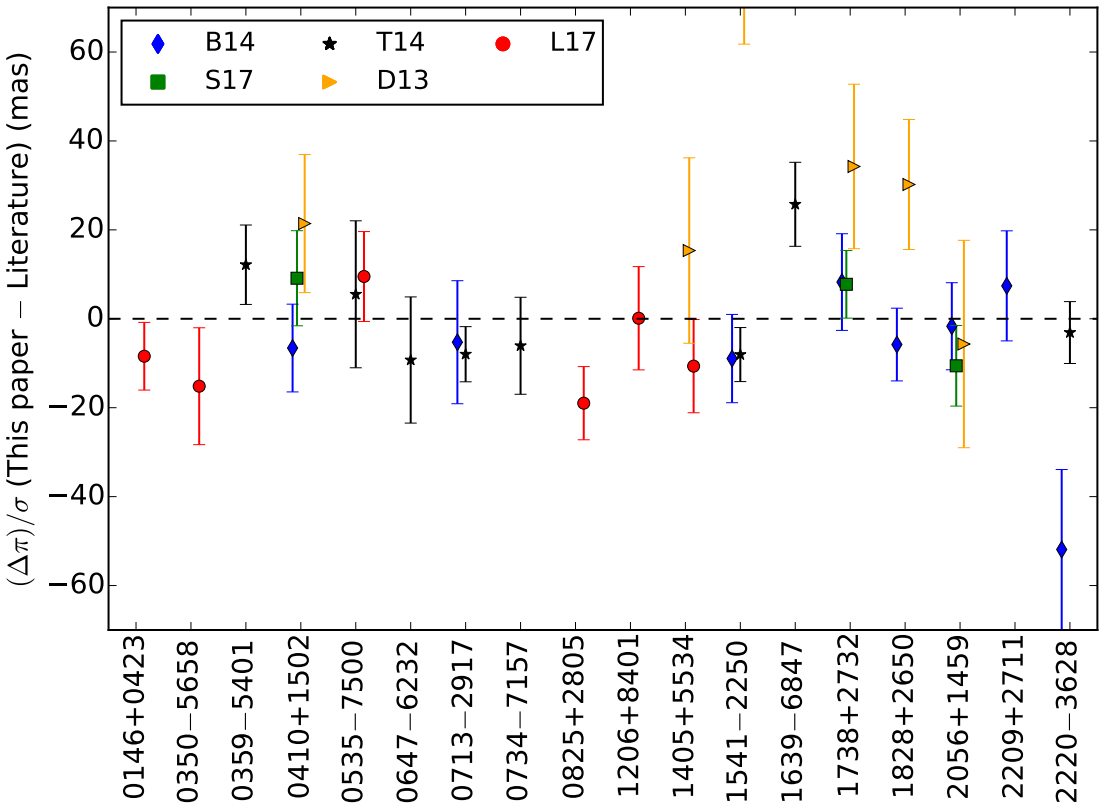

Figure 3.27: Comparison of the difference in parallax values from this paper with the literature, vs. target name. Differences from Beichman et al. (2014) are in blue diamonds, Tinney et al. (2014) in black stars, Leggett et al. (2017) in red circles, Smart et al. (2017) in green squares, and Dupuy & Kraus (2013) in yellow triangles. Note that the Dupuy & Kraus (2013) value for 1541 is off the chart, their parallax being miscalculated due to a blend with a background star in their dataset.

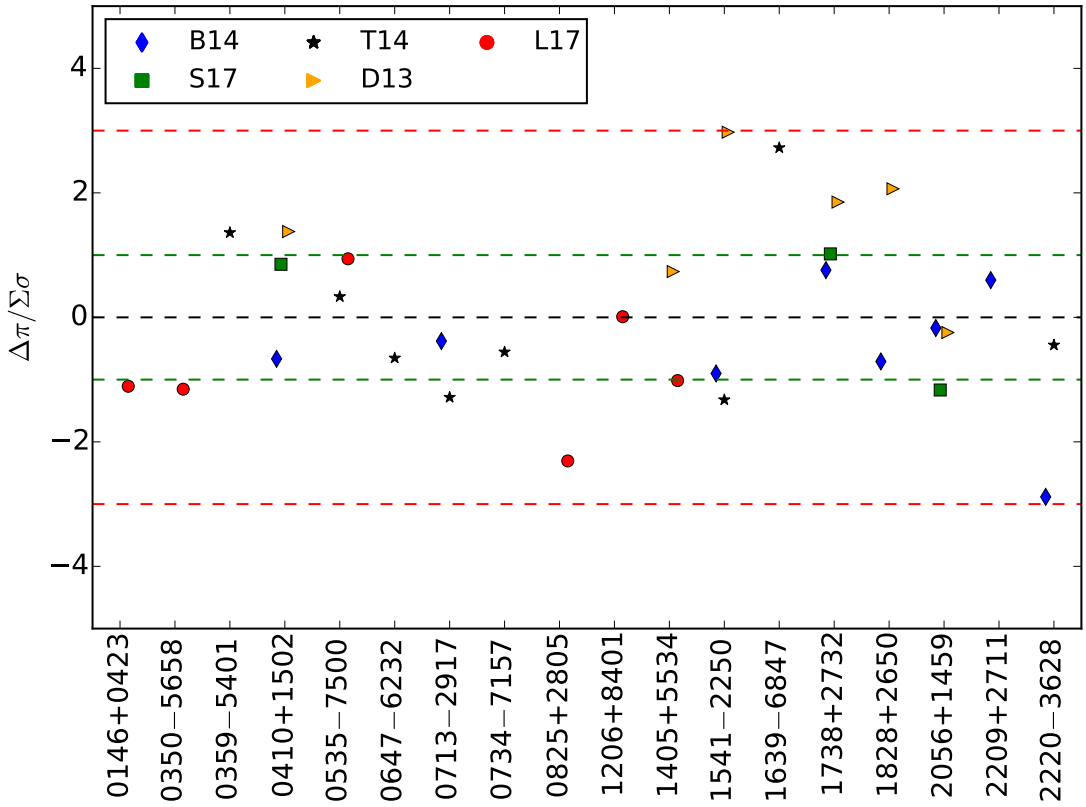

Figure 3.28: Fractional σ difference between this paper and the literature. Dashed green lines denote 1σ offsets and dashed red lines denote 3σ offsets. With a few exceptions, our measured parallaxes are consistent within 1σ to previously published values.

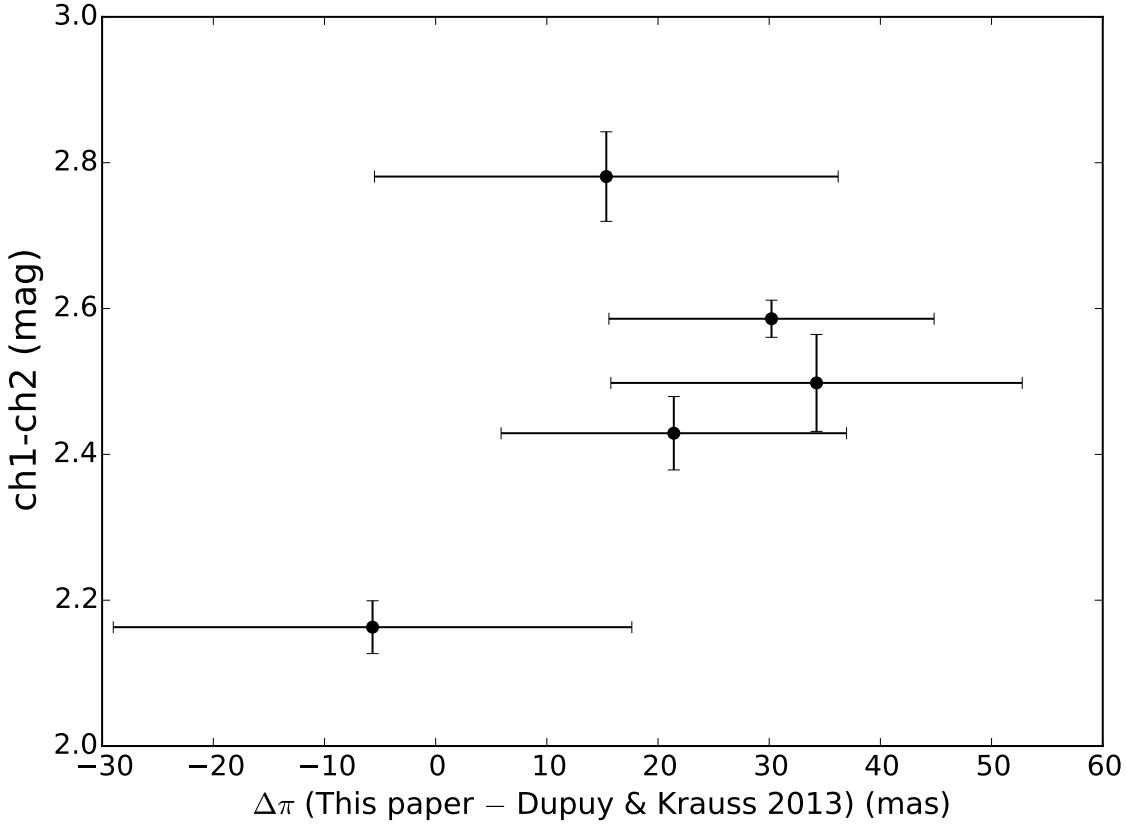

Figure 3.29: Comparison of parallax offset between our values and those of Dupuy & Kraus (2013) vs. [3.6]−[4.5] color. If the extremely red-sloped [3.6] bandpass were responsible for the offset, we would expect to see an increasing trend in offset vs. [3.6]−[4.5] color. A slight correlation is seen, though there is not enough data to draw a firm conclusion.

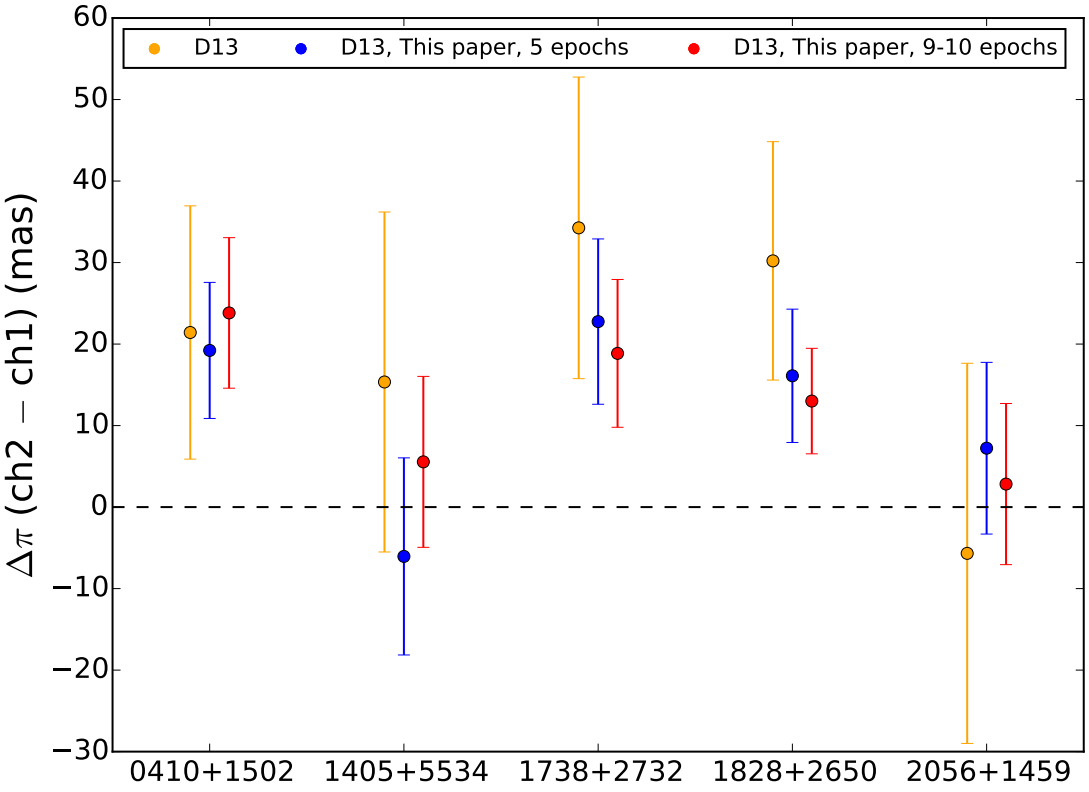

Figure 3.30: Comparison of parallaxes measured with [4.5] and [3.6], for targets overlapping the Dupuy & Kraus (2013) dataset. Parallax difference (mas) is plotted for each overlapping target. Data points have been offset to better show uncertainties. Yellow points are the original measurements from Dupuy & Kraus (2013). Blue points were measured by re-reducing the Dupuy & Kraus (2013) data and using our own fitting analysis. Red points were measured similarly to the blue points, with 9-10 additional epochs of [3.6] data included from the *Spitzer* archive. 1541 is not shown here, due to the blending with a background star and inability to determine a reasonable astrometric solution.

3.6.4 Color Magnitude Diagrams

We list the absolute magnitudes for all objects in J_{MKO}, H_{MKO}, [3.6], [4.5], $W1$, and $W2$, when available, in Table 3.6. In Figure 3.31, we plot four different color-magnitude diagrams (CMD)s, showing M_J vs. $J-W2$, M_H vs. $H-W2$, M_{W2} vs. $J-W2$, and $M_{[4.5]}$ vs. [3.6]−[4.5]. Data from this paper are plotted as filled circles and data from the literature are open symbols (Tinney et al. 2014: circles; Dupuy & Kraus 2013: diamonds). Every object is colored according to its spectral type, as shown in the legend. The CMDs show a tight trend, particularly in M_J vs. $J-W2$ and M_H vs. $H-W2$, in which the trends previously seen for earlier spectral types are continued, showing decreasing absolute magnitudes in the near-infrared as $J-W2$ colors redden.

We determined a weighted linear fit to both M_J vs. $J-W2$ and M_H vs. $H-W2$ and tabulate the coefficients in Table 3.7. Although these relations require two photometric observations to obtain a photometric distance estimate, we find that this relationship is much tighter than if we were to determine fits to the absolute magnitude vs. Spectral Type.

M_{W2} vs. $J-W2$ shows more scatter than the near-infrared color magnitude diagrams. Interestingly, M_{W2} vs. $J-W2$ appears to plateau in M_{W2} across the T/Y transition. It is unclear if this feature is real, or due to a bias (systematic or otherwise).

The $M_{[4.5]}$ vs. [3.6]−[4.5] plot shows significantly more cosmic scatter than the other panels in Figure 3.31. This is likely due to [3.6] being a non-ideal band for observing objects with significant CH_4 absorption. The blue tail of the 4.5 μm bandpass falls into the [3.6] filter transmission, giving late-T and Y an overall very red slope in [3.6]. It's possible that variations in gravity and/or metallicity cause this slope to shift, producing the observed scatter. It is likely that the $W2$ vs. $W1-W2$ CMD would show a much tighter correlation, because the $W1$ and $W2$ bandpasses were designed specifically for cold brown dwarfs; however, many targets only have limits on their $W1$ magnitudes.

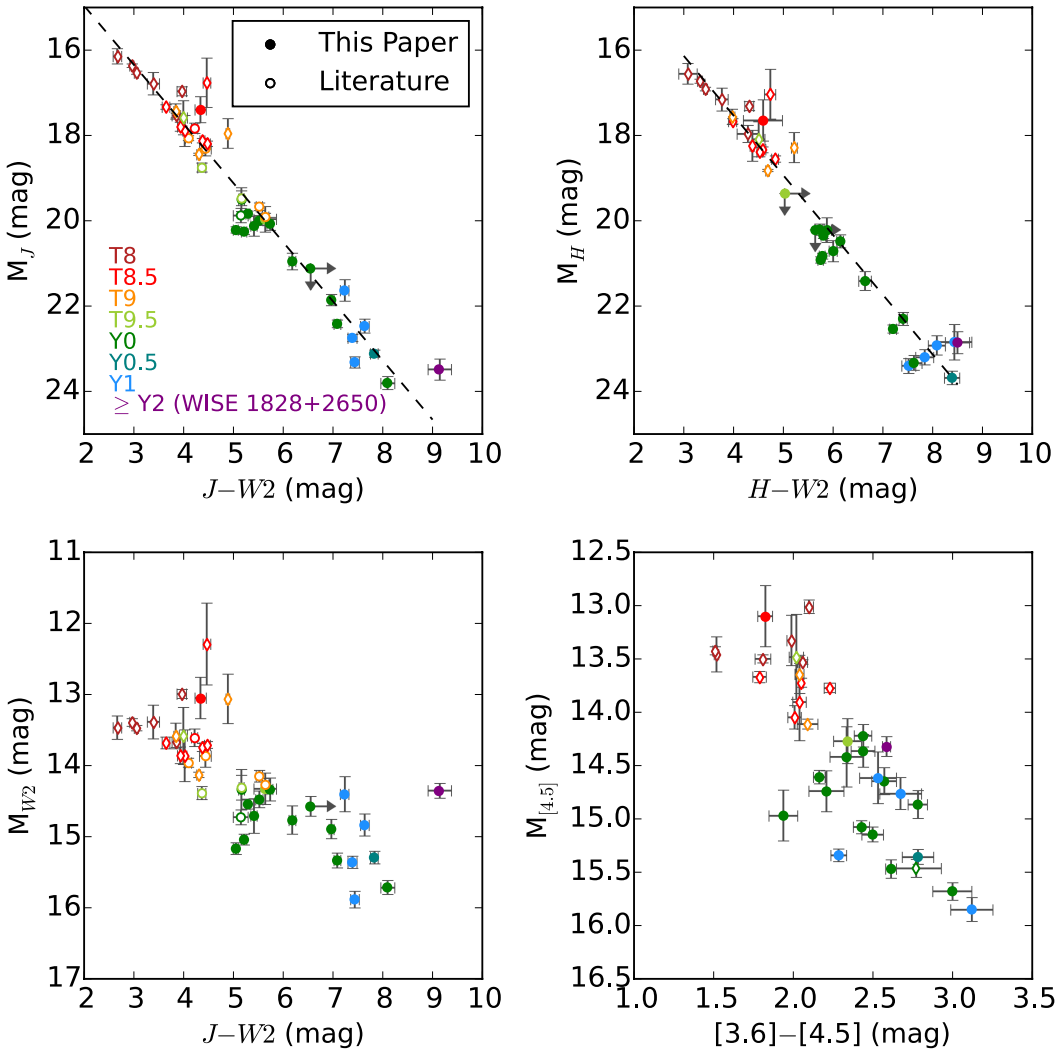

Figure 3.31: Color Magnitude diagrams for M_J vs. $J-W2$, M_H vs. $H-W2$, M_{W2} vs. $J-W2$, and $M_{[4.5]}$ vs. [3.6]-[4.5]. Open circles are from Tinney et al. (2014) and open diamonds are from Dupuy & Kraus (2013). Filled circles are from this paper. Objects are shaded according to the spectral types listed in the legend. Weighted linear fits to M_J vs. $J-W2$ and M_H vs. $H-W2$ are plotted in dashed black lines.

3.6.5 Absolute Magnitude vs SpT

Studying the relationship of the absolute magnitude emitted at each bandpass as a function of spectral type provides us with insight on the evolution of the brown dwarf spectral energy distribution as it cools over time. Earlier-type brown dwarfs tend to follow a narrow trend in absolute magnitude, with flux decreasing in each of the bands monotonically as a function of spectral type. Because spectral typing historically sorts objects by effective temperatures, we expected the Y dwarf sample to continue this trend. However, instead of a tight correlation between spectral type and absolute magnitude, we see a large amount of scatter, spanning as much as ~ 5 magnitudes within the Y0 spectral class alone. Figure 3.32 shows absolute magnitude in various near and mid-infrared bands as a function of spectral type, for this sample as well as other values taken from the literature.

Such a large spread in absolute properties cannot be explained by typical levels of variability (Cushing et al. 2016; Leggett et al. 2016) and must be indicative of a different physical mechanism. In Figure 3.32, each of the objects is colored according to $J - W2$ color cutoffs, as detailed in the legend. Here, we are using $J - W2$ as a proxy for temperature, based on Figure 18 from Schneider et al. (2015), which in turn utilizes the atmospheric models of Saumon et al. (2012), Morley et al. (2012), and Morley et al. (2014). Regardless of the type of clouds used in the atmospheric models, they all show a monotonic reddening of $J-W2$ as temperature decreases. When we separate objects by their $J-W2$ color, new trends appear in Figure 3.32. In particular, the Y0 dwarfs appear to cover a very broad range in effective temperatures, likely accounting for the ~ 5 orders of absolute magnitudes observed in the J band.

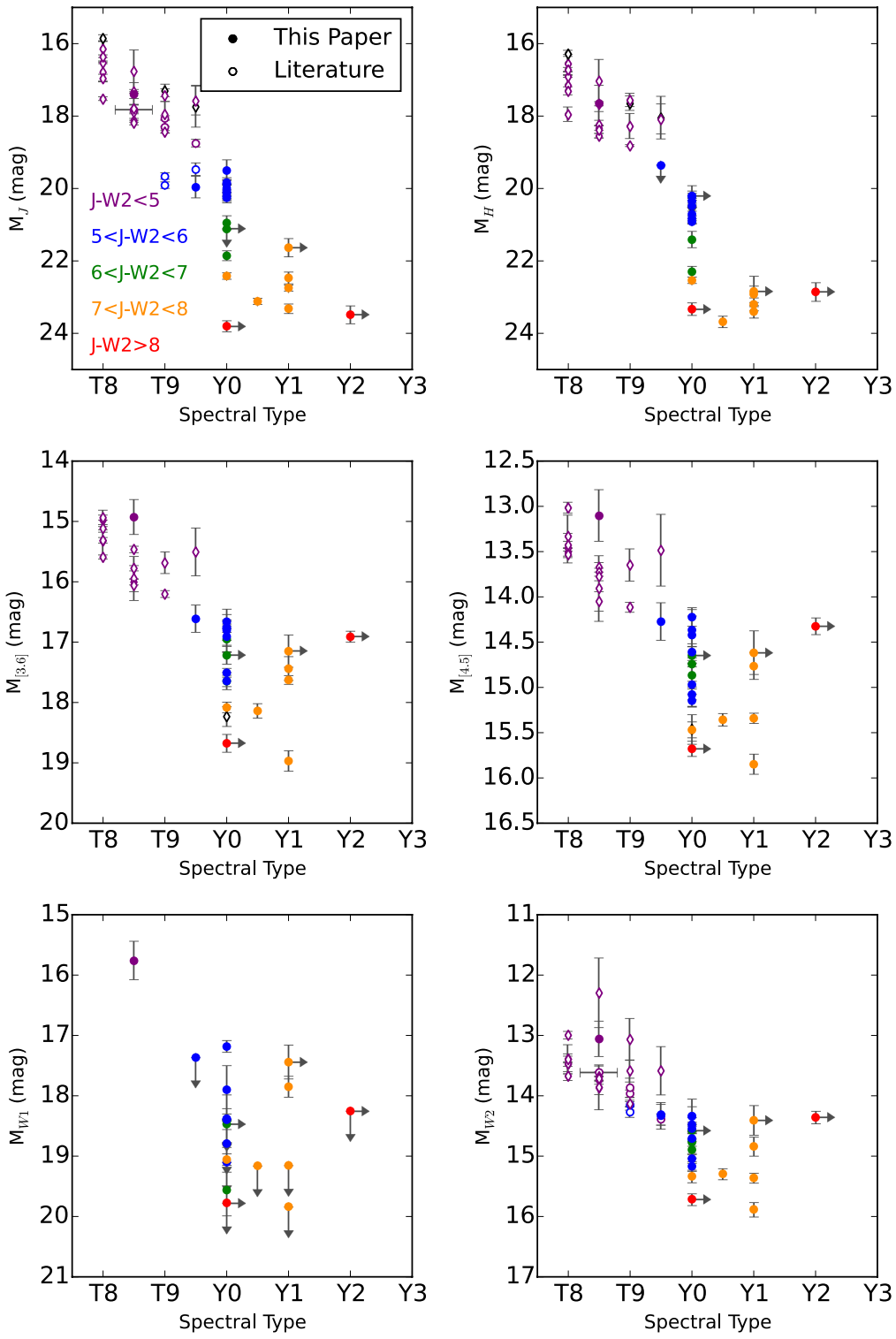

Figure 3.32: Absolute magnitude vs. Spectral Type. Open circles are from Tinney et al. (2014) and open diamonds are from Dupuy & Kraus (2013). Shaded objects are from this paper. Objects are shaded according to J-W2 color, as shown in the legend.

Table 3.6. Absolute Magnitudes

Object Name (1)	$\pi_{\rm trig}$ (mas) (2)	Distance (pc) (3)	M_J (mag) (4)	M_H (mag) (5)	$M_{[3.6]}$ (mag) (6)	$M_{[4.5]}$ (mag) (7)	M_{W1} (mag) (8)	M_{W2} (mag) (9)
WISE 0146+4234	45.575 ± 5.74	$21.94^{+3.16}_{-2.45}$	17.69 ± 0.37	17.00 ± 0.36	15.65 ± 0.29	13.36 ± 0.27	>17.43	13.38 ± 0.28
WISE 0336−0143	100.90±5.86	$9.91^{+0.61}_{-0.54}$	>21.12	>20.22	17.22 ±0.15	14.65 ± 0.13	18.47 ± 0.49	14.58 ± 0.14
WISE 0350−5658	168.84 ± 8.53	$5.92^{+0.32}_{-0.28}$	23.32 ± 0.13	23.40 ± 0.17	18.97 ± 0.17	15.85 ± 0.11	> 19.84	15.88 ± 0.12
WISE 0359−5401	75.36 ± 6.62	$13.27^{+1.28}_{-1.07}$	20.95 ± 0.20	21.41 ± 0.22	16.95 ± 0.22	14.74 ± 0.19	> 18.42	14.77 ± 0.20
WISE 0410+1502	153.42 ± 4.05	$6.52^{+0.18}_{-0.17}$	20.25 ± 0.06	20.83 ± 0.07	17.51 ± 0.07	15.08 ± 0.06	> 19.10	15.04 ± 0.07
WISE 0535−7500	79.51 ± 8.79	$12.58^{+1.56}_{-1.25}$	21.63 ± 0.25	22.84 ± 0.42	17.15 ± 0.26	14.62 ± 0.24	17.44 ± 0.28	14.41 ± 0.24
WISE 0647−6232	83.73 ± 5.68	$11.94^{+0.87}_{-0.76}$	22.47 ± 0.16	22.92 ± 0.22	17.44 ± 0.20	14.77 ± 0.15	> 19.15	14.84 ± 0.16
WISE 0713−2917	100.73 ± 4.74	$9.93^{+0.49}_{-0.45}$	20.00 ± 0.11	20.21 ± 0.13	16.66 ± 0.11	14.22 ± 0.10	> 18.79	14.48 ± 0.11
WISE 0734−7157	67.63 ± 8.68	$14.79^{+2.18}_{-1.68}$	19.50 ± 0.28	20.22 ± 0.29	16.76 ± 0.30	14.42 ± 0.28	17.90 ± 0.40	14.34 ± 0.28
WISE 0825+2805	139.02 ± 4.33	$7.19^{+0.23}_{-0.22}$	23.12 ± 0.08	23.68 ± 0.15	18.14 ± 0.12	15.36 ± 0.07	> 19.16	15.29 ± 0.09
WISE 1051−2138	49.27 ± 6.47	$20.3^{+3.1}_{-2.4}$	17.40 ± 0.30	17.65 ± 0.48	14.93 ± 0.29	13.10 ± 0.29	15.76 ± 6.84	13.06 ± 0.29
WISE 1055−1652	71.21 ± 6.82	$14.04^{+1.5}_{-1.2}$	19.97 ± 0.30	> 19.36	16.61 ± 0.22	14.27 ± 0.21	> 17.37	14.33 ± 0.22
WISE 1206+8401	85.12 ± 9.27	$11.75^{+1.44}_{-1.15}$	20.12 ± 0.24	20.71 ± 0.24	16.91 ± 0.25	14.97 ± 0.24	> 18.38	14.71 ± 0.24
WISE 1318−1758	48.06 ± 7.33	$20.81^{+3.74}_{-2.75}$	16.84 ± 0.38	16.12 ± 0.40	15.20 ± 0.34	13.12 ± 0.33	15.92 ± 0.37	13.07 ± 0.34
WISE 1405+5534	144.35 ± 8.60	$6.93\ ^{+0.44}_{-0.39}$	21.86 ± 0.13	22.30 ± 0.15	17.65 ± 0.14	14.87 ± 0.13	19.56 ± 0.42	14.89 ± 0.13
WISE 1541−2250	167.05 ± 4.19	$5.99\ ^{+0.154}_{-0.147}$	22.75 ± 0.08	23.20 ± 0.18	17.63 ± 0.07	15.34 ± 0.06	17.85 ± 0.17	15.36 ± 0.08
WISE 1639−6847	228.05 ± 8.93	$4.39^{+0.18}_{-0.17}$	22.42 ± 0.09	22.54 ± 0.09	18.08 ± 0.09	15.47 ± 0.09	19.06 ± 0.21	15.33 ±0.10

Table 3.6 (cont'd)

Object Name (1)	$\pi_{\rm trig}$ (mas) (2)	Distance (pc) (3)	M_J (mag) (4)	M_H (mag) (5)	$M_{[3.6]}$ (mag) (6)	$M_{[4.5]}$ (mag) (7)	M_{W1} (mag) (8)	M_{W2} (mag) (9)
WISE 1738+2732	136.26 ± 4.27	$7.34^{+0.24}_{-0.22}$	20.22 ± 0.07	20.92 ± 0.07	17.64 ± 0.09	15.15 ± 0.07	18.38 ± 0.17	15.17 ± 0.08
WISE 1828+2650	100.21 ± 4.23	$9.98^{+0.44}_{-0.40}$	23.48 ± 0.25	22.85 ± 0.26	16.91 ± 0.09	14.33 ± 0.09	> 18.25	14.36 ± 0.10
WISE 2056+1459	138.32 ± 3.86	$7.23^{+0.21}_{-0.20}$	19.83 ± 0.06	20.35 ± 0.07	16.77 ± 0.07	14.61 ± 0.06	17.18 ± 0.10	14.54 ± 0.07
WISE 2209+2711	154.41 ± 5.67	$6.48^{+0.25}_{-0.23}$	23.80 ± 0.15	23.33 ± 0.17	18.68 ± 0.14	15.68 ± 0.08	> 19.77	15.71 ± 0.10
WISE 2220−3628	84.10 ± 5.90	$11.89^{+0.90}_{-0.78}$	20.07 ± 0.15	20.48 ± 0.16	16.80 ± 0.17	14.37 ± 0.15	> 18.40	14.34 ± 0.16

Table 3.7. Coefficients for linear fits to Color-Magnitude Relations

Color (1)	c0 (2)	c1 (3)	rms (4)
M_J vs. $J-W2$	12.186	1.386	0.475
M_H vs. $H-W2$	11.935	1.401	0.544

Note. — These coefficients fit a line such that $M_X = c0 + c1 \times (M_X - W2)$, where X is the J or H photometry on the MKO system.

3.7 Discussion

3.7.1 Not all Y dwarfs are created equal

Y0 dwarfs span several magnitudes in M_J, and nearly two in $W2$, based on the near-infrared classification of Y0 dwarfs. As previously mentioned, we used $J-W2$ as a proxy for temperature to separate populations in Figure 3.32. The color cuts show that the Y0 class spans $>$ 4 magnitudes in $J-W2$ and also overlaps the $J-W2$ color space occupied by the Y1 and later-typed objects. These findings indicate that the classical near-infrared spectral typing method of sorting M, L, and T dwarfs by their J band spectral morphologies does not efficiently separate Y dwarfs by their respective temperatures. Y dwarfs, with $T_{\rm eff} \lesssim 500$ K, emit only a small fraction of their light in the near-infrared and would be best-characterized based on their mid-infrared spectra. This was noted in the Y dwarf discovery paper, Cushing et al. (2011); however, until the launch of JWST, observers have little hope of obtaining high SNR mid-infrared spectra of Y dwarfs- though some have tried (e.g. Skemer et al. 2016). The peak emission of a $\lesssim$ 500K brown dwarf falls in the ~ 3 – 10 μm range, causing the J band to lie on the Wien tail of the blackbody spectrum. Considering the above, we recommend that mid-infrared spectra (i.e. from JWST) be used to more fully-characterize the physical properties of these extremely cold objects. Below we examine some of the more interesting targets in our sample.

3.7.1.1 Notes on specific Y0 dwarfs

WISE 0146+4234 AB This object has discrepant near-infrared photometry in the literature due to its blended binary nature. For this reason, we have excluded it from our color-cuts and plot it in gray in Figures 3.31 and 3.32.

WISE 0336−0143 exhibits absolute magnitude and colors much more similar to Y dwarfs, than late-T dwarfs, as seen in Figures 3.31 and 3.32. We currently only have a limit on its near-infrared magnitudes, but our photometry agree with the later epoch of spectroscopy that this object is indeed a Y dwarf.

WISE 0734−7157 This particular dwarf is likely one of the warmest Y0's, based on its color and M_J. The best-fit temperature from Schneider et al. (2015) is 450 K, and Leggett et al. (2017) estimate its $T_{\rm eff}$ to be 435–465 K.

WISE 1639−6847 is the second coldest Y0, based on $J-W2$ color. It's location in color-magnitude space is much more similar to the Y1 objects. Leggett et al. (2017) estimate its $T_{\rm eff} \sim$ 360–390 K, coinciding with our findings.

WISE 2209+2711 This is the faintest Y0 dwarf in every absolute magnitude band we measure. It is also the reddest in Y0 in $J-$W2. From Schneider et al. (2015), the best fit model gives $T_{\rm eff}$=500–550K, $\log g$=4–4.5, 0.2–1.5 Gyr old. Leggett et al. (2017) estimate $T_{\rm eff}$=310–340 K, which agrees better with our estimates that this object is colder than most Y0's. Even if we re-classify this as a Y1, this would still be the faintest and reddest Y1. This object is also the reddest Y0 in $J-H$ and $H-W2$. It's mildly blue but not unusual in $Y-J$ (Schneider et al., 2015). If we use the $J-W2$ vs. Temperature plot from Schneider et al. (2015) to determine an effective temperature, this object should be only ∼300K. At such cold temperatures, the near-infrared flux is solely coming from the Wien tail. Our observations are thus not able to fully sample the peak of the Planck function, and thus a small shift in $T_{\rm eff}$ can cause a significant change in absolute magnitudes and colors. This particular target would be excellent for follow-up with JWST spectroscopy and imaging.

3.7.1.2 Y0.5

WISE 0825+2805 This target is the third-reddest object in this sample in $J-$W2 after WISE 1828+2650 and WISE 2209+2711, likely indicating its extremely cold nature.

3.7.1.3 ≥Y1 dwarfs

WISE 0350−5658 is the reddest in [3.6]−[4.5] in this sample, also the faintest in $M_{[3.6]}$ and $M_{[4.5]}$, and the faintest Y1 in M_J. It is likely extremely cold, probably matching the predicted $\sim$ 300 K from Schneider et al. (2015) and the 310–340 K from Leggett et al. (2017).

WISE 0535−7500 is the brightest Y1-classified object and yet it was classified as $\geq$ Y1 in Kirkpatrick et al. (2012). WISE 0535 is located on the outskirts of the Large Magellanic Cloud and is in a highly crowded field that partially contaminated the *HST* spectrum. This object would also benefit from follow-up observations in the mid-infrared.

WISE 1828+2650 is a known outlier that has thus far evaded a satisfactory explanation. Leggett et al. (2017) propose that the peculiar near- and mid-infrared colors could be due to an unseen or equal-mass binary, however there are a couple of problems with the binarity hypothesis. First, extreme redness cannot be explained with binarity. Based on evolutionary models, extremely cold Y dwarfs effectively cannot be young, and so a protoplanetary or debris disk makes an unlikely culprit for the enhanced [3.6] and [4.5]. Second, the amount by which this object is over-luminous is at least one mag (depending on the band) and the maximum over-brightness observed from an equal-mass binary is 0.75 mag.

3.7.1.4 Other Findings

The discovery of an additional Y dwarf, presented in this paper, brings the current total known Y dwarfs to 26. It has long been recognized that brown dwarfs cannot account for dark matter, and rather make up a fraction of the number of celestial objects compared to stars. However, it is likely that our sample of Y dwarfs within $\sim$10–20pc is incomplete. Their extremely cold nature makes them difficult to detect in proper-motion surveys. A dedicated

3–5 μm all sky survey with a smaller pixel scale than $WISE$ would likely find a handful more.

These objects are ideal for follow-up with JWST as we try to better understand star formation at the lowest masses and probe atmospheric conditions at the coldest temperatures. It may eventually be possible to spectroscopically differentiate between field brown dwarfs that have cooled to Y dwarf temperatures from the lowest-mass, Jupiter-sized exoplanets that have been ejected from their host system. Differing formation mechanisms predict different metallicity contents, but determining a metallicity will require 3–10 μm spectroscopy with JWST.

In the bottom-left panel of Figure 3.31, M_{W2} seems to plateau between $J-$W2 4–6 mag, where the majority of the T9–Y0 objects lie. It is possible that this represents a T/Y transition, perhaps due to the rainout of an opacity source or the appearance of the salt/sulfide clouds (Morley et al., 2012).

3.8 Summary

We present updated distance measurements for 22 late-T and Y dwarfs, measured from *Spitzer*/IRAC [4.5] data obtained over baselines of $\sim$ 2–7 years. We also present the discovery of one new Y dwarf and five new late-T dwarfs, based on spectra from Keck/NIRSPEC. With these distances, we probe the physical properties of Y dwarfs, and find that the Y dwarf spectral classifications are likely not ordering objects in a temperature-sensitive sequence. JWST mid-infrared spectra will probe the peak of the blackbody functions of these ultracool dwarfs and provide a better understanding of their physical characteristics.

CHAPTER 4

NIRSPEC Upgrade for the Keck II Telescope

4.1 Introduction

NIRSPEC is a cross-dispersed echelle spectrometer for the 1–5 μm wavelength regime deployed on the Nasmyth platform of the Keck II Telescope at W.M. Keck Observatory in Hawaii. The instrument features two modes, a moderate resolution (R$\sim$2,000) and a high-resolution (echelle) mode with R$\sim$ 25,000. It also has an independent infrared slit-viewing camera for acquisition and guiding. NIRSPEC was commissioned in 1999 by the IR Lab at UCLA (PI Ian McLean; McLean et al. 1998, 2000). Since its commissioning, NIRSPEC has proven to be one of the most versatile and useful instruments at Keck. NIRSPEC has contributed to over 350 refereed papers in such diverse science areas as water production rates in comets (Dello Russo et al., 2005); the characterization of the coolest brown dwarfs from WISE (Cushing et al., 2011); the discovery of water in the terrestrial planet forming zone of a protostellar disk (Salyk et al., 2008); the identification of a low redshift host galaxy of a GRB (Prochaska et al., 2004); and the study of gravitationally lensed Lyα emitters at 8.5<z<10.4 (Stark et al., 2007). However, infrared array technology has improved significantly over the past 15 years, and the NIRSPEC detectors and electronics are now outdated. We plan to upgrade the instrument to take advantage of improved infrared detector technology, improve the stability and serviceability of the instrument, and extend the lifetime of the instrument.

We will upgrade the current science detector from an Aladdin III InSb 1024x1024 array to a Teledyne HAWAII-2RG (H2RG) HgCdTe 2048x2048 array, which will have smaller pixels and is expected to have lower noise characteristics. Additionally, the current Slit-viewing Camera (SCAM) detector will be upgraded from its current 256x256 PICNIC array (which

only operates over 1–2.5 μm) to a Teledyne H2RG, also optimized for 1–5 μm. Extending the wavelength coverage of the SCAM will also require a new optical design optimized for the larger bandpass and smaller pixels. We will replace all of the transputer-based readout electronics with the Teledyne SIDECAR ASIC and SIDECAR Acquisition Module (SAM) boards, which are responsible for detector readout and control. Additional upgrades include replacing the entire transputer-based electronics systems, adding thermal and mechanical stability, and upgrading software. Motion control will be handled by a Galil controller, and thermal control will be monitored using Lakeshore temperature controllers.

As the Instrument Scientist for the NIRSPEC upgrade, I have been heavily involved with many aspects of the upgrade since 2012. My role includes optical systems characterization (Martin et al., 2014) and design (Martin et al., 2016), detector characterization and testing, electronics design and testing, mechanical prototyping and cryogenic testing, as well as project management and other general tasks related to the success of the upgrade. In this chapter, I highlight some of my major contributions to the NIRSPEC upgrade. First, I describe the current system, its limitations, and our planned upgrade in § 4.2 . Then, I discuss the characterization and testing of the new Spectrometer (SPEC) detector in § 4.3. Section 4.4 presents the new opto-mechanical design for the SCAM system. Section 4.5 presents work I have done to help test laser frequency combs on NIRSPEC, with the hope of using a laser comb as a precise wavelength calibrator to improve NIRSPEC's ability to measure precise radial velocities. I summarize the work in § 4.6.

4.2 NIRSPEC Instrument: Current Design and Planned Upgrade

4.2.1 Current Design

Light enters the NIRSPEC vacuum chamber and is reflected by an off-axis parabola (OAP) and fold-mirror assembly (similar to a K-mirror), which acts to both collimate the f/15 beam and fold the light path to reduce the size of the cryogenic vacuum chamber. This moveable

K-mirror can act as an image rotator to counteract the rotation of the sky on the slit plane while observing, or to orient extended objects onto the slit. Collimated light then passes through a filter wheel module containing two filter wheels with wide-band spectroscopic filters in various wavelength passbands, followed by a second (stationary, OAP) K-mirror assembly, which refocuses the light path as f/10 onto a slit wheel. The slit wheel contains mirrors tilted at 12° with respect to the optical axis, with slits of varying width and length cut into each surface. Slits of 0.″144, 0.″288, 0.″432, 0.″576, 0.″720 widths are available at lengths of 12″or 24″in high-resolution mode. In low-resolution mode, slits are available in widths of 0.″380, 0.″570, 0.″760, all with 42″ lengths. The science detector has a pixel scale of 0.″144 per 27-μm pixel in the dispersion direction and 0.″193 per 27-μm pixel in the spatial direction in the high-resolution mode and vice-versa in the low-resolution mode. The front face of each slit is a highly reflective gold surface that reflects light back onto the fold flat of the second K-mirror and into the SCAM.

The SCAM optical design is presented in McLean et al. (1998), and summarized here. The existing SCAM consists of a three-element refracting f/4.6 camera that images light from the slit plane onto the PICNIC 256x256 array. The slits were laser-cut into gold-coated copper mirrors, which are tilted by 12° such that the light that does not enter the spectrograph is reflected back onto two fold mirrors before entering the slit-viewing camera. A BaF_2 single element with a single aspheric surface produces almost collimated light from the f/10 beam, which is then focused onto the PICNIC array by a LiF/BaF_2 doublet in an f/4.6 beam, providing a plate scale of 0.″18 /pix and a 46″x46″ field of view (FOV). The optical quality met the original design specifications, which required at least 80% of the encircled energy to fall within one 40- μm pixel. Optical distortion was minimized during the optimization process. Specifications for the current design and the planned upgrade can be seen in Table 4.1. The SCAM allows for easy alignment of faint targets onto the slit when observing at 1–2.5 μm. For brighter objects, SCAM can be used for guiding.

Following the slit plane, an OAP mirror re-collimates the light into a 120-mm beam towards the echelle grating mechanism. For the high-resolution mode, the echelle grating is selected in the grating mechanism and is used in conjunction with a cross-dispersing grating

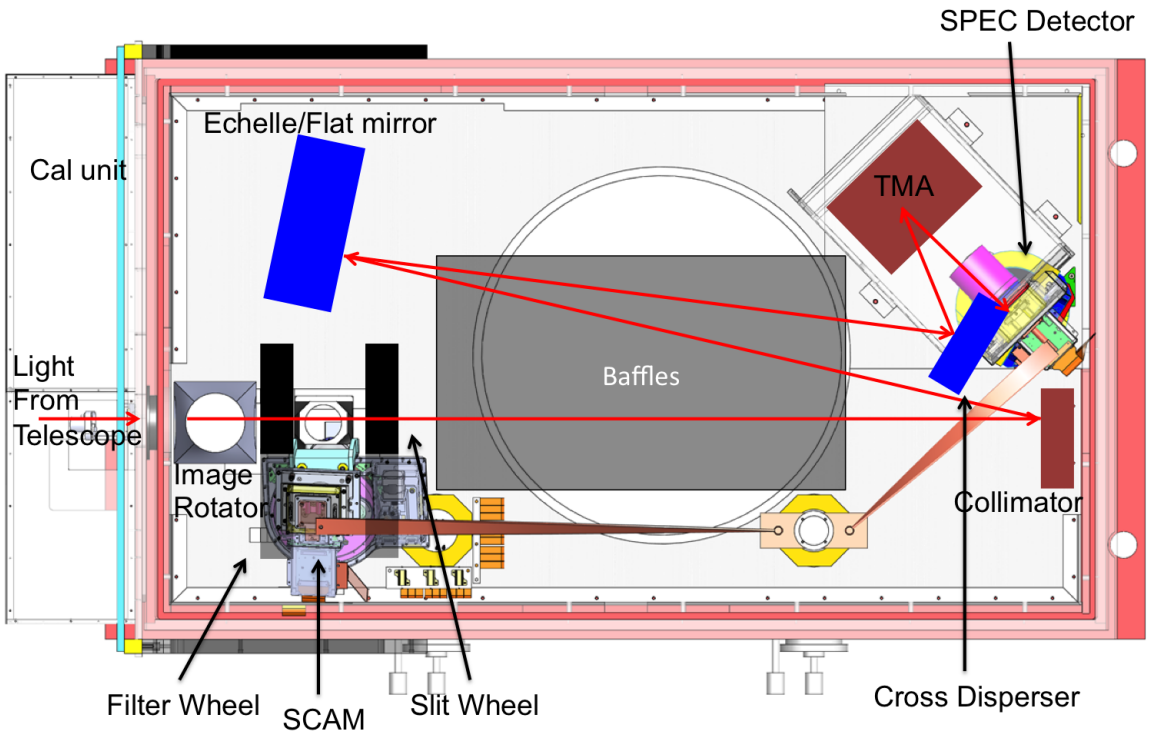

Figure 4.1: Simplified layout of the NIRSPEC cryostat, showing solid models of the SCAM and SPEC detector heads and boxes to represent the remaining components. The path that light follows through the instrument is shown in red arrows.

to produce a spectral resolving power of R=$\Delta\lambda/\lambda$∼25,000, which is then imaged by a three-mirror anastigmat (TMA) camera onto the Aladdin III detector. For low-resolution mode, a flat mirror is selected in the mechanism, and the cross-disperser grating alone provides R∼2,000 spectral resolution. By selecting various combinations of order-sorting filters and angles of the echelle and cross disperser gratings, it is possible to obtain spectra in any wavelength range from 1–5 μm.

The readout electronics for both the SCAM and spectrometer detectors, as well as the electronics used to control the instrument's various moving mechanisms, are implemented using Inmos Transputer based single-board computers. Inside the dewar, there are six moving mechanisms: 1) Rotator; 2) Filter Wheel 1; 3) Filter Wheel 2; 4) Slit Wheel; 5) Echelle grating mechanism; 6) Cross disperser grating turret. There are an additional three moving mechanisms inside the Calibration Unit, which sits in front of the NIRSPEC entrance window: 1) Hatch (Cal Unit cover); 2) Pinhole; 3) Flip mirror to allow light either from the telescope, or from the calibration unit.

4.2.2 Design limitations

The main limitations of the current design are the outdated detectors and readout electronics, which are much noisier than can be achieved with current infrared array technology. The transputer boards used for controlling the instrument's mechanisms and detector readouts, as well as the boards used for system housekeeping, are obsolete. There is cause for concern that if any of the current electronics required repair, they would be difficult or impossible to replace. Science detections are currently detector-noise-limited between sky lines, and spurious increases in noise on the science detector reduce efficiency during observations by up to a factor of $\sqrt{2}$. Additionally, the SCAM is only viable in the 1–2.5 μm regime, which can pose difficulty for aligning targets on the slit while taking observations in the L and M bands. The current method to do this requires imaging in the K or KL filter to align the target on the slit, before switching filters to take science observations. Differential atmospheric refraction and the relative brightness of targets in the various thermal infrared

bands can make this technique quite difficult, and make the observations much less efficient. Additionally, observers have had problems in the past with one of the PICNIC quadrants being non-responsive.

4.2.3 Planned Upgrade

In order to mitigate the limitations of the current design, we are planning several improvements to the instrument. Specifications for the current instrument and the planned upgrade are listed in Table 4.1 below.

4.2.3.1 Replacement science detector

The proposed upgrade will first replace the Aladdin III detector with a Teledyne H2RG with a 5-μm cutoff. The current science detector has much higher read noise and dark current than can be expected from the newest H2RG. In particular, read noise is expected to decrease from 65 e- to 15 e- (CDS frames), dark current will decrease from 0.7 to 0.01 e-/s, and the quantum efficiency (QE) is expected to increase from $\sim$70% to >95%. Currently, high-resolution detections are detector-noise limited between OH lines. We expect the reduction in the dark current and read noise will allow detections to become background/ photon-noise limited for faint/bright sources. The result of these improved noise characteristics are an increase in limiting magnitude of >1 mag, or more than a 6.25 times reduction in integration time required to achieve a given signal-to-noise ratio (SNR). We also expect a 5- to 10-fold increase in efficiency in the L and M bands from increased QE and lower dark current and read noise.

The pixel size will decrease from 27 μm to 18 μm, while the format of the detector will increase 4-fold in pixel count, from 1024x1024 to 2048x2048 pixels. The increased detection area and decreased pixel size will increase both spectral sampling and spectral range. Optical modeling in § 4.3 suggests that spectral resolution may also be increased if smaller slits are used. With the smaller pixels of the H2RG, the pixel scale will decrease to $0\farcs096$ per pixel because the OAPs and gratings will remain unchanged and their image quality is close to

Table 4.1. Current and Upgraded NIRSPEC Specifications

	Current System	Planned Upgrade
Wavelength Coverage:		
Science Detector	0.9–5.3 μm	0.9–5.3 μm
Slit Viewing Camera (SCAM)	0.9–2.5 μm	0.9–4.8 μm
High-Res mode Resolution	$\sim$ 25,000 ($0\farcs43$ slit)	$\sim$ 37,500 ($0\farcs29$ slit)[a]
Science Detector	Aladdin III InSb 1024x1024 27-μm pixels	Teledyne H2RG HgCdTe 2048x2048 18-μm pixels
SCAM Detector	PICNIC HgCdTe 256x256 40-μm pixels	Teledyne H2RG HgCdTe[b] 2048x2048 18-μm pixels
Detector Characteristics:		
Dark Current	0.7 e-/s	0.01 e-/s
Quantum Efficiency	70 %	$>$ 95%
Read Noise (CDS frames)	65 e-	15 e-

Note. — *a*) Increasing the spectral resolution is possible, but will require the use of a smaller slit. With the smaller pixels of the H2RG, a 3-pixel slit is only 0.29 $''$. *b*) The upgraded SCAM detector is an engineering-grade H2RG, but will only utilize a smaller, science-quality sub-array, not all 2048x2048 pixels.

diffraction-limited (Robichaud et al., 1998). Smaller pixels and better sampling will allow for longer integration times before detections reach the background limit, also increasing the efficiency of observations. The replacement detector will allow NIRSPEC to continue in its status as a workhorse instrument for the Keck II telescope for at least the next decade.

4.2.3.2 Replacement SCAM Detector

The second major component of the upgrade will be the replacement of the SCAM detector. The 256x256 PICNIC array can only observe in the 1–2.5 μm regime, which is a drawback for the current design. Currently observations conducted in M band require switching filters to K band to acquire the target, before taking exposures with the M-band filter. Having to align in a different filter decreases efficiency by a factor of $\sim$50%. Additionally, differential refraction between $\sim$2 μm and $\sim$4 μm makes it difficult to properly align targets on the slit. The replacement of the SCAM detector with a 1–5 μm H2RG (2048x2048 pixels) will be a great improvement for observations conducted in L and M bands. It will become much easier to align targets on the slit plane using SCAM after the upgrade, and the longer wavelength response will greatly increase efficiency when observing in these bands. This replacement also allows for the opportunity to redesign the SCAM optical system. The existing lenses have anti-reflective coatings viable for 1–2.5 μm and thus will have to be replaced. Replacing the PICNIC with a H2RG provides the freedom to redesign to optimize for such things as sensitivity, sampling, and field of view. In § 4.4, I present my design for the new SCAM optics.

4.2.3.3 New readout and control electronics

The final component to the upgrade will be a complete overhaul of the computing system. The transputer electronics used for reading out, controlling mechanisms, and housekeeping are now obsolete. Replacement of the readout electronics for both the SCAM and spectrometer detectors with the Teledyne SIDECAR ASIC will provide NIRSPEC with a modern system with much less readout noise that will also be free of the systematic noise present in

the current readout electronics. Control hardware will be replaced with more modern hardware currently implemented by Keck Observatory in other IR instruments such as MOSFIRE and OSIRIS. NIRSPEC will be able to share spare electronics with MOSFIRE, and its new user interface software will also take advantage of improvements implemented with the MOSFIRE instrument at Keck (Kulas et al., 2012).

4.3 Spectrometer detector upgrade

4.3.1 Optical modeling of the SPEC detector

The smaller pixel size of the H2RG will allow for 50 % better sampling and longer integration times, which greatly increases the sensitivity and usefulness of the instrument for doing groundbreaking science across many astronomical fields, including high red-shift galaxies, protostellar disks, brown dwarfs, and exoplanets. Because the H2RG has a larger format than the Aladdin III, I characterized the expected optical performance for the extended image plane. I used ZEMAX to study the focal plane of NIRSPEC for both the current and proposed designs to quantify throughput and spot size across the detector. I used root-mean-square (RMS) spot size and percentage of vignetting to quantify the image quality.

In Figures 4.2 and 4.3, I show estimated RMS spot size as a function of order and location on the detector to compare the Aladdin III and H2RG detectors in the J band ($\sim$1–1.3 μm) in high-resolution mode. The physical sizes of the detectors are shown in Figure 4.2 as dotted vertical lines and the one- and two-pixel sizes of each detector are marked in horizontal dashed lines. With the exception of the corners, the spot sizes are small enough to have 80% encircled energy fall within one or two pixels of the H2RG. We expect similar performance in other NIR spectral bands.

Figure 4.3 shows the results of our ray tracing, plotted as an image of the NIRSPEC focal plane. Shading of the blue dots represents percent throughput of the light. Lighter spots have lower throughput. Spots are enlarged to demonstrate the impact of location on RMS spot size. An example spot with 80% throughput and a 10 μm spot size is shown in

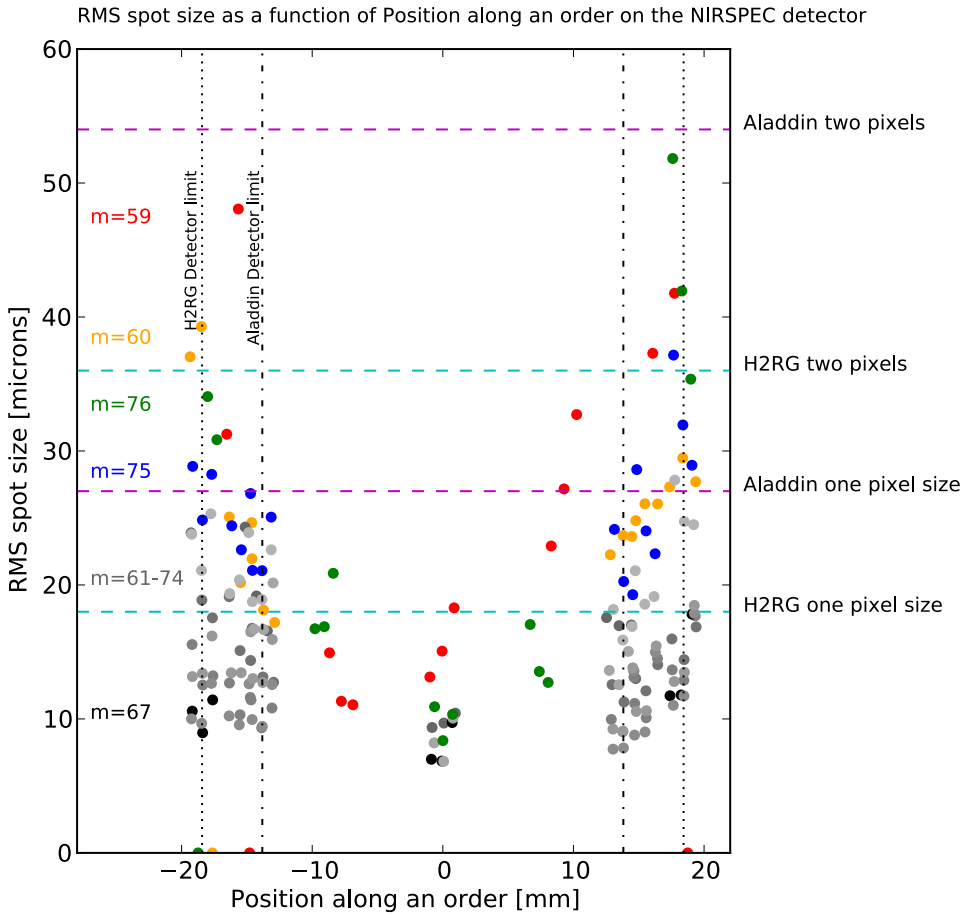

Figure 4.2: RMS spot size vs. position along an order (dispersion direction) on the detector. Different spectral orders are represented by different shaded dots. Spectral orders at the top and bottom of the detector are highlighted in color, because the edges of the detector are where we expect the poorest optical performance. The majority of the spot sizes are smaller than two H2RG pixels, indicating that we can expect improved pixel sampling with the H2RG compared to the Aladdin III. Analysis was performed for the J band ($\sim$1–1.3 μm, echelle orders 59–76) but is expected to produce similar results for the other NIR bands.

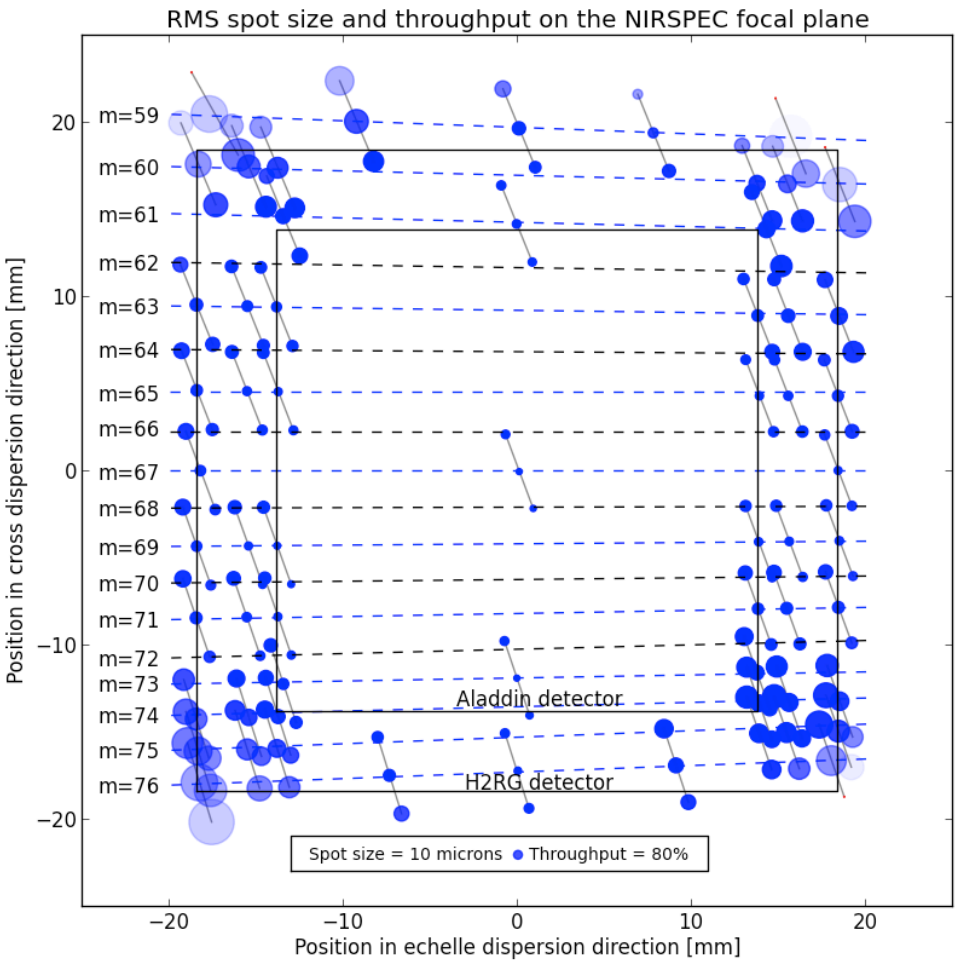

Figure 4.3: RMS spot size as a function of location on the NIRSPEC focal plane in J band (∼1–1.3 μm, echelle orders 59–76). Spot sizes were calculated at three locations along 30 $''$ slits along each order (tilted vertical lines). Lighter shaded dots have lower throughput, and red dots are completely vignetted by the instrument. Spot sizes are enlarged, but the majority of spot sizes fall within one or two pixels (18 or 36 μm for the H2RG). The slits are tilted because of the quasi-Littrow configuration of the spectrometer. Only the corners of the H2RG field have significantly lower throughput and larger spot sizes, but the overall improvement in spectral range is evident. We expect similar performance in the other NIR bands.

the bottom center as a reference. Boxes are drawn to denote the boundaries of the Aladdin III and H2RG detectors. Spectral orders are marked, along with the approximate lines they trace out on the detector. The slits are tilted because of the quasi-Littrow configuration of the spectrometer. From Figure 4.3, it is clear that the H2RG will offer a significant improvement over the current detector. Each order will have a larger spectral coverage, with acceptable spot sizes everywhere except the corners of the detector. All of the central orders have spot sizes smaller than two H2RG pixels; the majority of the spot sizes are under 30 μm. Throughput is also quite high; with the exception of the corners of the H2RG, throughput is greater than 80%.

This analysis did not take into account any errors in the optical system, such as any tip/tilt of the replacement detector surface. Our alignment tolerance allows for tip/tilt mis-alignments of up to XX arcseconds, which would result in poorer image quality.

4.3.2 Replacement Detector Head Prototyping and Initial Testing

Figure 4.4 shows a solid-model of the current opto-mechanical layout of the Aladdin III detector and its enclosure, known as the detector head. The upgrade must fit entirely within the existing dewar and cold-shield, so we had to design a replacement detector head that would align the new detector at the focal plane. We have already prototyped and tested the replacement detector head (Figure 4.5) within our test dewar in the lab at UCLA. I assisted in the assembly and testing of the detector head.

4.4 SCAM Upgrade

4.4.1 Planned Upgrade

The planned upgrade will replace the PICNIC array with a 5-μm cutoff H2RG. The transputers used to read out the PICNIC will be replaced with a Teledyne SIDECAR ASIC and SAM to readout the H2RG. All lenses will need to be replaced and the optical design will be redone, because the current optical design does not produce good image quality in the

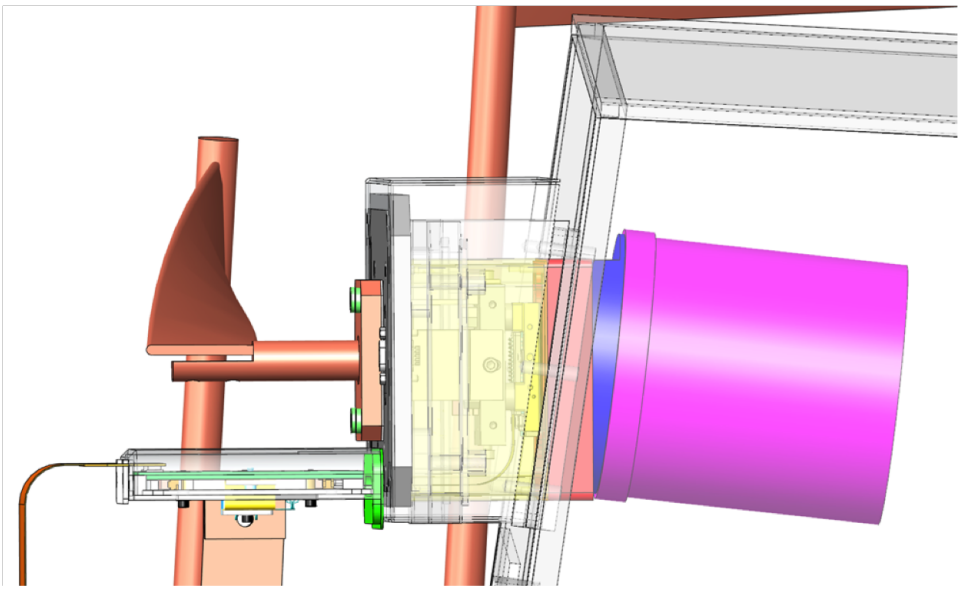

Figure 4.4: Solid model of the upgraded SPEC detector head. A copper cooling block is attached to the back of the detector head mounting plate. The H2RG sits on top of an A-frame structure, shown in yellow. The baffle is angled due to the optical design of the imaging three mirror anastigmat (TMA). A short ribbon cable connects the detector to the ASIC, which is mounted to the detector head mounting plate and has a separate cooling strap. A longer ribbon cable connects the ASIC to the SAM card, through a hermetic feedthrough in the dewar wall.

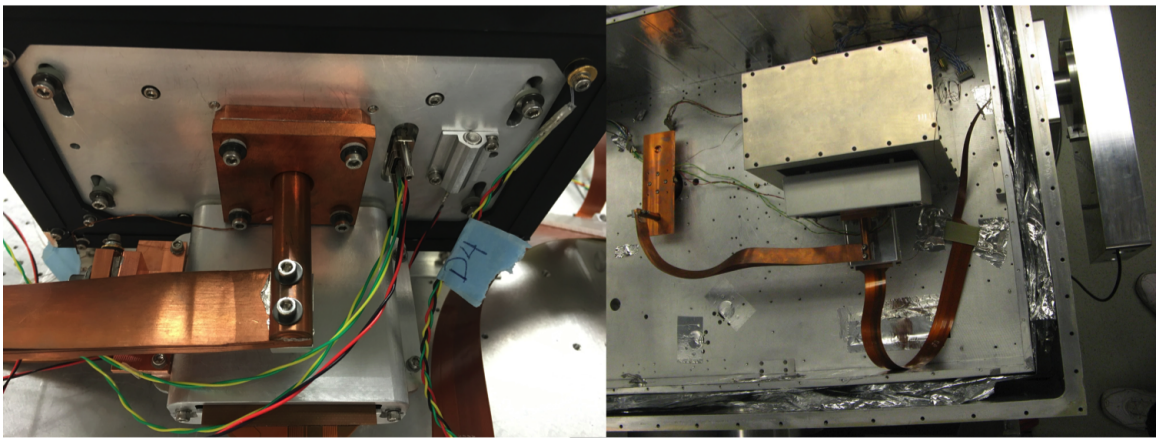

Figure 4.5: Prototype SPEC detector head installed inside our vacuum cryogenic test chamber in the lab.

L and M bands. The existing design's optical quality is also not good enough to maintain the same pixel scale on the smaller H2RG pixels. If we set the requirement of maintaining a similar pixel scale, this necessitates decreasing the f/# of the camera to f/2.3 from the current f/4.6. The FOV of the SCAM is limited by the size of the hole in the annular guide mirror, but it will increase slightly to 60″x 60″. With these design considerations in mind, it is clear that we will not use the entire focal plane of a H2RG, however, it was much easier for us to obtain an engineering-grade H2RG with a large enough section of good-quality pixels than to purchase an appropriately sized 1–5 μm array. The use of sub-arraying will likewise allow for faster readout times than the current 1.45 seconds, when reading out the full array at 100 kHz.

4.4.2 SCAM Opto-Mechanical Design Constraints

Space for the NIRSPEC upgrade is limited by the pre-existing mechanical structures within the dewar. The upgraded SCAM design will have to fit between the enclosures for the filter and slit wheels, and the focal length is constrained by the location of the cold shield (See Figure 4 in McLean et al. 1998) to be less than 300 mm from the last fold mirror to the image plane. In addition to these physical constraints, we are also constrained by the existing fore-optics, which we do not plan to change. The goal is to minimize image distortion and the number of refractive elements, while also achieving >80% encircled energy within 1 pixel, an achromatic design from 1–5 μm, and maintaining the 0.″18 /pixel plate scale.

In Martin et al. (2014), we showed that the thermal background from 3–5 μm saturates the H2RG in shorter time than the minimum exposure time for a nominal pixel clock rate of 100 kHz. The wide spectroscopic bands allow too much background to enter the SCAM and observing in the thermal infrared would be impossible with these filters. To mitigate this issue, we plan to insert a filter wheel within the SCAM optical path to provide narrowband K, L and M filters, as well as an "open" position for regular imaging in J, H, and K bands, where the sky background is much lower. The final constraints on the optics were chosen for manufacturability considerations. Within the merit function, we set requirements for lens

thicknesses to be at least 10% of the diameter and less than 15 mm total. We also required at least 1 mm of air spacing between the centers of each lens. Below I detail the major mechanical and optical considerations that I took into account when creating the ZEMAX merit function.

Mechanical Constraints

- First element $>$ 66 mm from slit plane, due to K2 mirror mount
- Total track $<$ 306 mm, to allow room for detector mount and ASIC inside the cold shield
- Element thicknesses $>$ 10% of their diameter
- Element edge thicknesses at least 3 mm, for ease of mounting
- Element central thicknesses between 1 and 15 mm
- Minimum distance between lens centers of 1 mm
- Minimum distance between lens edges of 3 mm
- Detector image plane $>$ 13 mm from last element

Optical Constraints

- Achromatic from 1–5 μm, optimized for central wavelengths at 1, 1.25, 1.65, 2.2 μm, as well as specific ranges chosen in the L and M bands.
- Antireflective coatings optimized for 1–5 μm in atmospheric transmission pass bands.
- Minimize amount of stray light in the system
- 80% of the light captured in 1 pixel everywhere on the array for all pass bands.
- Minimal image distortion
- Minimal number of refractive elements

- Maintain $\sim 0\farcs18$/pixel plate-scale. This requires a faster $\sim$ f/2.3 camera, compared to the current f/4.6 SCAM. The FOV will remain the same, because it is largely set by the size of the slit mirror.

SCAM Filter Wheel Constraints

Wideband spectroscopic filters in the spectrograph filter wheel and bright sky background in the L and M bands will cause the H2RG to saturate in less than the minimum exposure time of 1.54s. To mitigate this effect, we are introducing a filter wheel mechanism within the SCAM system. Requirements are listed below.

- 3 filters: Broadband 1–2.5 μm, L narrowband, and M narrowband
- L and M narrowband locations chosen from atmospheric windows and considering background estimates
- Wheel located near collimated space
- Filters $\leq$ 50 mm diameter
- Filters tilted at $\sim$ 2 deg to minimize ghosting
- Filter wheel located between 199 and 211 mm from slit plane due to mechanical constraints

4.4.3 SCAM Upgraded Optical Design

Using the requirements listed above, I created an initial optical design for the upgraded SCAM in ZEMAX. I input each of the constraints into a customized merit function and then optimized for RMS wavefront error of the centroid. I used 3 rings and 6 arms in Gaussian quadrature to optimize across 4 field locations (center, 2 corners, and one edge of our $46''$x $46''$FOV) and 6 wavelengths (1.0, 1.25, 1.65, 2.5, 3.8, 4.6 μm). I also updated the existing NIR glass catalog with data from the NASA Goddard project, CHARMS (Leviton & Frey, 2004), which provided high-precision data of index of refraction vs. wavelength at

cryogenic temperatures. The optical bench sits at $\sim$ 55K, so the indices of refraction of each infrared material were calculated for that temperature.

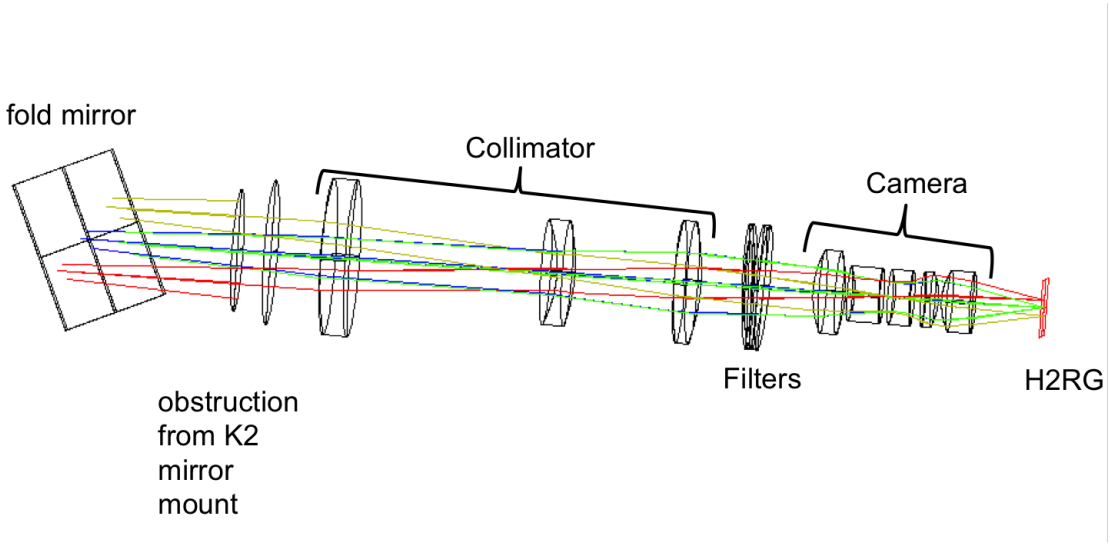

Figure 4.6: 3D Layout of the SCAM optical design, from ZEMAX.

Table 4.2. Optical Prescription for the Upgraded Slit-Viewing Camera

Optic Name	Radius of curvature (mm)	Thickness (mm)	material	Semi-diameter (mm)
Fold Mirror	Infinity	0	mirror	23.169
Air	—	73.858	Air	—
Collimator 1	121.798	9.348	ZnS	24.512
—	338.142	66.609	—	—
Collimator 2	−41.384	5.716	ZnSe	16.904
—	−57.235	31.770	—	—
Collimator 3	103.790	8.699	BaF_2	19.669
—	−69.288	15.15	—	—
Filter Config 1[a]	Infinity	5.0	BK7	20.0
—	—	15.78	—	—
Filter Config 2[a]	Infinity	1.0	Sapphire	20.0
—	—	2.17	—	—
—	Infinity	1.83	Silicon	20.0
—	15.78	—	—	
Camera 1	29.828	10.426	BaF_2	13.466
—	−44.394	3.000	—	—
Camera 2	−25.373	8.0	LiF	8.80
—	72.427	5.000	—	—
Camera 3	−25.366	4.809	ZnSe	8.80
—	80.438	4.686	—	—
Camera 4	−73.107	4.370	ZnS	8.80
—	−21.315	1.0	—	—
Camera 5	19.739	10.0	BaF_2	9.530
—	Infinity	22.779	—	—

[a]There are two configurations for the filters, one for J, H, K observations, and a second for L and M band observations. The short wavelength configuration only requires a single BK7 filter to block the long wavelength light. The second configuration requires a combination of a narrowband Sapphire filter and an ND3 Silicon filter.

My initial design attempted only using 3 lenses, similar to the original SCAM optical design. I was unable to achieve satisfactory optical quality and continuously increased the number of elements until an acceptable design could be produced. In Martin et al. (2016), I presented a preliminary design utilizing 10 optical elements. I eventually settled on using a Cooke Triplet collimator and a Double Gauss camera for my initial design parameters. After optimization, it became clear that I could remove one element from the camera and continue to meet our requirements. Each of the lenses is spherical, which is generally easier to manufacture. I also investigated using fewer lenses with conic constants in their curvatures, but was unable to reduce the overall number of elements. I iterated many times with the mechanical engineers in our lab, until we arrived at a design that met all of the optical and mechanical considerations. The resulting design consists of 8 spherical refractive elements and a filter substrate (Figure 4.6). The three collimating lenses are ZnS, ZnSe, and BaF_2, from left to right in the figure. The filter substrate was assumed to be CaF_2. The five camera lenses are BaF_2, LiF, ZnSe, ZnS, and BaF_2. The optical prescription is shown in Table 4.2 and solid models are shown in Figures 4.7 and 4.8.

4.4.3.1 Optical Performance

In Figure 4.9 I present spot diagrams of the focal plane for the four fields I used for the optimization. Each color represents a different wavelength. In all four fields and for each wavelength, the design meets our requirement of having the majority of the light fall within one 18 μm pixel. This is further demonstrated in Figure 4.10, where I plot the encircled energy vs. radius for each of the fields. All four fields reach >80% encircled energy within 1 pixel. The image quality in the design is mostly impacted by spherical aberrations in the center of the focal plane. Additional, higher order aberrations are more significant at the edges and corners of the field, though we are still able to maintain the majority of the light within one pixel.

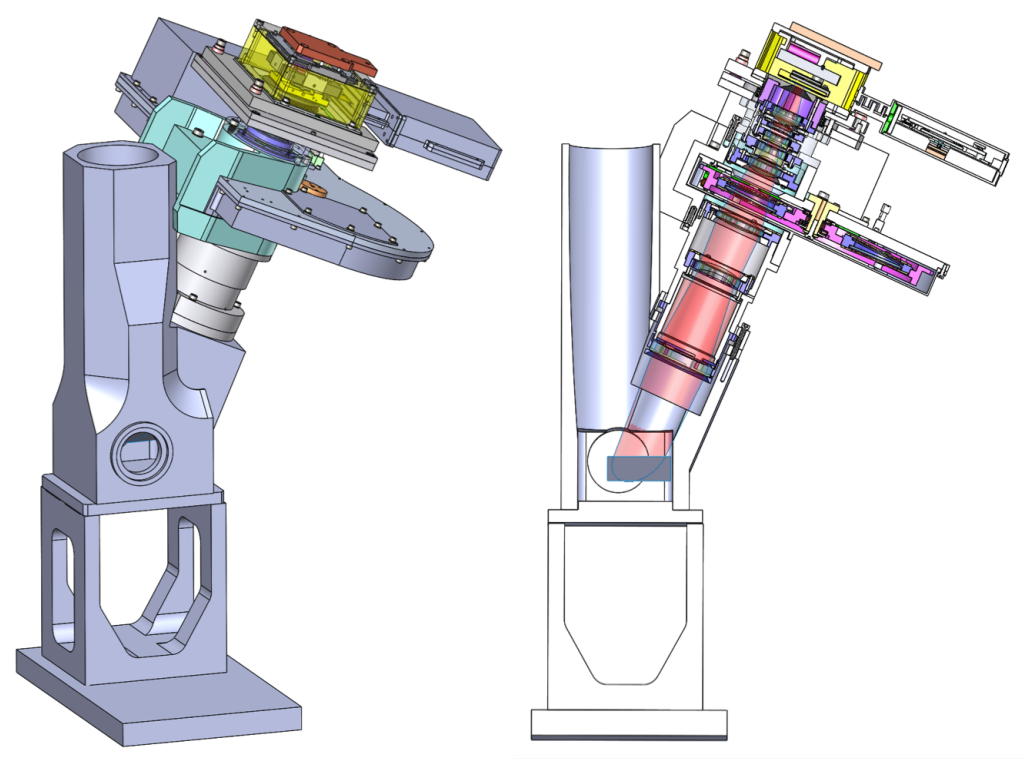

Figure 4.7: Left: Solid model of the SCAM opto-mechanical design, from the K2 mirror tower to the H2RG detector. Right: Solid model with cut-aways to show location of lenses and lens mounts.

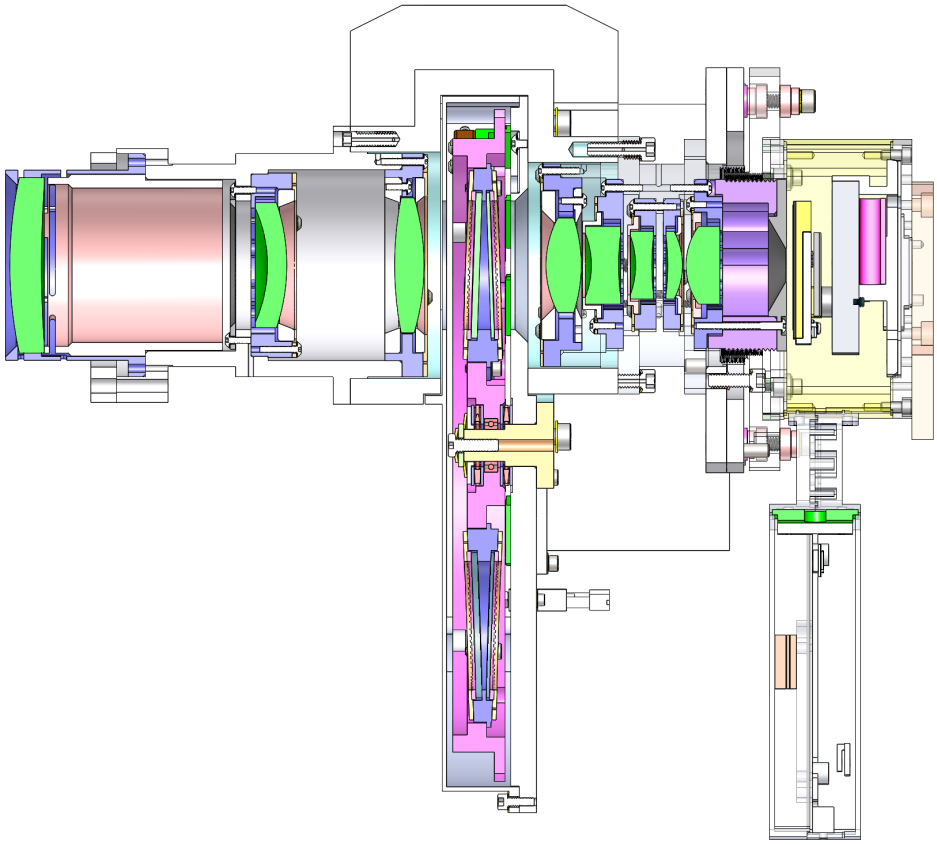

Figure 4.8: Zoomed-in view of the SCAM opto-mechanical design, showing the lenses inside of their respective lens mounts, the filter wheel, and the SCAM detector head.

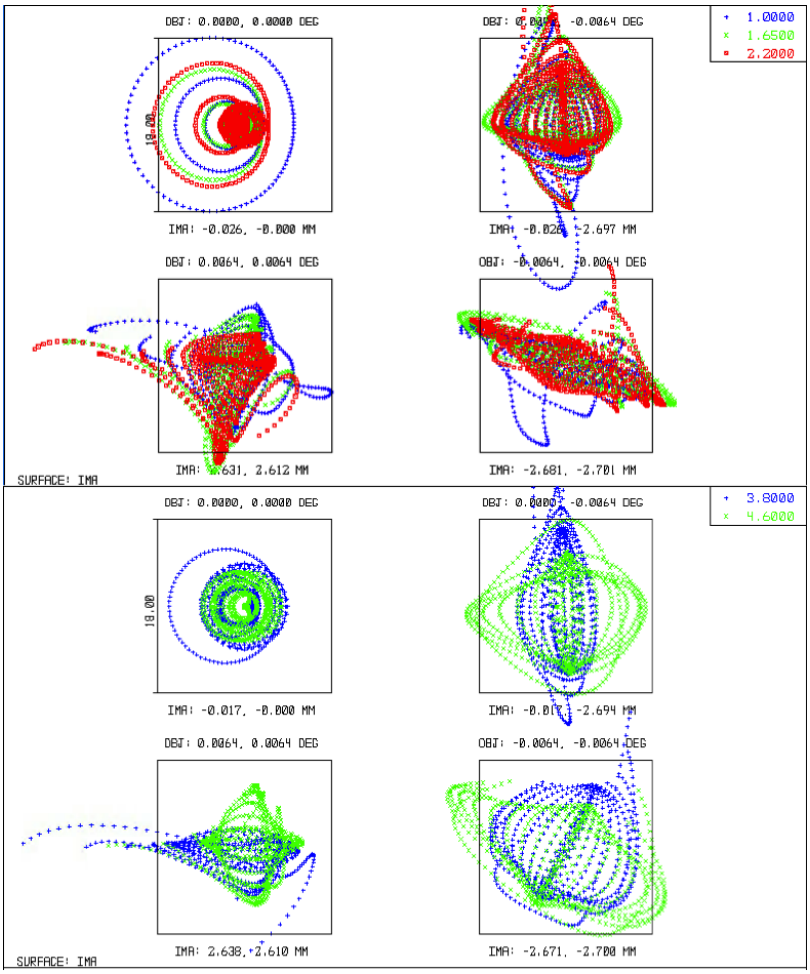

Figure 4.9: Spot diagrams for the two different configurations, showing image quality on the SCAM focal plane. Each diagram shows four different spots from four different field locations. The box drawn around each field is the size of a single 18 μm pixel.

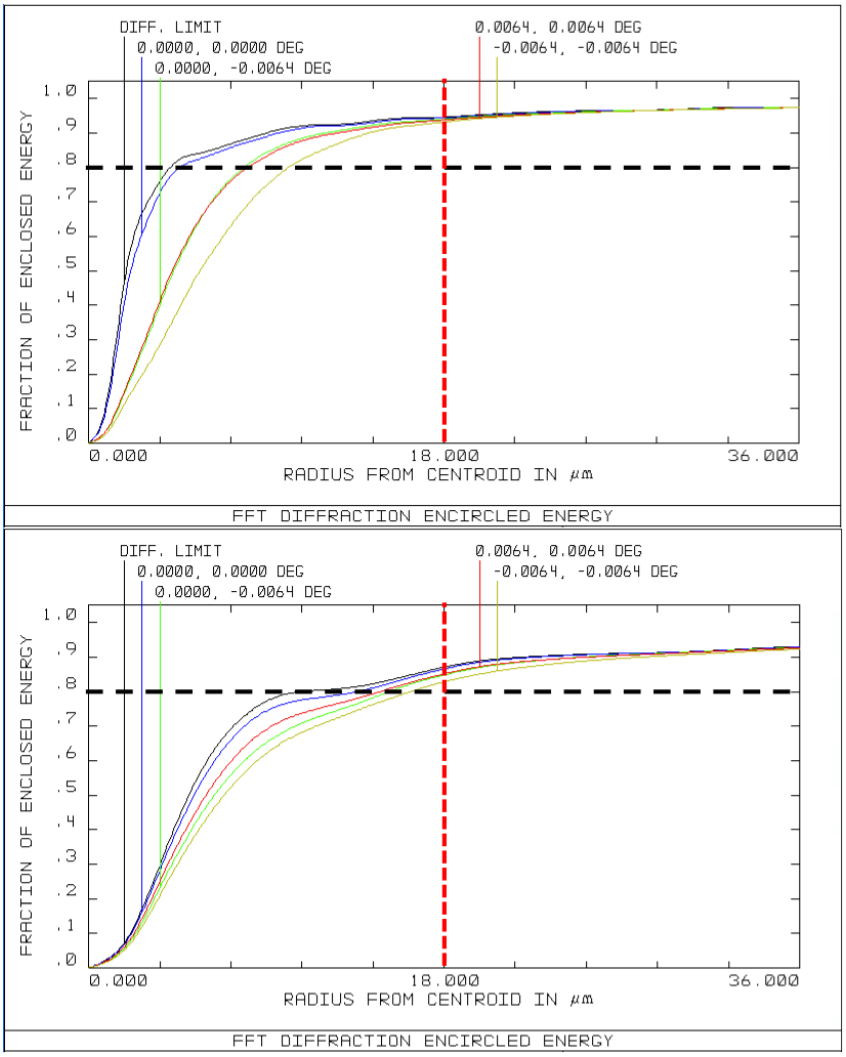

Figure 4.10: Encircled energy as a function of radius from the centroid, in μm. The top panel shows the first configuration, for short wavelengths, and the bottom panel shows the second configuration, for the longer wavelengths. A black dashed line denotes the 80% requirement, and a red dashed line marks one pixel. In every field and every wavelength, we meet our requirement.

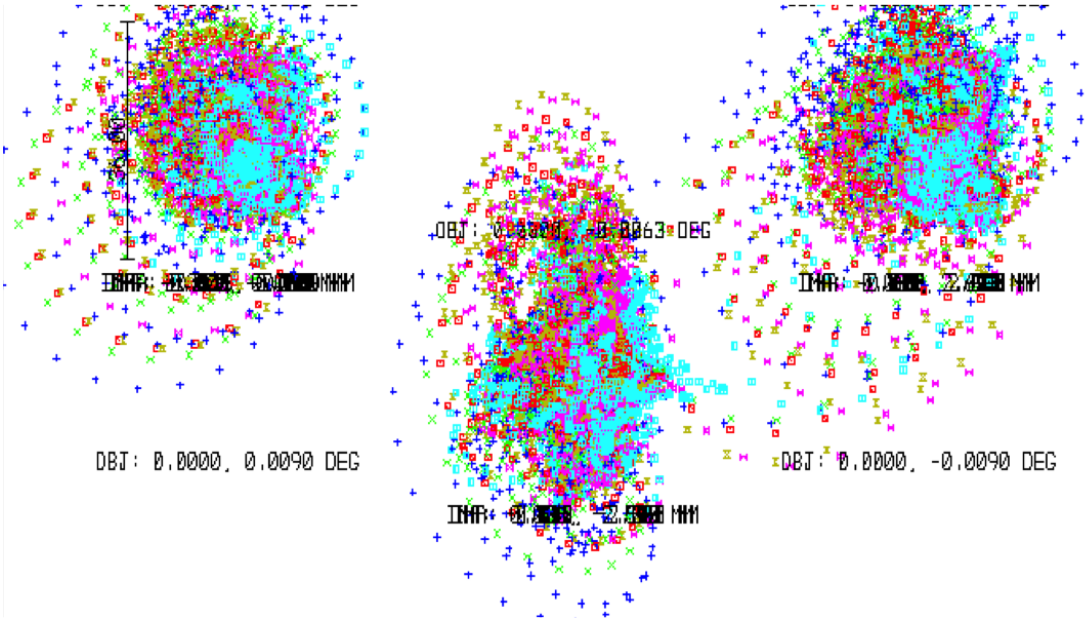

Figure 4.11: Spot diagrams showing the results of multiple Monte Carlo runs of a tolerancing analysis. The scale of the line drawn in the upper left is two H2RG pixels, equivalent to 36 μm.

4.4.3.2 Tolerance Analysis

I performed a tolerance analysis using ZEMAX to test for tolerances on each of the optical elements. I used typical machining tolerances of ± 0.05 mm on mechanical thickness, X/Y misalignment, and central glass thickness, and tolerances of $\pm 0.1^\circ$ on tip/tilt. I constrained radii of curvature to ± 0.1 %, per discussion with the manufacturer. I also used typical manufacturing tolerances on Abbe number and indices of refraction. ZEMAX performs a Monte Carlo style tolerance analysis, where it varies all values simultaneously, with randomly selected parameters drawn from a normal distribution with the cutoffs provided by the allowed tolerances. My results show that camera lenses 2, 3, and 4 are most critical to the optical quality. In Table 4.3, I list the top 5 offenders from the Monte Carlo simulation, and the effect that they would have on the RMS spot size, if they were at the limit of our tolerance. With the relatively loose tolerances I provided, we can expect >80% of the light to fall within a 2x2 pixel range, equivalent to $0\farcs36$ on a side, which is better than the typical seeing on Mauna Kea. Figure 4.11 shows spot diagrams from this tolerance analysis.

Table 4.3. SCAM Critical Tolerances

Optic Name	Tolerance	Effect on RMS Spot Size (μm)
Camera 3 – 4	Distance	2.23
Camera 4	Tip Y axis	1.92
Camera 1 – 2	Distance	1.86
Camera 3	Lens Thickness	1.81
Camera 2	Tip Y axis	1.73

4.5 Laser Frequency Comb Tests

Laser frequency combs are a rapidly developing technology for the use of spectroscopic characterization. Laser combs provide extremely stable and evenly spaced light in frequency space, which can be used to obtain extremely precise wavelength calibration for the purpose of high precision radial velocity measurements. I collaborated with researchers from Caltech and JPL to test several different laser combs on the NIRSPEC instrument. During these tests, I was responsible for NIRSPEC data acquisition, reduction, and analysis. In Yi et al. (2016), we presented the first results from a using line-referenced, electro-optical modulation frequency comb operating in the H band. Suh et al. (submitted) presents the results of a new soliton micro-resonator comb tested on NIRSPEC, both during the day and at night in an attempt to detect an extrasolar planet. My contributions to each of these projects is described below.

4.5.1 Yi et al. (2016)

In December 2014 and May 2015, we tested an electro-optical modulation laser frequency comb (EOM comb) during day-time tests with NIRSPEC. The EOM comb produces a spectrum of lines by using electro-optical modulation of a continuous-wave laser source that is stabilized to an atomic reference. The lines it produces are at frequencies that differ by integer multiples of the modulation frequency, added to the frequency of the reference, i.e. $f_N = f_0 \pm N f_m$. Our paper, Yi et al. (2016) provides detailed schematics on the production

of the EOM comb.

We used a series of 600 spectra taken over a ∼2 h time period to test the instrumental stability of NIRSPEC, as proof-of-concept and to determine whether future high precision radial velocity measurements could be taken with NIRSPEC. Figure 4.12a shows the laser comb illuminating more than six orders of the high-resolution echellogram in the H band. The echelle data were reduced in standard fashion, correcting for dark current and flat-field variations. Under this comb setting, a spectral grasp of ∼200 nm is covered, from 1,430 to 1,640 nm. A zoomed-in spectral extraction (Figure 4.12b) shows that individual comb lines are well resolved at NIRSPEC's resolution and spaced approximately 4 pixels apart (0.1 nm). The relative brightness of each order is plotted in Figure 4.12c.

Order 48, which had the highest SNR comb lines, was reduced following a standard procedure to correct for dark current and flat-field variations. Due to the quasi-Littrow configuration of the instrument, the slits appear tilted on the detector and the spectra have some curvature. We performed a spatial rectification using a flat-field image taken with a pinhole slit to mimic a bright compact object on the spectrum in order to account for this curvature. Wavelength calibration and spectral rectification to account for slit tilting were applied using the Ne, Kr, Ar and Xe arc lamps and the rectification procedure in the REDSPEC software written for NIRSPEC.

Instrumental stability was tested by performing a cross-correlation between the first comb spectrum in the 600 image series and each successive comb spectrum. The peak of the cross-correlation function corresponded to the drift, measured in pixels, between the images. Figure 4.13a demonstrates the power of the laser comb to provide a wavelength standard for the spectrometer. Over a period of roughly an hour the centroid of each comb line in Order 48 moved by about 0.05 pixel, equivalent to 0.0114 Å (equivalent to ∼200 m/s). By examining various internal NIRSPEC temperatures it is possible to show that this drift correlates to changes inside the instrument. Figure 4.13b shows changes in the temperatures measured at five different points within the instrument: the grating mechanism motor, an optical mounting plate, the top of the grating rotator mechanism, the base of the (unused) LN2 container and the three mirror anastigmat assembly. At these locations the

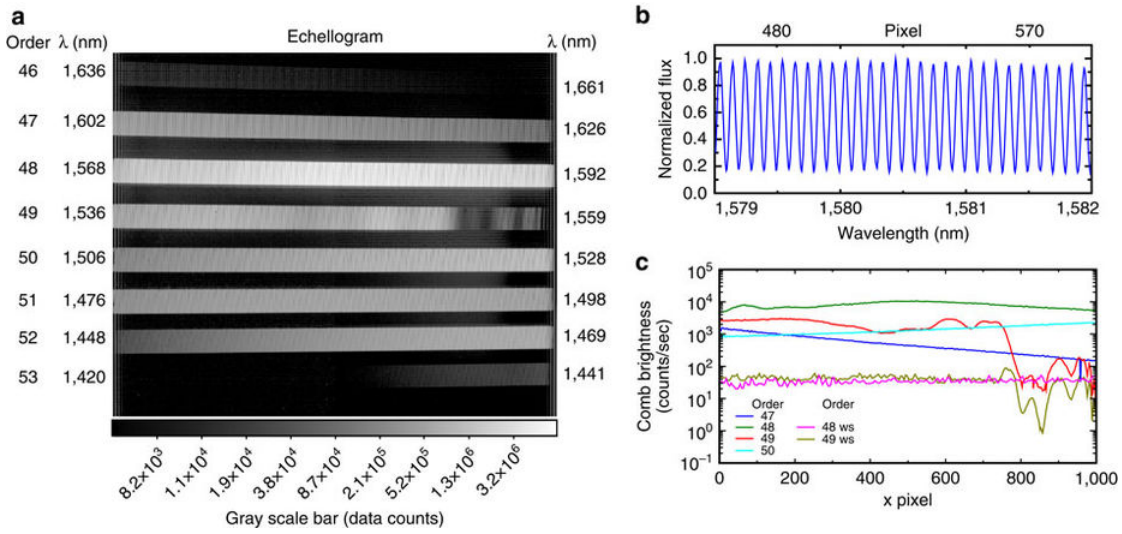

Figure 4.12: a) Full echellogram of the H band. b) zoom-in of the spectral extraction, showing resolved comb lines ($\sim$ 4-pixel spacing). c) Relative brightness of the comb in each order.

temperatures range from 50 to 75 K and have been standardized to fit onto a single plot: $\Theta_i(t) = (T_i(t) - < T >)/\sigma(T)$. Average values of each temperature show drifts of order 15–35 mK over this 1 h period. In its present configuration NIRSPEC is cooled using a closed cycle refrigerator without active temperature control–only the detector temperature is maintained under closed cycle control to $\sim$1 mK.

Examination of the wavelength and temperature drifts in the two figures reveals an obvious correlation. A simple linear fit of the wavelength drift to the five standardized temperatures reduces the temperature-induced wavelength drifts from 0.05 pixel per hour to a near-constant value with a standard deviation of σ=0.0017 pixel for a single-comb line (bottom curve in Figure 4.13a). While other mechanical effects may manifest themselves in other or longer time series, this small data set indicates the power of the laser comb to stabilize the wavelength scale of the spectrometer. At the present spectral resolution of NIRSPEC, R$\sim$25,000, and with over 240 comb lines in just this one order, we can set a limit on the velocity drift due to drifts within NIRSPEC of $c/R \times \sigma/\sqrt{\#\text{ lines}} < 1.5 m/s$ where c is the speed of light.

Thus, operation with a laser comb covering over 200 nm with more than 2,000 lines

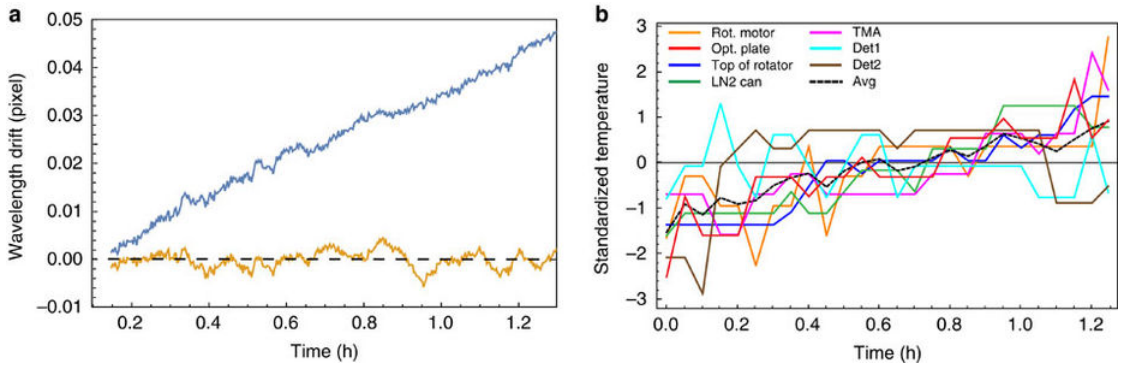

Figure 4.13: a) Wavelength drifts of NIRSPEC as measured by the laser comb, before and after removing the temperature dependence. b) Temperature changes within the NIRSPEC dewar, as a function of time.

in the H-band would allow much higher radial velocity precision than is presently possible using, for example, atmospheric OH lines, as a wavelength standard. NIRSPEC's ultimate RV precision will depend on many factors, including the brightness of the star, NIRSPEC's spectral resolution, and the ability to stabilize the input stellar light against pointing drifts and line profile variations.

4.5.2 Suh et al. (submitted)

In September 2017, we had the opportunity to perform on-sky testing of a soliton microresonator laser comb to attempt to detect an extrasolar planet around a bright star. We performed both day time and night time testing of the new soliton comb, as well as the original EOM comb, for reference.

Figure 4.14 shows the echellogram of the soliton microcomb measured by NIRSPEC (8 Echelle orders ranging from 1471 nm to 1731 nm, which represents almost the entire astronomical H-band). The raw echellograms were rectified spatially and spectrally. Individual comb lines are resolved at the NIRSPEC resolution of R$\sim$25,000 and spaced approximately 8 pixels apart (0.2 nm). Similar to our testing of the EOM comb, we performed many hours of time-series observations of the soliton comb. The comb itself is stable to $\sim$ 30 cm/s, though instrumental noise as seen in our first experiments limits NIRSPEC's ability to calibrate wavelengths to $\sim$ 5 m/s. Unfortunately, we were unable to detect the known exoplanet we

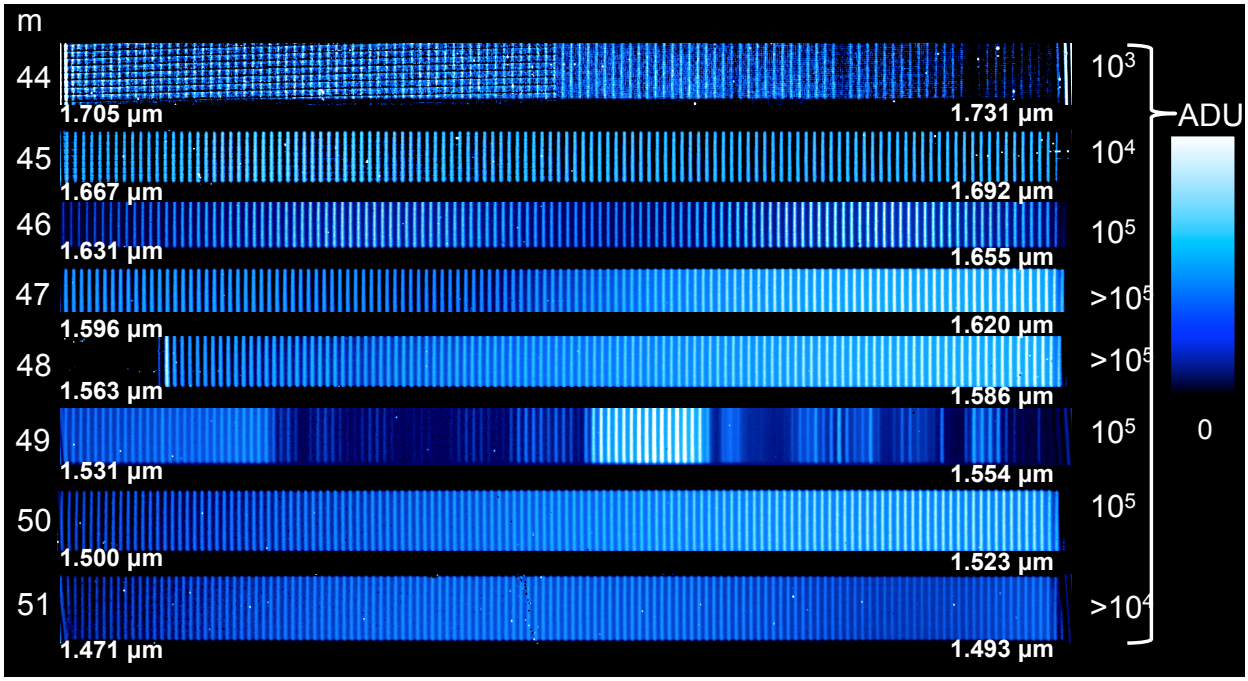

Figure 4.14: Full echellogram after spatial and spectral rectification, showing the wavelength coverage of the soliton laser comb during testing in September, 2017.

were looking for, due to the large instrumental instability relative to the radial velocity signal we were looking for.

We plan to mitigate some of these instrumental instabilities by adding temperature control to the main bench of NIRSPEC. With the addition of a Fiber Injection Unit, in the future it will be possible to take precise radial velocity measurements using upgraded NIRSPEC.

4.6 Summary

In this chapter, I presented highlights from my work as the Instrument Scientist for the NIRSPEC upgrade. First, I discussed the necessity and importance of upgrading NIRSPEC along with an outline of the components we are replacing or updating. Then, I presented the results from optical modeling of the spectrometer detector to characterize the expanded focal plane, showing that the upgrade will achieve improved sampling and spectral grasp. I also presented results from the prototype detector head, which we have tested in our lab inside

our vacuum cryogenic test chamber. Next, I presented my design for a new slit-viewing camera, that will operate in the 1–5 μm regime. I showed the design specifications and that it meets our opto-mechanical requirements. Last, I presented the results from several different tests to demonstrate the use of two different laser frequency combs on NIRSPEC as precision wavelength calibrators.

CHAPTER 5

Summary

This dissertation presents three research projects related to the study of brown dwarfs and infrared instrumentation. I use a combination of near infrared spectroscopy taken with the NIRSPEC instrument on the Keck II Telescope and mid-infrared imaging from the IRAC instrument on the *Spitzer Space Telescope* to study the atmospheres and physical properties of brown dwarfs. Alongside these observational projects, I work on the NIRSPEC upgrade for Keck, a project which seeks to replace the detectors, electronics, and motion control of the instrument in order to increase its efficiency and sensitivity. I briefly summarize each project below.

In Chapter 2, I present the analysis of a set of 228 J-band spectra of M, L, and T dwarfs in the NIRSPEC Brown Dwarf Spectroscopic Survey (BDSS; McLean et al. 2003). For the project, I observed many of the spectra, and reduced all of the spectra. I was responsible for the organization and quality-assurance of a large dataset gathered over 15 years using the NIRSPEC instrument on Keck. I measured K I Equivalent Widths and FeH absorption, both of which are known to correlate with the surface gravity of brown dwarfs. I compared to objects of known-age to calibrate the gravity features with age. In Martin et al. (2017), I showed that the gravity indicators can be useful for selecting targets younger than $\sim$30 Myr, but that these features can often be misleading and objects of similar ages and temperatures can have widely varying K I and FeH absorption strengths. Surprisingly, by the age of $\sim$100 Myr, we are not able to use gravity indicators to guarantee youth, an important consideration in determining new low-mass members of young moving groups. In addition to the surface gravity measurements, the paper presents 130 new J-band spectra of low-mass stars and brown dwarfs reduced and calibrated for the general public.

In Chapter 3, I present on work I started as a Visiting Graduate Student Fellow at IPAC. I observed late-type T and Y dwarf candidates with Keck/NIRSPEC. I reduced and analyzed their spectra and confirmed the discovery of 7 new ultracool dwarfs, including 1 new Y dwarf. I developed code to determine a more precise distortion map for the Spitzer IRAC channel 2 focal plane, using Gaia astrometric information to calibrate the precise locations of reference field stars, which I presented at Cool Stars 2016. I also developed code to measure astrometric fits to 22 late-T and Y dwarfs using IRAC channel 2 data as part of our Spitzer Parallax Program (PI: Kirkpatrick). With my code, I measured parallaxes to three new late-T dwarfs and three new Y dwarfs, and updated parallaxes for 15 Y dwarfs. I measured absolute magnitudes of late-T and Y dwarfs and calculated photometric distances for objects lacking astrometric measurements (Martin et al., submitted; Kirkpatrick et al. in prep). These measurements are critical for understanding the absolute physical properties of the coldest brown dwarfs and for determining the functional form of the substellar mass function, which has implications for star formation theory and whether or not there is a low-mass cutoff to star formation. I found that the near-infrared spectral typing sequence is no longer a good temperature indicator for Y dwarfs, because objects of the same spectral type spanned several magnitudes in M_J. The James Webb Space Telescope will have the capability of observing these Y dwarfs in the 3–10 μm regime, where they emit most of their light.

Chapter 4 highlights work I have done as the Instrument Scientist for the NIRSPEC upgrade for W. M. Keck Observatory. The upgrade will replace the spectrometer and slit-viewing camera detectors with Teledyne H2RG arrays, replace the slit-viewing camera to extend its wavelength coverage to 1–5 μm, and replace all transputer electronics with updated motion control and electronic devices. My role on the NIRSPEC upgrade team has included detector characterization and testing of the H2RG arrays, as well as characterizing the expected performance of the upgraded instrument (Martin et al., 2014). I work with our software and mechanical engineers to perform mechanical prototyping and vacuum cryogenic testing of the upgraded detector head in the UCLA IR lab. I have also created a new optical design for the slit-viewing camera (Martin et al., 2016). I used ZEMAX optical design

software to create and evaluate a new slit-viewing camera capable of observing from 1–5 μm, an improvement from the current 1–2.5 μm capabilities.

I also present work done as part of the team to test a laser frequency comb as a wavelength calibration tool for precision radial velocity studies. I co-ran observing runs in Dec 2014, May 2015, and Sep 2017 to test two different laser frequency combs with the NIRSPEC instrument. I reduced and analyzed data of the laser comb images to demonstrate the capabilities of the laser comb as a precise radial velocity wavelength calibration tool. The laser comb data allowed us to test for instrumental stability of NIRSPEC and measure instrumental fluctuations in the wavelength solution, which will be used to upgrade the instrument to provide further stability. My work contributed to Yi et al. (2016), the first demonstration of a laser-frequency comb as a wavelength calibration technique at an astronomical observatory, and Suh et al., submitted, a follow-up study showing a novel soliton laser comb used to attempt to detect an extrasolar planet.

Our team passed the design review for the NIRSPEC upgrade in Fall 2017, and over the coming months I will be working to test detectors, assemble and align the optomechanical components, test electronics and motion controllers, and update software. We will commission the instrument starting in late Summer 2018.

Bibliography

Allard, F., Homeier, D., & Freytag, B. 2012, Royal Society of London Philosophical Transactions Series A, 370, 2765

Aller, K. M., Liu, M. C., Magnier, E. A., et al. 2016, ApJ, 821, 120

Allers, K. N., & Liu, M. C. 2013, The Astrophysical Journal, 772, 79

Allers, K. N., Liu, M. C., Dupuy, T. J., & Cushing, M. C. 2010, ApJ, 715, 561

Allers, K. N., Jaffe, D. T., Luhman, K. L., et al. 2007, ApJ, 657, 511

Allers, K. N., Liu, M. C., Shkolnik, E., et al. 2009, The Astrophysical Journal, 697, 824

Ardila, D., Martín, E., & Basri, G. 2000, The Astronomical Journal, 120, 479

Artigau, É., Doyon, R., Lafrenière, D., et al. 2006, The Astrophysical Journal Letters, 651, L57

Baraffe, I., Chabrier, G., Barman, T. S., Allard, F., & Hauschildt, P. H. 2003, A&A, 402, 701

Baraffe, I., Homeier, D., Allard, F., & Chabrier, G. 2015, A&A, 577, A42

Barrado y Navascués, D., Béjar, V. J. S., Mundt, R., et al. 2003, Astronomy and Astrophysics, 404, 171

Basri, G., & Martín, E. L. 1999, The Astrophysical Journal, 510, 266

Bate, M. R. 2005, MNRAS, 363, 363

Becklin, E. E., & Zuckerman, B. 1988, Nature, 336, 656

Beichman, C., Gelino, C. R., Kirkpatrick, J. D., et al. 2014, ApJ, 783, 68

Béjar, V. J. S., Osorio, M. R. Z., & Rebolo, R. 1999, The Astrophysical Journal, 521, 671

Béjar, V. J. S., Zapatero Osorio, M. R., Rebolo, R., et al. 2011, The Astrophysical Journal, 743, 64

Bell, C. P. M., Mamajek, E. E., & Naylor, T. 2016, in IAU Symposium, Vol. 314, IAU Symposium, ed. J. H. Kastner, B. Stelzer, & S. A. Metchev, 41–48

Best, W. M. J., Liu, M. C., Magnier, E. A., et al. 2015, ApJ, 814, 118

Bouvier, J., Stauffer, J. R., Martin, E. L., et al. 1998, Astronomy and Astrophysics, 336, 490

Briceño, C., Hartmann, L., Stauffer, J., & Martín, E. 1998, The Astronomical Journal, 115, 2074

Briceño, C., Luhman, K. L., Hartmann, L., Stauffer, J. R., & Kirkpatrick, J. D. 2002, The Astrophysical Journal, 580, 317

Brown, A. G. A., de Geus, E. J., & de Zeeuw, P. T. 1994, A&A, 289, 101

Burgasser, A. J. 2004, ApJS, 155, 191

Burgasser, A. J. 2007, The Astronomical Journal, 134, 1330

Burgasser, A. J. 2008, in Astronomical Society of the Pacific Conference Series, Vol. 384, 14th Cambridge Workshop on Cool Stars, Stellar Systems, and the Sun, ed. G. van Belle, 126

Burgasser, A. J., Bardalez-Gagliuffi, D. C., & Gizis, J. E. 2011a, AJ, 141, 70

Burgasser, A. J., Blake, C. H., Gelino, C. R., Sahlmann, J., & Bardalez Gagliuffi, D. 2016a, ArXiv e-prints, arXiv:1605.05390

Burgasser, A. J., Cruz, K. L., & Kirkpatrick, J. D. 2007, The Astrophysical Journal, 657, 494

Burgasser, A. J., Geballe, T. R., Leggett, S. K., Kirkpatrick, J. D., & Golimowski, D. A. 2006, ApJ, 637, 1067

Burgasser, A. J., Geballe, T. R., Leggett, S. K., Kirkpatrick, J. D., & Golimowski, D. A. 2006, The Astrophysical Journal, 637, 1067

Burgasser, A. J., Kirkpatrick, J. D., Liebert, J., & Burrows, A. 2003, ApJ, 594, 510

Burgasser, A. J., Kirkpatrick, J. D., McElwain, M. W., et al. 2003a, The Astronomical Journal, 125, 850

Burgasser, A. J., Marley, M. S., Ackerman, A. S., et al. 2002, ApJ, 571, L151

Burgasser, A. J., Sitarski, B. N., Gelino, C. R., Logsdon, S. E., & Perrin, M. D. 2011b, ApJ, 739, 49

Burgasser, A. J., Witte, S., Helling, C., et al. 2009, The Astrophysical Journal, 697, 148

Burgasser, A. J., Kirkpatrick, J. D., Brown, M. E., et al. 1999, The Astrophysical Journal Letters, 522, L65

Burgasser, A. J., Wilson, J. C., Kirkpatrick, J. D., et al. 2000a, The Astronomical Journal, 120, 1100

Burgasser, A. J., Kirkpatrick, J. D., Cutri, R. M., et al. 2000b, The Astrophysical Journal Letters, 531, L57

Burgasser, A. J., Kirkpatrick, J. D., Brown, M. E., et al. 2002, The Astrophysical Journal, 564, 421

Burgasser, A. J., Kirkpatrick, J. D., Burrows, A., et al. 2003b, The Astrophysical Journal, 592, 1186

Burgasser, A. J., Lopez, M. A., Mamajek, E. E., et al. 2016b, ApJ, 820, 32

Burningham, B., Pinfield, D. J., Lucas, P. W., et al. 2010, MNRAS, 406, 1885

Burrows, A., Hubbard, W. B., Lunine, J. I., & Liebert, J. 2001, Reviews of Modern Physics, 73, 719

Burrows, A., Sudarsky, D., & Lunine, J. I. 2003, ApJ, 596, 587

Burrows, A., Marley, M., Hubbard, W. B., et al. 1997, ApJ, 491, 856

Canty, J. I., Lucas, P. W., Roche, P. F., & Pinfield, D. J. 2013, Monthly Notices of the Royal Astronomical Society, 435, 2650

Carey, S. J., Surace, J. A., Glaccum, W. J., et al. 2010, in Proc. SPIE, Vol. 7731, Space Telescopes and Instrumentation 2010: Optical, Infrared, and Millimeter Wave, 77310N

Castro, P. J., Gizis, J. E., Harris, H. C., et al. 2013, The Astrophysical Journal, 776, 126

Chiu, K., Fan, X., Leggett, S. K., et al. 2006, The Astronomical Journal, 131, 2722

Close, L. M., Siegler, N., Freed, M., & Biller, B. 2003, The Astrophysical Journal, 587, 407

Cohen, M., & Kuhi, L. V. 1979, The Astrophysical Journal Supplement Series, 41, 743

Comeron, F., Rieke, G. H., Burrows, A., & Rieke, M. J. 1993, The Astrophysical Journal, 416, 185

Cruz, K. L., Kirkpatrick, J. D., & Burgasser, A. J. 2009, The Astronomical Journal, 137, 3345

Cruz, K. L., Reid, I. N., Liebert, J., Kirkpatrick, J. D., & Lowrance, P. J. 2003, The Astronomical Journal, 126, 2421

Cushing, M. C., Kirkpatrick, J. D., Gelino, C. R., et al. 2014, AJ, 147, 113

Cushing, M. C., Marley, M. S., Saumon, D., et al. 2008, ApJ, 678, 1372

Cushing, M. C., Kirkpatrick, J. D., Gelino, C. R., et al. 2011, ApJ, 743, 50

Cushing, M. C., Hardegree-Ullman, K. K., Trucks, J. L., et al. 2016, ApJ, 823, 152

Dahn, C. C., Harris, H. C., Vrba, F. J., et al. 2002, The Astronomical Journal, 124, 1170

Delfosse, X., Tinney, C. G., Forveille, T., et al. 1997, Astronomy and Astrophysics, 327, L25

Dello Russo, N., Bonev, B. P., DiSanti, M. A., et al. 2005, ApJ, 621, 537

Dupuy, T. J., & Kraus, A. L. 2013, Science, 341, 1492

Dupuy, T. J., & Liu, M. C. 2012, ApJS, 201, 19

EROS Collaboration, Goldman, B., Delfosse, X., et al. 1999, Astronomy and Astrophysics, 351, L5

Faherty, J. K., Burgasser, A. J., Cruz, K. L., et al. 2009, AJ, 137, 1

Faherty, J. K., Riedel, A. R., Cruz, K. L., et al. 2016, ApJS, 225, 10

Festin, L. 1998, Monthly Notices of the Royal Astronomical Society, 298, L34

Filippazzo, J. C., Rice, E. L., Faherty, J., et al. 2015, ApJ, 810, 158

Gagné, J., Burgasser, A. J., Faherty, J. K., et al. 2015a, ApJ, 808, L20

Gagné, J., Lafrenière, D., Doyon, R., Malo, L., & Artigau, É. 2014, The Astrophysical Journal, 783, 121

Gagné, J., Lafrenière, D., Doyon, R., Malo, L., & Artigau, É. 2015b, ApJ, 798, 73

Gagné, J., Faherty, J. K., Cruz, K. L., et al. 2015c, ArXiv e-prints, arXiv:1506.07712

Gagné, J., Faherty, J. K., Mamajek, E. E., et al. 2016, ArXiv e-prints, arXiv:1612.02881

Gaia Collaboration, Brown, A. G. A., Vallenari, A., et al. 2016a, A&A, 595, A2

Gaia Collaboration, Prusti, T., de Bruijne, J. H. J., et al. 2016b, A&A, 595, A1

Geballe, T. R., Knapp, G. R., Leggett, S. K., et al. 2002, ApJ, 564, 466

Geers, V., Scholz, A., Jayawardhana, R., et al. 2011, The Astrophysical Journal, 726, 23

Gizis, J. E. 2002, The Astrophysical Journal, 575, 484

Gizis, J. E., Kirkpatrick, J. D., & Wilson, J. C. 2001, The Astronomical Journal, 121, 2185

Gizis, J. E., Monet, D. G., Reid, I. N., et al. 2000, The Astronomical Journal, 120, 1085

Gizis, J. E., Reid, I. N., Knapp, G. R., et al. 2003, The Astronomical Journal, 125, 3302

Green, R. M. 1985, Spherical astronomy

Greene, T. P., & Meyer, M. R. 1995, ApJ, 450, 233

Greene, T. P., & Young, E. T. 1992, The Astrophysical Journal, 395, 516

Hall, P. B. 2002, The Astrophysical Journal Letters, 564, L89

Haro, G., & Chavira, E. 1966, Vistas in Astronomy, 8, 89

Hauschildt, P. H., Baron, E., & Allard, F. 1997, ApJ, 483, 390

Hawley, S. L., Covey, K. R., Knapp, G. R., et al. 2002, The Astronomical Journal, 123, 3409

Hayashi, C., & Nakano, T. 1963, Progress of Theoretical Physics, 30, 460

Henry, T. J., & Kirkpatrick, J. D. 1990, The Astrophysical Journal Letters, 354, L29

Ingalls, J. G., Krick, J. E., Carey, S. J., et al. 2012, in Proc. SPIE, Vol. 8442, Space Telescopes and Instrumentation 2012: Optical, Infrared, and Millimeter Wave, 84421Y

Jenkins, J. S., Ramsey, L. W., Jones, H. R. A., et al. 2009, The Astrophysical Journal, 704, 975

Kellogg, K., Metchev, S., Gagné, J., & Faherty, J. 2016, ApJ, 821, L15

Kendall, T. R., Delfosse, X., Martín, E. L., & Forveille, T. 2004, Astronomy and Astrophysics, 416, L17

Kirkpatrick, J. D. 1992, Ph.D. Thesis, 7

Kirkpatrick, J. D. 2005, ARA&A, 43, 195

Kirkpatrick, J. D., Barman, T. S., Burgasser, A. J., et al. 2006, ApJ, 639, 1120

Kirkpatrick, J. D., Beichman, C. A., & Skrutskie, M. F. 1997, The Astrophysical Journal, 476, 311

Kirkpatrick, J. D., Dahn, C. C., Monet, D. G., et al. 2001, AJ, 121, 3235

Kirkpatrick, J. D., Henry, T. J., & McCarthy, Jr., D. W. 1991, The Astrophysical Journal Supplement Series, 77, 417

Kirkpatrick, J. D., Liebert, J., Cruz, K. L., Gizis, J. E., & Reid, I. N. 2001, Publications of the Astronomical Society of the Pacific, 113, 814

Kirkpatrick, J. D., Reid, I. N., Liebert, J., et al. 1999, ApJ, 519, 802

Kirkpatrick, J. D., Reid, I. N., Liebert, J., et al. 2000, The Astronomical Journal, 120, 447

Kirkpatrick, J. D., Cruz, K. L., Barman, T. S., et al. 2008, ApJ, 689, 1295

Kirkpatrick, J. D., Looper, D. L., Burgasser, A. J., et al. 2010, The Astrophysical Journal Supplement Series, 190, 100

Kirkpatrick, J. D., Cushing, M. C., Gelino, C. R., et al. 2011, ApJS, 197, 19

Kirkpatrick, J. D., Gelino, C. R., Cushing, M. C., et al. 2012, ApJ, 753, 156

Kirkpatrick, J. D., Schneider, A., Fajardo-Acosta, S., et al. 2014, The Astrophysical Journal, 783, 122

Knapp, G. R., Leggett, S. K., Fan, X., et al. 2004, The Astronomical Journal, 127, 3553

Konopacky, Q. M., Ghez, A. M., Barman, T. S., et al. 2010, The Astrophysical Journal, 711, 1087

Kramida, A., Ralchenko, Y., Reader, J., & Team, N. A. 2015, NIST Atomic Spectra Database

Kraus, A. L., White, R. J., & Hillenbrand, L. A. 2005, The Astrophysical Journal, 633, 452

Kulas, K. R., McLean, I. S., & Steidel, C. C. 2012, in Proc. SPIE, Vol. 8453, High Energy, Optical, and Infrared Detectors for Astronomy V, 84531S

Kumar, S. S. 1962, AJ, 67, 579

—. 1963, ApJ, 137, 1121

Lawrence, A., Warren, S. J., Almaini, O., et al. 2007, MNRAS, 379, 1599

Leggett, S. K., Morley, C. V., Marley, M. S., & Saumon, D. 2015, ApJ, 799, 37

Leggett, S. K., Morley, C. V., Marley, M. S., et al. 2013, ApJ, 763, 130

Leggett, S. K., Tremblin, P., Esplin, T. L., Luhman, K. L., & Morley, C. V. 2017, ApJ, 842, 118

Leggett, S. K., Geballe, T. R., Fan, X., et al. 2000, The Astrophysical Journal Letters, 536, L35

Leggett, S. K., Cushing, M. C., Hardegree-Ullman, K. K., et al. 2016, ApJ, 830, 141

Lépine, S., Rich, R. M., & Shara, M. M. 2003, The Astronomical Journal, 125, 1598

Lépine, S., Shara, M. M., & Rich, R. M. 2002, The Astronomical Journal, 124, 1190

Leviton, D. B., & Frey, B. J. 2004, in Proc. SPIE, Vol. 5494, Optical Fabrication, Metrology, and Material Advancements for Telescopes, ed. E. Atad-Ettedgui & P. Dierickx, 492–504

Line, M. R., Teske, J., Burningham, B., Fortney, J. J., & Marley, M. S. 2015, ApJ, 807, 183

Line, M. R., Marley, M. S., Liu, M. C., et al. 2017, ApJ, 848, 83

Lodders, K. 1999, ApJ, 519, 793

Lodieu, N., Deacon, N. R., & Hambly, N. C. 2012a, Monthly Notices of the Royal Astronomical Society, 422, 1495

Lodieu, N., Deacon, N. R., Hambly, N. C., & Boudreault, S. 2012b, Monthly Notices of the Royal Astronomical Society, 426, 3403

Looper, D. L., Kirkpatrick, J. D., & Burgasser, A. J. 2007, The Astronomical Journal, 134, 1162

Looper, D. L., Kirkpatrick, J. D., Cutri, R. M., et al. 2008, ApJ, 686, 528

Low, C., & Lynden-Bell, D. 1976, MNRAS, 176, 367

Lowrance, P. J., Becklin, E. E., Schneider, G., et al. 2005, The Astronomical Journal, 130, 1845

Lowrance, P. J., Carey, S. J., Ingalls, J. G., et al. 2014, in Proc. SPIE, Vol. 9143, Space Telescopes and Instrumentation 2014: Optical, Infrared, and Millimeter Wave, 914358

Lucas, P. W., Roche, P. F., Allard, F., & Hauschildt, P. H. 2001, MNRAS, 326, 695

Luhman, K. L. 2012, ARA&A, 50, 65

—. 2013, ApJ, 767, L1

—. 2014, ApJ, 786, L18

Luhman, K. L., Briceño, C., Stauffer, J. R., et al. 2003, The Astrophysical Journal, 590, 348

Luhman, K. L., Burgasser, A. J., & Bochanski, J. J. 2011, ApJ, 730, L9

Luhman, K. L., & Esplin, T. L. 2016, AJ, 152, 78

Luhman, K. L., Hernández, J., Downes, J. J., Hartmann, L., & Briceño, C. 2008, The Astrophysical Journal, 688, 362

Luhman, K. L., Liebert, J., & Rieke, G. H. 1997, The Astrophysical Journal Letters, 489, L165

Luhman, K. L., & Mamajek, E. E. 2012, The Astrophysical Journal, 758, 31

Luhman, K. L., Whitney, B. A., Meade, M. R., et al. 2006, The Astrophysical Journal, 647, 1180

Luyten, W. J. 1979a, A catalogue of stars with proper motions exceeding 0”5 annually (Catalog)

—. 1979b, New Luyten catalogue of stars with proper motions larger than two tenths of an arcsecond; and first supplement; NLTT. (Catalog)

Mace, G. N., Kirkpatrick, J. D., Cushing, M. C., et al. 2013, The Astrophysical Journal Supplement Series, 205, 6

Mace, G. N., Kirkpatrick, J. D., Cushing, M. C., et al. 2013, ApJ, 777, 36

Macintosh, B., Graham, J. R., Barman, T., et al. 2015, Science, 350, 64

Malo, L., Doyon, R., Lafrenière, D., et al. 2013, ApJ, 762, 88

Mamajek, E. E. 2005, The Astrophysical Journal, 634, 1385

Mamajek, E. E., Bartlett, J. L., Seifahrt, A., et al. 2013, AJ, 146, 154

Marley, M. S., & Robinson, T. D. 2014, ArXiv e-prints, arXiv:1410.6512

Martin, E. C., Fitzgerald, M. P., McLean, I. S., Kress, E., & Wang, E. 2016, in Proc. SPIE, Vol. 9908, Ground-based and Airborne Instrumentation for Astronomy VI, 99082R

Martin, E. C., Fitzgerald, M. P., McLean, I. S., et al. 2014, in Proc. SPIE, Vol. 9147, Ground-based and Airborne Instrumentation for Astronomy V, 914781

Martin, E. C., Mace, G. N., McLean, I. S., et al. 2017, ApJ, 838, 73

Martín, E. L., Basri, G., Gallegos, J. E., et al. 1998, The Astrophysical Journal Letters, 499, L61

Martín, E. L., Brandner, W., Bouvier, J., et al. 2000a, The Astrophysical Journal, 543, 299

Martín, E. L., Delfosse, X., Basri, G., et al. 1999, The Astronomical Journal, 118, 2466

Martín, E. L., Delfosse, X., & Guieu, S. 2004, The Astronomical Journal, 127, 449

Martín, E. L., Dougados, C., Magnier, E., et al. 2001, The Astrophysical Journal Letters, 561, L195

Martín, E. L., Koresko, C. D., Kulkarni, S. R., Lane, B. F., & Wizinowich, P. L. 2000b, The Astrophysical Journal Letters, 529, L37

Martin, E. L., Rebolo, R., & Zapatero-Osorio, M. R. 1996, The Astrophysical Journal, 469, 706

Mayor, M., & Queloz, D. 1995, Nature, 378, 355

McCallon, H. L., Fowler, J. W., Laher, R. R., Masci, F. J., & Moshir, M. 2007, PASP, 119, 1308

McGovern, M. R., Kirkpatrick, J. D., McLean, I. S., et al. 2004, The Astrophysical Journal, 600, 1020

McLean, I. S., Graham, J. R., Becklin, E. E., et al. 2000, in Society of Photo-Optical Instrumentation Engineers (SPIE) Conference Series, Vol. 4008, Society of Photo-Optical Instrumentation Engineers (SPIE) Conference Series, ed. M. Iye & A. F. Moorwood, 1048–1055

McLean, I. S., McGovern, M. R., Burgasser, A. J., et al. 2003, ApJ, 596, 561

McLean, I. S., Prato, L., Kim, S. S., et al. 2001, ApJ, 561, L115

McLean, I. S., Prato, L., McGovern, M. R., et al. 2007, The Astrophysical Journal, 658, 1217

McLean, I. S., Becklin, E. E., Bendiksen, O., et al. 1998, in Society of Photo-Optical Instrumentation Engineers (SPIE) Conference Series, Vol. 3354, Society of Photo-Optical Instrumentation Engineers (SPIE) Conference Series, ed. A. M. Fowler, 566–578

Metchev, S. A., Heinze, A., Apai, D., et al. 2015, ApJ, 799, 154

Monnier, J. D., Che, X., Zhao, M., et al. 2012, ApJ, 761, L3

Morley, C. V., Fortney, J. J., Marley, M. S., et al. 2012, ApJ, 756, 172

Morley, C. V., Marley, M. S., Fortney, J. J., et al. 2014, ApJ, 787, 78

Muzerolle, J., Hillenbrand, L., Calvet, N., Briceño, C., & Hartmann, L. 2003, The Astrophysical Journal, 592, 266

Mužić, K., Scholz, A., Geers, V., Jayawardhana, R., & Tamura, M. 2012, The Astrophysical Journal, 744, 134

Nakajima, T., Oppenheimer, B. R., Kulkarni, S. R., et al. 1995, Nature, 378, 463

Natta, A., Testi, L., Comerón, F., et al. 2002, Astronomy and Astrophysics, 393, 597

Naud, M.-E., Artigau, É., Malo, L., et al. 2014, ApJ, 787, 5

Padoan, P., Nordlund, Å., Kritsuk, A. G., Norman, M. L., & Li, P. S. 2007, ApJ, 661, 972

Pavlenko, Y. V., Jones, H. R. A., Lyubchik, Y., Tennyson, J., & Pinfield, D. J. 2006, Astronomy and Astrophysics, 447, 709

Pecaut, M. J., Mamajek, E. E., & Bubar, E. J. 2012, ApJ, 746, 154

Prato, L., Mace, G. N., Rice, E. L., et al. 2015, ApJ, 808, 12

Probst, R. G. 1983, The Astrophysical Journal Supplement Series, 53, 335

Prochaska, J. X., Bloom, J. S., Chen, H.-W., et al. 2004, ApJ, 611, 200

Prosser, C. F. 1994, The Astronomical Journal, 107, 1422

Rebolo, R., Zapatero Osorio, M. R., Madruga, S., et al. 1998, Science, 282, 1309

Rebolo, R., Zapatero Osorio, M. R., & Martín, E. L. 1995, Nature, 377, 129

Reid, I. N., Cruz, K. L., Kirkpatrick, J. D., et al. 2008, The Astronomical Journal, 136, 1290

Reid, I. N., Gizis, J. E., Kirkpatrick, J. D., & Koerner, D. W. 2001, AJ, 121, 489

Reid, I. N., Kirkpatrick, J. D., Gizis, J. E., et al. 2000, The Astronomical Journal, 119, 369

Reid, I. N., Lewitus, E., Allen, P. R., Cruz, K. L., & Burgasser, A. J. 2006, AJ, 132, 891

Reiners, A., & Basri, G. 2009, ApJ, 705, 1416

Ribas, I. 2003, Astronomy and Astrophysics, 400, 297

Rice, E. L., Barman, T., Mclean, I. S., Prato, L., & Kirkpatrick, J. D. 2010, The Astrophysical Journal Supplement Series, 186, 63

Rice, E. L., Faherty, J. K., Cruz, K., et al. 2011, in Astronomical Society of the Pacific Conference Series, Vol. 448, 16th Cambridge Workshop on Cool Stars, Stellar Systems, and the Sun, ed. C. Johns-Krull, M. K. Browning, & A. A. West, 481

Rieke, G. H., & Rieke, M. J. 1990, The Astrophysical Journal Letters, 362, L21

Robichaud, J. L., Zellers, B., Philippon, R., McLean, I. S., & Figer, D. F. 1998, in Proc. SPIE, Vol. 3354, Infrared Astronomical Instrumentation, ed. A. M. Fowler, 1068–1076

Ruiz, M. T., Leggett, S. K., & Allard, F. 1997, The Astrophysical Journal Letters, 491, L107

Salyk, C., Pontoppidan, K. M., Blake, G. A., et al. 2008, ApJ, 676, L49

Saumon, D., & Marley, M. S. 2008, ApJ, 689, 1327

Saumon, D., Marley, M. S., Abel, M., Frommhold, L., & Freedman, R. S. 2012, ApJ, 750, 74

Schmidt, S. J., West, A. A., Hawley, S. L., & Pineda, J. S. 2010, AJ, 139, 1808

Schneider, A. C., Cushing, M. C., Kirkpatrick, J. D., et al. 2014, AJ, 147, 34

Schneider, A. C., Windsor, J., Cushing, M. C., Kirkpatrick, J. D., & Wright, E. L. 2016, ApJ, 822, L1

Schneider, A. C., Cushing, M. C., Kirkpatrick, J. D., et al. 2015, ApJ, 804, 92

Schneider, D. P., Greenstein, J. L., Schmidt, M., & Gunn, J. E. 1991, The Astronomical Journal, 102, 1180

Sheppard, S. S., & Cushing, M. C. 2009, The Astronomical Journal, 137, 304

Simon, M., Bender, C., & Prato, L. 2006, ApJ, 644, 1183

Sivarani, T., Lépine, S., Kembhavi, A. K., & Gupchup, J. 2009, The Astrophysical Journal Letters, 694, L140

Skemer, A. J., Morley, C. V., Allers, K. N., et al. 2016, ApJ, 826, L17

Skrutskie, M. F., Cutri, R. M., Stiening, R., et al. 2006, AJ, 131, 1163

Slesnick, C. L., Carpenter, J. M., & Hillenbrand, L. A. 2006, The Astronomical Journal, 131, 3016

Smart, R. L., Ioannidis, G., Jones, H. R. A., Bucciarelli, B., & Lattanzi, M. G. 2010, A&A, 514, A84

Smart, R. L., Apai, D., Kirkpatrick, J. D., et al. 2017, MNRAS, 468, 3764

Smart, W. M., & Green, R. M. 1977, Textbook on Spherical Astronomy, 446

Stark, D. P., Ellis, R. S., Richard, J., et al. 2007, ApJ, 663, 10

Stauffer, J., Hamilton, D., Probst, R., Rieke, G., & Mateo, M. 1989, The Astrophysical Journal Letters, 344, L21

Stauffer, J. R., Schultz, G., & Kirkpatrick, J. D. 1998, The Astrophysical Journal Letters, 499, L199

Stauffer, J. R., Navascués, D. B. y., Bouvier, J., et al. 1999, The Astrophysical Journal, 527, 219

Stauffer, J. R., Hartmann, L. W., Fazio, G. G., et al. 2007, The Astrophysical Journal Supplement Series, 172, 663

Strauss, M. A., Fan, X., Gunn, J. E., et al. 1999, The Astrophysical Journal Letters, 522, L61

Stumpf, M. B., Brandner, W., Henning, T., et al. 2008, ArXiv e-prints, 0811, 556

Thompson, M. A., Kirkpatrick, J. D., Mace, G. N., et al. 2013, Publications of the Astronomical Society of the Pacific, 125, 809

Tinney, C. G., Faherty, J. K., Kirkpatrick, J. D., et al. 2014, ApJ, 796, 39

—. 2012, ApJ, 759, 60

Tremblin, P., Amundsen, D. S., Chabrier, G., et al. 2016, ApJ, 817, L19

van Biesbroeck, G. 1944, The Astronomical Journal, 51, 61

—. 1961, The Astronomical Journal, 66, 528

Vrba, F. J., Strom, K. M., Strom, S. E., & Grasdalen, G. L. 1975, The Astrophysical Journal, 197, 77

White, R. J., Ghez, A. M., Reid, I. N., & Schultz, G. 1999, The Astrophysical Journal, 520, 811

Wilking, B. A., Greene, T. P., & Meyer, M. R. 1999, The Astronomical Journal, 117, 469

Wilking, B. A., Meyer, M. R., Robinson, J. G., & Greene, T. P. 2005, The Astronomical Journal, 130, 1733

Wilson, J. C., Kirkpatrick, J. D., Gizis, J. E., et al. 2001, The Astronomical Journal, 122, 1989

Wilson, J. C., Eikenberry, S. S., Henderson, C. P., et al. 2003, in Proc. SPIE, Vol. 4841, Instrument Design and Performance for Optical/Infrared Ground-based Telescopes, ed. M. Iye & A. F. M. Moorwood, 451–458

Winters, J. G., Sevrinsky, R. A., Jao, W.-C., et al. 2017, AJ, 153, 14

Wolf, M. 1919, Veroeffentlichungen der Badischen Sternwarte zu Heidelberg, 7, 195

Wright, E. L., Eisenhardt, P. R. M., Mainzer, A. K., et al. 2010, AJ, 140, 1868

Yi, X., Vahala, K., Li, J., et al. 2016, Nature Communications, 7, 10436

York, D. G., Adelman, J., Anderson, Jr., J. E., et al. 2000, AJ, 120, 1579

Zapatero Osorio, M. R., Béjar, V. J. S., Martín, E. L., et al. 2000, Science, 290, 103

Zapatero Osorio, M. R., Béjar, V. J. S., Rebolo, R., Martín, E. L., & Basri, G. 1999, The Astrophysical Journal Letters, 524, L115

Zapatero Osorio, M. R., Rebolo, R., Martín, E. L., et al. 1997, The Astrophysical Journal Letters, 491, L81

Zuckerman, B., & Song, I. 2004, ARA&A, 42, 685

—. 2009, A&A, 493, 1149

Zuckerman, B., Vican, L., Song, I., & Schneider, A. 2013, ApJ, 778, 5